

Temperature and Burnup Correlated FCCI in U- 10Zr Metallic Fuel

William J. Carmack

May 2012



The INL is a U.S. Department of Energy National Laboratory
operated by Battelle Energy Alliance

Temperature and Burnup Correlated FCCI in U-10ZR Metallic Fuel

William J. Carmack

May 2012

**Idaho National Laboratory
Idaho Falls, Idaho 83415**

<http://www.inl.gov>

**Prepared for the
U.S. Department of Energy
Office of Nuclear Energy
Under DOE Idaho Operations Office
Contract DE-AC07-05ID14517**

**TEMPERATURE AND BURNUP CORRELATED FCCI IN U-10ZR METALLIC
FUEL**

A Dissertation

Presented in Partial Fulfillment of the Requirements for the

Degree of Doctor of Philosophy

with a

Major in Nuclear Engineering

in the

College of Engineering

University of Idaho

by



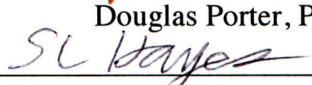
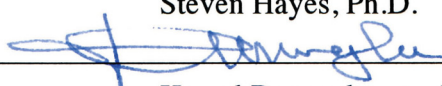
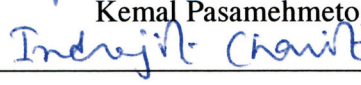
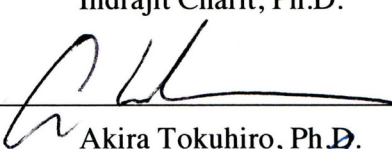
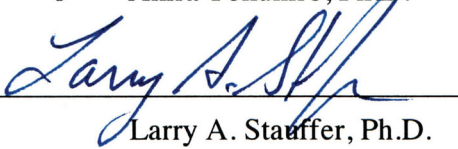
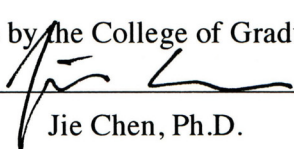
William J. Carmack

May 2012

Major Professor: Fred Gunnerson, Ph.D.

AUTHORIZATION TO SUBMIT DISSERTATION

This dissertation of William J. Carmack, submitted for the degree of Doctor of Philosophy (Ph.D.) with a major in Nuclear Engineering and titled "Temperature and Burnup Correlated FCCI in U-10Zr Metallic Fuel," has been reviewed in final form. Permission, as indicated by the signatures and dates given below, is now granted to submit final copies to the College of Graduate Studies for approval.

Major Professor	 Fred Gunnerson, Ph.D.	Date <u>5/7/2012</u>
Committee Members	 Douglas Porter, Ph.D.	Date <u>5/7/2012</u>
	 Steven Hayes, Ph.D.	Date <u>5/12/12</u>
	 Kemal Pasamehmetoglu, Ph.D.	Date <u>5/7/12</u>
	 Indrajit Charit, Ph.D.	Date <u>5/7/12</u>
Department Administrator	 Akira Tokuhira, Ph.D.	Date <u>5/7/12</u>
Discipline's College Dean	 Larry A. Stauffer, Ph.D.	Date <u>5/15/12</u>
Final Approval and Acceptance by the College of Graduate Studies		 Jie Chen, Ph.D.
		Date <u>6/6/12</u>

Abstract

Metallic fuels are proposed for use in advanced sodium cooled fast reactors and provide a number of advantages over other fuel types considering their fabricability, performance, recyclability, and safety. Resistance to cladding “breach” and subsequent release of fission products and fuel constituents to the nuclear power plant primary coolant system is a key performance parameter for a nuclear fuel system. In metallic fuel, FCCI weakens the cladding, especially at high power-high temperature operation, contributing to fuel pin breach. Empirical relationships for FCCI have been developed from a large body of data collected from in-pile (EBR-II) and out-of-pile experiments [1]. However, these relationships are unreliable in predicting FCCI outside the range of EBR-II experimental data. This dissertation examines new FCCI data extracted from the MFF-series of prototypic length metallic fuel irradiations performed in the Fast Flux Test Facility (FFTF). The fuel in these assemblies operated a temperature and burnup conditions similar to that in EBR-II but with axial fuel height three times longer than EBR-II experiments. Comparing FCCI formation data from FFTF and EBR-II provides new insight into FCCI formation kinetics.

A model is developed combining both production and diffusion of lanthanides to the fuel-cladding interface and subsequent reaction with the cladding. The model allows these phenomena to be influenced by fuel burnup (lanthanide concentrations) and operating temperature. Parameters in the model are adjusted to reproduce measured FCCI layer thicknesses from EBR-II and FFTF. The model predicts that, under appropriate conditions, rate of FCCI formation can be controlled by either fission product transport or by the reaction rate of the interaction species at the fuel-cladding interface.

This dissertation will help forward the design of metallic fuel systems for advanced sodium cooled fast reactors by allowing the prediction of FCCI layer formation in full length reactor designs. This should improve lifetime prediction of fuel performance capability for new advanced sodium cooled fast reactors with extended core designs.

Acknowledgement

Much of the experimental data presented and analyzed in this dissertation was generated and collected as a result of the efforts of numerous scientists and technicians at the Pacific Northwest National Laboratory, its predecessor Westinghouse-Hanford contractor, the Idaho National Laboratory and its predecessor Argonne National Laboratory-West. Their efforts are acknowledged, and their contributions to the field of nuclear science and engineering are sure to be appreciated by future generations of the nuclear community.

This work would not be possible had it not been for the many scientists and engineers responsible for metallic fuel development initiated in the EBR-II and FFTF reactors. These experiments are an invaluable national resource, some of which we are only now beginning to be analyzed. Many of the people responsible have passed on or have retired but their legacy and contributions will be remembered.

I would like to recognize and express my gratitude for the efforts of Dr. David Wootan at the PNNL. Dr. Wootan generated the power histories of the MFF-3 and MFF-5 assemblies using the run reports and data from the FFTF run logs.

The development of a multi-physics model is only possible due to the efforts of a dedicated group of scientists and engineers at the Idaho National Laboratory. Their efforts and assistance in utilizing the MOOSE/BISON environment are greatly appreciated.

I would like to thank my committee for their guidance and support during the course this work, especially Dr. Gunnerson for his acceptance of this dissertation well after his official retirement.

Finally, I would like to thank my family for their support, especially my Mother and Father who have always valued education.

This manuscript has been authored by a contractor of the U.S. Government for the U.S. Department of Energy, Office of Nuclear Energy, Science, and Technology (NE), under DOE-NE Idaho Operations Office Contract DEAC0705ID14517. Accordingly, the U.S. Government retains a nonexclusive, royalty-free license to publish or reproduce the published form of this contribution, or allow others to do so, for U.S. Government purposes.

Table of Contents

ABSTRACT	iii
ACKNOWLEDGEMENT	v
TABLE OF CONTENTS	vii
LIST OF FIGURES	ix
LIST OF TABLES	xiv
LIST OF ACRONYMS	xv
1 INTRODUCTION	1
1.1 BACKGROUND	1
1.2 METALLIC FUEL STEADY-STATE PERFORMANCE	3
1.3 THIS WORK	9
2 X447 EBR-II EXPERIMENT	11
2.1 AS-BUILT CONDITION	13
2.2 IRRADIATION CONDITIONS AND PERFORMANCE HISTORY	15
2.3 POSTIRRADIATION EXAMINATION	20
2.3.1 5 at. % Burnup Examinations (DP-03, 06, 69, 81)	20
2.3.1.1 DP-69 Postirradiation Examination	21
2.3.1.2 DP-81 Postirradiation Examination	23
2.3.2 10 at. % Burnup Examinations (DP-04, DP-11, DP-70, DP-75)	25
2.3.2.1 DP-04 Postirradiation Examination	26
2.3.2.2 DP-11 Postirradiation Examination	28
2.3.2.3 DP-70 and DP-75 Postirradiation Examination	36
3 MFF-3 AND MFF-5 FFTF EXPERIMENTS	40

3.1	AS-BUILT CONDITION	40
3.2	IRRADIATION CONDITIONS AND PERFORMANCE HISTORY	42
3.3	POSTIRRADIATION EXAMINATION	50
4	FCCI FORMATION WITH BURNUP AND TEMPERATURE	56
4.1	U-10Zr METALLIC FUEL EXPERIMENT DATA	56
4.2	U-19Pu-10Zr METALLIC FUEL EXPERIMENT DATA	64
5	BURNUP AND TEMPERATURE DEPENDANT FCCI MODEL	68
5.1	COUPLED THERMAL AND MASS DIFFUSION MODEL	69
5.1.1	<i>Conservation of Energy</i>	70
5.1.2	<i>Conservation of Mass</i>	71
5.1.3	<i>Verification of Soret and Fickian Diffusion BISON Kernels</i>	75
5.1.4	<i>Mesh Representation of Metallic Fuel Pin</i>	77
5.2	BISON MODEL COMPARED TO X447 AND MFF FCCI MEASUREMENTS	79
6	CONCLUSION	90
7	REFERENCES	92
	APPENDIX A - Metallographic Montages of X447 DP-69 Fuel Pin	96
	APPENDIX B - Metallographic Montages of X447 DP-04 Fuel Pin	103
	APPENDIX C - Metallographic Montages of X447 DP-70 Fuel Pin	111
	APPENDIX D - Metallographic Montages of X447 DP-75 Fuel Pin	123
	APPENDIX E - Metallographic Montages of MFF-3 and MFF-5 Fuel Pins	134
	APPENDIX F - Example BISON Model Input	145

List of Figures

Figure 1. Schematic of a metallic, sodium bonded, fast reactor fuel pin.....	1
Figure 2. FCCI between U-19Pu-10Zr and D9 austenitic stainless steel cladding.....	7
Figure 3. FCCI between U-19Pu-10Zr and HT-9 ferritic-martensitic stainless steel cladding.....	8
Figure 4. Photographs of the DP-70 and DP-75 pin breaches.	12
Figure 5. X447 Sub-Assembly Configuration.	15
Figure 6. Peak Linear Power for each EBR-II Cycle during X447 irradiation.....	16
Figure 7. Peak Inner Cladding Temperature for each EBR-II Cycle during X447 irradiation.....	17
Figure 8. Comparison of X447 Pin Power and Peak Inner Cladding Temperature Profiles. Values based on EFPD weighted values across all irradiation cycles.....	17
Figure 9. Axial Linear Power and temperature profiles for X447 Pin DP69. Values based on EFPD weighted values across all irradiation cycles.....	18
Figure 10. Axial Linear Power and temperature profiles for X447 Pin DP-04. Values based on EFPD weighted values across all irradiation cycles.....	18
Figure 11. Axial Linear Power and temperature profiles for X447 Pin DP-11. Values based on EFPD weighted values across all irradiation cycles.....	19
Figure 12. Axial Linear Power and temperature profiles for X447 Pin DP-70. Values based on EFPD weighted values across all irradiation cycles.....	19
Figure 13. Axial Linear Power and temperature profiles for X447 Pin DP-75. Values based on EFPD weighted values across all irradiation cycles.....	20
Figure 14. Axial burnup and pin diameter at 4.7 at. % for DP-69.....	22

Figure 15. Gross metallography of the DP-69 pin showing microstructure axially along the pin with FCCI thickness shown in μm	22
Figure 16. Typical 100 μm thick fuel-cladding interaction found in the DP-69 pin.	23
Figure 17. Neutron Radiograph of five X447 Pins - DP-81 is bottom pin in radiograph.....	24
Figure 18. Axial burnup and pin diameter at 4.8 at. % for DP-81	24
Figure 19. Radial microprobe elemental scan for uranium and zirconium in DP-81	25
Figure 20. Gross metallography of the DP-04 pin showing microstructure axially along the pin with FCMI thickness shown in μm	26
Figure 21. Etched view of the cladding in the region of greatest interaction at the 35 cm elevation of DP-04 (200X).....	27
Figure 22. Axial pin diametral profilometry with local burnup and radiograph of DP-04....	27
Figure 23. Axial pin diametral profilometry with local burnup and neutron radiograph of DP-11	29
Figure 24. Line scan and elemental analyses locations in DP-11 at 35.6 cm fuel column height.....	30
Figure 25. Microprobe scan of U-Zr distribution across the radial cross-section of DP-11 (Line X in Figure 24).	31
Figure 26. Distribution of iron and chromium across the radial cross section of DP-11 (Line X).....	32
Figure 27. Radial distribution of fission products across radial cross-section of DP-11 (Line X).....	33
Figure 28. Radial distribution of Mo and Pd fission products across DP-11 (Line X).....	34
Figure 29. Uranium-Zirconium distribution near cladding in an area of high FCCI.....	34
Figure 30. Cladding component distribution in a localized zone of high-FCCI.....	35

Figure 31. Radial distribution of fission products in a region of high-FCCI.....	36
Figure 32. Axial pin diametral profilometry with local burnup and radiograph of DP-70....	37
Figure 33. Gross metallography of the DP-70 pin showing microstructure axially along the pin with FCMI thickness shown in μm	38
Figure 34. Axial pin diametral profilometry with local burnup and radiograph of DP-75....	38
Figure 35. Gross metallography of the DP-75 pin showing microstructure axially along the pin with FCMI thickness shown in μm	39
Figure 36. FFTF Cycle 12B-1 Core Loading and positions of MFF-3 and MFF-5.	44
Figure 37. MFF-3 (4th Row Pin 193045) peak pin power (W/cm) and peak inner cladding temperature ($^{\circ}\text{C}$).....	46
Figure 38. Axial Linear Power and PICT profiles for MFF-3 Pin 193045. Values based on EFPD weighted values across all irradiation cycles.	47
Figure 39. MFF-5 (4 th Row Pin 195011) peak pin power (W/cm) and peak inner cladding temperature ($^{\circ}\text{C}$).	48
Figure 40. Axial Linear Power and PICT profiles for MFF-5 Pin 195011. Values based on EFPD weighted values across all irradiation cycles.	48
Figure 41. Photographs of the MFF-3 and MFF-5 assemblies following removal of the upper handling socket. Pins 193045 and 195011 have been marked along with the center pins for identification purposes.....	49
Figure 42. Profilometry analysis of MFF-5 – 195011 fuel pin overlaid with neutron radiograph.	53
Figure 43. Profilometry analysis of MFF-3 – 193045 fuel pin overlaid with neutron radiograph	53
Figure 44. MFF-5 Pin 195011 Neutron Radiography superimposed on gamma scan.....	53

Figure 45. MFF-3 Pin 193045 Neutron Radiography superimposed on gamma scan.....	53
Figure 46. Gross metallography of the MFF-3 pin 193045 showing microstructure along the axial length of the fuel column.	54
Figure 47. Gross metallography of the MFF-5 pin 195011 showing microstructure along the axial length of the fuel column.	55
Figure 48. 100 X magnification optical photomicrograph of high FCCI region of MFF-3 Pin 193045 at $X/L = 0.98$ - Sample 83T.....	55
Figure 49. FCCI formation axially along the DP-69 fuel pin from the X447 experiment. ...	58
Figure 50. FCCI formation axially along the DP-04 fuel pin from the X447 experiment.	59
Figure 51. FCCI formation axially along the DP-70 fuel pin from the X447 experiment.	60
Figure 52. FCCI formation axially along the DP-75 fuel pin from the X447 experiment.	61
Figure 53. FCCI formation axially along the 193045 fuel pin from the MFF-3 experiment.	62
Figure 54. FCCI formation axially along the 195011 fuel pin from the MFF-5 experiment.	63
Figure 55. Relative Gamma scanning data for Pin 181193 of the IFR-1 (U-19Pu-10Zr) experiment in FFTF [31].....	66
Figure 56. FCCI measurements for IFR-1 Pin 181193 [31].	67
Figure 57. Formation of a lanthanide fuel-cladding interaction layer at the inner surface of the cladding	73
Figure 58. Diagram depicting the mechanism and boundary conditions present in the diffusion of fuel, cladding, and fission product constituents leading to the formation of fuel-cladding interaction.....	73
Figure 59. Assignment of boundary conditions for simple cube geometry	76
Figure 60. Coupled Solution Soret in a simple cube geometry with $C(0, t) = 1$, $C(1, t) = 0$	77

Figure 61. Solution to Soret kernel check using Mathematica [42].	77
Figure 62. 2-dimensional finite element mesh representation of X447 fuel geometry used as input in BISON calculation.	78
Figure 63. Graphical representation of BISON boundary condition assignments.....	79
Figure 64. Plot of measured and BISON predicted FCCI thickness versus fuel centerline temperature.	82
Figure 65. Plot of measured and BISON predicted FCCI thickness versus inner cladding temperature.	83
Figure 66. Plot of equation (1) for various temperatures of interest to interaction layer formation.....	84
Figure 67. Time averaged inner cladding temperature, measured FCCI thickness, and predicted FCCI thickness for X447 DP-70 Fuel Pin versus axial fuel column location.....	84
Figure 68. Time averaged inner cladding temperature, measured FCCI thickness, and predicted FCCI thickness for MFF-5 195011 fuel pin versus axial fuel column location.....	86
Figure 69. Graph depicting BISON simulation exceeding reaction rate correlation prediction indicating possibility of surface reaction controlled FCCI formation.	86
Figure 70. Comparative plot of normalized power profiles typical of EBR-II and FFTF.....	87
Figure 71. X447 DP-75 Cycle-by-cycle Cumulative Burnup and BISON model incremental FCCI formation.	88

List of Tables

Table 1. Nominal composition of D-9 and HT-9 Steels..... 6

Table 2. X447 Nominal Design Features..... 13

Table 3. DP-11 Zonal Radial Composition Summary 31

Table 4. Nominal Design Features of MFF-3 and MFF-5 Assemblies 42

Table 5. Summary of MFF-3 and MFF-5 initial test operating conditions. 43

Table 6. Summary of FCCI data from X447, MFF-3, MFF-5, and IFR-1. 65

Table 7. Summary of BISON generated calculation results for X447 and MFF fuel pins..... 81

List of Acronyms

ANL-W	Argonne National Laboratory – West
BOC	Beginning of cycle
BOL	Beginning of life
CRBR	Clinch River Breeder Reactor
D9	Common designation for 20% cold-worked stainless steel
DFR	Dounreay Fast Reactor
EBR-I	Experimental Breeder Reactor I
EBR-II	Experimental Breeder Reactor II
EPMA	Electron probe micro-analysis
EOC	End of cycle
EFPD	Effective full power day
FCCI	Fuel Cladding Chemical Interaction
FCLT	Fuel centerline temperature
FCCI	Fuel-cladding chemical interaction
FFTF	Fast Flux Test Facility
HT-9	Common designation for ferritic-martensitic steel
HFEF	Hot Fuel Examination Facility
ICP-MS	Inductively-coupled plasma mass spectrometry
IFR	Integral Fast Reactor
INL	Idaho National Laboratory
MFF	Experiment designation for the FFTF MFF series of experiments
MOOSE	Multi-physics Object Oriented Simulation Environment
PICT	Peak inner cladding temperature

PNNL	Pacific Northwest National Laboratory
SAFE	Steady state and transient thermal Analysis of LMR Fuel Elements
X447	Experiment designation for the EBR-II X447 experiment

1 INTRODUCTION

1.1 *Background*

Fast reactor development programs have been conducted over the past five decades. Originally, early fast reactor developers in the United States favored metallic fuel due to its high fissile density and compatibility with sodium. As metallic fuels continued in development it was discovered that low smear density allowed fuel operation to higher burnups [2]. The goal of fuel development programs for future fast reactors is to develop and qualify for operation, a nuclear fuel system that performs all of the functions of a conventional fast spectrum nuclear fuel while also destroying recycled actinide transmutation products. Such a fuel would provide a mechanism for closure of the nuclear fuel cycle and provide a path for the disposition of the actinide products formed in light water reactor fuel. Metallic fuels are candidates for this application, based on documented performance of metallic fast reactor fuels and the early results of fuel tests currently being conducted in U.S. and international transmutation fuel development programs [3].

Metallic fuel, shown schematically in Figure 1, was selected for fueling many of the first reactors in the United States, including the Experimental Breeder Reactors- I and II (EBR-I & EBR-II) in Idaho, the FERMI-I reactor in Michigan, and the Dounreay Fast Reactor (DFR) in the United Kingdom [4, 5]. Metallic U-Pu-Zr alloys were the reference fuel for the United States Integral Fast Reactor (IFR) program [6]. An extensive database on the performance of advanced metallic fuels was generated as a result of the operation of these reactors and the IFR program.

The EBR-II operational and fuel qualification data includes the irradiation of over 30,000 Mark-II driver fuel pins [7, 8], 13,000 Mark-III/IIIA/IV (U-10Zr alloy) driver fuel pins, and over 600 U-Pu-Zr fuel pins [2, 9] from 1964 to 1994 as well as the remote fabrication and irradiation in EBR-II of approximately 35,000 Mark-I driver fuel pins from 1964 to 1969 [6]. Mark-II driver fuel was qualified for 8 at. % burnup, while Mark-III A driver fuel was qualified for 10 at. % burnup. Mark-III A driver fuel was limited to 10 at. % due to swelling of the 316 stainless steel fuel assembly hardware. U-Pu-Zr and U-Zr pins clad in Type 316, D9 or HT9 cladding reached terminal burnup values of 15 to >19 at. % burnup without breach [10, 11]. Some 2-sigma high-temperature assemblies reached 11 to 12 at. % burnup without breach [12]. In addition to EBR-II irradiations, over 1,050 U-10Zr fuel pins and 37 U-Pu-Zr fuel pins were irradiated in the FFTF to burnup values above 14 at. % and 9 at. %, respectively [13] in order to qualify metallic fuel for FFTF core conversion. The significance of these irradiation tests was to (1) effectively qualify U-Zr as driver fuel for FFTF

(91.4 cm core height), and (2) demonstrate that there were no metallic fuel performance behaviors affected by fuel pin length that were obscured by the relatively short core height of EBR-II (34.3 cm core height) [2]. The FFTF fuel design had a much higher aspect ratio (length/diameter) and the core environment creates a much larger peak-to-average fission

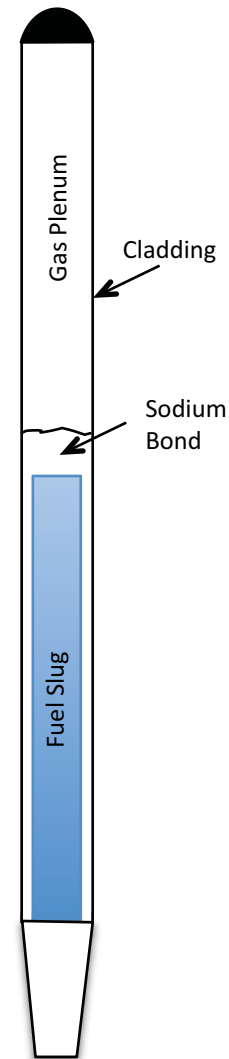


Figure 1. Schematic of a metallic, sodium bonded, fast reactor fuel pin.

rate. Crawford et al. [2] provide an extensive review of historical U.S. conventional fast reactor fuel technology with an expanded discussion of this information.

Typically the fuel section of the metallic fuel pin, as shown in Figure 1 contains the fissile uranium, uranium-plutonium, or a mixture of uranium-plutonium and minor actinides. The fuel is stabilized using typically a 10 to 30 wt. % addition of zirconium to both increase the melting point and to minimize FCCI. The fuel slug is thermally bonded with the cladding using sodium. The sodium bond provides a very high thermal conductivity medium by which heat is easily transferred to the cladding and reactor coolant. A fission gas collection plenum is provided to capture the released fission product gases. The fuel and sodium have typically been sealed inside an austenitic or ferritic-martensitic (FM) stainless steel cladding. Current fast reactor designs employ the low swelling FM stainless steels. Future designs may employ FM steel in which a fine oxide powder has been dispersed to improve high-temperature strength, stress rupture properties, and resistance to radiation hardening.

1.2 Metallic Fuel Steady-State Performance

A fast reactor fuel pin is a cylindrical volume of fuel, containing a relatively high concentration of fissile material and sealed in stainless steel cladding. The fuel produces heat and fission products, the latter causing the fuel to swell as lower density fission products are created and as gaseous fission products nucleate into bubbles in the fuel. Eventually swelling allows pores/bubbles to inter-connect, and fission gas is released to a gas plenum designed to collect it. Thus, the gas pressure increases in the sealed cladding as the fuel is ‘burned’. The cladding creeps as the stress builds, with the strain rate increasing with increasing temperature.

In metallic fuels, the cladding wall thickness is thinned and weakened by FCCI, caused by inter-diffusion of fuel and fission products with the cladding components. The thinning and pressurization processes combine to eventually cause creep rupture of the cladding if the fuel is allowed to proceed to higher burnup.

FCCI accelerates cladding creep rupture, the life limiting phenomena in the operation and performance of sodium cooled fast reactor metallic fuels. Early investigations of fuel-cladding chemical reaction were conducted by Walter and Lahti [14] and by Zegler and Walter [15]. These researchers tested the compatibility of a U-Pu based fuel with a variety of Zr-, Ni-, and V- based cladding materials and their research provided some of the initial basis for establishing 10 wt. % Zr (22.4 at. %) addition to uranium based fuels as a minimum. They discovered that at peak cladding temperatures above 715°C, a eutectic reaction between inter-diffusing fuel and cladding components can produce a liquid phase that hastens cladding attack. Zegler and Walter found that below 715°C, inter-diffusion layers formed with a nickel rich region in the fuel (assuming Ni-based or austenitic stainless steel cladding) and a nickel-depleted layer in the cladding.

Quantification of the interaction layer thicknesses in out-of-pile experiments was found to be not reproducible at cladding temperatures below 590°C. Quantification of in-pile developed interaction layers was found to be quantifiable and reproducible. Using out-of-pile couples, Zegler et al [15], quantified the interaction between U-5Fs and various steels finding an Arrhenius temperature dependence between the diffusivity (D) and the penetration depth (p), and time (t) according to the relationship, $p^2 = D \times t$. Fs is the symbol used to designate fissium, a simulated mixture of noble-metal fission products produced in equilibrium with the original EBR-II melt-refining pyrometallurgical recycle process. Fissium composition was comprised of 2.4 wt% Mo, 1.9 wt% Ru, 0.3 wt% Rh,

0.2 wt% Pd, 0.1 wt% Zr, and 0.01 wt.% Nb. A similar relationship has been used by Inagaki et al. [16] to develop a reaction rate relationship for the formation of interaction layers between cerium doped U-10Zr fuel diffusion couples with ferritic-martensitic cladding in out-of-pile tests. Inagaki's work has yielded a diffusivity value dependent upon the exponential of the inverse of temperature.

Pahl, et al. [17] provide an excellent descriptive overview of FCCI between metallic fuel and stainless steel cladding. FCCI is characterized by the inter-diffusion of fuel constituents with cladding constituents. Keiser [18] has shown that inter-diffusion is primarily attributed to Fe and Ni from steel cladding and diffusion of the lanthanide fission products (La, Ce, Nd, Sm, Pr) from the fuel into the cladding. Note that 'eutectic' melting temperatures between these components can be very low (Fe/Ce is 592 °C and Ni/Ce is 483°C). Most research efforts studying FCCI in metallic fuel [14, 15, 17] have indicated that FCCI is dependent upon the fuel-cladding temperature and the burnup (or exposure time) of the fuel but the mechanistic relationships have not been determined and shown with comparison to in-pile experimental data. An incubation period prior to FCCI formation has been observed up to approximately 2 at. % burnup prior to observing an interaction [18]. Zr-based rind is typically found on the outer surface of as-fabricated zirconium alloyed fuel slugs cast using injection casting methods. Following swelling of the fuel slug to the point of contact with the inner cladding surface, interaction can begin, but a residual Zr layer initially inhibits reaction. Eventually the Zr layer breaks down and reincorporates with the fuel matrix allowing fuel constituents to interact with cladding constituents.

Keiser [19] provides an analysis on the fuel-cladding interaction layer composition and phase structure by examining both in-pile irradiation experiments and out-of-pile diffusion couples between U-Zr and D-9 and U-Pu-Zr and D-9 and HT-9 cladding. The

nominal compositions of D-9 and HT-9 steels are provided in Table 1 as reported by Liebowitz and Blomquist [20].

Table 1. Nominal composition of D-9 and HT-9 Steels.

wt. %	Fe	Cr	C	Si	Mn	W	V	Mo	Ni	Ti
D9	Bal.	13.5	0.04	0.75	2.0	0	0	2.0	15.5	0.25
HT9	Bal.	12.0	0.2	0.25	0.2	0.5	0.5	1	0.5	0

Keiser [19] provides summaries of the element trace analyses performed on a variety of metallic fuel and cladding combinations irradiated in the EBR-II. Keiser reported that phase formation in FCCI layers. He found that on the fuel side of the interface, Fe and Ni are both found to diffuse into the fuel, Fe as far as 250 μm and Ni as far as 20 μm . On the cladding side, Ce, Nd, and Sm were found to diffuse the deepest into the cladding region. Keiser [19] concluded the following from his studies:

- The lanthanide fission products penetrate the deepest into HT9 and D9 cladding, forming phases with Fe and Ni.
- In ternary, U-Pu-Zr fuel, Pu is the primary fuel constituent that penetrates furthest in the cladding. For binary, U-Zr fuel, uranium penetrates the cladding.
- Of the steel cladding constituents, Fe and Ni diffuse in the fuel and form phases with U, Pu, and Zr. A Ni-depletion layer is found to form in austenitic cladding, D9. Cr becomes enriched at the cladding interface but does not penetrate into the fuel nor react with fuel.
- Near the fuel-cladding interface, light and dark contrast (high Z and low Z) phases can be observed on the fuel side of the interface that containing lanthanide fission products and Pd. Precipitate particles containing Zr, Mo, Tc, Ru, Rh, and Pd are observed in the fuel near the cladding.
- The Zr rind on the fuel surface is a barrier to interaction and remains intact at lower fuel temperatures and lower power during operation.

- Maximum fuel-cladding interaction occurs at the combined high power and high temperature region of a fuel pin. The largest penetrations into the cladding are observed for fuel pins with ternary U-Pu-Zr fuel and austenitic stainless steel (D9) cladding.

Figure 2 and Figure 3 depict examples of FCCI between Zr-alloy metallic fuel and austenitic (D9) and ferritic-martensitic (HT-9) stainless steel cladding, respectively. Note the layer of nearly pure lanthanide fission products next to the cladding in Figure 2. Figure 3 shows the two types of interaction in the case of the ferritic-martensitic cladding where the higher concentration of carbon in the cladding designed to stabilize the martensitic phase has been depleted (decarburized) in a layer next to the fuel (large hardness indents indicate the softer ferrite layer). The layer to the left of the ferrite layer is the classic FCCI layer and the small indents reflect the higher hardness of this layer. The unaltered martensite is seen to the right of the interaction layers.

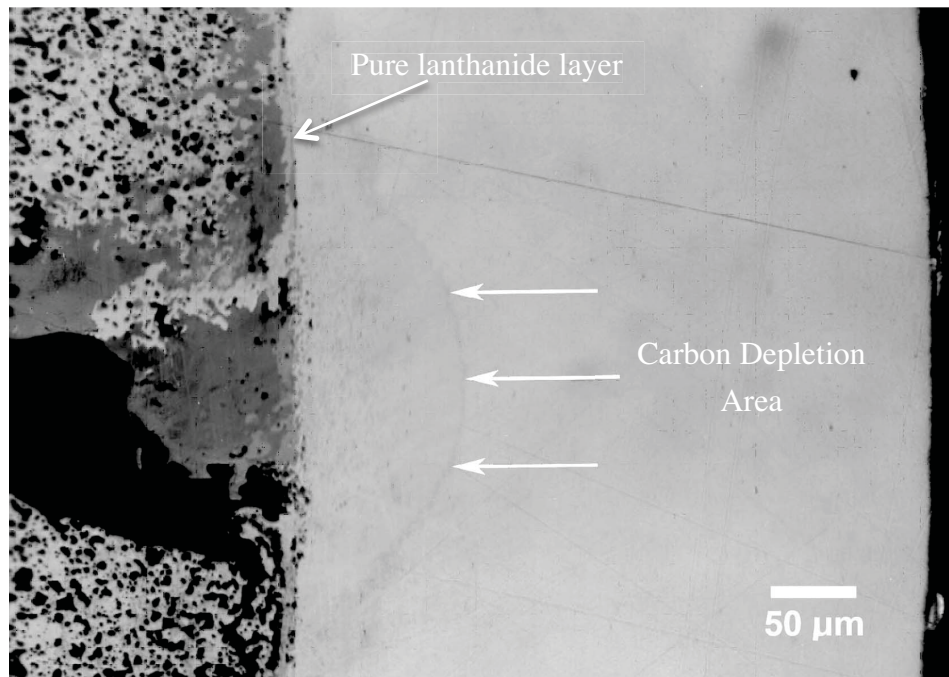


Figure 2. FCCI between U-19Pu-10Zr and D9 austenitic stainless steel cladding.

Empirical relationships have been developed from a large body of research through a combination of in-pile and out-of-pile research, development, and experimentation. Cohen et al. [21] have shown that significant in-pile acceleration of the FCCI rate is experienced over similar condition out-of-pile experiments. The study of FCCI in metallic fuels has led to the quantification of in-pile failure rates to establish a burnup and temperature dependent limit to preclude failure of fuel pins. This limit has been developed primarily using data from the EBR-II reactor experiments and specifically from the failure rate experienced in the X447 experiment for U-Zr binary alloy fuel in HT-9 ferritic-martensitic cladding. The formation of fuel-cladding interaction layers, phases, and degradation of cladding strength are diffusion controlled and dependent upon the diffusion kinetics of the fuel, cladding, and lanthanide constituents found in the fuel-cladding system. Most research in this area has indicated diffusion controlled kinetics but no effort has yielded a mechanistic model of the migration of lanthanide species and formation of FCCI layer.

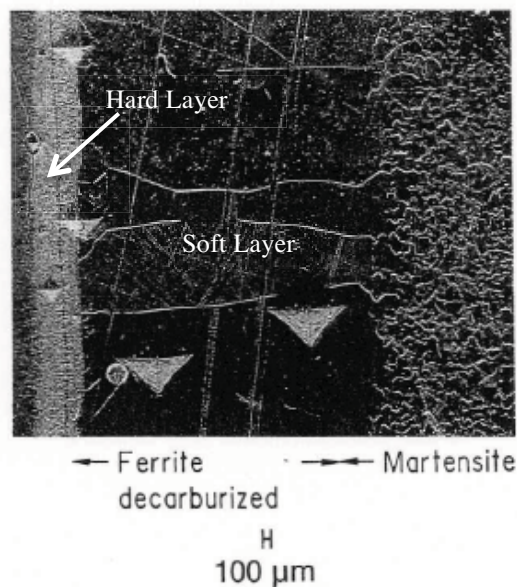


Figure 3. FCCI between U-19Pu-10Zr and HT-9 ferritic-martensitic stainless steel cladding.

1.3 This Work

The purpose of this dissertation is to examine the relationship between the formation of FCCI in the metallic fuel system and the burnup and operating temperature of the fuel. It is shown that the data available from EBR-II experiments and from the Fast Flux Test Facility (FFTF) experiments can be used to aid in the development of a mechanistic FCCI model.

One of the most important EBR-II experiments in this regard was X447. This experiment was conducted at relatively high power and achieved significantly high operating temperatures over the life of the experiment. This experiment will be reviewed and postirradiation results reported in this dissertation. The data from this experiment provide an excellent validation case for the proposed development of a predictive interaction model. The EBR-II core was 34.3 cm tall. The design of the reactor was such that the peak temperature in the fuel occurred near the top of the fuel column. While burnup/fission and heating rate decreases at the top of the fuel column, the EBR-II burnup profile was relatively flat with the peak-to-average axial linear heat rating at approximately 1.08. The result of this combination was that breach due to FCCI typically occurred near the top of the fuel column where the lanthanide fission product concentration was high, the cladding temperature a maximum, and resulting FCCI high.

Alternatively, the FFTF, with a 91.4 cm tall fuel column and a chopped cosine-shaped flux profile, had a core with the peak cladding temperature at the top of the fuel column but the peak burnup and peak fuel centerline temperature lower in the fuel column. The MFF series of metallic fuel irradiations provides an important potential comparison between data generated in EBR-II and that expected in a larger scale fast reactor. Note that

the FFTF fuel was designed as a prototype for the Clinch River Breeder Reactor (CRBR), although CRBR was never built.

The MFF-3 and MFF-5 qualification assemblies operated in FFTF to > 10 at. % burnup with no pin breaches. All fuel pins contained tag gas identification modules. The MFF-3 assembly operated to 13.8 at. % burnup with a peak inner cladding temperature of 643°C. The MFF-5 assembly operated to 10.1 at. % burnup with a peak inner cladding temperature of 651°C. This can be compared to the two pin breaches experienced in X447 at approximately 10 at. % burnup and peak inner cladding temperatures of 648°C and 638°C respectively. Note that the gas plenum volume/fuel volume ratio for the MFF pins was 1.6 to 1.8 and for X447 pins was 1.4 so the stress on the cladding at a given burnup could be slightly higher in X447 as compared to MFF. Postirradiation examination of the middle to top of the fuel column from a pin in MFF-3 and MFF-5 has been conducted to establish the extent of FCCI present and possibly show how the MFF pins did not breach as opposed to those in X447.

The FCCI data obtained from the X447, MFF-3, and MFF-5 experiments is used to compare to interaction layer thickness predictions generated by a multi-physics model developed to explain the production and migration behavior of lanthanide species as a function of temperature and burnup levels found in typical metallic fuel pins during operation in either EBR-II or in FFTF sized cores.

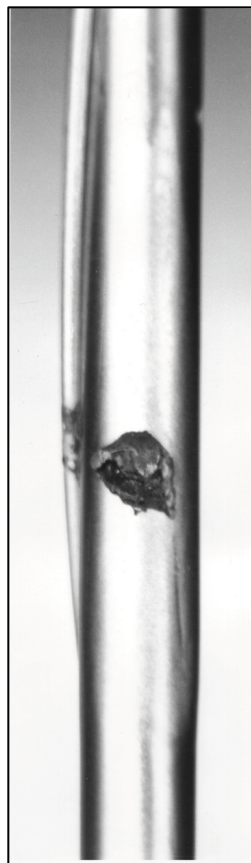
2 X447 EBR-II EXPERIMENT

The use of metallic fuels in sodium-cooled fast reactors, especially in cases where ferritic-martensitic stainless steel alloys such as HT9 are used for cladding, is thought to be limited to peak cladding temperatures to approximately 620°C [2]. Stress rupture properties of the cladding and FCCI create the limiting conditions.

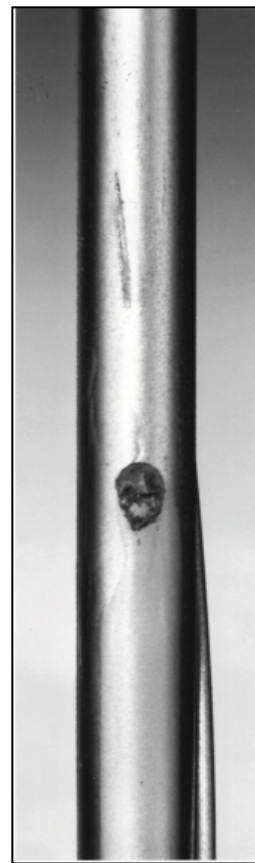
The X447 experiment was designed to investigate these issues and was previously performed in the Experimental Breeder Reactor II (EBR-II) between 1988 and 1992. A selection of the postirradiation examination information was then published in 1993 [22]. It is the purpose of this summary to provide a more detailed account of those and other unpublished examinations to better describe the performance of metallic fuel operated at high temperatures.

The X447 experiment was conducted in the EBR-II as part of the Integral Fast Reactor program's development and testing of metallic fuel. After achieving a burnup of 5 at. % (288 EFPD), the assembly was removed from the reactor, reconstituted as X447A, and reinserted into the reactor. No fuel pin failures were detected or observed at this interim burnup but four fuel pins were selected from the assembly and subjected to postirradiation examination. After re-insertion into EBR-II, the X447A experiment achieved 10 at. % burnup (641 EFPD) and was removed from the reactor. The experiment was designed to operate at high temperature (630°C to 660°C PICT), near the 2-sigma operational limit for metallic fuel in EBR-II; at these temperatures, it was expected to undergo extensive FCCI. The high cladding temperatures were also expected to challenge the creep rupture resistance of the cladding alloy, HT-9, as fission gas pressure increased and FCCI thinned the cladding wall.

After achieving 10% burnup fuel pin failure was detected by measurement of fission gas in the reactor plenum and confirmed by identification of the Xe-tag gas composition that had been added to X447 pin plenums. The assembly was removed from the reactor for postirradiation examination, and two breached pins identified, one in pin DP-70 and one in pin DP-75. Photographs of the breach locations on pins DP-70 and DP-75 are shown in Figure 4. Six HT-9 clad fuel pins from the experiment were destructively examined, including two pins at 4.7% burnup and four pins at 10% burnup. The postirradiation examination will be reviewed here as it pertains to the subject of this dissertation.



DP-70



DP-75

Figure 4. Photographs of the DP-70 and DP-75 pin breaches.

2.1 As-Built Condition

The nominal design features for the X447 assembly are shown in Table 2. All fuel pins in the sub-assembly were of U-10Zr fuel composition with 5.82 mm diameter fuel slugs. The fuel column heights were all 34.29 cm nominal with a 1.4 plenum-to-fuel volume ratio. The sub-assembly was a 61-pin arrangement with rows 1, 2, and 3 occupied with fuel pins having HT-9 cladding. Fuel pins having D9 cladding occupied rows 4, 5, and 6. provides a schematic of the pin arrangement of the X447 experiment. During reconstitution, four pins (DP-81, DP-69, DP-03, and DP-06) were replaced and the X447A subassembly reloaded into the EBR-II reactor. As indicated by the figure, DP-70 and DP-75 experienced breach near 10 at. % burnup during the 155B cycle.

Table 2. X447 Nominal Design Features

Nominal Design Features of Mark-III Fuel Pins	
Fuel Alloy Composition	U-10Zr
Fuel Slug Diameter	0.173-in. (5.82-mm)
Fuel Slug Length	13.5-in. (34.29 cm)
Fuel Plenum Volume	7.5 cm ³ at 25°C
Ratio of Plenum to Fuel Volume (cold)	1.4
Cladding Material	D9 or HT9
Cladding outer Diameter	0.230-in. (5.84-mm)
Cladding Wall Thickness	0.015-in. (0.381 mm)
Fuel Pin Length	29.5-in. (74.93 cm)
Fuel Smeared Density	75%
Fuel theoretical density	15.8 g/cm ³
Wire Wrap Diameter/Pitch	0.042-in./6-in. (1.07 mm/ 15.24 cm)
Sodium volume	1.9 cm ³ at 25°C
Sodium Fill Above Fuel	0.25-in. (0.635 cm)
Axial Fuel Restrainer	None
Subassembly Type	Modified D-61
Hex-can material – First	304 SS
Hex-can material – Second	316 SS
Maximum Pin Linear Power	11 kW/ft (360 W/cm)
Maximum Cladding Temperature	658°C
Maximum Fuel Temperature	752°C

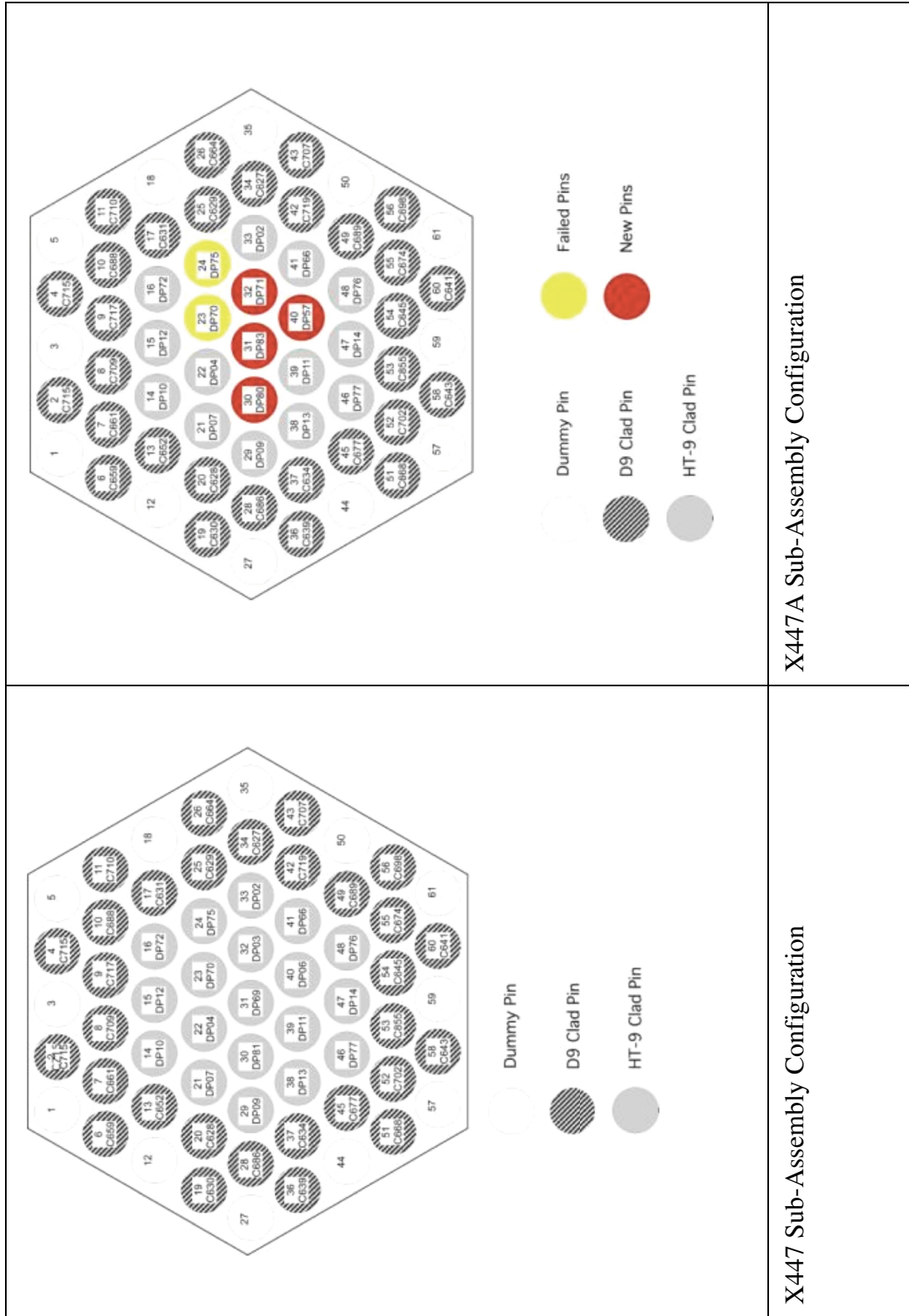


Figure 5. X447 Sub-Assembly Configuration.

2.2 *Irradiation Conditions and Performance History*

Key parameters governing the X447 and X447A assemblies during irradiation are the peak linear power and the peak inner cladding temperature. The cycle-by-cycle peak linear power histories for the high burnup pins examined, DP-04, DP-11, DP-70, and DP-75, are shown in Figure 6. Linear power is near its peak at beginning of life due to the larger amount of fissile material present in the pins. The X447 subassembly was designed to run at significantly higher power (typically between 295 and 328 W/cm) in order to achieve higher pin temperatures and higher burnup. The cycle-by-cycle peak inner cladding temperature histories for the DP-04, DP-11, DP-70, and DP-75 pins are shown in Figure 7. All of the pins operated at temperatures above 630°C during their entire irradiation histories. DP-11 operated for the first cycle at nearly 690°C. Axial power and temperature profiles are shown for the DP-70 pin at beginning of life in Figure 8. In EBR-II power and temperature typically peaks near the top of the fuel column. The difference in operating conditions between these four pins can be used to assess causes for differences in pin performance, such as cladding creep and FCCI. In this analysis this is done by comparing the axial power, local burnup, and temperature distributions between the pins and correlating with the formation of FCCI as a function of axial elevation.

The axial power and temperature profiles for the DP-04, DP-11, DP-70, and DP-75 pins were calculated using the SAFE code [23]. The calculation of power and temperature distributions was performed for each irradiation cycle to obtain a specific temperature power and temperature distribution for each cycle. These temperatures and powers were then used for cycle-by-cycle FCCI analysis. For ease of reporting, calculated point values reported were obtained by calculating an EFPD weighted average across all cycles. This EFPD time averaged value is used to communicate the importance of considering the

temperature of operation during the entire irradiation history, not just the peak. Figure 9 through Figure 13 show the EFPD time weighted average of the axial power distribution as well as fuel centerline, inner cladding, outer cladding, and coolant temperature distributions for the DP-04, DP-11, DP-70, and DP-75 fuel pins. The temperature distributions are all seen to peak near the top of the fuel column.

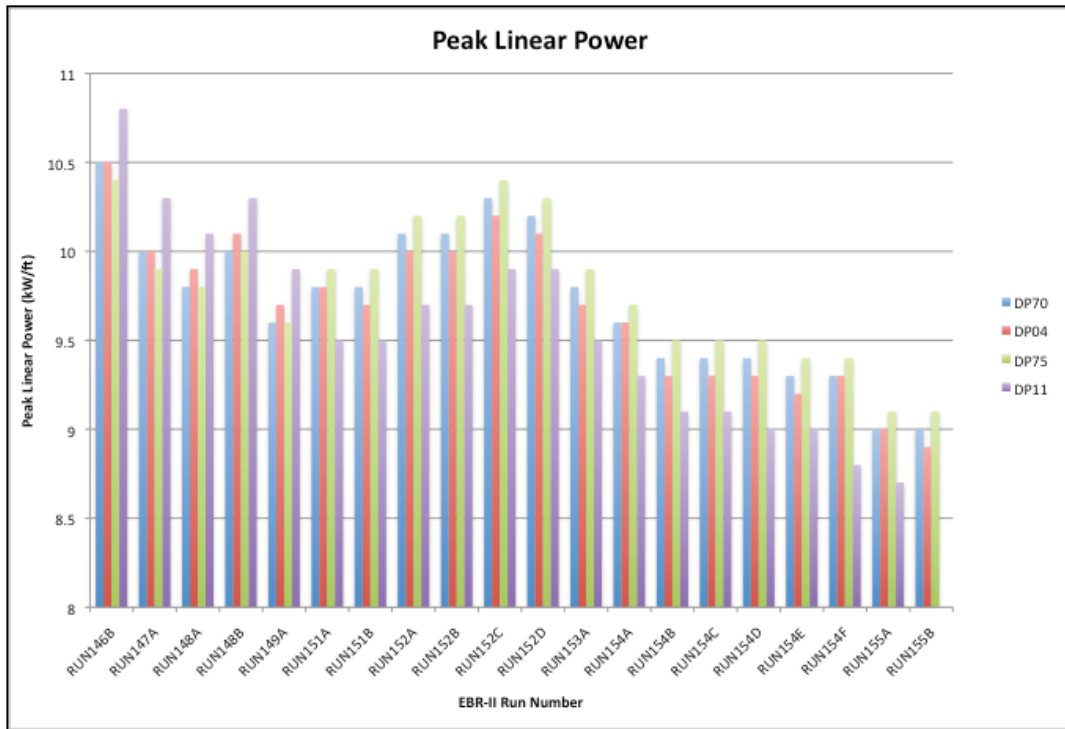


Figure 6. Peak Linear Power for each EBR-II Cycle during X447 irradiation.

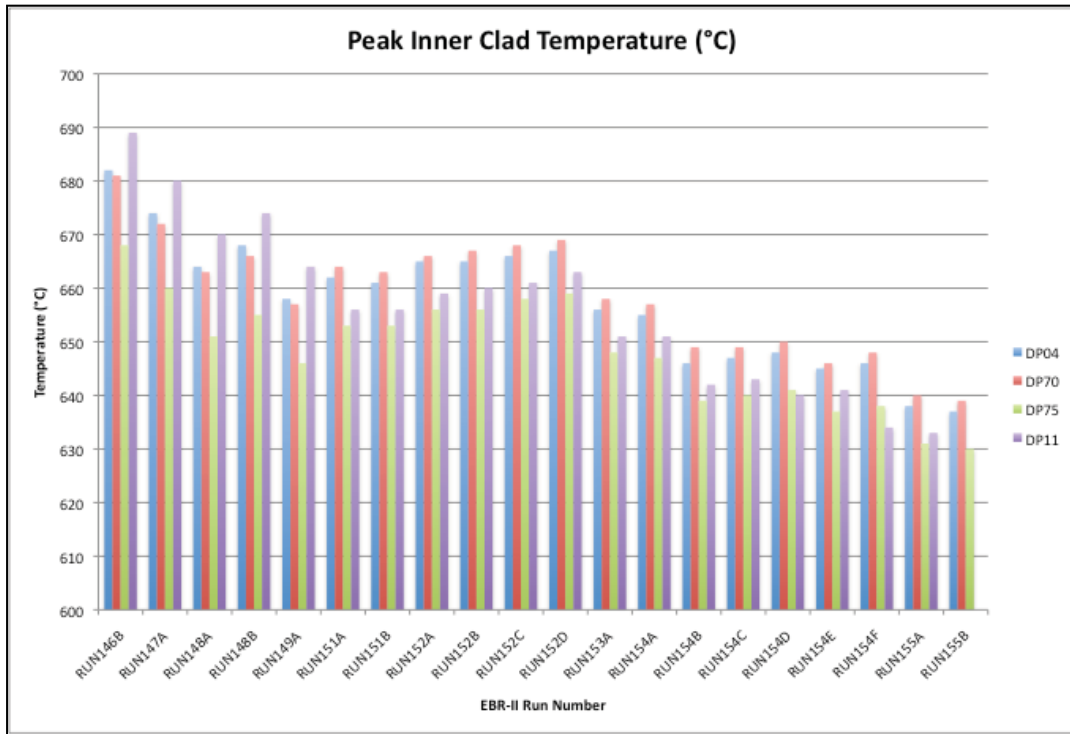


Figure 7. Peak Inner Cladding Temperature for each EBR-II Cycle during X447 irradiation.

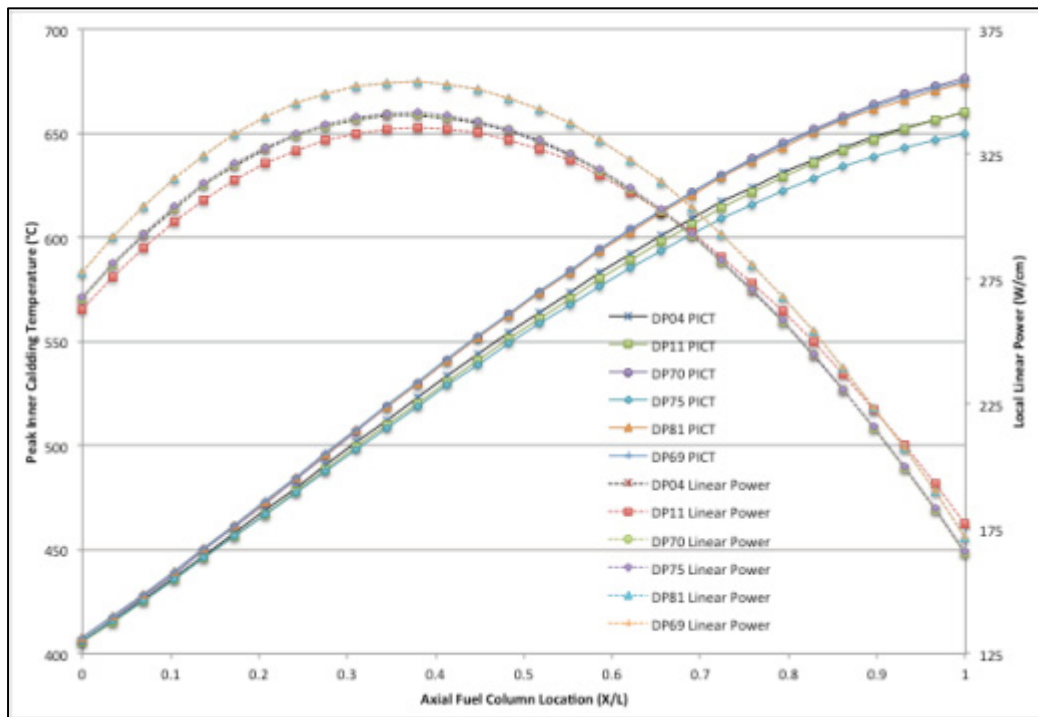


Figure 8. Comparison of X447 Pin Power and Peak Inner Cladding Temperature Profiles. Values based on EFPD weighted values across all irradiation cycles.

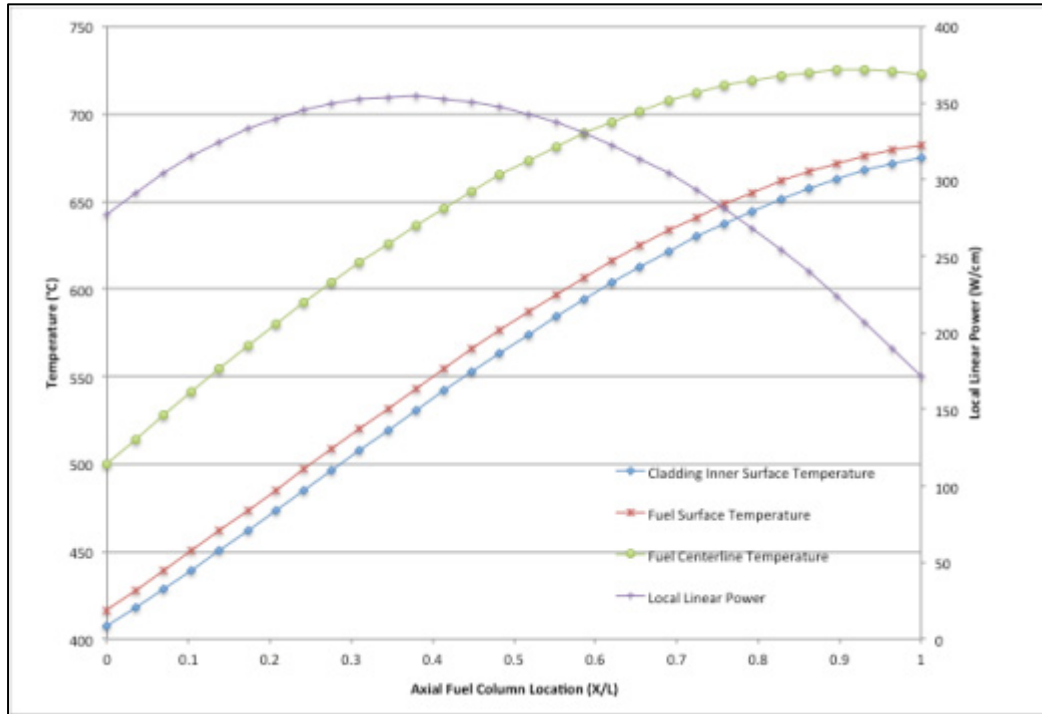


Figure 9. Axial Linear Power and temperature profiles for X447 Pin DP69. Values based on EFPD weighted values across all irradiation cycles.

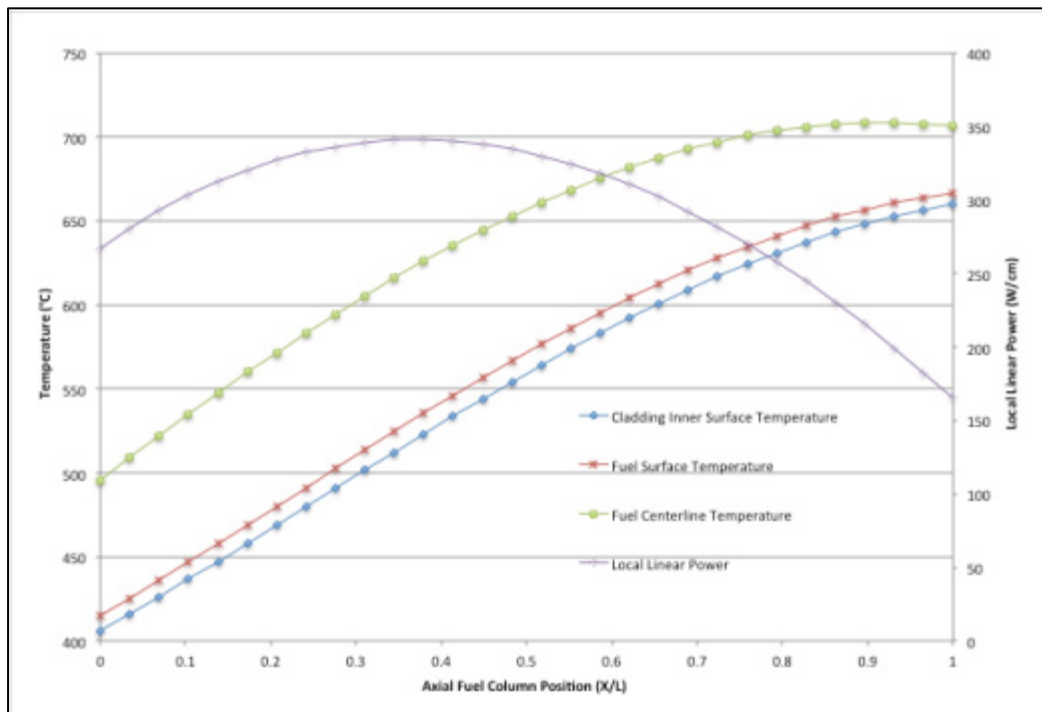


Figure 10. Axial Linear Power and temperature profiles for X447 Pin DP-04. Values based on EFPD weighted values across all irradiation cycles.

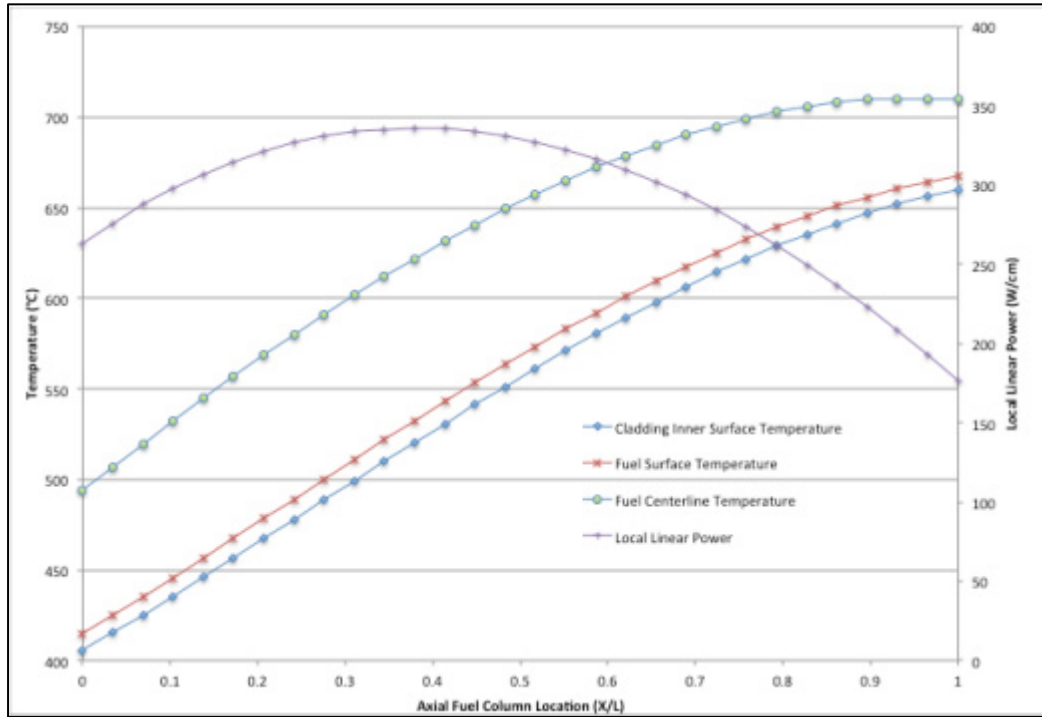


Figure 11. Axial Linear Power and temperature profiles for X447 Pin DP-11. Values based on EFPD weighted values across all irradiation cycles.

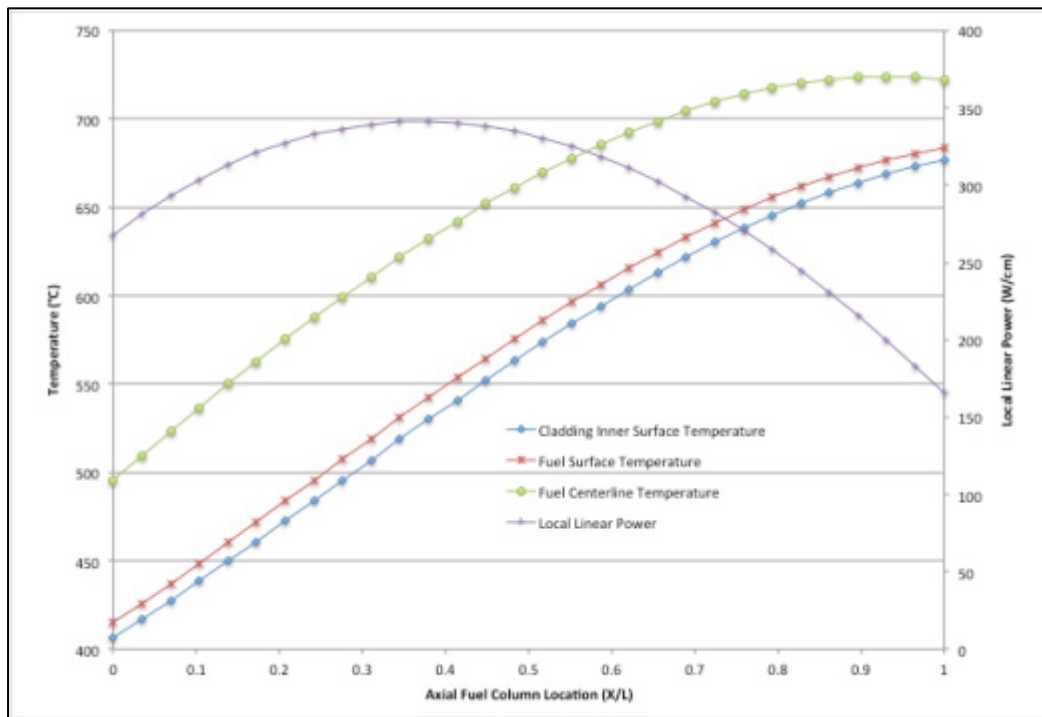


Figure 12. Axial Linear Power and temperature profiles for X447 Pin DP-70. Values based on EFPD weighted values across all irradiation cycles.

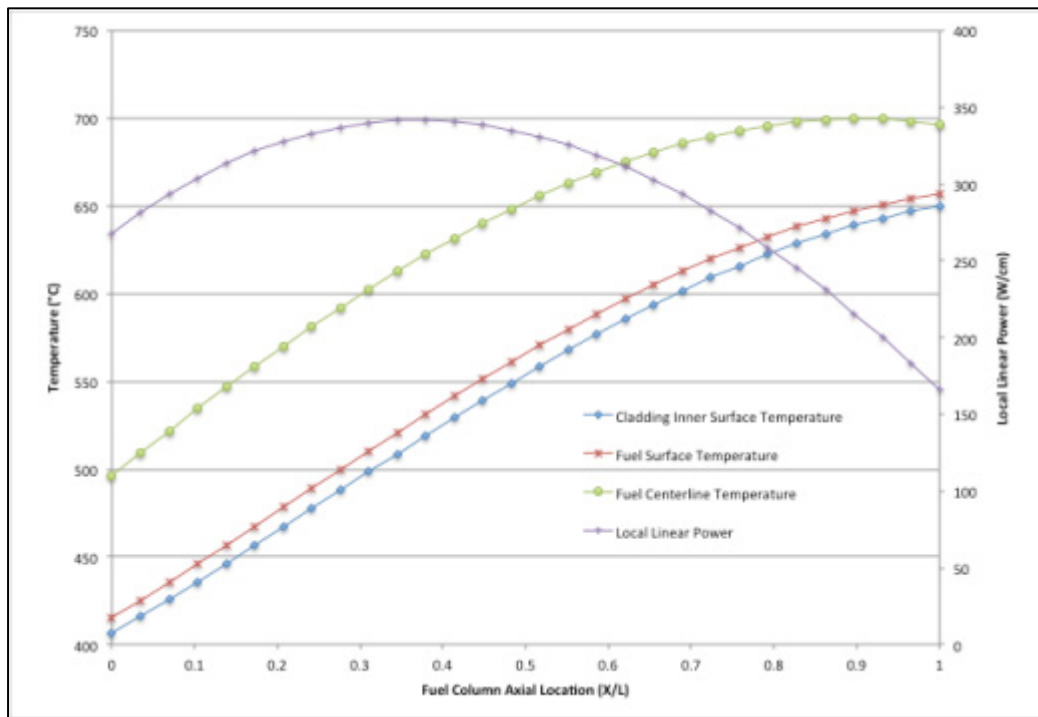


Figure 13. Axial Linear Power and temperature profiles for X447 Pin DP-75. Values based on EFPD weighted values across all irradiation cycles.

2.3 Postirradiation Examination

2.3.1 5 at. % Burnup Examinations (DP-03, 06, 69, 81)

As described above, four pins were removed from the X447 assembly at 4.8 at. % burnup, DP-03, 06, 69, and 81. Initially, postirradiation examination was non-destructive and included neutron radiography, pin profilometry (axial diameter profile), and gamma scanning analysis. The results of these examinations yield significant information on the fuel and materials behavior and suggest what destructive examinations may be most useful to fully understand possible mechanisms responsible for the observed behavior. Because the significance and performance of the X447 assembly was not fully understood at the time of postirradiation examinations at 4.8 at. %, full postirradiation examination was not conducted on all four pins. DP-69 and DP-81 received radiography, profilometry, and

gamma scanning examination. DP-03 and DP-06 received profilometry but no other postirradiation examination. DP-69 and DP-81 were destructively examined with DP-69 receiving optical metallographic analysis and DP-81 receiving both optical metallographic analysis and electron probe microanalysis (EPMA).

2.3.1.1 DP-69 Postirradiation Examination

The DP-69 pin was located at the center of the assembly. The axial local burnup and pin diametral profilometry measurement of the DP-69 pin at 4.7 at. % peak burnup are shown in Figure 14. The localized peak strain can be seen to occur at the top of the fuel column and although not the location of peak burnup, corresponds to nearly the highest fuel centerline and cladding temperatures. The peak strain at the top of the fuel column can be estimated at 0.6%, where local burnup and average inner cladding temperature were 2.4 at. % burnup and 667°C, respectively.

B.G. Carlson conducted the optical microscopy of the DP-69 pin at the Hot Fuel Examination Facility (HFEF) in 1989 [24]. Gross microstructural behavior of the DP-69 fuel pin is shown in Figure 15. The formation of a typical three-zone ring structure, formed with different phase mixtures and compositions that depend on the fuel operating temperature were observed near the top of the fuel column (see Figure 15). This has previously been modeled considering diffusion between adjoining phase fields created by the radial temperature gradient that spans a miscibility gap in the phase diagram of the U-Zr system [25]. Full metallography cross-sections of the DP-69 fuel pin at 6 different axial locations can be found in Appendix A along with details of the local burnup, time averaged inner cladding and fuel centerline temperature data.

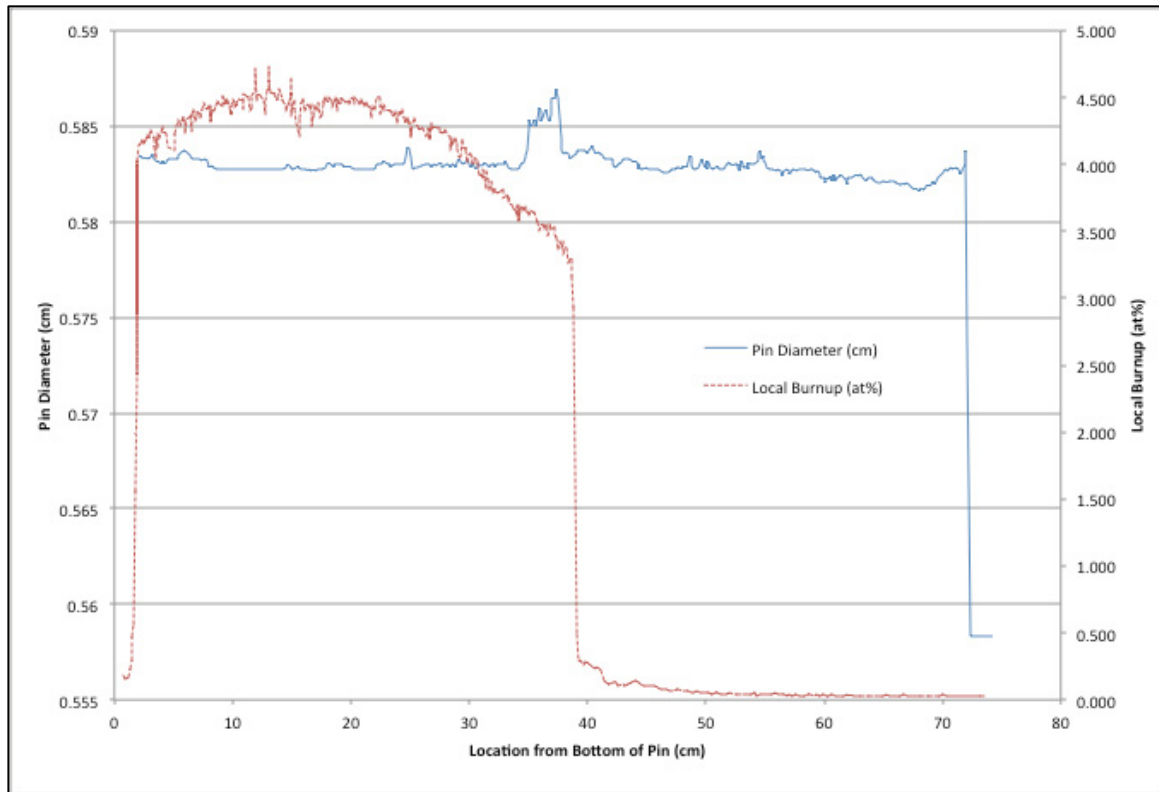


Figure 14. Axial burnup and pin diameter at 4.7 at. % for DP-69.

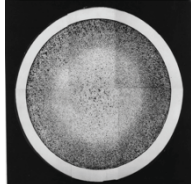
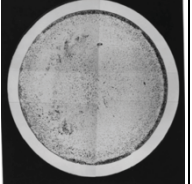
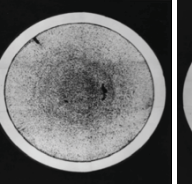
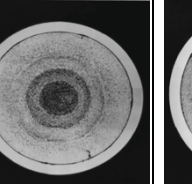
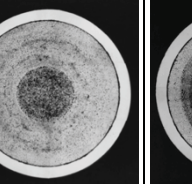
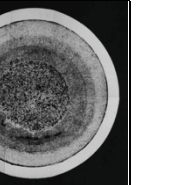
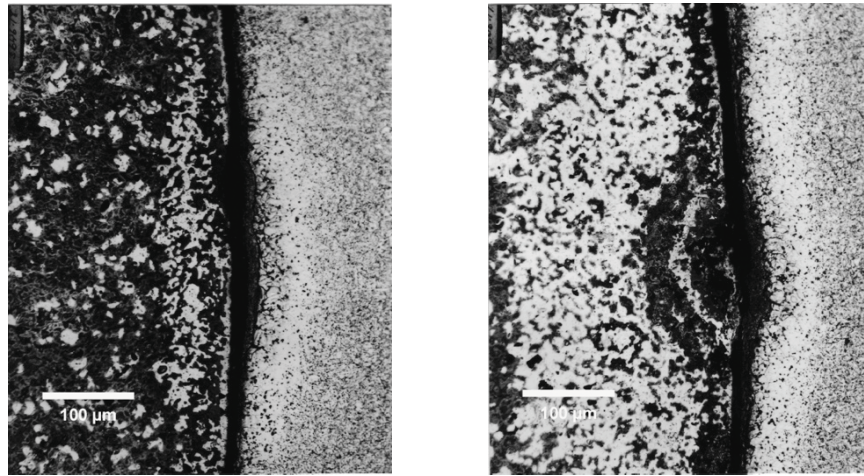
X/L = 0.19	0.46	0.74	0.85	0.95	1.0
4.8 at%	4.9 at%	4.1 at%	3.45 at%	2.7 at%	2.4 at%
463 °C	552 °C	626 °C	648 °C	664 °C	667 °C
0 μm	0 μm	51 μm	51 μm	102 μm	102 μm
					

Figure 15. Gross metallography of the DP-69 pin showing microstructure axially along the pin with FCCI thickness shown in μm .

Figure 16 shows a 200X metallography sample from DP-69 at the 34.5 cm height (top of the fuel column) location. The FCCI formation seen in this photomicrograph is typical of that found in metallic fuel. Penetration of cladding constituents into the fuel

region, concentration of lanthanide fission products at the fuel surface, and penetration of lanthanide fission products into the cladding characterize the formation of FCCI.



NaOH etch 200 X

As polished 200 X

Figure 16. Typical 100 μ m thick fuel-cladding interaction found in the DP-69 pin.

2.3.1.2 DP-81 Postirradiation Examination

The DP-81 fuel pin was examined following irradiation to a peak burnup of 4.8 at. %. A neutron radiograph of the DP-81 fuel pin is shown in Figure 17. The axial burnup and pin diametral profilometry analyses of the DP-81 pin at 4.8 at.% burnup are shown in Figure 18 and are very similar to that of DP-69. The localized peak strain (0.4%) can be seen to occur at the top of the fuel column.

Sanecki et al. performed the electron microprobe analysis of samples from the DP-81 pin in the Alpha-Gamma Hot Cell Facility at Argonne National Laboratory in 1991 [26]. The overall results indicated typical redistribution and FCCI common for U-10Zr metallic fuel. The radial scan of uranium and zirconium in a transverse radial cross-section is shown in Figure 19 from an area having no fuel-cladding interaction, 28.9 cm from the bottom of the fuel column. The scan extended from the center of the fuel pin radially out to the cladding. Three distinct zones can be identified. Zone A includes the fuel centerline and exhibits Zr enrichment to 26 wt.% and uranium depletion to 74 wt.%. Zone B, the

intermediate zone exhibits Zr depletion to values less than 1 wt.% and uranium enrichment to near 100%. Zone C, nearest the cladding, exhibits phase segregation with three distinct phases: two with low concentrations of Zr and one, UZr_2 , concentrated in Zr. As will be seen later these two (5 at. % burnup) pins exhibit initial FCCI and strain behavior that contribute to fuel pin failure.

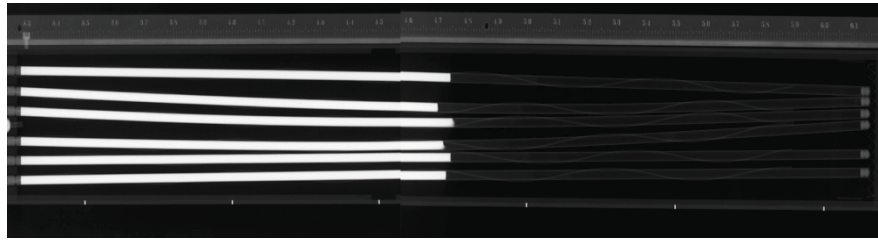


Figure 17. Neutron Radiograph of five X447 Pins - DP-81 is bottom pin in radiograph.

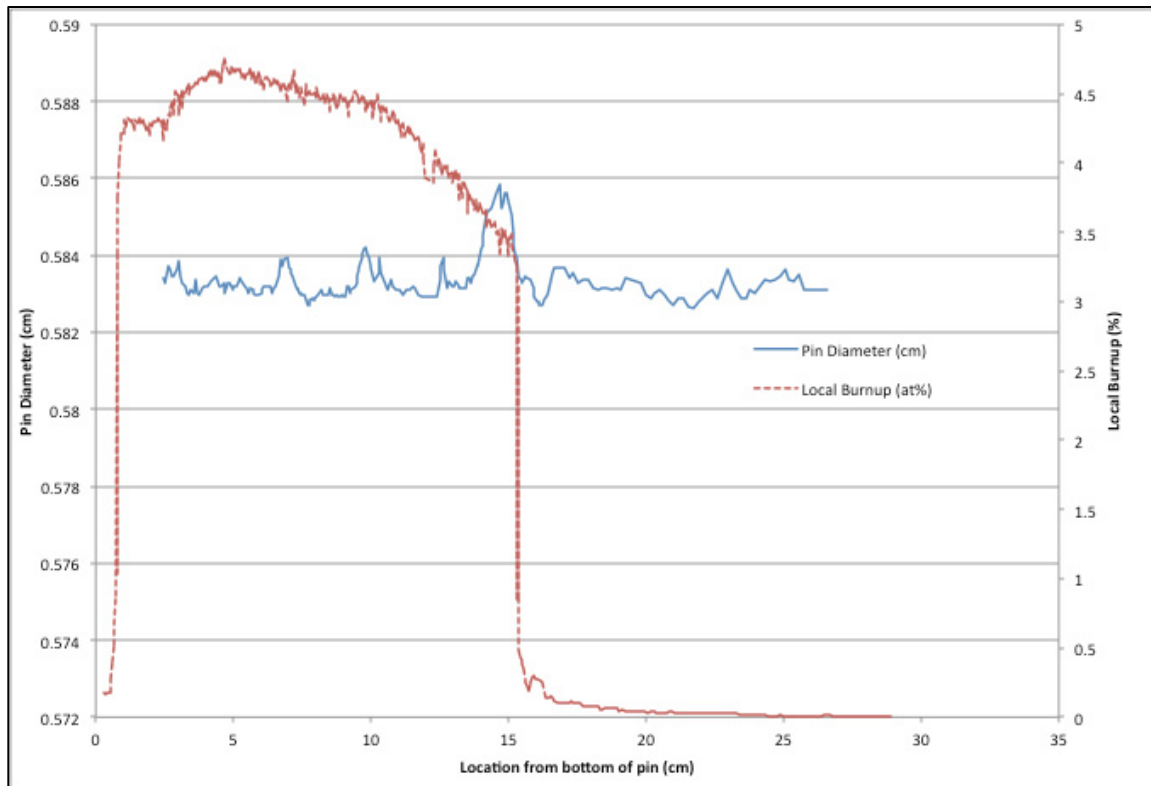


Figure 18. Axial burnup and pin diameter at 4.8 at. % for DP-81.

A second specimen from the DP-81 fuel pin was taken approximately 1.9 cm below the top of the fuel column. This specimen indicated 71 μm of FCCI primarily due to lanthanide fission products penetrating into the cladding. Elemental dot maps at this location indicated 81 μm of Ni depletion in the FCCI zone.

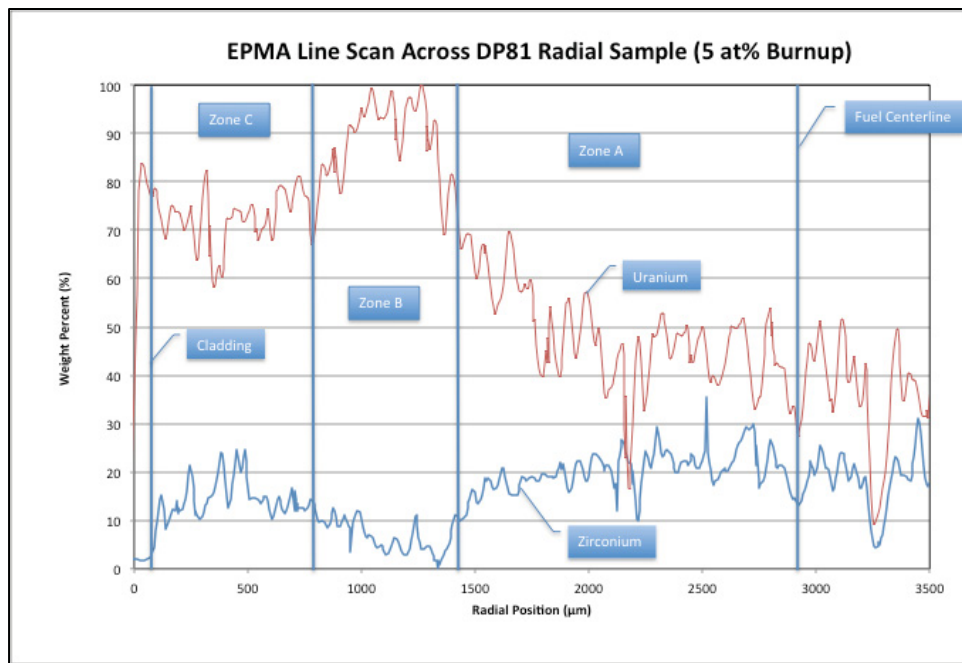


Figure 19. Radial microprobe elemental scan for uranium and zirconium in DP-81.

2.3.2 10 at. % Burnup Examinations (DP-04, DP-11, DP-70, DP-75)

The X447A experiment continued irradiation to 10 at. % burnup at which time fuel pin breach was detected by EBR-II reactor operations staff. Upon initial disassembly of the X447A experiment two fuel pins were found to be breached, DP-70 and DP-75. Four fuel pins were examined during postirradiation examination, DP-04, DP-11, DP-70, and DP-75. DP-04 and DP-11 were examined in addition to the breached fuel pins because their irradiation conditions, temperature, and burnup, were similar to that of DP-70 and DP-75.

2.3.2.1 DP-04 Postirradiation Examination

The DP-04 pin experienced temperature and power conditions similar to that experienced by the DP-70 and DP-75 pins but the DP-04 pin did not experience failure. Figure 20 shows the gross microstructure axially along the DP-04 fuel pin. Distinct lanthanide phases are visible in the fuel microstructure, much of it at or near the outer diameter of the fuel. Cladding thinning has occurred in a few areas with FCCI interaction measuring up to $150\ \mu\text{m}$ (6 mils) in some locations. The sample taken at the $X/L = 1$ elevation displays cracks $75\ \mu\text{m}$ (~ 3 mils) deep in the area of maximum interaction. Decarburization of the cladding outer diameter is also present on most of these samples to a depth of 12 to $25\ \mu\text{m}$. Figure 21 shows an etched view of a cladding sample taken at the 35 cm elevation in DP-04. Penetration of lanthanides is seen in the cladding and migration of cladding components (especially Fe) is seen in the fuel region. Decarburization has also been observed on the inner diameter of the cladding as was shown in Figure 3, but was not confirmed in these examinations nor included with the lanthanide infiltration measurements.

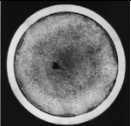
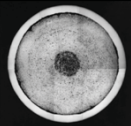
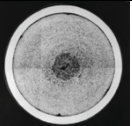
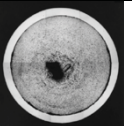
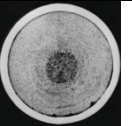
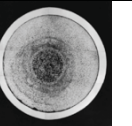
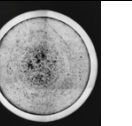
X/L = 0.69	0.86	0.94	0.95	0.97	0.98	1.0
9.2 at%	7.5 at%	6.4 at%	5.9 at%	5.8 at%	5.6 at%	5.3 at%
606°C	634°C	644°C	649°C	649°C	650°C	652°C
69 μm	114 μm	127 μm	152.4 μm	152.4 μm	140 μm	152.4 μm
						

Figure 20. Gross metallography of the DP-04 pin showing microstructure axially along the pin with FCMI thickness shown in μm .

Full metallographic cross-sections of the DP-04 fuel pin at seven different axial locations can be found in Appendix B along with estimates of local burnup and fission density and time averaged inner cladding and fuel centerline temperatures.

Most of the HT-9 pins from the X447 experiment with 10 at. % burnup experienced 2% cladding strain at the top of the fuel column. Figure 22 shows the local burnup along the DP-04 axial length as well as the variation in the cladding diameter measured using laser profilometry.

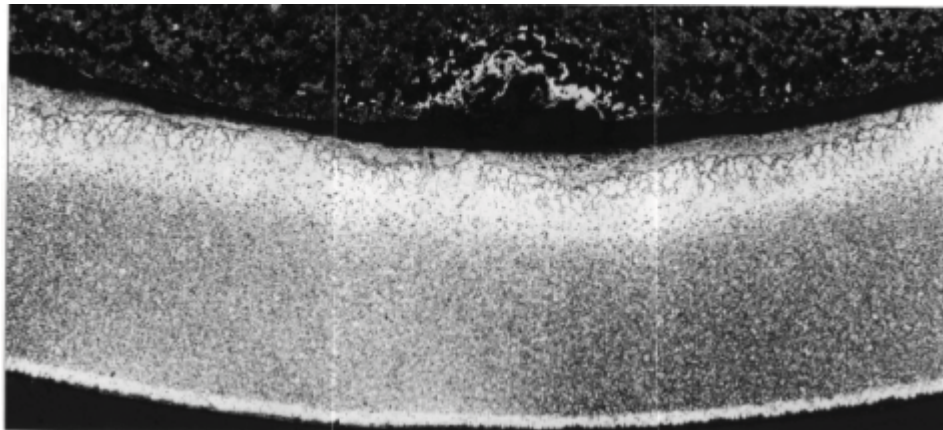


Figure 21. Etched view of the cladding in the region of greatest interaction at the 35 cm elevation of DP-04 (200X).

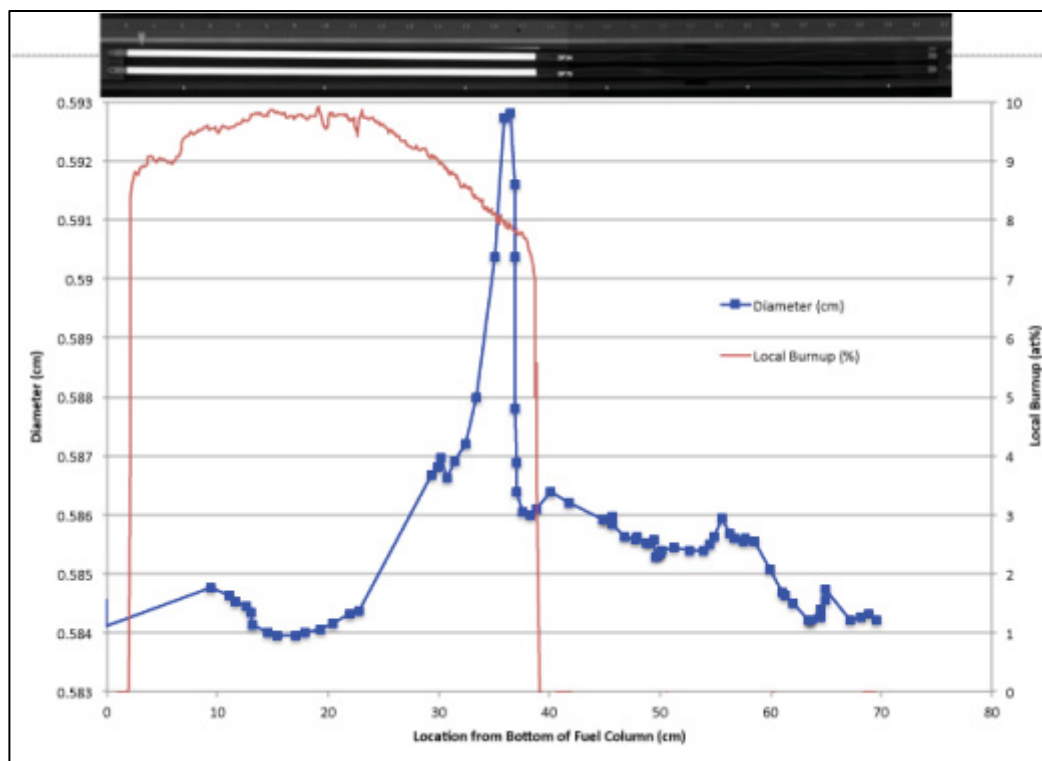


Figure 22. Axial pin diametral profilometry with local burnup and radiograph of DP-04.

2.3.2.2 DP-11 Postirradiation Examination

The DP-11 fuel pin exhibited behavior very similar to the DP-04 fuel pin operating between 630°C and 660°C peak inner cladding temperature. The DP-11 pin achieved a peak burnup just under 10 at. % and experienced approximately 2% strain in the cladding at the top of the fuel column but did not experience breach and failure. The results of fuel pin profilometry analysis of the DP-11 fuel pin can be seen in Figure 23.

Saneki et al. performed electron microprobe analysis of fuel pin DP-11 at the Argonne National Laboratory Alpha Gamma facility in 1993 [27]. The analysis was completed on a sample taken from the 37.5 cm location (from bottom of the fuel pin). This location corresponds to the approximate failure location observed in fuel pins DP-70 and DP-75. Fuel pin DP-11 achieved approximately 10 at. % burnup and operated with cladding temperatures between 630 and 660°C, similar to DP-70 and DP-75. It therefore provides an excellent comparison with DP-70 and DP-75. The EPMA examination of DP-11 provided a semi-quantitative measure of the radial distribution of fuel constituent elements, the areal distribution of fuel constituents at selected radial locations, the radial and areal distribution of fuel constituent elements at a location of major fuel-cladding interaction, linear and areal distribution of fuel constituents at a location of minimal fuel-cladding interaction, and provided composition of features of interest found in the fuel microstructure.

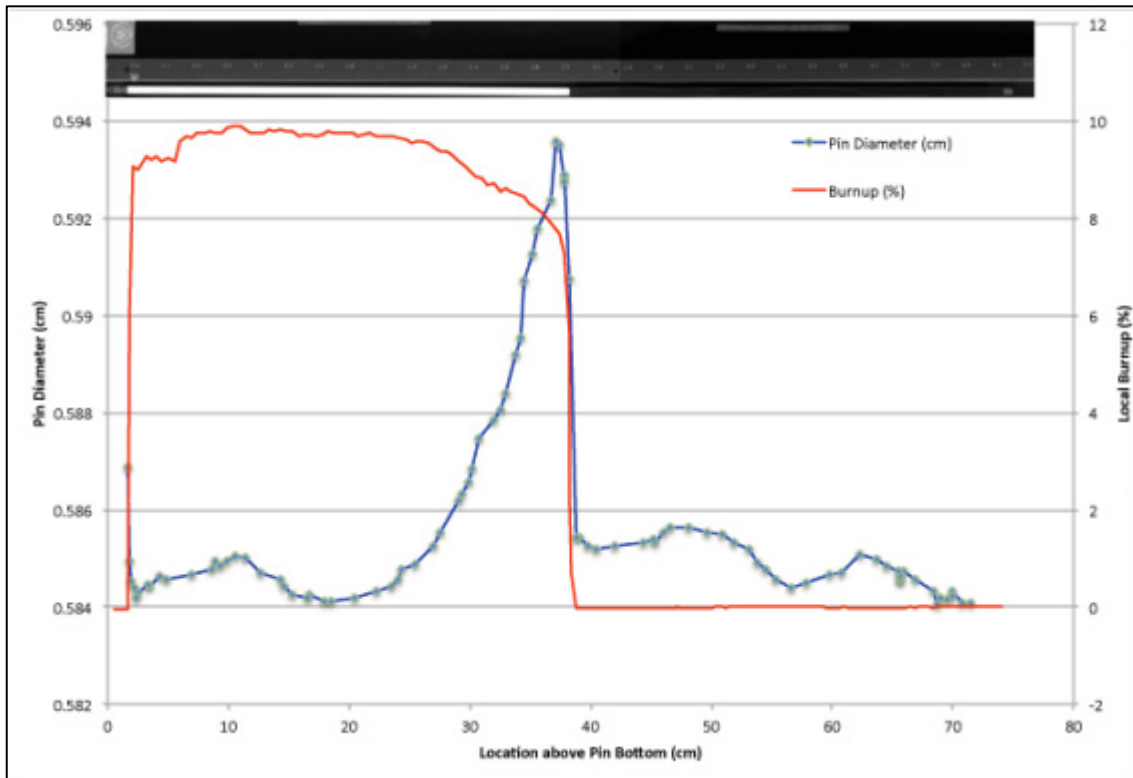


Figure 23. Axial pin diametral profilometry with local burnup and neutron radiograph of DP-11.

The radial distributions of uranium and zirconium found in the DP-11 fuel pin are shown in Figure 25. The analyses were performed along Line X shown in Figure 24. The fuel centerline is found at approximately $2550\ \mu\text{m}$ in the fuel sample cross-section. The cladding is shown on the left of the figure. Three distinct compositional zones can be identified and are distinguished by their difference in zirconium concentration. Zone A includes the fuel center and is elevated in zirconium concentration to between 14 and 34 wt.%. Zone B is a region exhibiting zirconium depletion leaving approximately 0 to 3 wt.% zirconium concentrations.

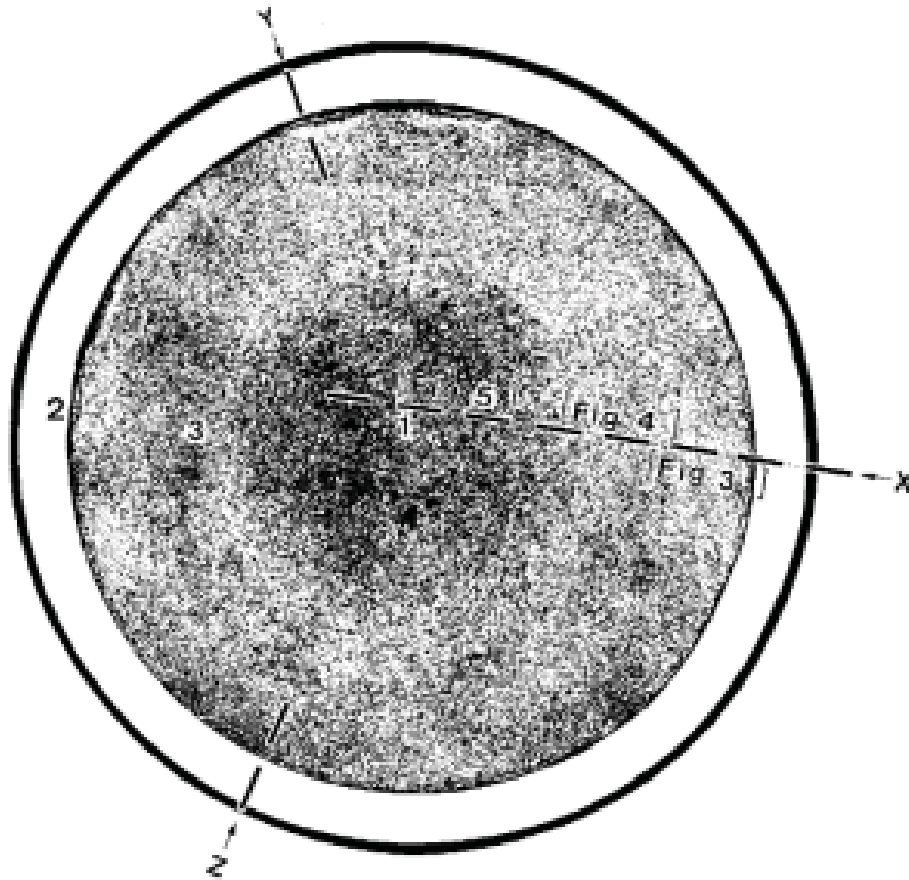


Figure 24. Line scan and elemental analyses locations in DP-11 at 35.6 cm fuel column height.

The outer, Zone C, layer exhibits approximately 9 wt.% zirconium, nominal for U-10Zr fuel. The large variations in concentration measured by EPMA, shown in Figure 25, are due to a large number of discrete particles and high porosity found in the fuel microstructure, but also indicate real variation in the composition of the fuel microstructure. Analysis of fission product distribution indicated that most of these particles are comprised of zirconium rich phases, but others included a combination of Ce, Pr, and Nd, with a few particles containing Ba or Cs fission products. Table 3 shows a summary of the zonal composition found in the DP-11 EPMA sample.

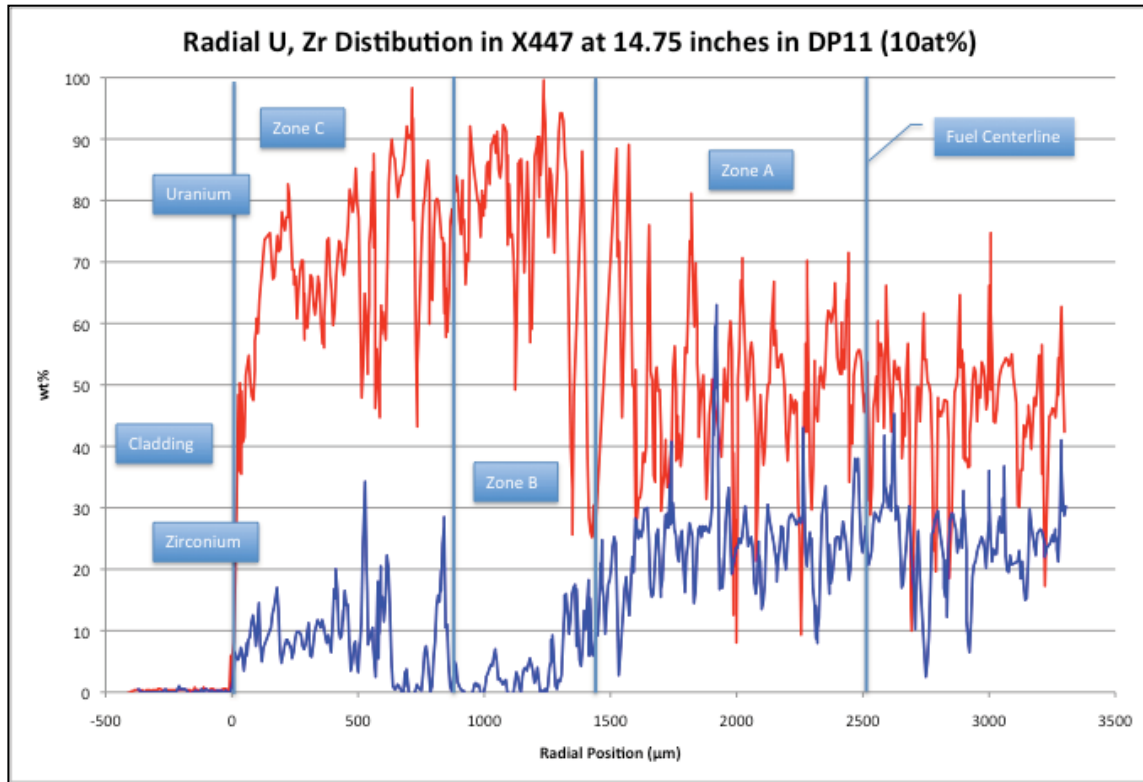


Figure 25. Microprobe scan of U-Zr distribution across the radial cross-section of DP-11 (Line X in Figure 24).

Table 3. DP-11 Zonal Radial Composition Summary

Zone	Zr Composition Range	Zr Average	Uranium Average
Central	14 to 34 wt.%	30	68
Mid	0 to 3 wt.%	2	100
Outer	9 wt.%	9	87

The analysis of cladding component migration into the fuel region is exemplified in Figure 26 showing an analysis of iron and chromium migration across the radial extent of the DP-11 sample. Very little chromium migration was found but iron was found up to 300 μm into the fuel region from the cladding inner diameter.

Due to limitations in the measurement system, the analysis for low concentration elements such as the fission products was semi-quantitative. Figure 27 shows a graph of the distribution of Cs, Ba, La, Ce, Sm, and Pr across the radial cross-section of the DP-11 sample. With the exception of Sm, the fission products were typically found concentrated

together as particulates in the fuel region of the sample. Samarium appeared to be evenly distributed throughout the fuel matrix. The figure also shows that there was some buildup and probably reaction of Nd, Pr, Ce, and La at the fuel-cladding interface.

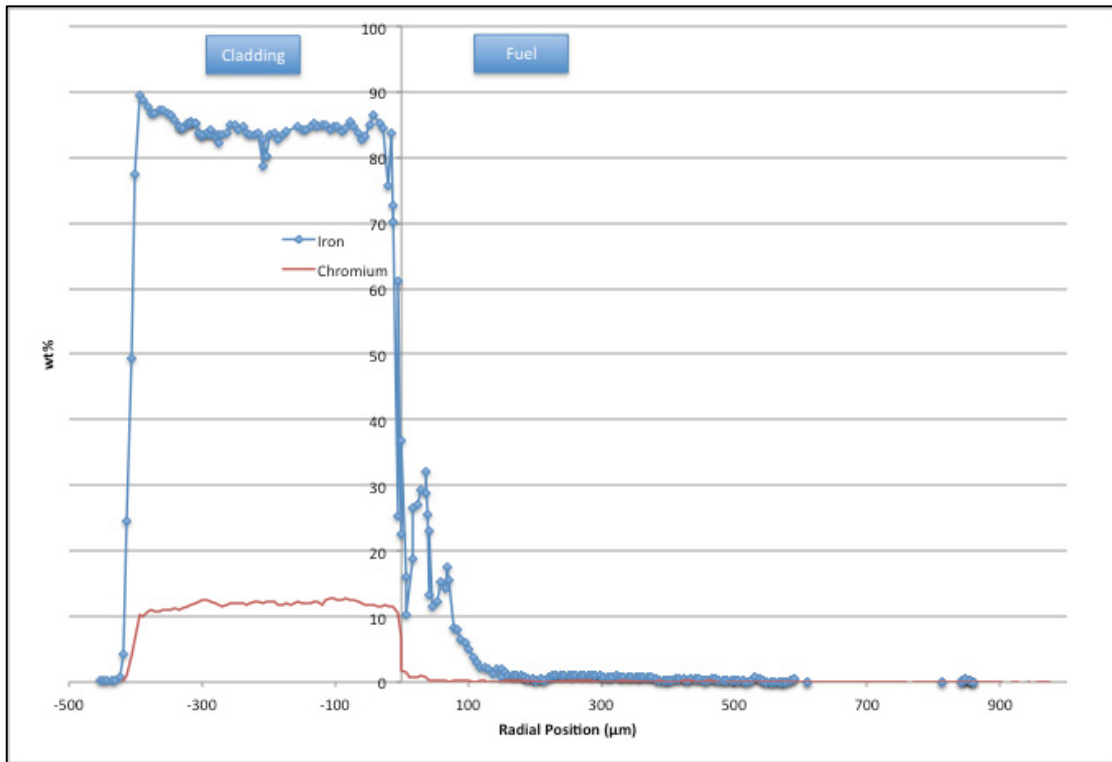


Figure 26. Distribution of iron and chromium across the radial cross section of DP-11 (Line X).

The distribution of molybdenum and palladium seen in Figure 28 showed relatively even distribution across the fuel matrix, but there was some evidence of a higher concentration of palladium at the fuel-cladding interface. Palladium has been shown previously to concentrate with and perhaps form compounds with lanthanide fission products that accumulate at the fuel-cladding interface [18].

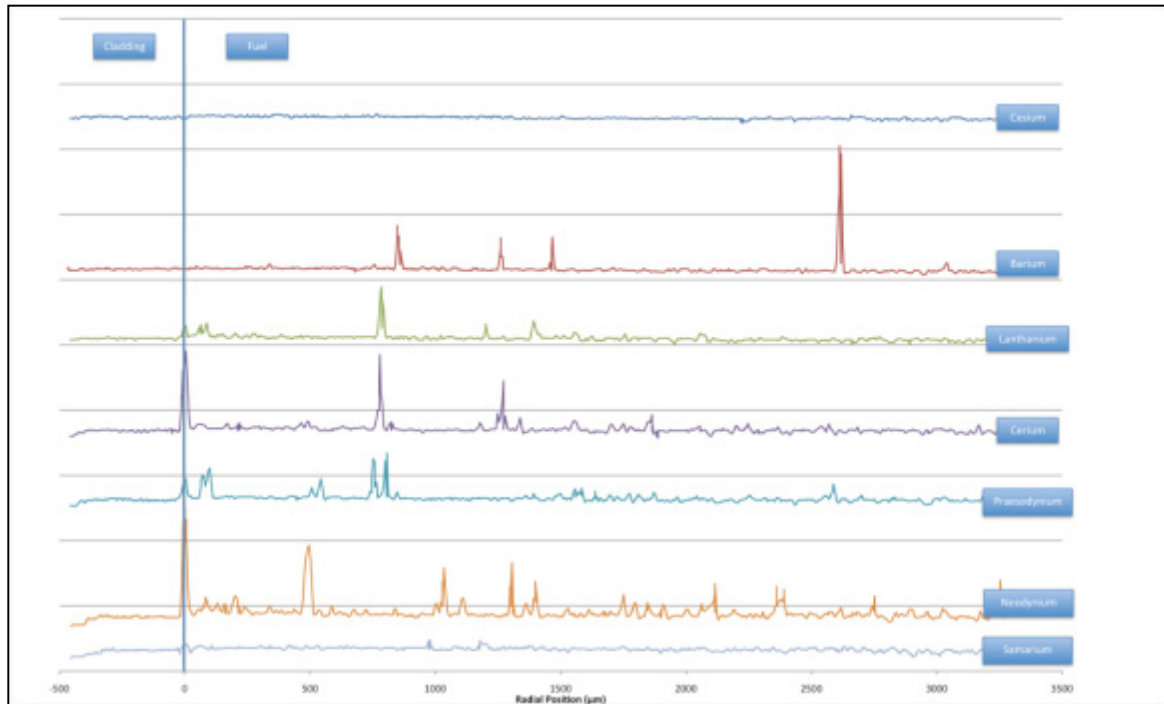


Figure 27. Radial distribution of fission products across radial cross-section of DP-11 (Line X).

Based on the general analysis of the DP-11 fuel cross-section, specific areas of interest were identified for more detailed examination. Detailed analysis of the fuel-cladding interface was conducted in a region of high fuel-cladding interaction and in a region of low fuel-cladding interaction. Both areas were analyzed similar to the radial cross section analysis shown above to investigate the U, Zr distribution, the migration of cladding components into the fuel, and the distribution of fission products.

Detailed EPMA analysis was performed in an area of localized high FCCI and versions of the data shown in Figures 29, 30, and 31 have been published previously by Kim et al. [28]. The analyses of species distribution in a high-FCCI region were taken across Line Y as shown in Figure 24. The uranium and zirconium distribution 350 μm from the cladding into the fuel is shown in Figure 29. Uranium content averaged 70 wt.% and

zirconium approximately 10 wt.% but the analysis indicated that fuel segregated into separate phases with non-fuel regions present.

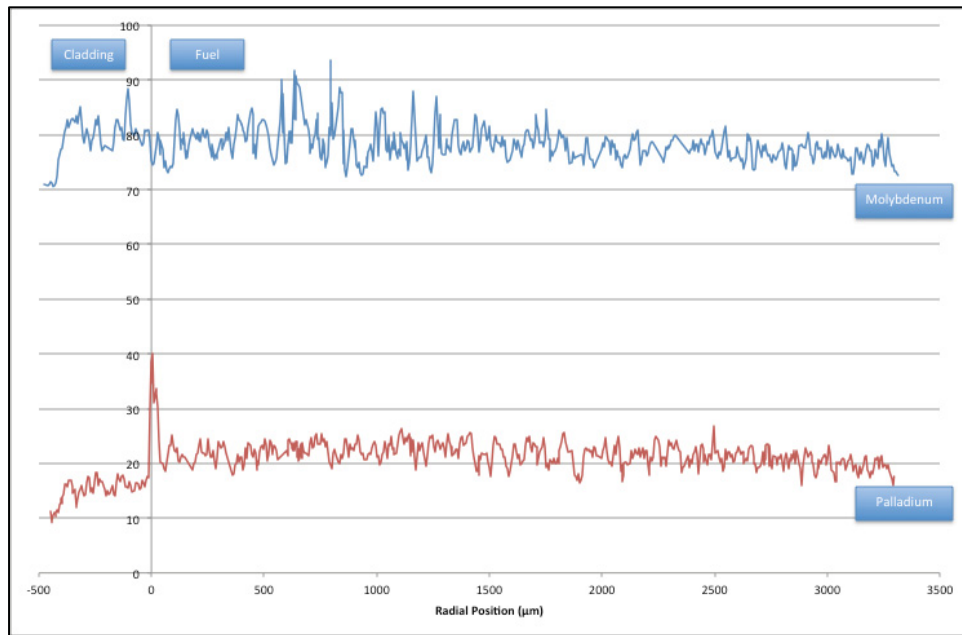


Figure 28. Radial distribution of Mo and Pd fission products across DP-11 (Line X).

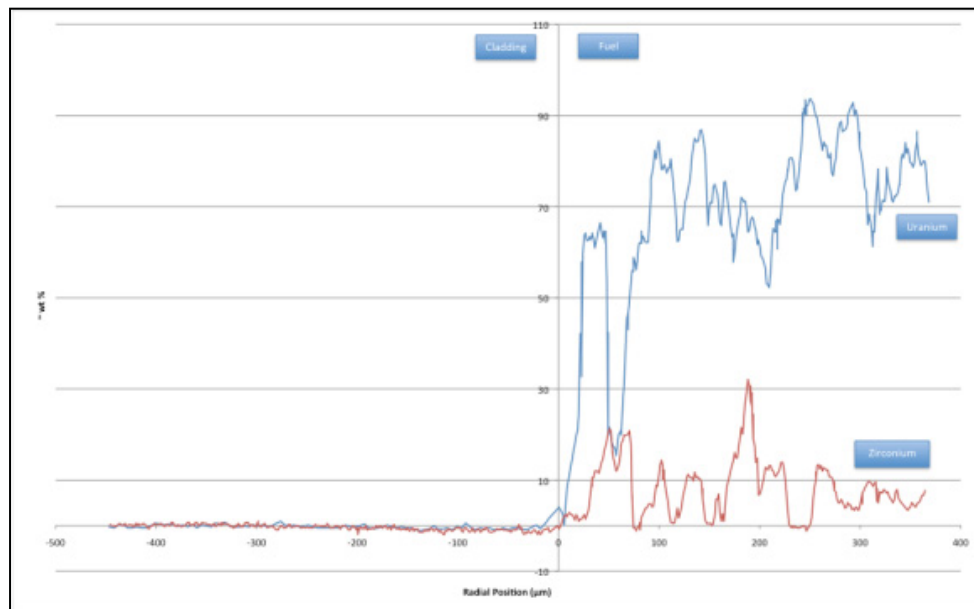


Figure 29. Uranium-Zirconium distribution near cladding in an area of high FCCI.

The distribution of cladding components found in the localized zone of high-FCCI is shown in Figure 30. The iron and nickel both diffused into the fuel, iron significantly

depleted in the first 50 μm of cladding; Cr remained in the cladding. The iron found in precipitate phases extended 300 μm into the fuel. The nickel, nominally only 0.5 wt. % in as-fabricated HT-9 cladding, showed a progressive increase with distance in the fuel until it reached 1 to 2 wt.%, 350 μm in the fuel. Figure 30 shows the primary role that iron plays in formation of FCCI. The first 50 μm of the cladding clearly shows significant iron depletion. The iron from the depleted zone appears to migrate into the fuel region to form fuel-cladding interaction layer.

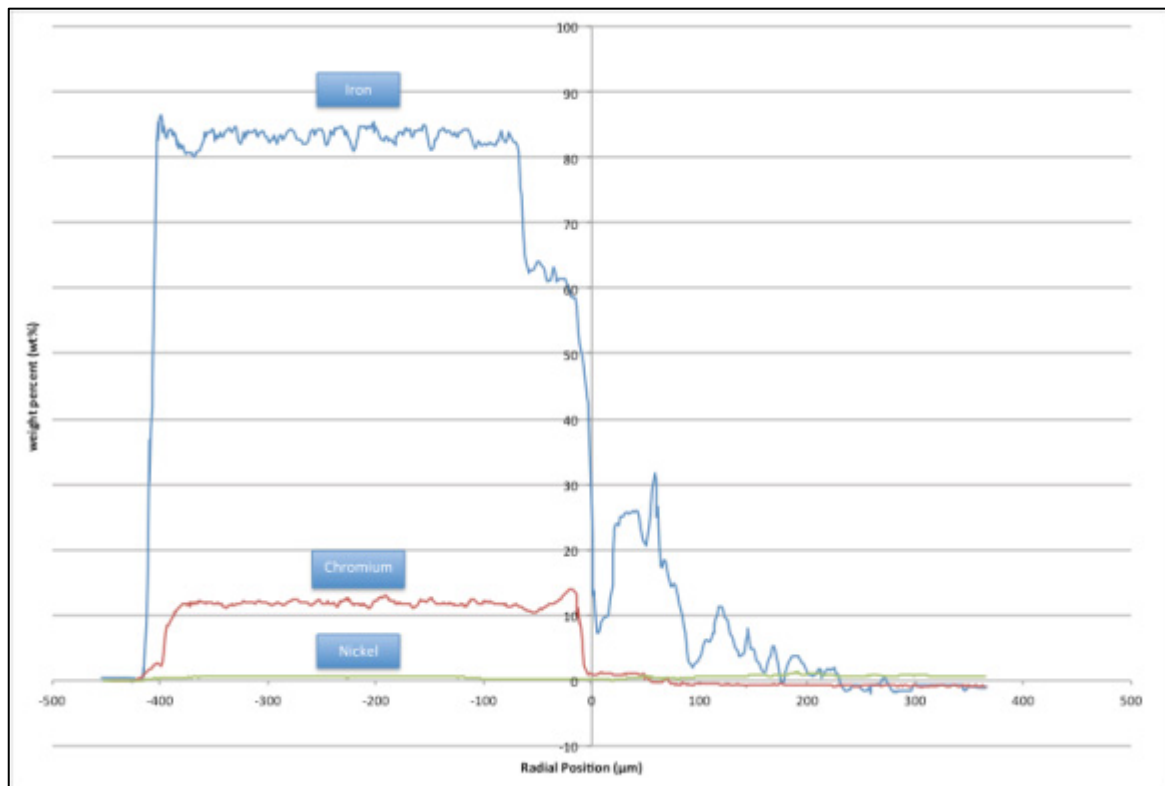


Figure 30. Cladding component distribution in a localized zone of high-FCCI.

A semi-quantitative analysis of fission product species in the region of high-FCCI at the fuel-cladding interface is shown in Figure 31. The graph shows the distribution of Cs, Ba, Pr, La, Ce, Nd, and Sm across the radial cross-section of the DP-11 sample. The figure shows the typical behavior of fission products in the formation of precipitates in the fuel

region. Ce and Nd have also penetrated nearly 100 μm into the cladding. La, Pr, and Sm were also present in the cladding but at relatively lower concentration.

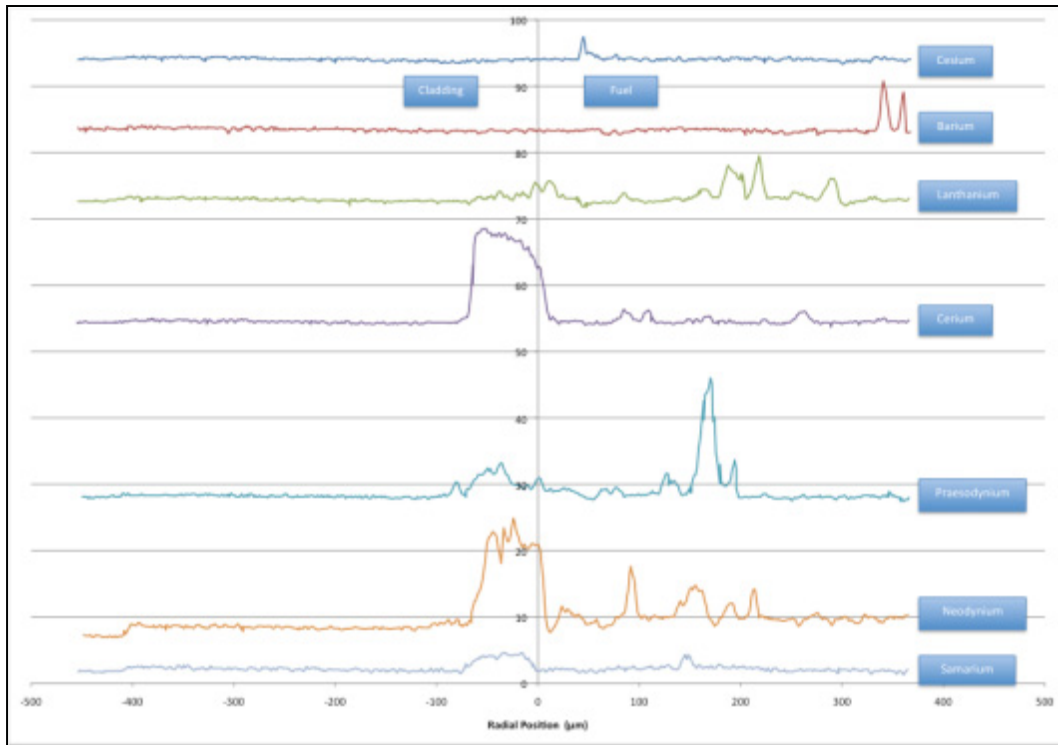


Figure 31. Radial distribution of fission products in a region of high-FCCI.

2.3.2.3 DP-70 and DP-75 Postirradiation Examination

DP-70 and DP-75 were the two breached pins in the X447 assembly. They were examined extensively at the Hot Fuel Examination Facility (HFEF). It is important to note the differences between these two pins and other pins in the X447 assembly that did not breach.

Figure 32 and Figure 34 show the axial burnup and pin diameter for pins DP-70 and DP-75. Note that DP-75 (shown in Figure 34) exhibited a maximum change in diameter nearly three times as large as that observed for unbreached pins DP-04 and DP-11. The diameter change observed for DP-70 was comparable to the unbreached pins. HT-9 tube ruptures often show localized strain rate instability when stressed at high temperatures and a

localized bulge can occur before rupture [29]. It is not known over what amount of time this instability occurs prior to breach, but the DP-70 failed at lower strain, perhaps before the onset of this strain-rate instability.

Figure 33 and Figure 35 show the gross metallography and change along the axial length of the fuel columns of DP-70 and DP-75, respectively. The metallography of both pins showed significant fuel restructuring as expected at this burnup for metallic fuel and also shows the FCCI formation along the axial length of the fuel column. Full metallography cross-sections of the DP-70 and DP-75 fuel pins at different axial locations can be found in Appendices C and D, respectively, along with details of the local burnup and calculated peak cladding and fuel centerline temperatures.

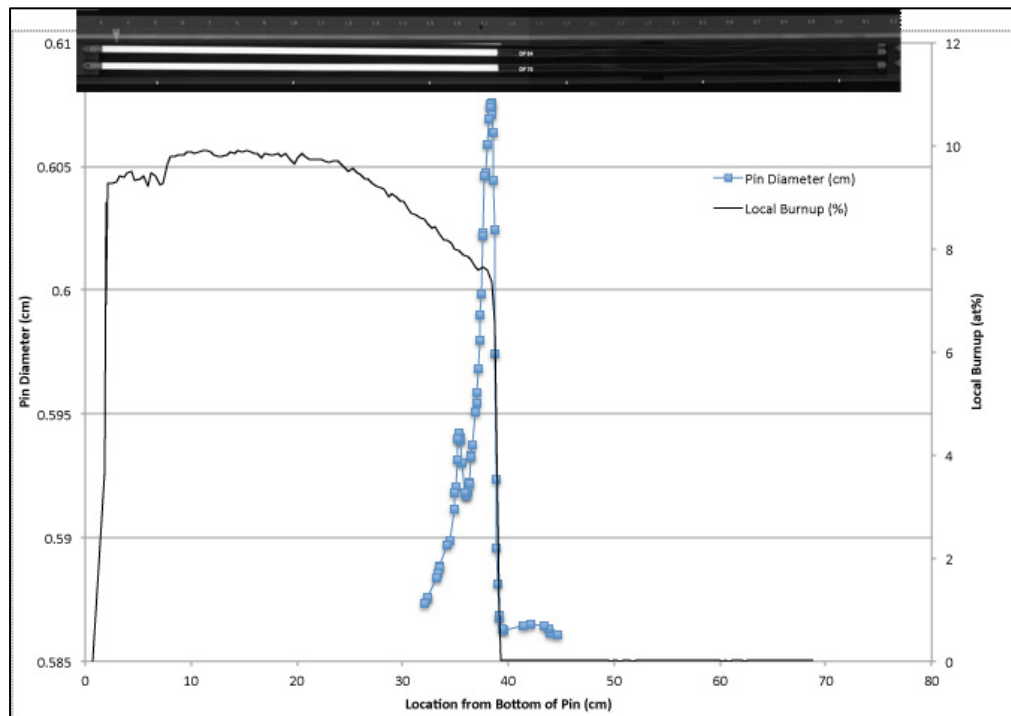


Figure 32. Axial pin diametral profilometry with local burnup and radiograph of DP-70.

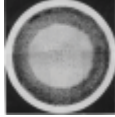
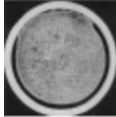
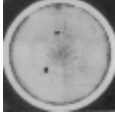
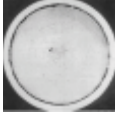
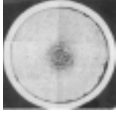
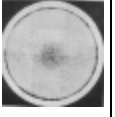
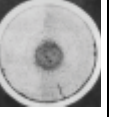
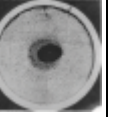
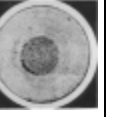
X/L=0.18	0.49	0.62	0.71	0.84	0.92	0.94	0.95	0.97
10.2 at%	10.6 at%	9.9 at%	9.3 at%	7.7 at%	6.8 at%	6.5 at%	6.3 at%	6.1 at%
457°C	543°C	582°C	599°C	628°C	638°C	639°C	641°C	643°C
0 μm	0 μm	28 μm	25 μm	86.4 μm	116 μm	97 μm	91.4 μm	127 μm
								

Figure 33. Gross metallography of the DP-70 pin showing microstructure axially along the pin with FCMI thickness shown in μm .

As presented earlier, Figure 8 shows the expected axial temperature profile and the axial local linear power for DP-04, DP-11, DP-70, and DP-75 fuel pins based on their effective full power day normalized irradiation power history. The linear power and temperature profiles for the four pins were similar, but with DP-70 and DP-75 having slightly higher power and temperature than DP-04 and DP-11.

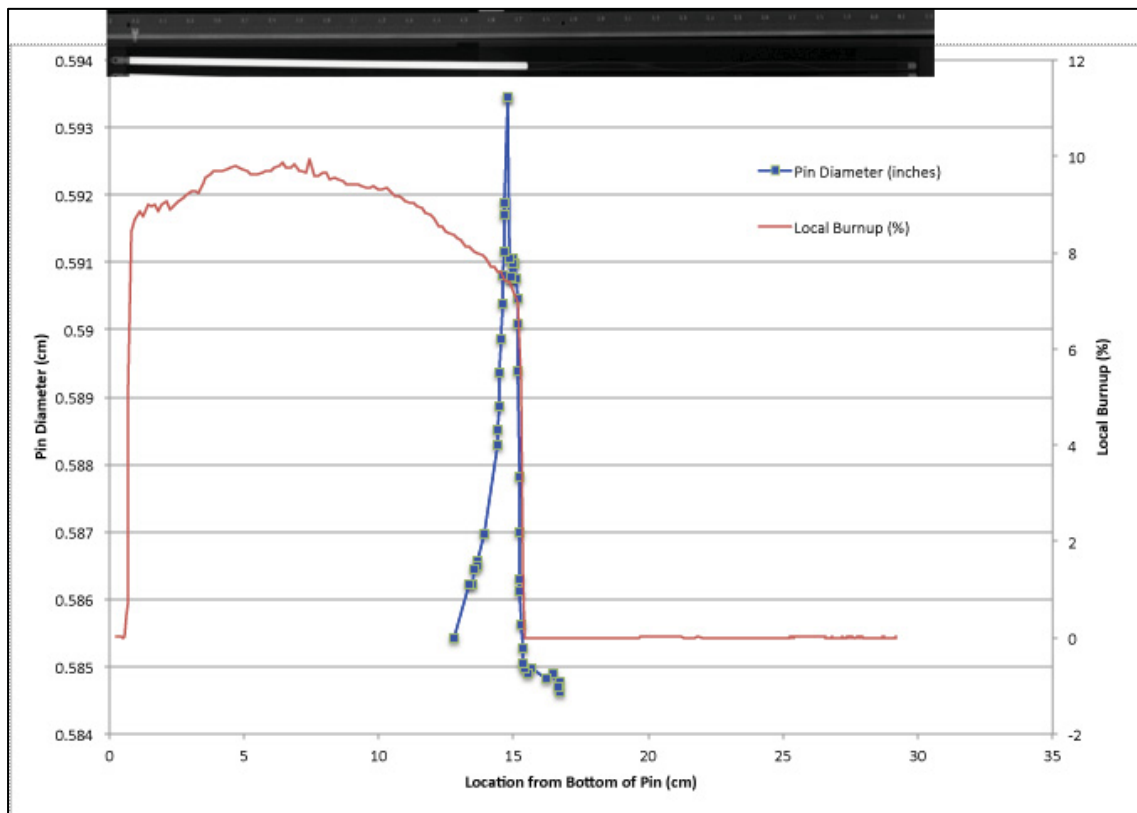


Figure 34. Axial pin diametral profilometry with local burnup and radiograph of DP-75.

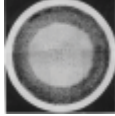
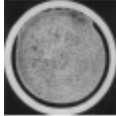
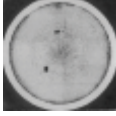
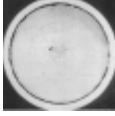
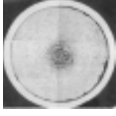
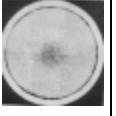
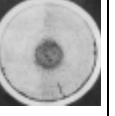
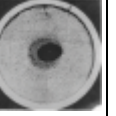
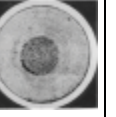
X/L=0.19	0.44	0.68	0.81	0.898	0.92	0.93	0.98	1.0
10.2 at%	10.7 at%	9.5 at%	8.2 at%	7.3 at%	7.0 at%	6.8 at%	6.5 at%	6.3 at%
457 °C	533 °C	596 °C	622 °C	635 °C	637 °C	640 °C	642 °C	644 °C
0 μm	13 μm	13 μm	64 μm	127 μm	127 μm	140 μm	146 μm	152 μm
								

Figure 35. Gross metallography of the DP-75 pin showing microstructure axially along the pin with FCCI thickness shown in μm .

The data collected during the examination of the X447 experiment is important to forwarding the understanding of metallic fast reactor fuels. X447 was designed to operate at high temperature to investigate FCCI with respect to temperature. The experiment experienced cladding failures due to FCCI near the top of the fuel column coinciding with the location of maximum cladding strain and maximum FCCI. The DP-75 fuel pin provides FCCI layer formation at relatively high temperatures and medium burnup levels.

3 MFF-3 and MFF-5 FFTF Experiments

The MFF series of metallic fuel irradiations [30] provides an important potential comparison between data generated in EBR-II and that expected in a larger scale fast reactor. The Fast Flux Test Facility (FFTF) reactor contained standard fuel with a 91.4 cm (36-inch) tall fuel column and a chopped cosine neutron flux profile resulted in a core with peak cladding temperature at the top of the fuel column but with peak burnup near the centerline of the core. The peak fuel centerline temperature was midway between the core center and the top of fuel, lower in the fuel column than that in the EBR-II X447 experiment. The MFF-3 and MFF-5 qualification assemblies operated in FFTF to greater than 10 at. % burnup with no pin breaches. All fuel pins contained tag gas identification modules. The MFF-3 assembly operated to 13.8 at. % burnup with a peak inner cladding temperature of 643°C. The MFF-5 assembly operated to 10.1 at. % burnup with a peak inner cladding temperature of 651°C. This can be compared to the two pin breaches experienced in X447 at approximately 10 at. % burnup and peak inner cladding temperatures of 648°C and 638°C respectively. To understand the performance differences in the pins from these two reactors, operating at similar peak cladding temperatures, postirradiation examination of a pin from MFF-3 and MFF-5 has been conducted to establish the extent of FCCI present, a known contributor to the X447 pin breaches.

3.1 *As-Built Condition*

The as-built conditions of MFF-3 and MFF-5 were very similar. The primary difference was a small design change in the fuel plenum volume. The plenum length in MFF-5 was increased over that of MFF-3 by 10.2 cm. The MFF-5 assembly was designed to achieve an ultimately higher burnup than that of MFF-3 but operate at a lower temperature for longer life. The cladding thickness of MFF-5 fuel pins was also 0.025 mm

thinner than that of the MFF-3 fuel pins. These slight design changes were to allow the MFF-5 assembly to achieve longer life in FFTF and in doing so, the nominal operating conditions were expected to be slightly less challenging than that of MFF-3. In practice the MFF-5 assembly was operated to 10 at. % burnup whereas MFF-3 was operated to 13.8 at. % burnup. Both assemblies were removed from FFTF in 1994 when the reactor was placed in shutdown mode. The nominal design features of the MFF-3 and MFF-5 assemblies are provided in Table 4.

The MFF-3 assembly contained 169 pins (0.270 in. diameter) in an HT9 duct. The HT9 cladding and wire wrapped fuel pins contained U-10Zr fuel sodium bonded to the cladding. The fuel was enriched (32.4 wt.% U-235) to operate at power levels representative of high (2-sigma) power and temperature conditions in a FFTF metallic core (617 W/cm and 649°C peak cladding mid-wall at beginning of life (BOL)). The fuel column was bounded by an Inconel 600 lower reflector, and had no upper reflector or upper blanket.

The MFF-5 assembly contained 169 pins (6.86 mm diameter) in an HT9 duct. The HT9 cladding and wire wrapped fuel pins contained U-10Zr fuel sodium bonded to the cladding. The fuel was enriched (31.0 wt.% U-235) to operate at power levels representative of peak conditions in a FFTF metallic core (558 W/cm and 621°C peak cladding mid-wall at BOL). The fuel column was bounded by an Inconel 600 lower reflector and had no upper reflector or upper blanket. The MFF-5 test assembly was prototypic of a previously projected FFTF Series III driver fuel assembly. This design included a 10.2 cm longer plenum than that of MFF-3. In order to increase fuel pin plenum size, the MFF-5 assembly included a redesigned handling socket and lower shield assembly which resulted in elevating the fuel pins 10.2 cm and thus increasing the plenum length

relative to pins from MFF-3, but maintained the same pin length and axial fuel position as that of the Series I and II drivers in FFTF. A lower axial reflector, 6.35 cm in length, was used to fix the elevation of the fuel in the pin. The balance of the lower shielding (compared to Series I and II drivers) was provided by the new assembly design.

Table 4. Nominal Design Features of MFF-3 and MFF-5 Assemblies

	MFF-3	MFF-5
Fuel Alloy Composition	U-10Zr	U-10Zr
Fuel Slug Diameter	0.196-in. (4.98-mm)	0.196-in. (4.98-mm)
Fuel Slug Length	36-in. (91.44 cm)	36-in. (91.44 cm)
Fuel Plenum Volume	28.9 cm ³ at 25°C	31.5 cm ³ at 25°C
Plenum to Fuel Volume Ratio	1.63	1.79
Cladding Material	HT9	HT9
Cladding Outer Diameter	0.270-in. (6.86-mm)	0.270-in. (6.86-mm)
Cladding Wall Thickness	0.022-in. (0.559 mm)	0.021-in. (0.533 mm)
Fuel Pin Length	93.75-in. (238.1 cm)	93.75-in. (238.1 cm)
Fuel Smeared Density	75%	74%
Fuel theoretical density	15.8 g/cm ³	15.8 g/cm ³
Wire Wrap Dia./Pitch	0.0535-in./6-in. (1.35 mm/ 15.24 cm)	0.0535-in./6-in. (1.35 mm/ 15.24 cm)
Sodium volume	6.2 cm ³ at 25°C	6.2 cm ³ at 25°C
Sodium Fill Above Fuel	1.0-in. (2.54 cm)	1.0-in. (2.54 cm)
Axial Fuel Restrainer	None	None
Subassembly Type	HT-9	HT-9
Hex-can material – First	HT-9	HT-9
Hex-can material – Second	HT-9	HT-9
Maximum Pin Linear Power	18.7 kW/ft (613 W/cm)	17 kW/ft (557 W/cm)
Max. Cladding (midwall) Temp.	640 - 650°C	620 °C
Maximum Fuel Temperature	860 °C	825 °C

3.2 Irradiation Conditions and Performance History

MFF-3 began irradiation in Cycle 10C in core location 2404. MFF-5 began irradiation in Cycle 11B-1 in core location 1304. Figure 36 shows the FFTF core map for cycle 12B-1 indicating the locations of the MFF-3 and MFF-5 assemblies during irradiation. The assemblies were irradiated in these positions throughout their duration in FFTF. Table 5 shows the initial predicted test operating parameters for the MFF-3 and MFF-5 assemblies at the beginning of cycle (BOC) for the insertion cycle.

Table 5. Summary of MFF-3 and MFF-5 initial test operating conditions.

Test	Cycle	Core Position	Calc T_{outlet} (°C)	Flow Rate (kg/hr)	Flow Rate (m ³ /s)	Fission Power (MW)	Axial PF	Radial PF	Peak W/cm
MFF-3	B10C	2404	580	92210	113	7.867	1.24	1.066	608
MFF-5	B11B1	1304	570	90881	112	7.360	1.21	1.058	553

*MFF-3 was irradiated for 726.2 EFPD, MFF-5 was irradiated for 503 EFPD.

The peak linear power for each assembly was calculated by multiplying the assembly fission power, a factor accounting for the difference in the power deposited in the pin (fuel and cladding) and the fission power, and the radial and axial peaking factors. The pin energy deposition for the U-10Zr metallic fuel pins differs from the standard MOX ((U, Pu)O₂) fuel pins in FFTF because the U-235 enriched pins release less energy per fission than pins driven by Pu-239 fission and have a different overall composition due to the internal sodium and zirconium in the metallic fuel pins. The difference in pin energy deposition rates for these metallic fuel pins was accounted for in the calculated peak pin powers.

The total heat distribution for the FFTF core (including non-fueled components) was obtained by combining the local direct fission heat production with other nuclear heat sources, such as gamma ray absorption, charged particle reactions and neutron scattering recoils. The energy produced from all of these sources was combined and adjusted so that the total was properly normalized for a recoverable heat energy of 291 MW at full power for Cycles 9 through 12 (previously 400 MW for Cycles 1 through 8).

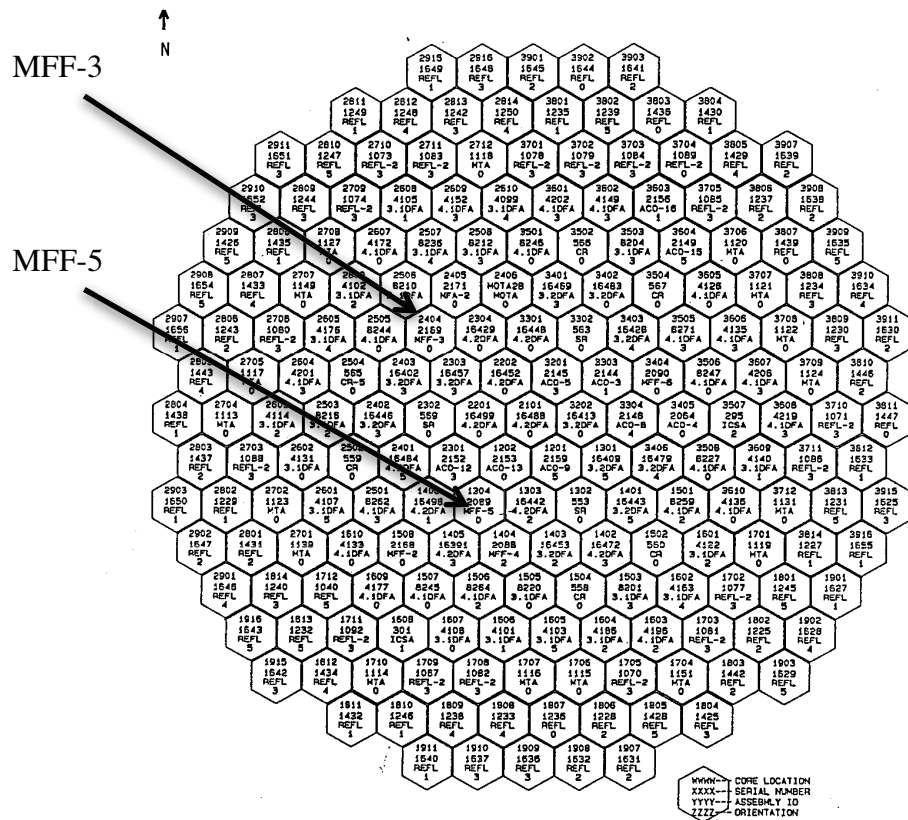


Figure 36. FFTF Cycle 12B-1 Core Loading and positions of MFF-3 and MFF-5.

Based on the deposited energy distribution and nominal sodium flow rates for each core component, the outlet temperature for each component was calculated at beginning of cycle and end of cycle. The assembly flow rates varied slightly from cycle to cycle as the core loadings changed. The assembly flows were based on a calculated core pressure drop at the total reactor flow rate of 7.59×10^6 kg/hr.

The assembly subchannel flow temperatures were calculated using the SUPERENERGY thermal hydraulic code and SIEX fuel performance code. The SAFE code was used to calculate the pin temperature axial distributions including the fuel centerline, peak inner cladding temperatures, and the cladding wall temperatures.

The SUPERENERGY code is a sub-channel code designed specifically for hexagon shaped, wire wrapped pin bundles and was used to calculate the FFTF core assembly mixed-mean outlet temperatures, the assembly sub-channel temperatures of all core assemblies, the core assembly duct wall temperatures, and the temperature of the reflector assembly coolant channels. The assembly mixed mean outlet temperatures were used as a basis for comparison to the FFTF above-core instrumentation data and to show that the core loading plans were in compliance with FFTF technical specifications prior to reactor operation. The sub-channel temperatures were used in design analyses of test pins, postirradiation data correlation of test pins, and for lifetime analyses of driver fuel pins. The duct wall temperatures were used in the structural analyses of the individual assemblies and of the core restraint system. The flow field was described in terms of two correlated parameters, a sub-channel mixing parameter and a swirl flow parameter. These two parameters, along with the energy equation and a sub-channel flow split model, completely describe the temperature field in a pin bundle. The mixing parameters and flow split correlations were based on extensive experimental test data. The pin power distributions from HEDPIN were used as part of the input in determining the sub-channel temperatures.

Normalized pin power distributions were calculated using the HEDPIN computer program based on interpolating the fission powers from the calculational mesh to the pin positions. The pin power distributions and sub-channel coolant temperatures were used to determine fuel pin temperature and power profiles using the SAFE computer code, in an identical manner to that performed for the EBR-II X447 experiment fuel pins for each cycle. From this analysis two pins were identified for detailed temperature and axial power distribution analysis and full non-destructive and destructive postirradiation examination. Pin serial number 193045 (a 4th row pin) from the MFF-3 assembly and pin serial number

195011 (a 4th row pin) from the MFF-5 assembly appeared to have experienced high power and hence high temperature operation, nearly peak for the assembly. Because of the orientation of the assemblies during their irradiation history, some of the 4th row pins tend to be the highest power pins and hence the highest temperature pins in the assembly over the life of the assembly. Figure 37 provides a cycle to cycle history of the peak pin power and the peak inner cladding temperature for Pin 193045. Figure 38 shows the axial linear power profile and axial temperature profiles for Pin 193045.

The analysis of the pin was conducted in the same manner as that for the X447 pins described above using the SAFE thermal analysis code. Particular attention should be called to the axial power profile and the extent to which it drops off in the upper half of the fuel column. This causes the fuel pin centerline temperature to peak at a position lower in the relative axial height with respect to the top of the fuel column than that of X447 pins. This same behavior is also seen in the MFF-5 Pin 195011. The cycle to cycle peak pin power and peak inner cladding temperature are shown in Figure 39. The axial linear power profile and axial temperature profiles for Pin 193045 are shown in Figure 40.

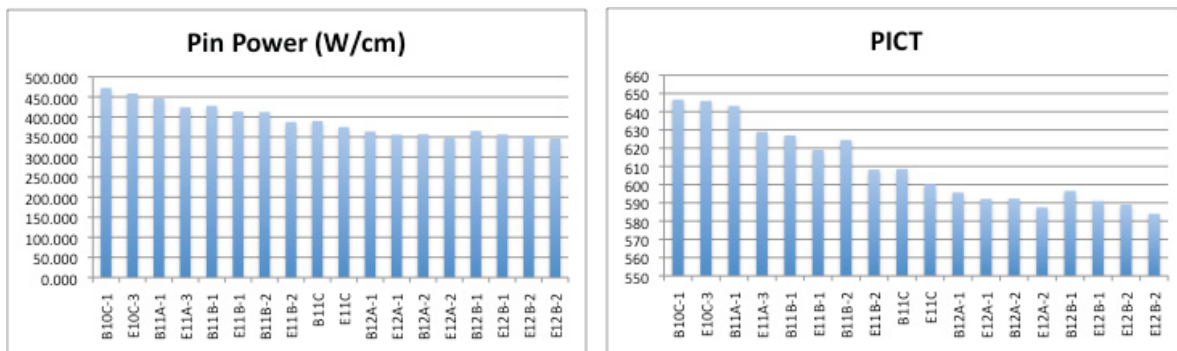


Figure 37. MFF-3 (4th Row Pin 193045) peak pin power (W/cm) and peak inner cladding temperature (°C).

Following this analysis, Pin 193045 and Pin 195011 were selected from the MFF-3 and MFF-5 assemblies for postirradiation examination. In addition to non-destructive analysis, the pins were sectioned and examined metallographically to determine the extent of FCCI and the correlation with axial position, burnup, and operating temperature. Circles in indicate the locations of Pins 193045 and 195011 in their assemblies. Pins 193045 and 195011 are near the high power region of the assembly but may not be the highest power pins.

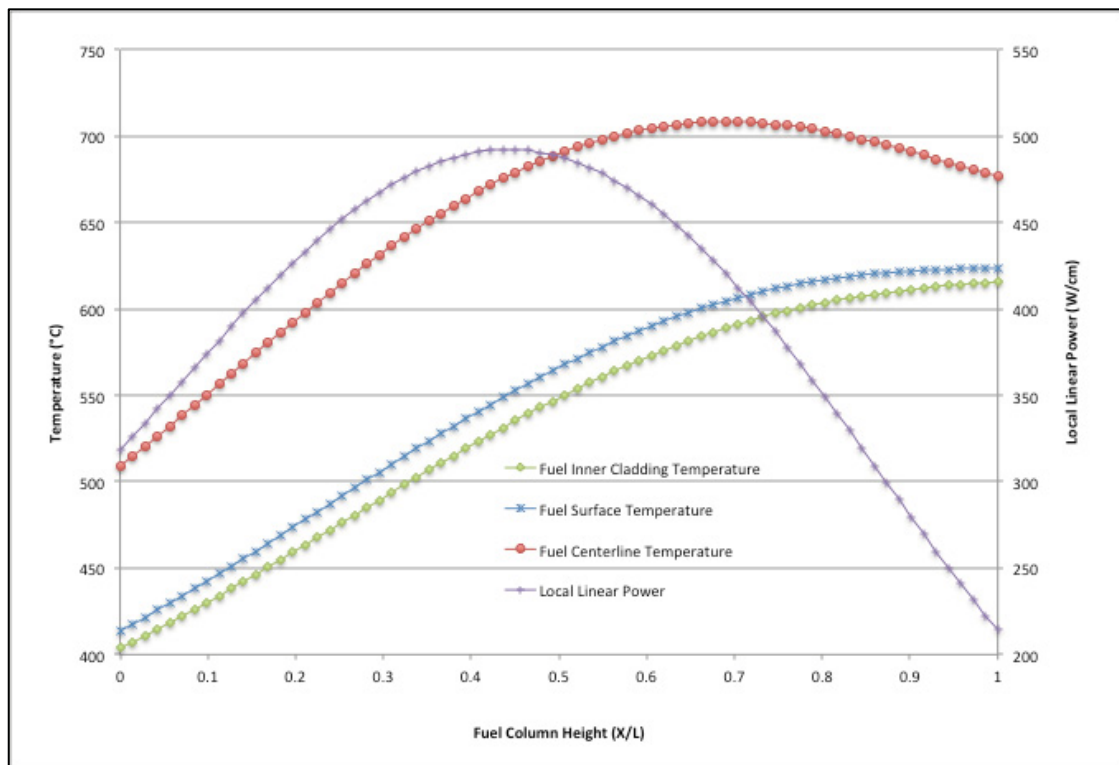


Figure 38. Axial Linear Power and PICT profiles for MFF-3 Pin 193045. Values based on EFPD weighted values across all irradiation cycles.

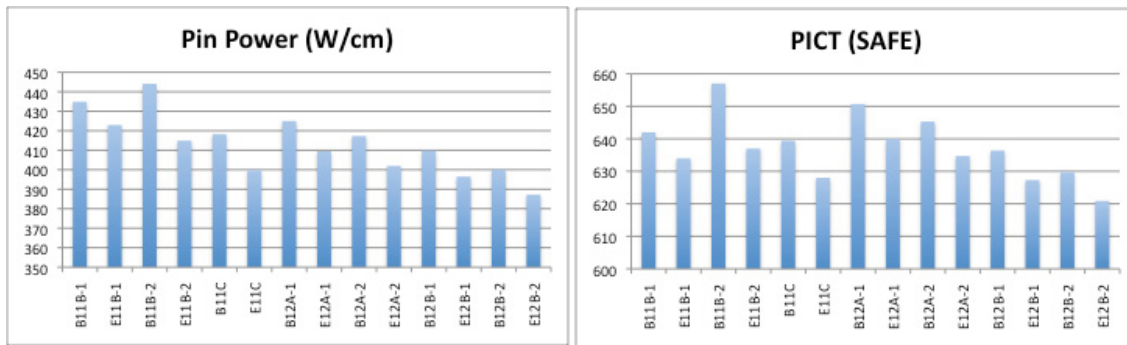


Figure 39. MFF-5 (4th Row Pin 195011) peak pin power (W/cm) and peak inner cladding temperature (°C).

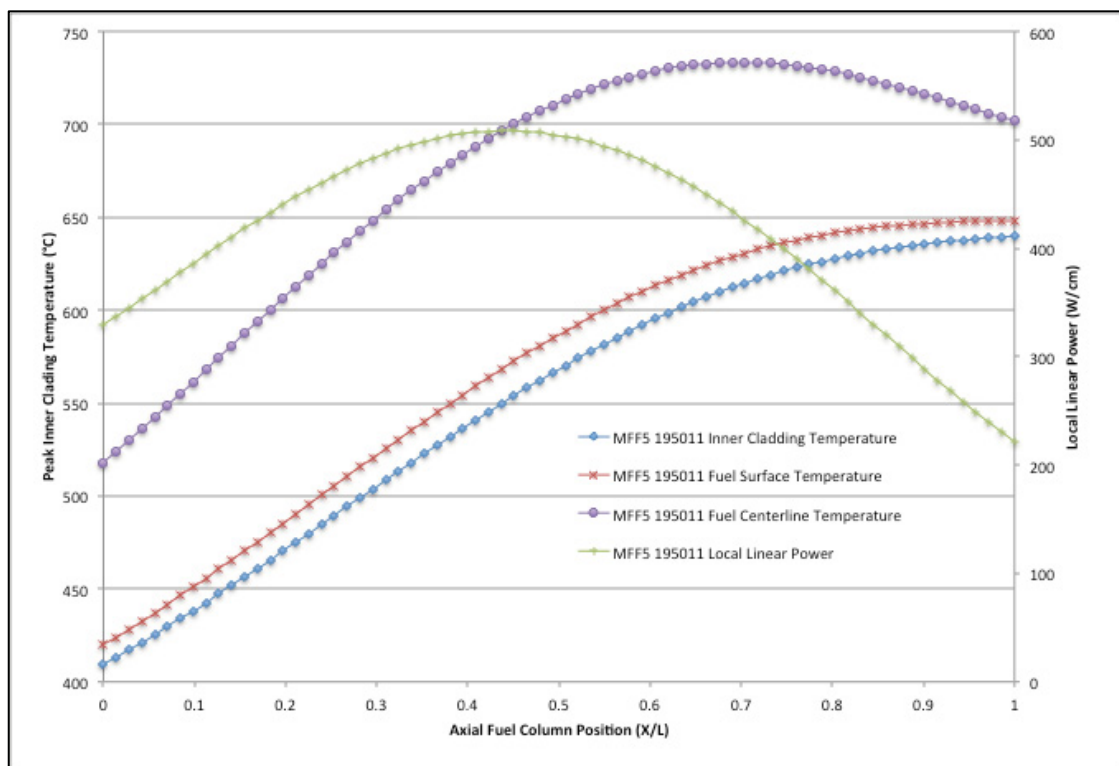


Figure 40. Axial Linear Power and PICT profiles for MFF-5 Pin 195011. Values based on EFPD weighted values across all irradiation cycles.

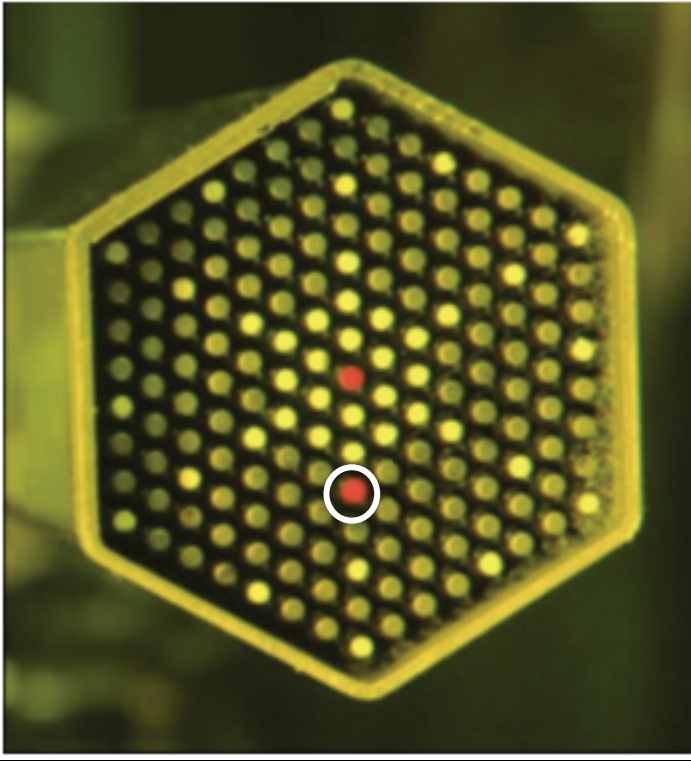
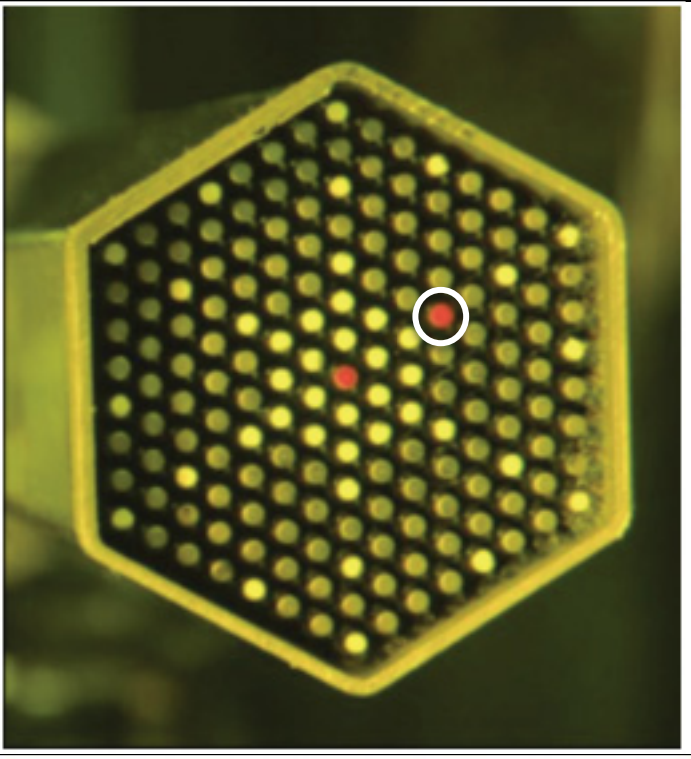
	<p>Pins selected from MFF-3 marked red. (locating notched positioned upper left corner.) White pins retained for future testing.</p>
	<p>Pins selected from MFF-5 marked red (locating notched positioned upper left corner.) White pins retained for future testing.</p>

Figure 41. Photographs of the MFF-3 and MFF-5 assemblies following removal of the upper handling socket. Pins 193045 and 195011 have been marked along with the center pins for identification purposes.

3.3 *Postirradiation Examination*

Postirradiation examination of fuels from the MFF-3 and the MFF-5 assemblies has recently been completed. One high temperature pin was removed from the MFF-3 assembly and one high temperature pin was removed from the MFF-5 assembly. Non-destructive and destructive examinations were then completed. Pin serial numbers 193045 and 195011 were subjected to neutron radiography, pin profilometry, gamma scan, fission gas sampling and analysis, metallography, micro-hardness, and isotopic chemical analysis.

Following removal from the assembly, no visible defects were observed. Neutron radiography and pin profilometry were completed and then the spiral spacer wire wraps were removed. Following removal of the spiral wraps, the pins were analyzed by axial gamma-ray spectroscopy (i.e., gamma-scanning). Destructive examination was initiated with pin puncturing and fission gas sampling and analysis. This was followed by sectioning, sampling, and polishing metallographic samples as well as burnup measurement. During metallographic examination, microhardness testing was also performed. Burnup samples were taken at locations adjacent to those selected for metallographic analysis and were analyzed by inductively coupled plasma-mass spectrometry for isotopic and elemental composition determination.

provides the results of a spiral profilometry scan of the 195011 fuel pin. This analysis indicates that a peak strain of 0.5% was developed over the course of the irradiation of the fuel pin. Similar to , provides a profilometry scan of the 193045 fuel pin indicating that a peak strain of 1.3% was experienced. The higher strain is expected in 193045 due to the higher burnup and neutron exposure of the assembly.

Figure 44 provides the results of gamma scanning of MFF-5 fuel pin 195011. Due to the time between the end of irradiation and gamma scanning many of the fission products of

interest in gamma scanning had decayed below the sensitivity limit of the gamma-scanning instrument. Three isotopes, Co-60, Cs-134, and Eu-154 were found to provide adequate signals for gamma scanning analysis. Co-60 provides a measure of the activation of the cladding ferritic-martensitic steel. Cesium is known to form a solution with sodium, migrate with sodium, and as such provides an indication of the location of sodium distribution inside the fuel pin. As seen in Figures 44 and 45, there is a normal sodium plug on top of the fuel column. There is a small amount of sodium at the bottom of the fuel column. The Co-60 signal can be attributed to steel components of the fuel pin. The large signal at the bottom of the fuel pin coincides with the lower Inconel reflector used to position the fuel column with respect to the FFTF reactor core. The Eu-154 is a fission product that is usually used to indicate relative burnup in the fuel but in the case of these two pins most of the Eu-154 has decayed to the point that the signal is not useful for this analysis. Burnup is measured and reported later by chemical isotopic analysis at specific sample locations. However, Eu-154 is the only lanthanide isotope that remains radioactive to a level that can be detected. Neutron radiography and gamma scanning are used to develop a specific cutting plan for metallographic and isotopic burnup analysis.

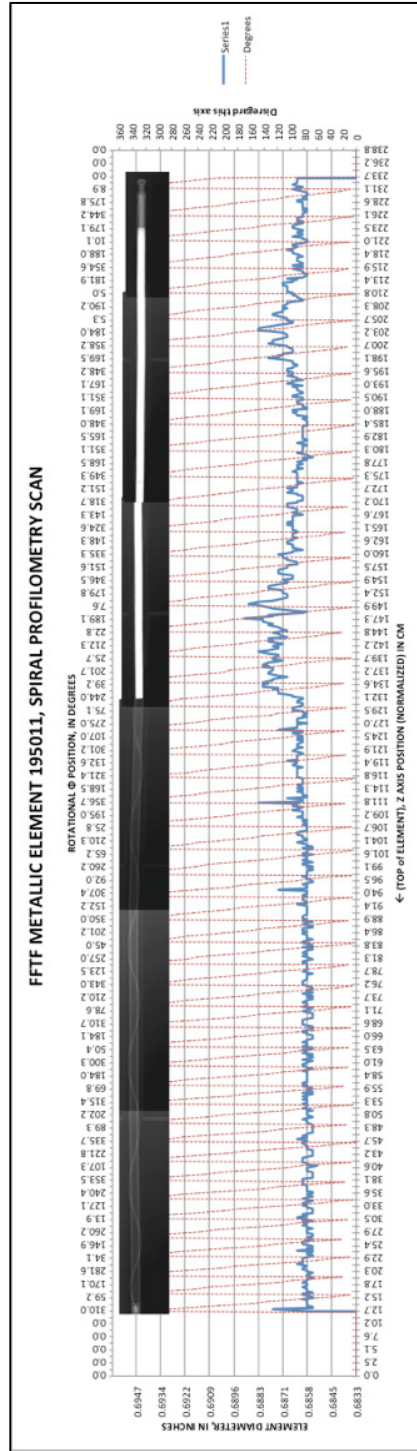


Figure 42. Profilometry analysis of MF5-5 – 195011 fuel pin overlaid with neutron radiograph.

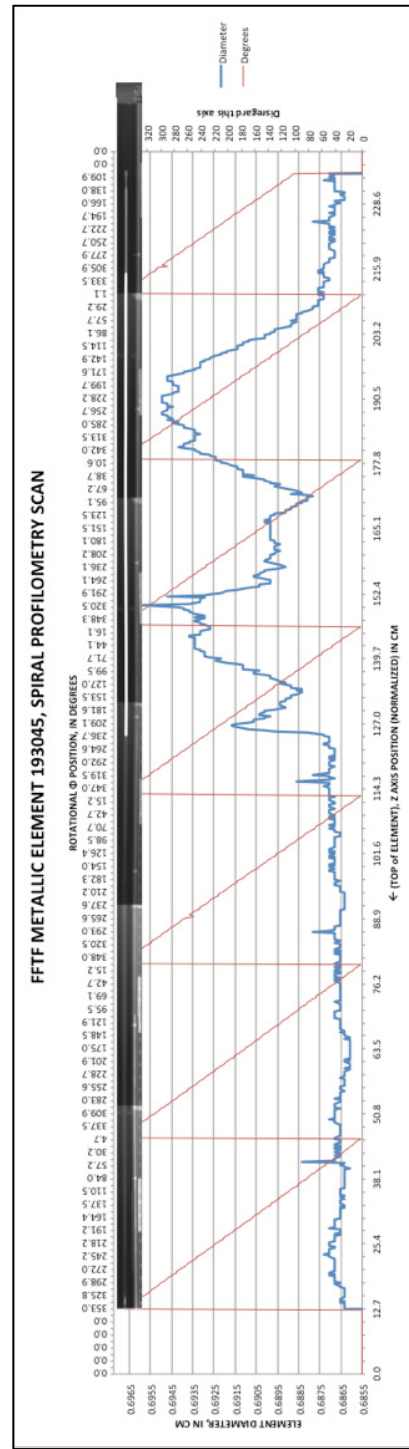


Figure 43. Profilometry analysis of MF3-3 – 193045 fuel pin overlaid with neutron radiograph.

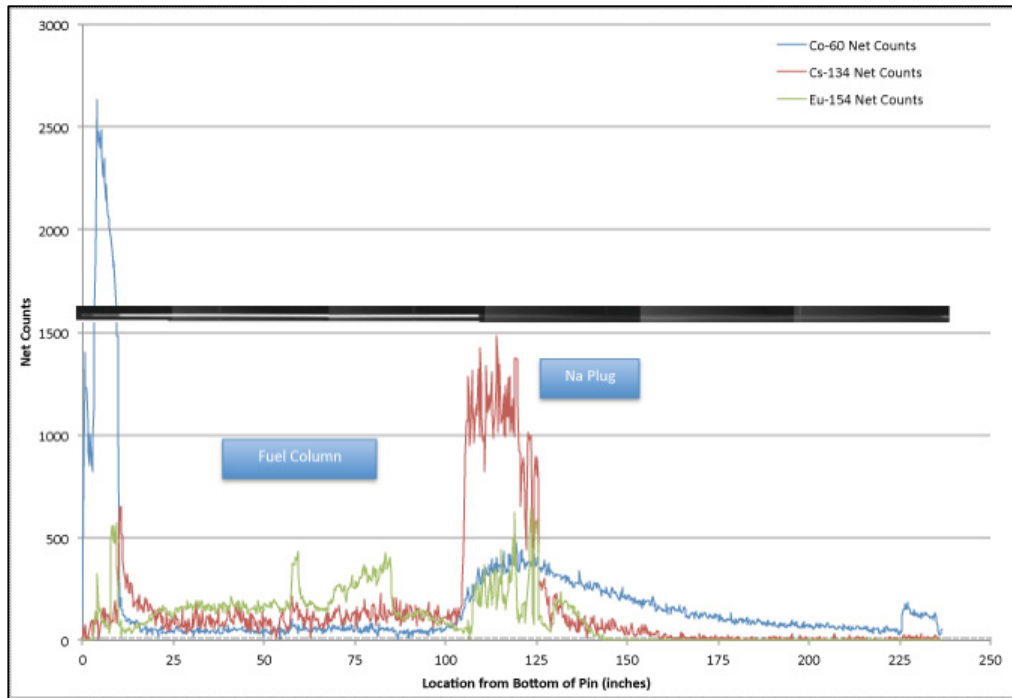


Figure 44. MFF-5 Pin 195011 Neutron Radiography superimposed on gamma scan.

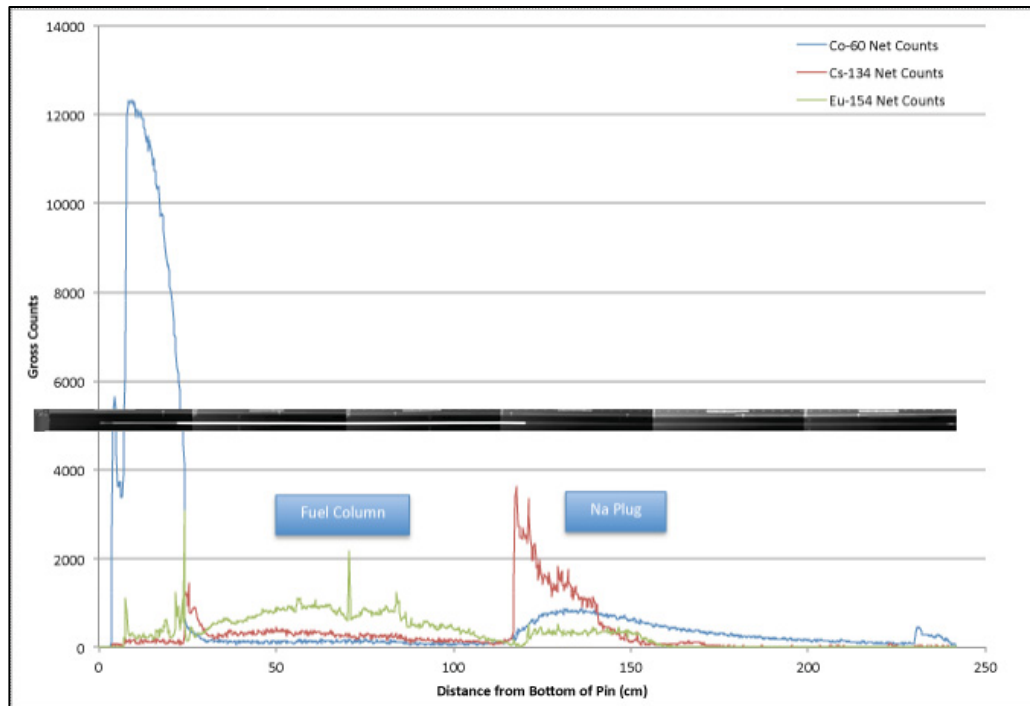


Figure 45. MFF-3 Pin 193045 Neutron Radiography superimposed on gamma scan.

Metallographic sections and burnup samples were taken from five axial locations in both the 193045 and 195011 fuel pins. The locations specified included the 0.03, 0.25, 0.5, 0.75, and 0.96 X/L locations corresponding to a sample from the top and bottom of the fuel column and three additional evenly spaced locations including a sample from the middle of the fuel column. The metallography of pin 193045 and 195011 was as expected for U-10Zr metallic alloy fuel irradiated to these burnups. Restructuring of the fuel microstructure experienced in the MFF experiments is typical of U-10Zr metallic alloy fuel. Figure 46 and Figure 47 summarize the results of metallographic analysis of the 193045 and 195011 fuel pins. The local average burnup determined by ICP-MS analysis, the peak inner cladding temperature, and the observed FCCI thickness are also summarized. Appendix E provides detailed metallographic results for the MFF-3 and MFF-5 fuel pins.

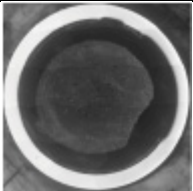
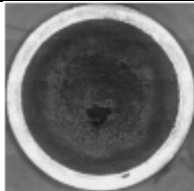
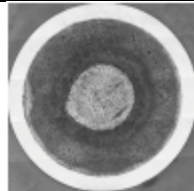
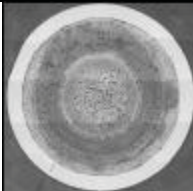
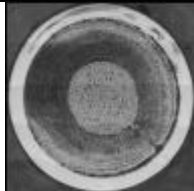
X/L = 0.03 8.4 at% 413 °C 0 μm	0.25 11.3 at% 475 °C 0 μm	0.49 12.4 at% 550 °C 0 μm	0.74 9.1 at% 604 °C 76.2 μm	0.98 5.7 at% 615 °C 152.4 μm
				

Figure 46. Gross metallography of the MFF-3 pin 193045 showing microstructure along the axial length of the fuel column.

Figure 48 is a 100X optical photomicrograph of a high FCCI region of the MFF-3 193045 fuel pin at the X/L=0.98 axial location. Extent of FCCI can be clearly seen in this sample resulting in approximately 150 μm of interaction layer thickness.

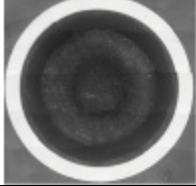
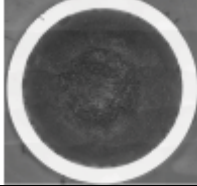
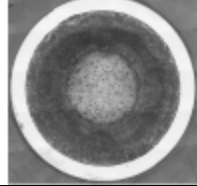
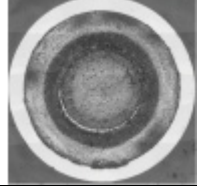
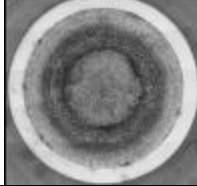
X/L = 0.03 6.7 at% 414 °C 0 μ m	0.24 8.9 at% 480 °C 0 μ m	0.48 9.8 at% 556 °C 0 μ m	0.72 8.1 at% 612 °C 50.8 μ m	0.96 4.8 at% 635 °C 25.4 μ m
				

Figure 47. Gross metallography of the MFF-5 pin 195011 showing microstructure along the axial length of the fuel column.

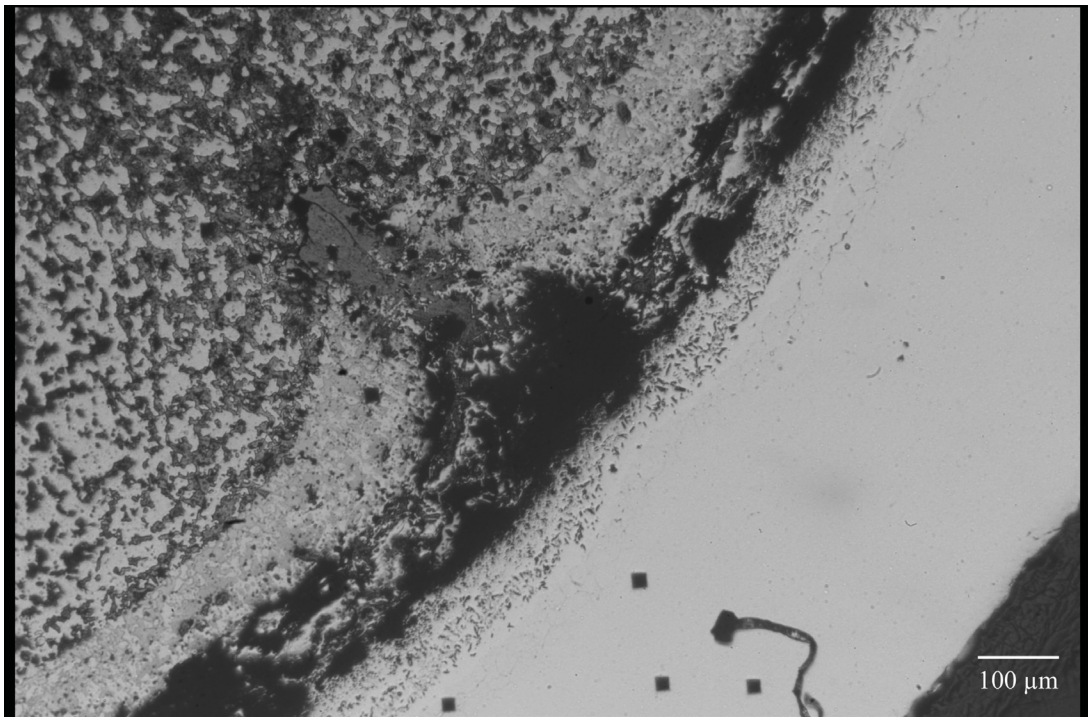


Figure 48. 100 X magnification optical photomicrograph of high FCCI region of MFF-3 Pin 193045 at X/L = 0.98 - Sample 83T.

The experimental data obtained from the MFF-3 and MFF-5 fuel pins provide a measure of the formation of FCCI layer at locations with lower temperatures than those found in the X447 fuel pins but with a broader range of burnups and exposure time. The MFF-3 experiment achieved significantly higher burnup than did the X447 experiment.

4 FCCI formation with Burnup and Temperature

A key issue associated with the capability of metallic fuel is the formation of FCCI as it weakens the cladding and ultimately contributes to cladding failure. FCCI is dependent upon the production of lanthanide fission products during the irradiation process and the migration of these species to the fuel-cladding interface for reaction/interaction with cladding constituents. The migration of the lanthanide species is strongly tied to temperature. Previous experimental studies of FCCI indicate a correlation between FCCI formation and fuel operating temperature and burnup [18]. Table 7 provides a summary of data taken from the X447, MFF-3, MFF-5, and IFR-1 (U-Pu-Zr) experiments. The data indicates the axial location of measurements from the bottom of the fuel column. Local burnup is calculated by scaling the reported cycle to cycle pin average burnup to the normalized pin power profile for each cycle. Calculated time averaged inner cladding and fuel centerline temperatures are also reported. In addition to the U-10Zr experiments, data is provided from the IFR-1, U-Pu-Zr, experiment reported by Porter and Tsai [31].

4.1 *U-10Zr metallic fuel experiment data*

The FCCI measured during metallographic analysis is reported for each axial location. The data show a relationship to burnup, fuel centerline temperature and the peak inner cladding temperature. The FCCI formed in EBR-II fuel pins peaks near the top of the fuel column. This is because the lanthanide fission product generation is high at this point and the temperature at the fuel-cladding interface is also highest at this point. The fuel centerline temperature is also high at this location and is at or near its peak in most cases.

The extent of FCCI reaction in the DP-69 pin takes place at fairly high temperatures coupled with a high-power generation rate. The formation of FCCI thickness can be seen to peak at the top of the fuel column where the power is near its peak and the temperatures are

at a peak. The DP-04 fuel pin FCCI results shown in provide an interesting comparison to that found in and for the DP-70 and DP-75 fuel pins. DP-04 had very similar irradiation conditions but did not experience failure whereas DP-70 and DP-75 experienced failure. One possible explanation is that the gas pressurization and load on the cladding in DP-04 may have been lower than that in DP-70 and DP-75 as DP-04 experienced slightly lower burnup than DP-70 and DP-75. DP-04 was most likely near failure at the end of the irradiation period, having in excess of $150\text{ }\mu\text{m}$ of FCCI layer formation at the top of the fuel column which is about 40% of the wall thickness.

Figures 53 and 54 provide similar presentation of irradiation and FCCI results for the two fuel pins examined from the MFF-3 and MFF-5 FFTF assemblies. The differences between power profile and resulting temperature profile can be immediately seen when compared with that from the X447 experiment pins. The power profile is seen to peak lower in the fuel column relative to the top of the fuel, and the fuel temperatures begin to drop before reaching the top of the fuel column. This is especially true in the case of the fuel centerline temperature. FCCI is lower than that found in the X447 fuel pins when compared at similar burnups. The MFF-5 assembly reached 10 at. % burnup and operated at similar temperatures to those found in the X447 experiment, namely, fuel centerline temperatures near 700°C and PICT near 650°C . But the FCCI layer was much thinner than that in the X447 pins and peaked at a fuel column location of $X/L = 0.7$ ($50\mu\text{m}$) and dropped to $25\text{ }\mu\text{m}$ at the top of the fuel column. This is similar to the behavior observed by Porter and Tsai [31] for the IFR-1 experiment.

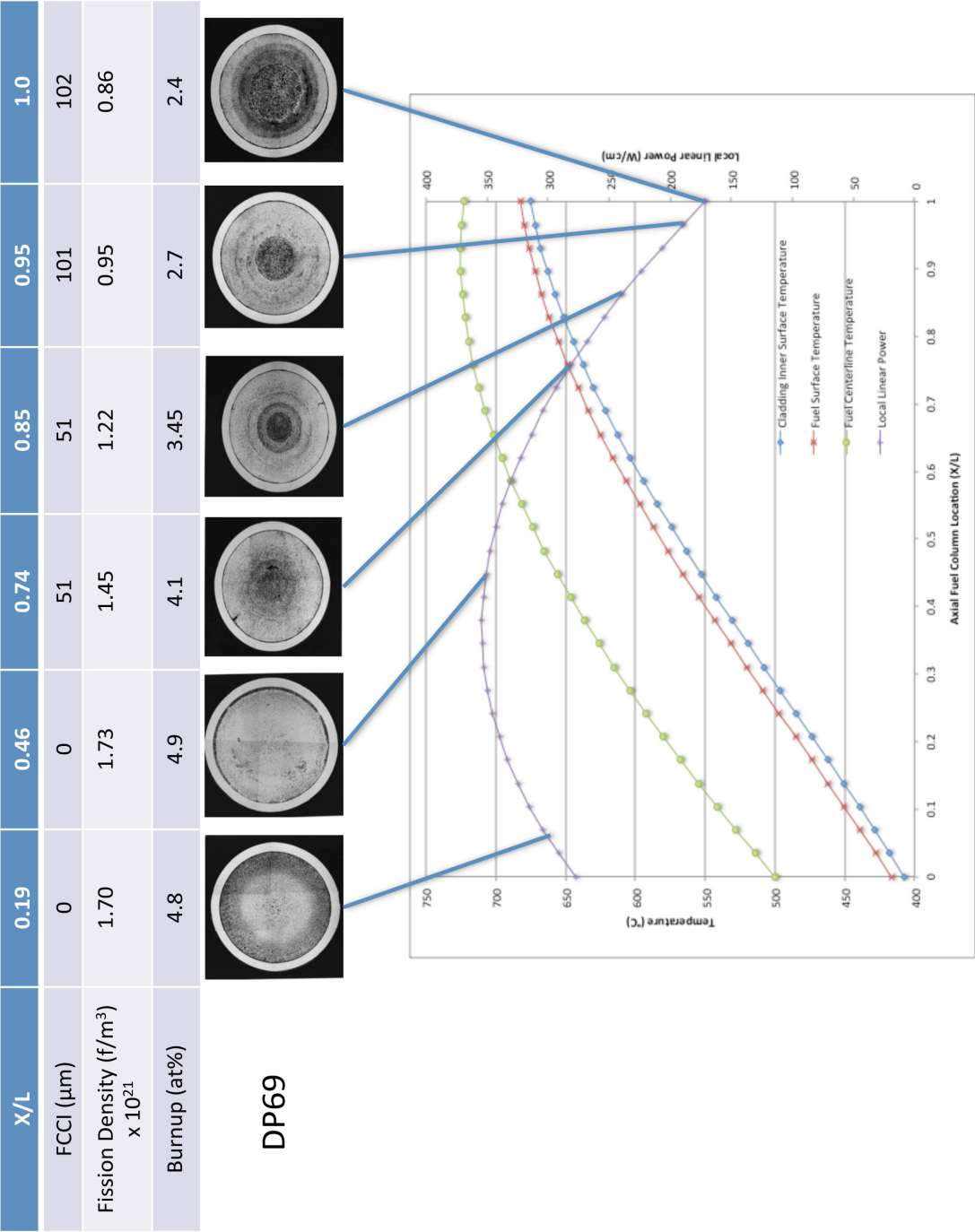


Figure 49. FCCI formation axially along the DP-69 fuel pin from the X447 experiment.

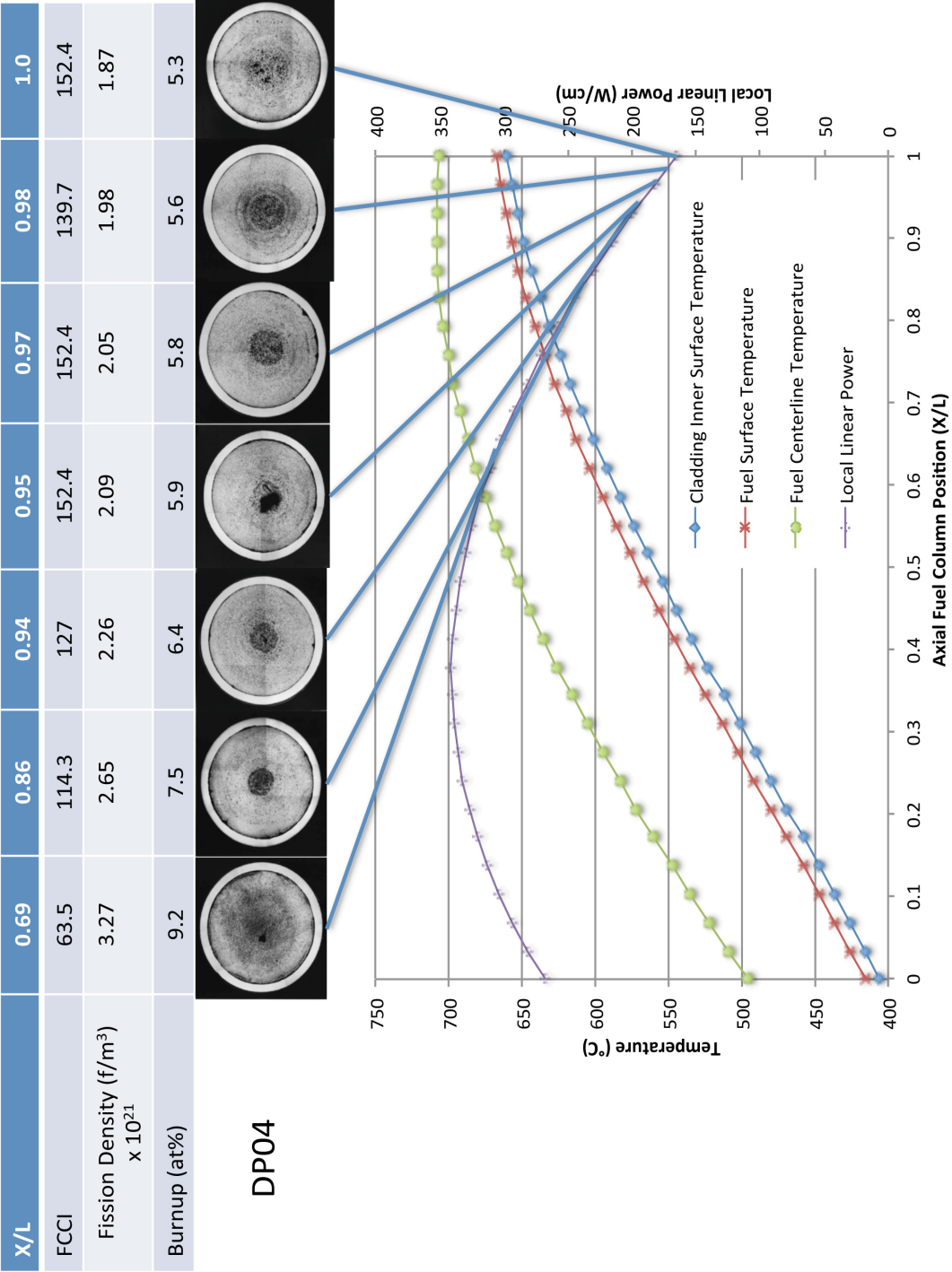


Figure 50. FCCI formation axially along the DP-04 fuel pin from the X447 experiment.

X/L	0.18	0.49	0.62	0.71	0.84	0.92	0.94	0.95	0.97	0.98	1.0
FCCI (μm)	0	0	27.9	25.4	86.4	117	96.5	91.4	127	140	89
Fission Density (f/m^3) $\times 10^{21}$	3.61	3.75	3.50	3.29	2.72	2.40	2.30	2.23	2.16	2.09	2.01
Burnup (at%)	10.2	10.6	9.9	9.3	7.7	6.8	6.5	6.3	6.1	5.9	5.7

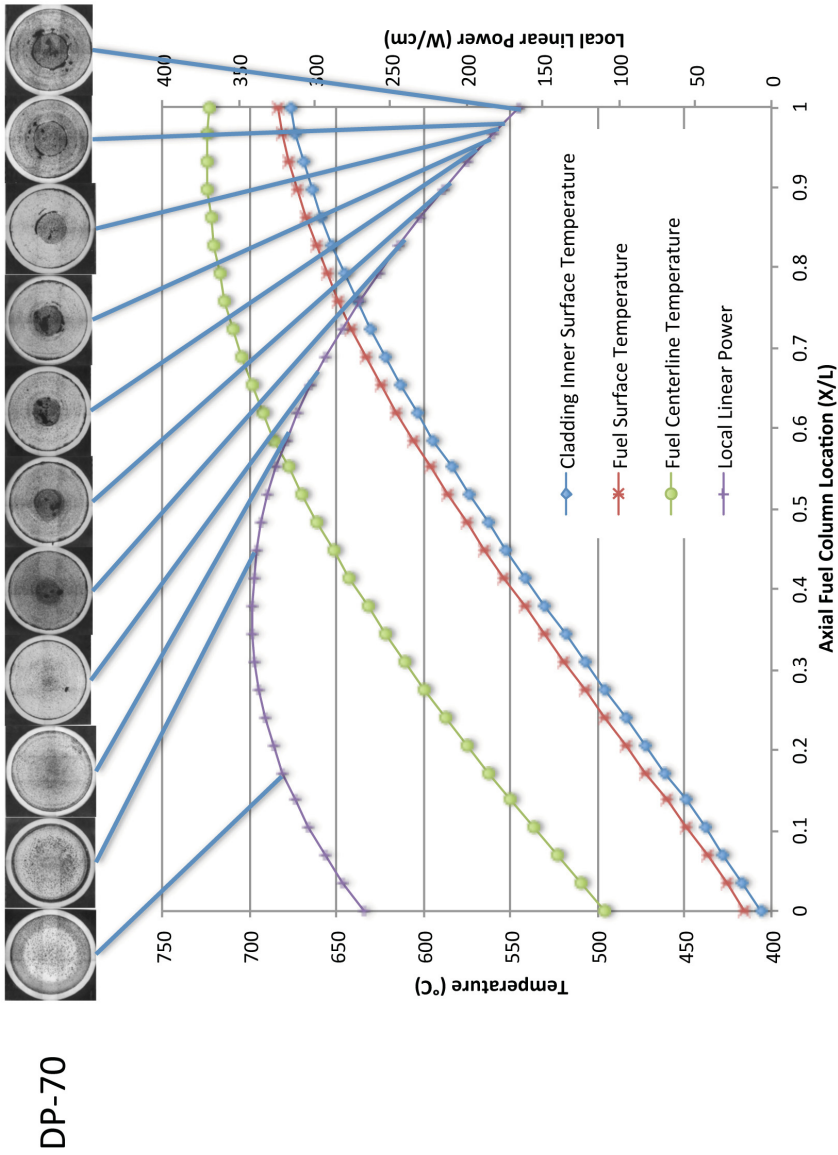


Figure 51. FCCI formation axially along the DP-70 fuel pin from the X447 experiment.

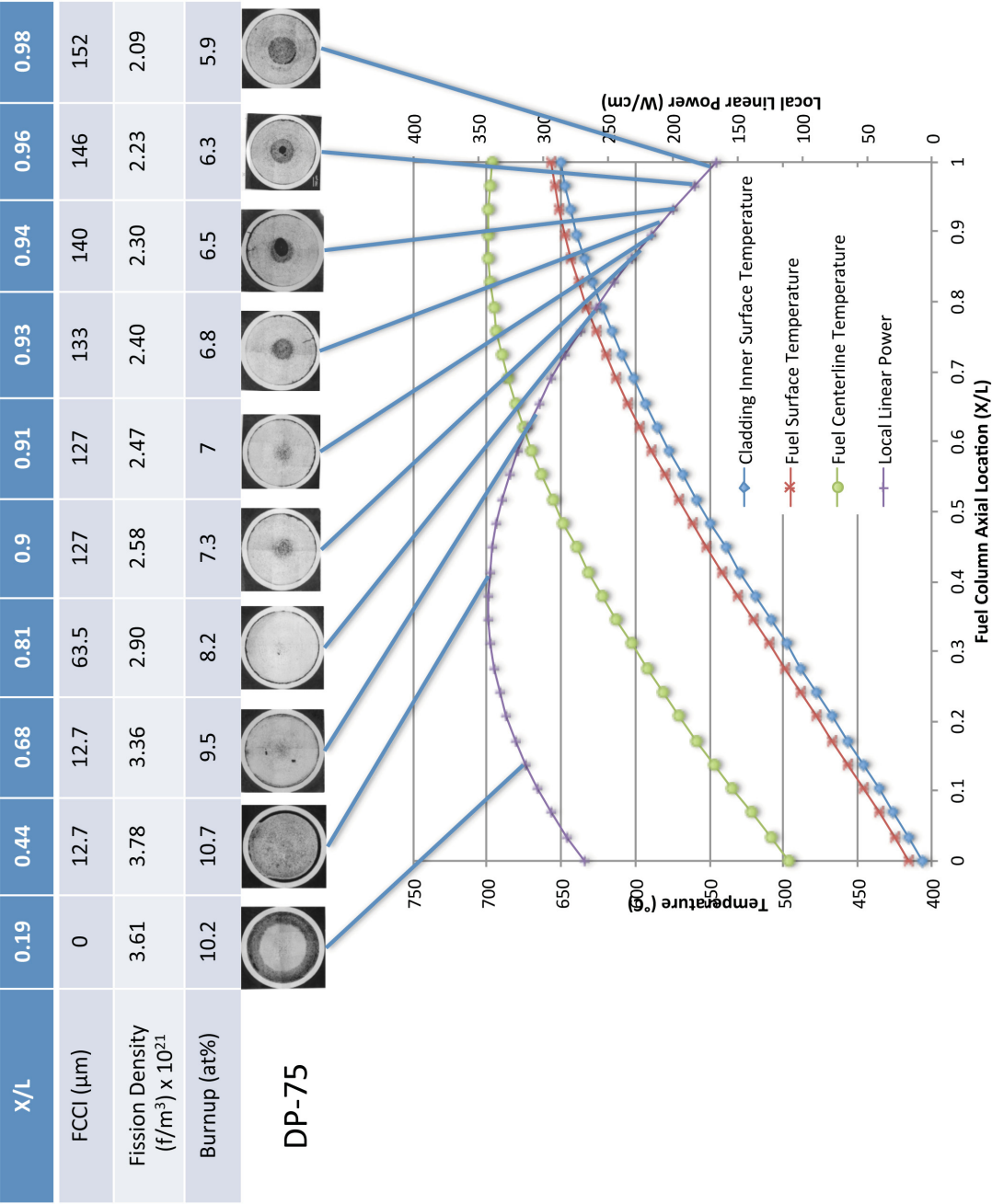


Figure 52. FCCI formation axially along the DP-75 fuel pin from the X447 experiment.

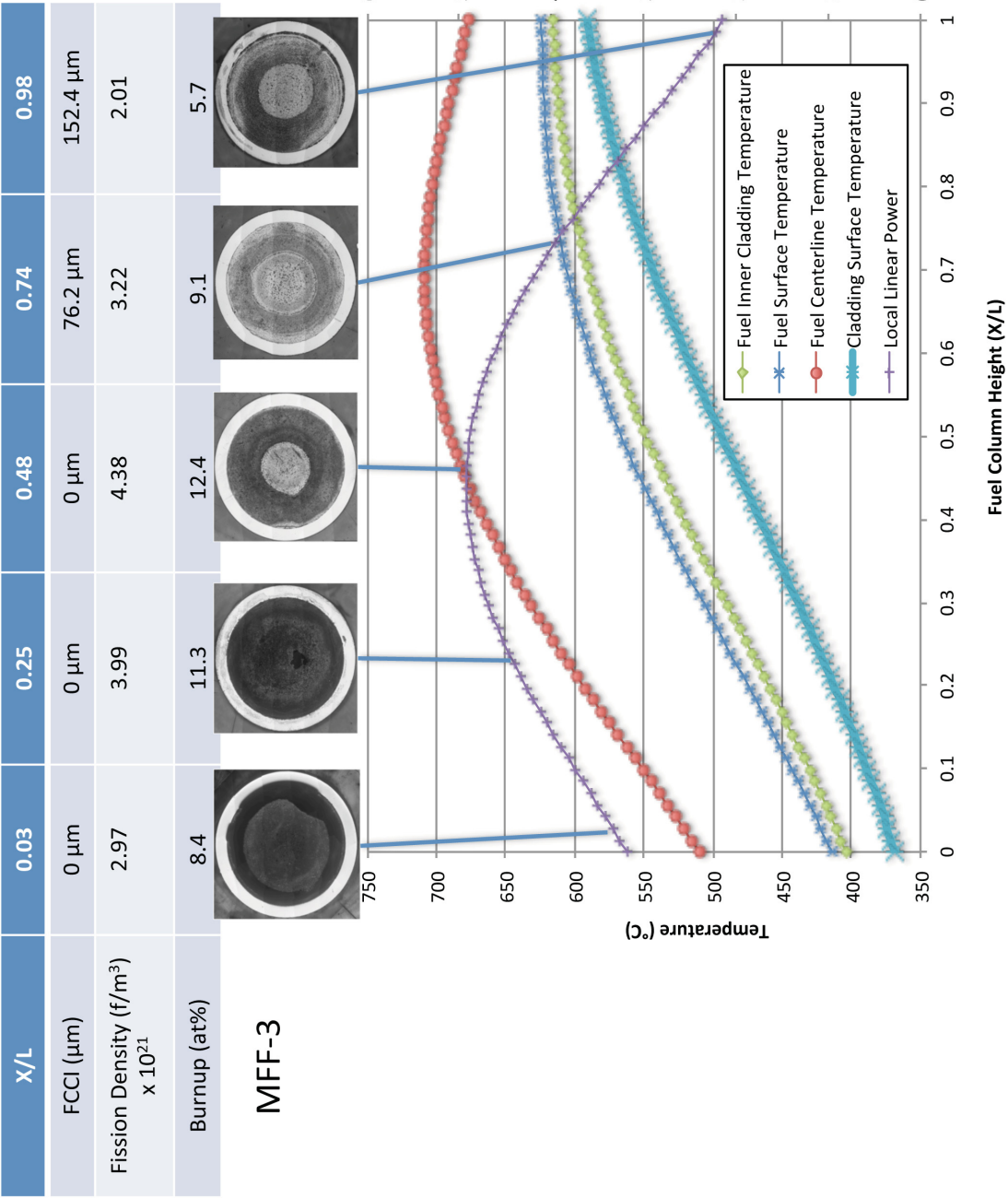


Figure 53. FCCI formation axially along the 193045 fuel pin from the MFF-3 experiment.

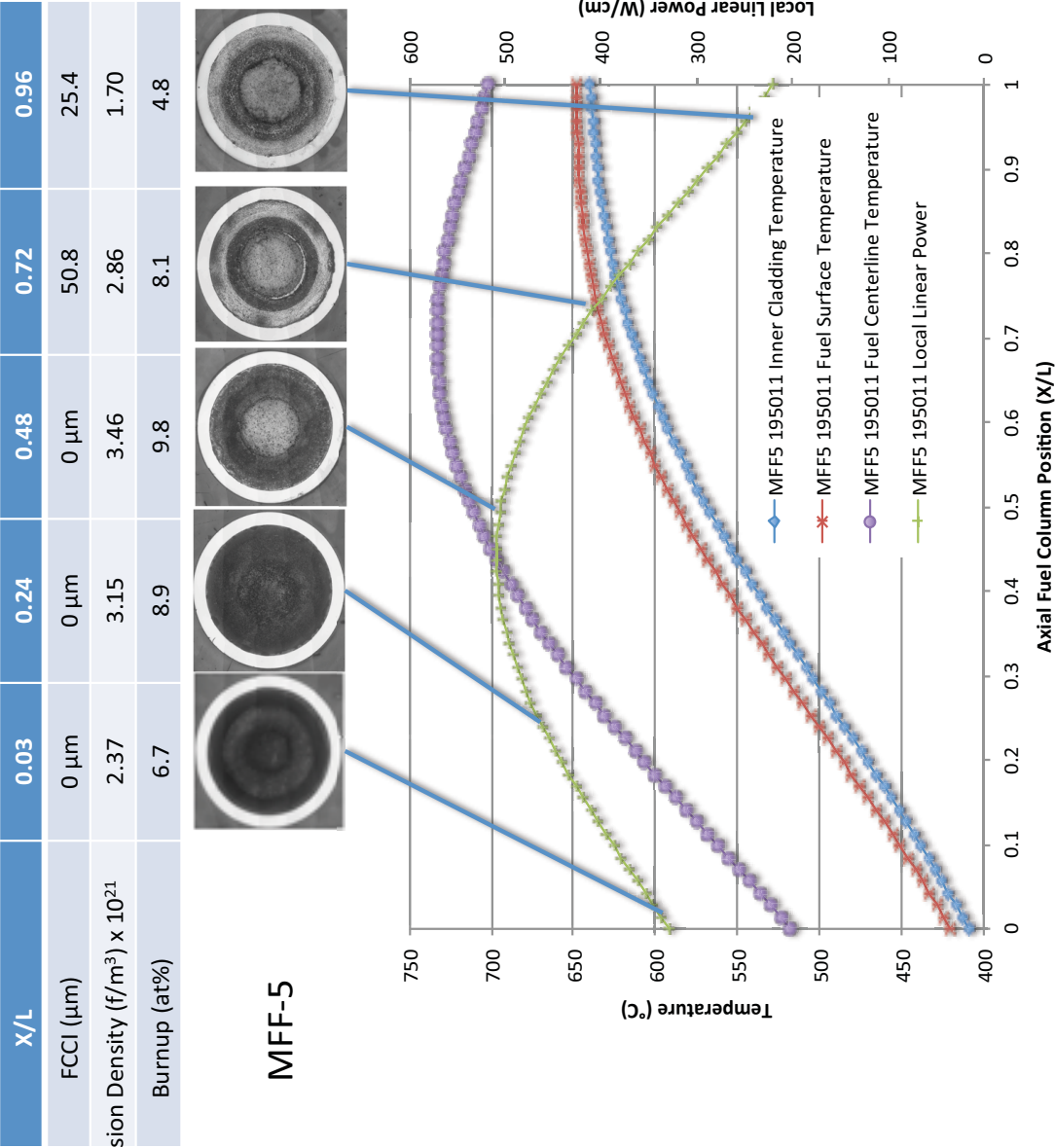


Figure 54. FCCI formation axially along the 195011 fuel pin from the MF5-5 experiment.

The MFF-3 fuel pin operated to a peak burnup of 13.8 at. % and operated with a fuel centerline temperature that peaks at 710°C at a fuel height of $X/L = 0.7$, dropping off to a fuel centerline temperature of 675°C at the top of the fuel column. It is important to note that although the data collected on the MFF-3 pin did not show a pronounced drop in FCCI at the top of the fuel column, it is apparent that the FCCI in the pin is much lower than that experienced in the X447 experiments in EBR-II. A summary of the data collected in the X447 experiments and in the MFF-3 and MFF-5 assembly postirradiation examination and analysis is presented in Table 6. Also shown in the table is data collected from the IFR-1 experiment and reported by Porter and Tsai [31]. The IFR-1 (U-Pu-Zr) data shows similar behavior to that found in U-Zr experiments.

4.2 *U-19Pu-10Zr metallic fuel experiment data*

Results from the analysis of data from the IFR-1 experiment conducted in the FFTF at about the same time as the MFF experiment have been published by Porter and Tsai [31]. Gamma scanning analysis was conducted soon after removal of the experiment from the reactor. Unfortunately, similar data is not available from the MFF-3 and MFF-5 pins examined in this study. The time between reactor removal and postirradiation of the MFF assemblies was simply too long (approximately 30 years) and many of the burnup and activation product markers have decayed to a point that they are no longer resolvable with gamma scanning measurements. Figure 55 shows the gamma scanning data collected on the IFR-1 Pin number 181193. It shows a profile over the axial height of the fuel column consistent with the Rh-106 burnup profile typical of FFTF. The Cs-137 signal indicates typical migration to the sodium bond areas of the fuel pin, consistent with metallic fuel behavior found in FFTF and EBR-II experiments.

Table 6. Summary of FCCI data from X447, MFF-3, MFF-5, and IFR-1.

S/A	X/L0	Burnup (at%)	Fission Density (fission/m ³)	Height from BOF (cm)	Measured Max Depth (μm)	Time Ave. Fuel Centerline Temperature (°C)	Time Ave. Cladding Inner Temperature (°C)
X447 DP69	0.19	4.8	1.70E+21	7	0	574	463
	0.46	4.9	1.73E+21	17.1	0	661	552
	0.74	4.1	1.45E+21	25.4	50.8	713	626
	0.85	3.45	1.22E+21	29.2	50.8	720	648
	0.95	2.7	9.54E+20	32.385	101.6	720	664
	1	2.43	8.59E+20	34.3	101.6	718	667
X447 DP04	0.69	9.2	3.27E+21	24.8	63.5	693	606
	0.86	7.5	2.65E+21	30.7	114.3	704	634
	0.94	6.4	2.26E+21	34.5	127	705	644
	0.95	5.9	2.09E+21	34.3	152.4	704	649
	0.97	5.8	2.05E+21	34.9	152.4	703	649
	0.98	5.6	1.98E+21	35.6	139.7	703	650
	1	5.3	1.87E+21	36.2	152.4	701	652
X447 DP70	0.18	10.2	3.61E+21	7	0	563	457
	0.49	10.6	3.75E+21	17.1	0	648	543
	0.62	9.9	3.50E+21	22.9	27.94	677	582
	0.71	9.3	3.29E+21	25.4	25.4	688	599
	0.84	7.7	2.72E+21	30.7	86.36	700	628
	0.92	6.8	2.40E+21	33.7	116.84	702	639
	0.94	6.5	2.30E+21	34.3	96.52	702	641
	0.95	6.3	2.23E+21	34.9	91.44	702	643
	0.97	6.1	2.16E+21	35.6	127	701	644
	0.98	5.9	2.09E+21	36.2	139.7	701	645
	1	5.7	2.01E+21	36.8	88.9	700	647
X447 DP75	0.19	10.2	3.61E+21	7	0	581	457
	0.44	10.7	3.78E+21	17.1	12.7	659	533
	0.68	9.5	3.36E+21	25.4	12.7	707	596
	0.81	8.2	2.90E+21	30.5	63.5	721	622
	0.9	7.3	2.58E+21	33.7	127	724	635
	0.91	7	2.47E+21	34.3	127	724	637
	0.93	6.8	2.40E+21	34.9	133.35	725	640
	0.94	6.5	2.30E+21	35.6	139.7	724	642
	0.96	6.3	2.23E+21	36.1	146.05	724	644
	0.98	5.9	2.09E+21	36.8	152.4	724	646
MFF5 195011	0.03	6.7	2.37E+21	2.54	0	532	414
	0.24	8.9	3.15E+21	22.9	0	628	480
	0.48	9.8	3.46E+21	45.72	0	712	556
	0.72	8.1	2.86E+21	68.6	50.8	736	612
	0.96	4.8	1.70E+21	91.4	25.4	709	635
MFF3 193045	0.03	8.4	2.97E+21	2.54	0	527	413
	0.25	11.3	3.99E+21	22.9	0	619	475
	0.49	12.4	4.38E+21	45.7	0	700	550
	0.74	9.1	3.22E+21	68.5	76.2	712	604
	0.98	5.7	2.01E+21	91.44	152.4	682	615

^a – Calculated temperatures are EFPD averaged over the irradiation cycle histories.

The interesting feature found and explained analytically by Porter and Tsai is that an increasing Ce-144 activity near the top of the fuel column is observed as Ce migrates

radially from the interior of the fuel slug to the outer surface of the fuel resulting in higher gamma scanning signature for C-144. The Ce-144 signal has less self-shielding as it migrates from the interior of the fuel pin and collects as fuel-cladding interaction product on the inner diameter of the cladding. This is not seen in the gamma scanning data collected on the MFF-3 and MFF-5 fuel pins presented above because by the time gamma scanning was conducted on MFF-3 and MFF-5 the Ce-144 lanthanide fission product had decayed away below the detectable limit of the gamma scanning instrument.

Confirming this is the data shown in Figure 56. Porter and Tsai report the FCCI layer thickness across the axial fuel column measured during optical metallography examination. The data show that the FCCI peaks near the peak of the axial power profile and reduces back to zero at the top of the fuel column.

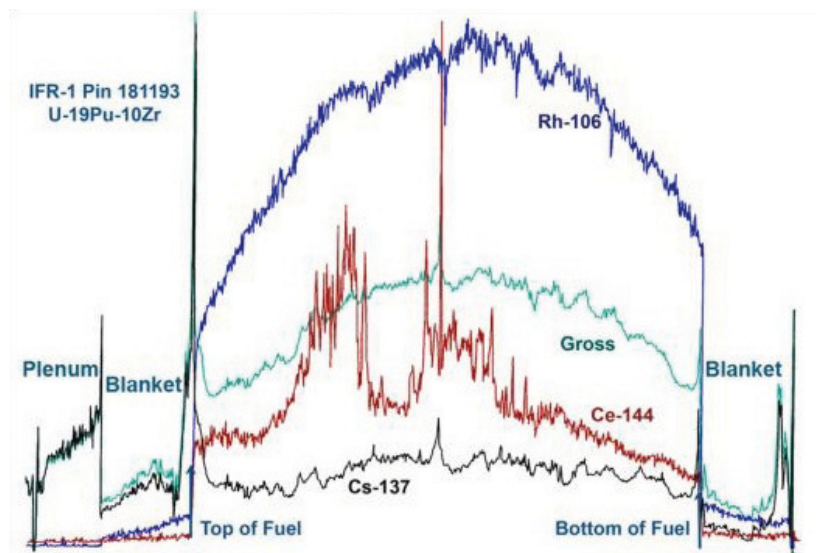


Figure 55. Relative Gamma scanning data for Pin 181193 of the IFR-1 (U-19Pu-10Zr) experiment in FFTF [31].

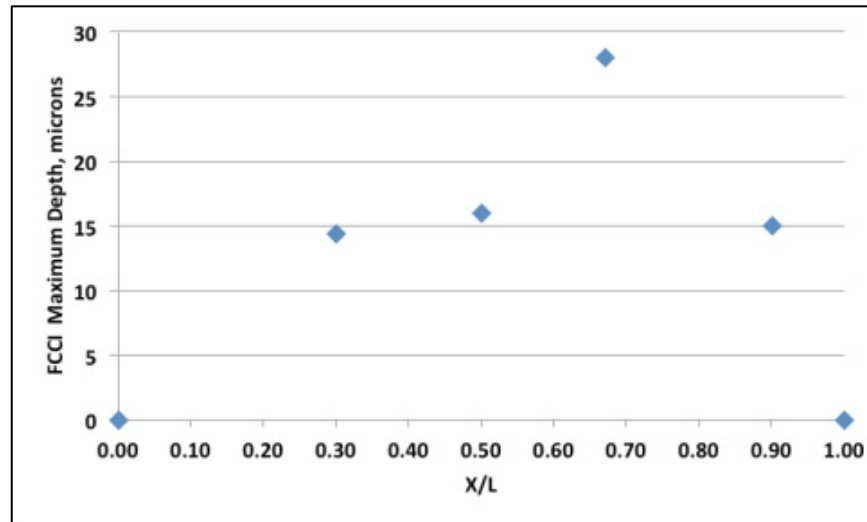


Figure 56. FCCI measurements for IFR-1 Pin 181193 [31].

5 BURNUP AND TEMPERATURE DEPENDANT FCCI MODEL

FCCI in metallic fuel is dependent upon many factors including the concentration and mobility of the lanthanide fission products, mobility of cladding component species, and the burnup and temperature conditions in the fuel pin. Specific aspects of FCCI and the formation of interaction layers have been studied by a number of investigators [14, 15, 18, 19, 32]. However, the mechanism of transport of the lanthanide fission products is not well understood. Finding essentially pure deposits of lanthanide fission products in pores or at the cladding surface may lead one to think vapor phase transport is responsible, although the vapor pressure of lanthanide fission products varies by eleven orders of magnitude at 1000 K (Ce versus Sm) [33] so a FCCI rate dependence based upon vapor transport is unlikely, especially since Ce and Sm are both found in the FCCI layer in ratios near the ratio of their fission yields after cooling [18]. Recently, Mariani et al. [34] have suggested that a liquid-phase transport mechanism may explain the experimental observations based on dissolution in sodium and/or cesium, although they do not offer a model for this phenomenon.

The redistribution of U, Pu, and Zr in metallic fuels has been studied and provides guidance on how a model for lanthanide fission product migration may be developed. Hofman et al. [25] published a model using data collected on the DP-11 and DP-81 fuel pins from the X447 experiment conducted in the EBR-II reactor as the basis for uranium and zirconium redistribution. These researchers utilized a combined Soret and Fickian diffusion model to predict the redistribution of U, Zr, and Pu in metallic fuels. Kim et al. [35] conducted similar work for U-Pu-Zr using a (U, Pu) – Zr pseudo-binary phase diagram, comparing with data from the X419 experiment. Karahan [36] has incorporated these models into the FEAST code to predict constituent redistribution in U-Zr and U-Pu-Zr fuels.

Ogata et al. [37] have used the method derived by Tournier [38] to estimate the diffusion coefficients for Ce in U-Zr alloy as 2×10^{-13} m²/sec at 1123 K and 6×10^{-14} m²/sec at 1023 K based on furnace tests of Ce-Fe diffusion couples. In addition, similar to Zegler et al. [15], Inagaki and Ogata [16] have recently determined a rate dependency in FCCI layer thickness growth with temperature and time according to,

$$\delta = \sqrt{K} * \sqrt{t}, \quad (1)$$

where,

δ = thickness [m],

$K = 1.84 \times 10^{-8} \times \exp\left(-\frac{11200}{T}\right)$ [m²/sec],

t = time [sec].

A coordinated model for FCCI layer formation, involving both lanthanide transport and reaction with the cladding can be generated by producing each model and coupling them to allow rate control from either process.

5.1 *Coupled Thermal and Mass Diffusion Model*

The Idaho National Laboratory (INL) has developed a multi-dimensional, multi-physics software suite for fuel performance simulation. The general framework is implemented in the Multi-physics Object Oriented Simulation Environment (MOOSE) [39] and the BISON [40] computer codes. The BISON code has been adapted to a variety of physical geometries with a variety of physical phenomena incorporated into its solution set. In BISON, a kernel can be thought of as a “piece” of physics or a mathematical operator in a partial differential equation (PDE). Kernels can be coupled together or used repeatedly to form the required set of PDE’s for a particular application. In the case of the formation of FCCI in metallic fuels, simultaneous solution of the diffusion equation for species transport in conjunction with the heat conduction equation describing the heat transfer and development of temperature gradients is required. For this study the model assumes no

axial heat transfer and no axial species migration, although there is some indication of this in experimental data.

The model to represent the formation of FCCI coupled with the temperature, power, and burnup in metallic fuel should be able to provide the radial temperature profile and the amount of lanthanide fission products transported to the fuel-cladding interface. There are two aspects to this activity, solution of the heat conduction equation for the radial temperature profile and solution of the diffusion equation(s) for the radial concentration of lanthanide fission products and transport to the fuel-cladding interface. This methodology is used to develop a solution to the coupled system of equations (PDEs); the heat conduction equation and diffusivity equation for the lanthanide fission product, cerium. Results from this model will be used to compare with FCCI data taken during postirradiation examination of the X447, MFF-3, and MFF-5 experiment assemblies.

5.1.1 Conservation of Energy

Assuming that fission is uniformly distributed at constant rate q in the fuel, the governing equation for heat conduction is described by

$$\rho \cdot c_p \frac{\partial T}{\partial t} - \nabla \cdot (k \nabla T) - q = 0, \quad (2)$$

where T , k , ρ , c_p , q , and t are the temperature, thermal conductivity, density, specific heat, internal heat generation, and time respectively. For this investigation thermal properties were assumed constant. The solution to the heat transfer equation is developed fixing the cladding outer diameter temperature to a known value. At the centerline of the fuel, the heat flux will be 0, hence $q'' = 0$ at $r = 0$.

5.1.2 Conservation of Mass

Mass transport is modeled with the diffusion equation;

$$\frac{\partial C}{\partial t} + (\nabla \cdot J) - S = 0, \quad (3)$$

where C , J , S , and t are concentration, mass flux, internal mass source, and time, respectively. The solution to the diffusion equation should be specific to the chemical species of interest. At the fuel-cladding interface, the following are considered to be of interest; Ce, Nd, Sm, Ln, Pr fission products and Fe and Ni cladding components. At this time the model only considers the migration of cerium. This effort focuses on cerium as a representative for the lanthanide fission products because the most data is available in the literature on cerium. The behavior of the full set of lanthanide fission products can be incorporated as the availability of diffusion data for the lanthanide fission products in metallic fuel becomes available.

The diffusion coefficient is dependent upon temperature, and therefore, the system of equations must be solved simultaneously. The temperature dependent diffusion coefficient is fully coupled to the temperature field. Note that this development highlights a powerful capability in BISON: multiple diffusion kernels can be solved simultaneously and this can be used to track multiple chemical species in the fuel and cladding.

S is the source of lanthanide species of interest from fission. It is determined by the local power and its relationship to fission rate multiplied by the fission yield of the species of interest.

A new kernel was required to describe the Soret effect term for diffusion in the MOOSE/BISON framework. Soret effect diffusion is driven by a temperature gradient coupled with a concentration field. The new kernel coupled with an existing Arrhenius diffusion kernel and a source term determined by fission rate provides the solution to the

mass diffusion equation shown above. In the relationship for mass flux, the Soret term is the second term in the equation for mass flux:

$$\vec{J} = -D(T) \left[\nabla C + \frac{Q^*}{FR} \frac{C}{T^2} \nabla T \right], \quad (4)$$

where C , D , and Q^* denote the lanthanide species concentration, diffusion coefficient, and heat of transport, respectively. Diffusion coefficients are strongly temperature dependent and typically defined using an Arrhenius form;

$$D(T) = A_0 \cdot e^{-Q/RT} \quad (5)$$

where A_0 is the pre-exponential factor, Q is the activation energy, and R is the universal gas constant. The Soret term is dependent upon concentration C , a shape function F , the gas constant R , and the heat of transport Q^* . The heat of transport, the shape function, and the diffusion coefficient can all be functions of temperature but these dependencies are not known for the diffusion of lanthanides in the metallic fuel system. The model developed here and implemented in the MOOSE/BISON framework is fully capable of solving the mass diffusion equation with these functional dependencies as future experimental data becomes available on lanthanide diffusion mechanisms. For the purposes of this effort the diffusion coefficient is assumed to take an Arrhenius form dependent upon temperature. The heat of transport and the geometric shape function are assumed to be constant with temperature and concentration.

The goal is now to use this diffusion model used to predict transport of lanthanide fission products to the cladding, and use this to predict a FCCI layer thickness as lanthanides are transported to the fuel-cladding interface. To do this, the interface needs to provide a boundary condition for the diffusion through the fuel.

A key boundary condition required to obtain a solution to equation (3) is specification of the flux of lanthanides at the fuel-cladding boundary, J_i . Specifying a rate of FCCI reaction can be used to specify the boundary flux. It will influence the concentration at the interface and thus the transport rate of lanthanides supplied to the interaction layer. If the formation of the FCCI layer is controlled by the rate of reaction at the fuel surface then the relationship given in equation (1) determines the rate of layer formation. If the formation of FCCI layer is controlled by the diffusion of lanthanide to the fuel surface then the rate of layer formation is less than that predicted by equation (1).

The model calculates the time dependent concentration profiles of lanthanides (Ce is this case) through the radius of the fuel. The lanthanide flux at the fuel surface as calculated by equation (4), can be used to estimate the layer thickness. The flux of lanthanides at the fuel surface is related to layer thickness, δ [m], by

$$\vec{J} = \frac{\delta * \rho}{MW * t} \quad (6)$$

where,

$$\vec{J} = \text{Flux [mol/m}^2\text{-sec]},$$

$$\delta = \text{thickness [m]},$$

$$t = \text{time [secs]},$$

$$MW = \text{molecular weight of Ce}_2\text{Fe}_{17} \text{ interaction layer (1215 g/mol)},$$

$$\rho = \text{density of Ce}_2\text{Fe}_{17} [7700 \text{ kg/m}^3] [41].$$

\vec{J} can be obtained from the BISON model and is the integrated flux over the fuel surface, or

$$\vec{J} = \int -D(T) * (\nabla C \cdot n) dA \quad (7)$$

where,

∇C = gradient of concentration,

n = normal vector,

$D(T)$ = effective diffusion coefficient operating on ∇C .

$D(T)$ in Equation (7) is taken to be the combination of the Fickian diffusion coefficient and the Soret diffusion coefficient shown in Equation (1) as they are operating on ∇C .

5.1.3 Verification of Soret and Fickian Diffusion BISON Kernels

It is standard practice in the development of the BISON framework that when a new physics kernel is written, a simple test problem is used to verify the solution. In this case the Soret term was verified using the Mathematica [42] software package. Solution to the mass diffusion equation with a Soret term is difficult analytically so Mathematica was used to verify the MOOSE/BISON Soret kernel. The assignment of boundary conditions to a simple 1x1x1 cube is shown in Figure 59. A constant temperature of 1200°C is specified on one face of the cube while a constant temperature of 1100°C is specified on the opposing face. A constant concentration value is specified at the 1200°C face of unity and a constant concentration of zero is specified at the 1100°C face. All other faces are specified with a Neumann boundary condition such that the heat and mass flux is zero, hence adiabatic and impermeable. The concentration gradient is then solved assuming that only Soret diffusion is active in the volume using the MOOSE/BISON framework.

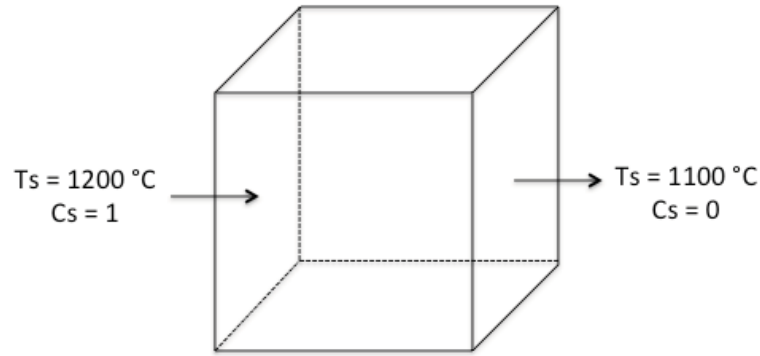


Figure 59. Assignment of boundary conditions for simple cube geometry.

The solution determined by BISON is shown in Figure 60. The temperature gradient through the cube is shown on the top left with a corresponding temperature gradient shown in the bottom left. The resulting concentration gradient is depicted on the right side of the figure with the lower right x-y plot showing the detailed concentration gradient initiating at 1 on the left side of the cube and dropping to zero asymptotically on the right side (1100°C) side of the cube.

A similar solution can be obtained from the Mathematica software package. Figure 61 shows the resulting solution to the above described cube geometry using Mathematica. Mathematica has trouble solving this problem with the boundary condition at $x = 1$ changing from the initial condition of $C(x,0) = 1$ to the $x = 1$ boundary condition of $C(1, t) = 0$ and although not exact the solution results show similar form.

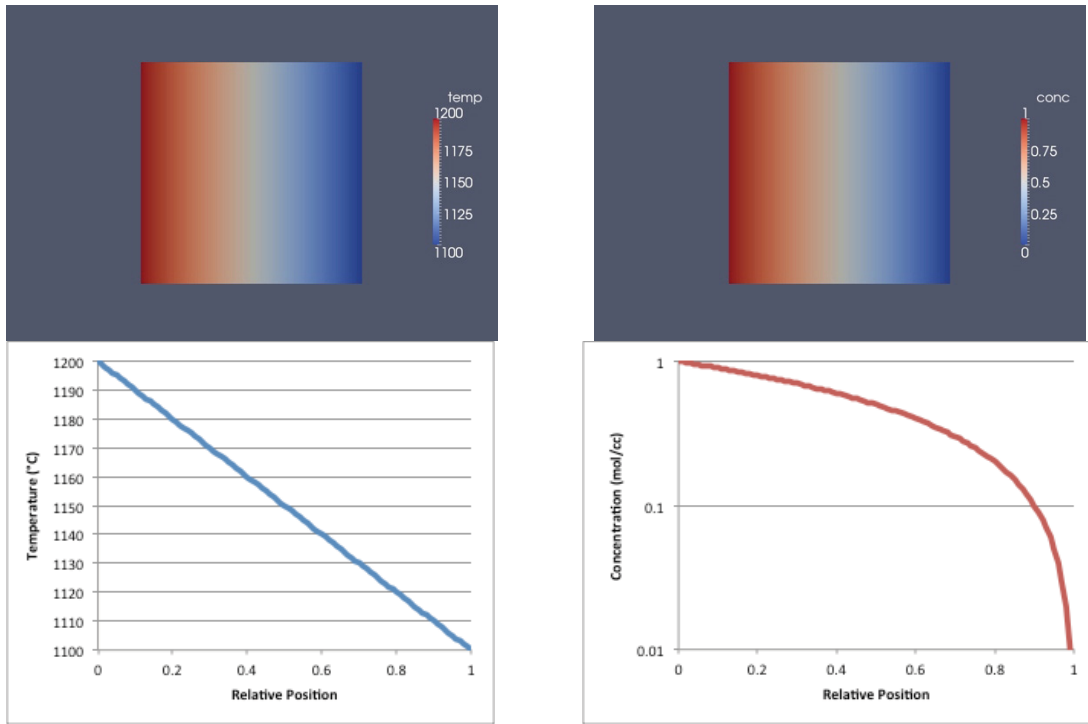


Figure 60. Coupled Solution Soret in a simple cube geometry with $C(0, t) = 1$, $C(1, t) = 0$.

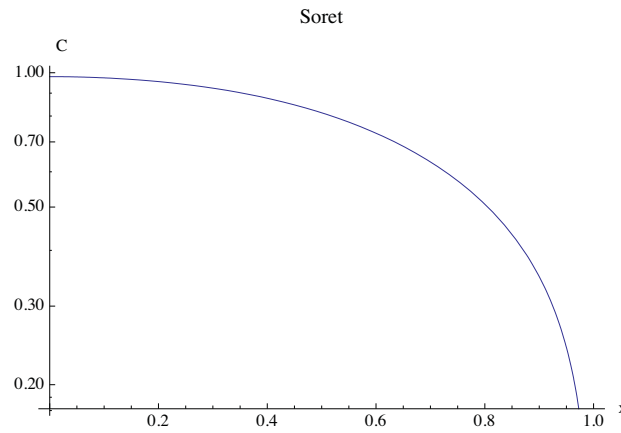


Figure 61. Solution to Soret kernel check using Mathematica [42].

5.1.4 Mesh Representation of Metallic Fuel Pin

The HT-9 clad metallic fuel model shown in Figure 8 is represented in the BISON environment by a two-dimensional finite element mesh shown in Figure 62. The mesh is constructed to provide the best representation of the geometry considering the numerical representation of the diffusion of lanthanide constituents to the fuel-cladding interface. The model does not consider or include the possibility of the existence of a Zr-rind on the outer

diameter of the fuel early in life, which is known to delay the reaction of lanthanide constituents with cladding.

Figure 63 provides a summary designation of the finite element model block and sideset designations. These designations are utilized by the MOOSE/BISON calculation environment to apply boundary conditions to the model. The finite element mesh generator, CUBIT [43], is used to construct the fuel system representation, designate the blocks and sidesets, and generate the mesh.

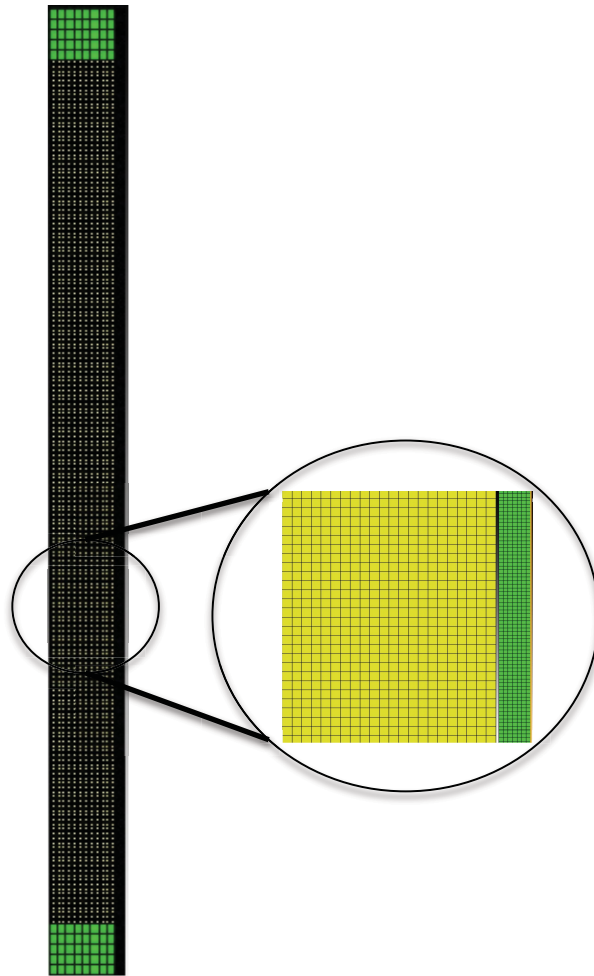


Figure 62. 2-dimensional finite element mesh representation of X447 fuel geometry used as input in BISON calculation.

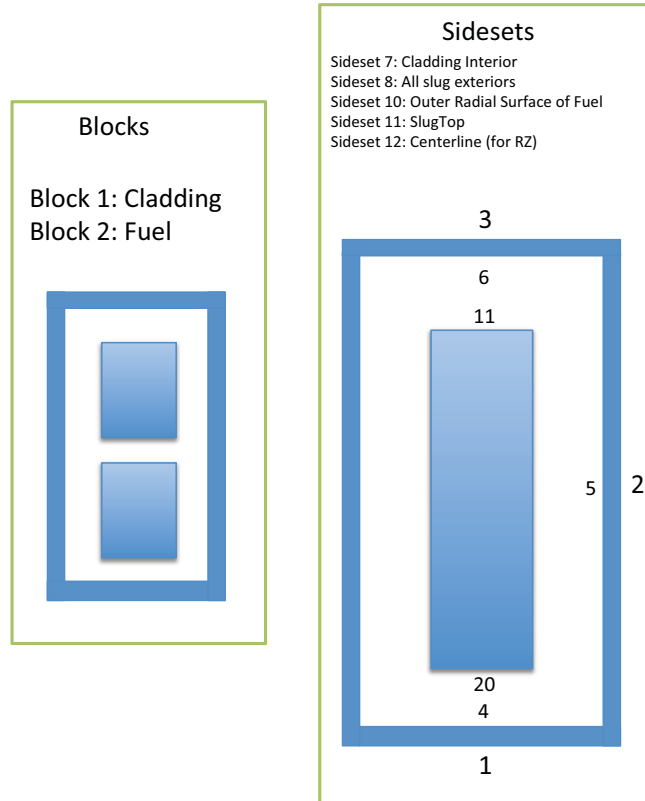


Figure 63. Graphical representation of BISON boundary condition assignments.

5.2 BISON Model Compared to X447 and MFF FCCI Measurements

Using the mesh developed above a calculation at each experimental fuel sample location was performed using the BISON framework utilizing both Soret and Fickian diffusion models for each irradiation cycle as temperature and power distributions change from cycle to cycle and a reaction rate boundary condition at the fuel-cladding interface.

An example input file for the 0.19 X/L location in DP-69 with outer cladding temperature specified as 438°C (711 K), simulating Cycle 146B conditions, is provided in Appendix F. Results of the BISON calculation for FCCI thickness at each sample location alongside the measured experiment thicknesses are shown Table 7.

There are two issues associated with this calculation of thickness. First, the diffusion coefficients used are estimated beginning with the Ogata model and out-of-pile data [37] and adjusting the A_0 coefficient two orders of magnitude lower to match as best as

possible the experimental data. Secondly, the values used in the functional rate equation at the fuel surface are also estimated to best represent the experimental data. The values generated and presented in Table 7 using the BISON framework utilize diffusion equation coefficients of $A_0 = 0.005 \text{ m}^2/\text{s}$, $Q = 340820 \text{ [J/mol]}$, and $Q^* = 20000 \text{ [J/mol]}$ and a rate constant dependent on temperature, $K = 1.84\text{e-}8 \times \exp(-\frac{11200}{T}) \text{ [m}^2/\text{sec}]$. These coefficients can be adjusted in both the cladding and the fuel blocks of the model to impact the rate of material transport to the fuel-cladding interface and reaction with cladding components.

The model predicts the migration of a single species of lanthanide material simulating the buildup at an interface between the fuel block and the cladding block. Figure 64 is a plot of the measured FCCI layer thicknesses obtained during metallography and the BISON model predicted thickness versus the fuel centerline temperature. The data and the model both indicate and predict that there is no FCCI layer formation below 650°C fuel centerline temperature. Figure 65 is a similar plot of the FCCI formation versus the inner cladding temperature and the data and the model both predict no FCCI formation below 550°C. The formation of FCCI layers is dependent on the temperature distribution in the fuel pin. The diffusion of fission product species is dependent upon the temperature gradient in the fuel according to Fickian and Soret diffusion relationships and the formation of FCCI at the fuel-cladding interface is dependent upon the temperature at the interface.

Table 7. Summary of BISON generated calculation results for X447 and MFF fuel pins.

S/A	X/L0	Burnup (at%)	Measured Max Depth (μm)	Moose Bison Predicted FCCI (μm)	Time Ave. Fuel Centerline Temperature ($^{\circ}\text{C}$)	Time Ave. Cladding Inner Temperature ($^{\circ}\text{C}$)
X447 DP69	0.19	4.8	0	0	574	463
	0.46	4.9	0	3	661	552
	0.74	4.1	50.8	61	713	626
	0.85	3.45	50.8	110	720	648
	0.95	2.7	101.6	136	720	664
	1	2.43	101.6	130	718	667
X447 DP04	0.69	9.2	63.5	53	693	606
	0.86	7.5	114.3	125	704	634
	0.94	6.4	127	143	705	644
	0.95	5.9	152.4	145	704	649
	0.97	5.8	152.4	146	703	649
	0.98	5.6	139.7	142	703	650
	1	5.3	152.4	139	701	652
X447 DP70	0.18	10.2	0	0	563	457
	0.49	10.6	0	2	648	543
	0.62	9.9	27.94	18	677	582
	0.71	9.3	25.4	42	688	599
	0.84	7.7	86.36	102	700	628
	0.92	6.8	116.84	123	702	639
	0.94	6.5	96.52	125	702	641
	0.95	6.3	91.44	125	702	643
	0.97	6.1	127	126	701	644
	0.98	5.9	139.7	127	701	645
	1	5.7	88.9	125	700	647
X447 DP75	0.19	10.2	0	0	581	457
	0.44	10.7	12.7	2	659	533
	0.68	9.5	12.7	31	707	596
	0.81	8.2	63.5	81	721	622
	0.9	7.3	127	108	724	635
	0.91	7	127	113	724	637
	0.93	6.8	133.35	119	725	640
	0.94	6.5	139.7	122	724	642
	0.96	6.3	146.05	123	724	644
	0.98	5.9	152.4	126	724	646
MFF5 195011	0.03	6.7	0	0	532	414
	0.24	8.9	0	0	628	480
	0.48	9.8	0	20	712	556
	0.72	8.1	50.8	149	736	612
	0.96	4.8	25.4	84	709	635
MFF3 193045	0.03	8.4	0	0	527	413
	0.25	11.3	0	0	619	475
	0.49	12.4	0	27	700	550
	0.74	9.1	76.2	138	712	604
	0.98	5.7	152.4	70	682	615

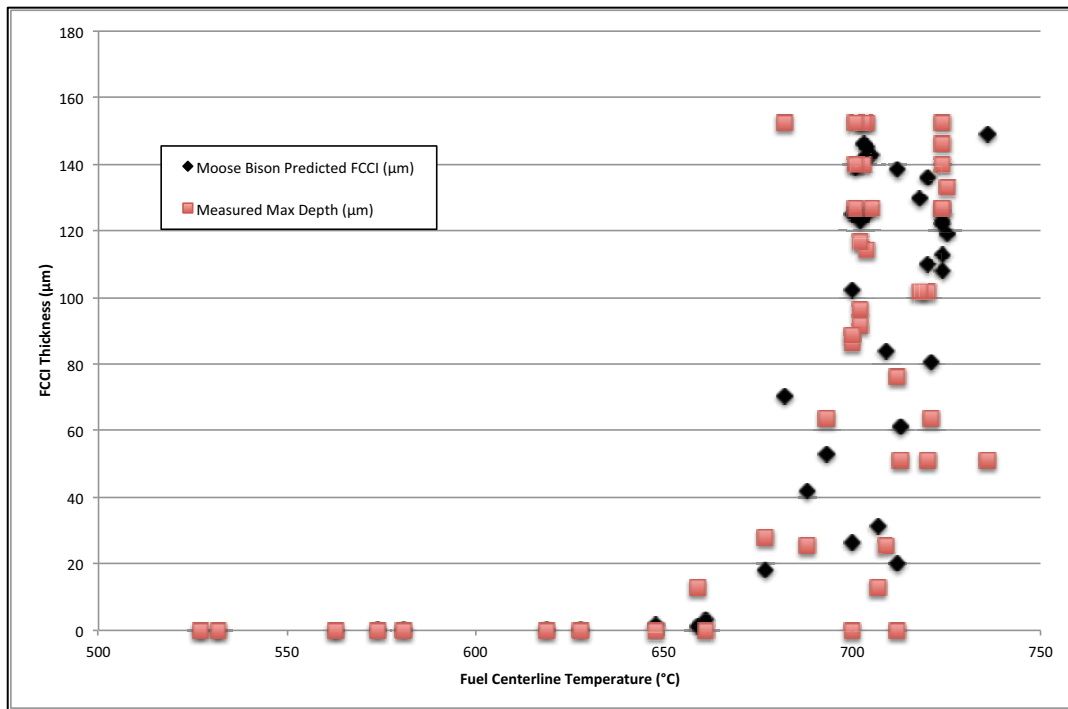


Figure 64. Plot of measured and BISON predicted FCCI thickness versus fuel centerline temperature.

The reaction rate of formation at the interface is complicated and is dependent upon diffusion kinetics in the fuel and cladding as well as the interaction layer as it forms. These kinetics are not completely understood but as a best estimate, the reaction rate equation used in this work is dependent upon temperature and time. Figure 66 shows a plot of the FCCI layer thickness formation versus time for temperatures typical of metallic fuel in EBR-II and FFTF using equation 1. The dependency upon temperature is apparent with a large drop in the predicted formation between 720 °C and 520°C. According to the relationship, fuel-cladding interaction layer thickness would be predicted to be well below 100 μm when the fuel-cladding interface temperature is below 520°C.

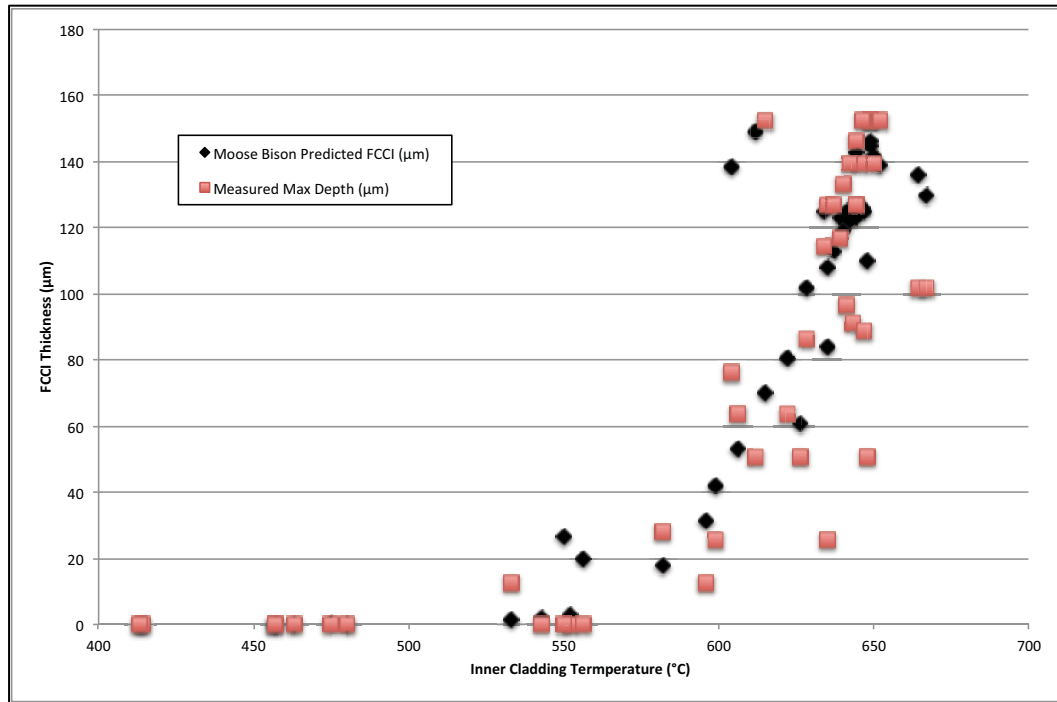


Figure 65. Plot of measured and BISON predicted FCCI thickness versus inner cladding temperature.

The dependency on temperature can be seen in the experimental data shown in Table 7 above and the BISON model predictions when compared along the axial length of a fuel pin. A reduction in fuel-cladding interaction layer formation has been observed at the top of the fuel column in full-length MFF-5 fuel pin post irradiation examination data as shown in Table 7. The BISON model predicts this behavior. Figure 67 shows a plot of the time average inner cladding temperature for each sample location for the DP-70 fuel pin, the measured FCCI layer thickness, the BISON simulation predicted thickness, and the thickness predicted by the Equation 1 rate relationship.

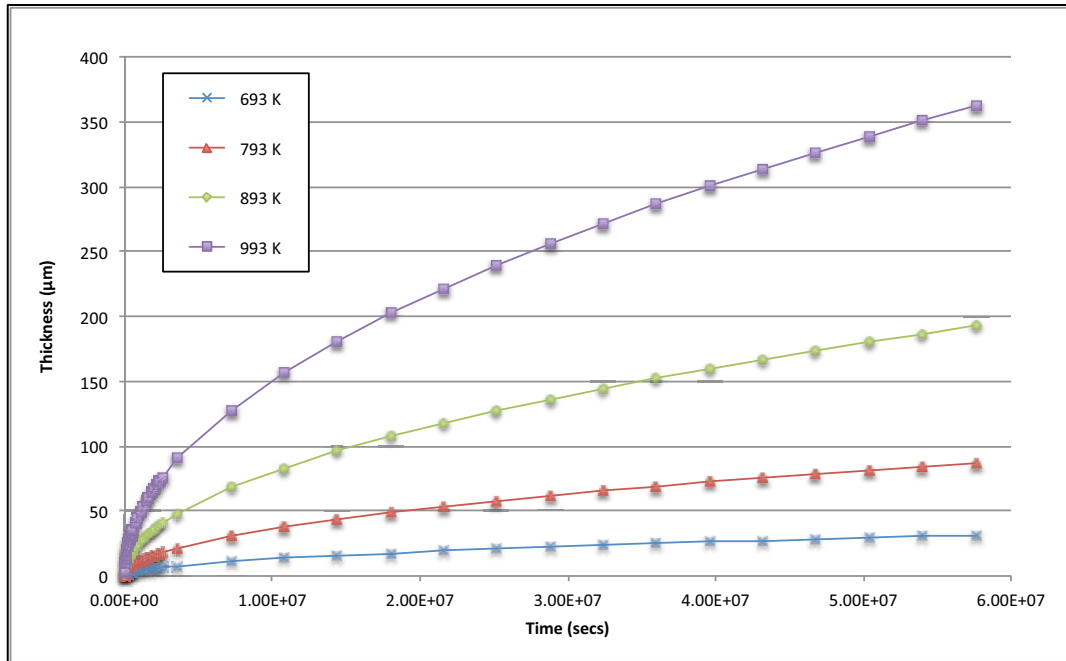


Figure 66. Plot of equation (1) for various temperatures of interest to interaction layer formation.

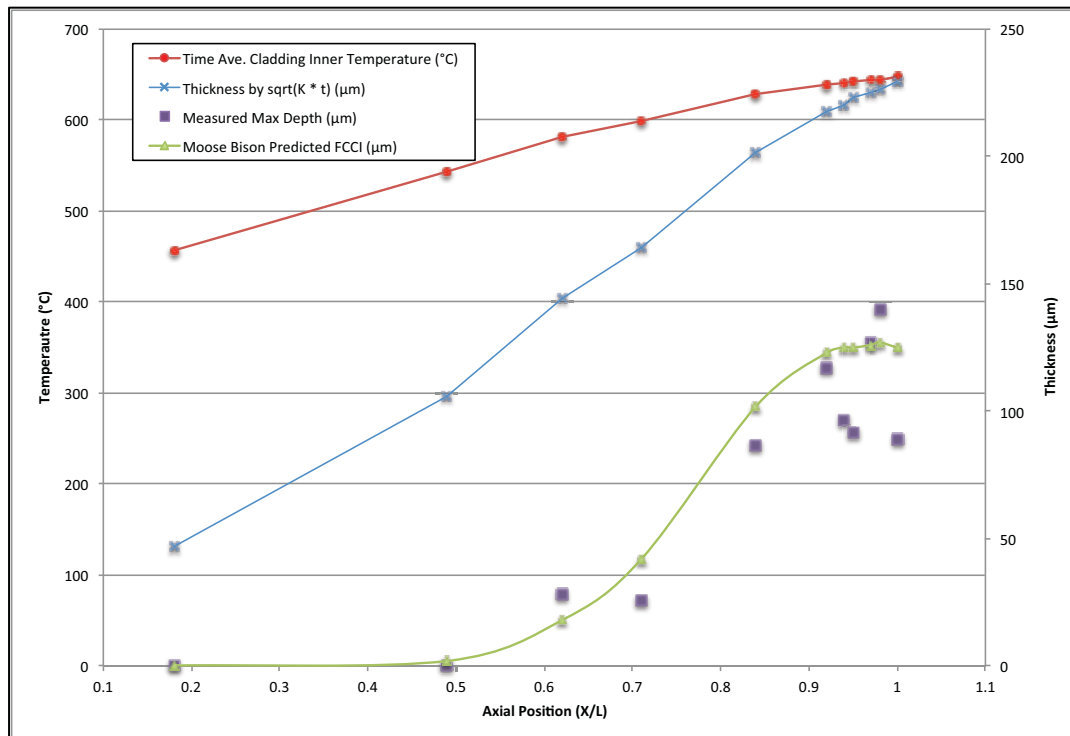


Figure 67. Time averaged inner cladding temperature, measured FCCI thickness, and predicted FCCI thickness for X447 DP-70 Fuel Pin versus axial fuel column location.

The graph indicates that very little FCCI layer forms below the mid-plane ($0.5 X/L$) of the fuel pin due to lower fuel centerline and inner cladding temperatures, even though lanthanide generation may be high below axial core mid-plane due to the power profile peaking near centerline. FCCI formation occurs in the top half of the fuel pin because temperatures are high enough to transport lanthanides to the fuel-cladding interface and also high enough for reaction and formation at the fuel-cladding interface. At the top of the fuel column, the fuel centerline temperature begins to decrease slightly (even though fuel-cladding interface temperature remains high) and hence the amount of formation is decreased due to less transport to the interface. The measured data in X447 fuel pins does not indicate this, but the model predicts a slight decrease at the top of the fuel column. This behavior is more pronounced in longer fuel pins and has been observed in full-length FFTF IFR-1 and MFF-5 fuel pins. Figure 68 shows a plot, similar to Figure 67, for the MFF-5 195011 fuel pin but using artificially high diffusion rates. The experimental data from the MFF-5 fuel pin showed a distinct drop from $50 \mu\text{m}$ of FCCI thickness at $X/L = 0.75$ to $25 \mu\text{m}$ at $X/L = 0.98$. The BISON simulation of these conditions predicts this same trend at the top of the fuel column, but unfortunately over-predicts the thickness expected to form. This over-prediction is mostly likely due to need for refined diffusion and reaction rate coefficients as well as error in the temperature profile calculations. To illustrate FCCI surface reaction rate control conditions, Figure 69 depicts the simulation of the MFF-5 195011 fuel pin using artificially high diffusion coefficients in the BISON simulation. At the peak temperature and power location the BISON simulation predicts that the FCCI thickness is higher than that of the reaction rate correlation. This is an indication of where the surface reaction rate would be rate controlling.

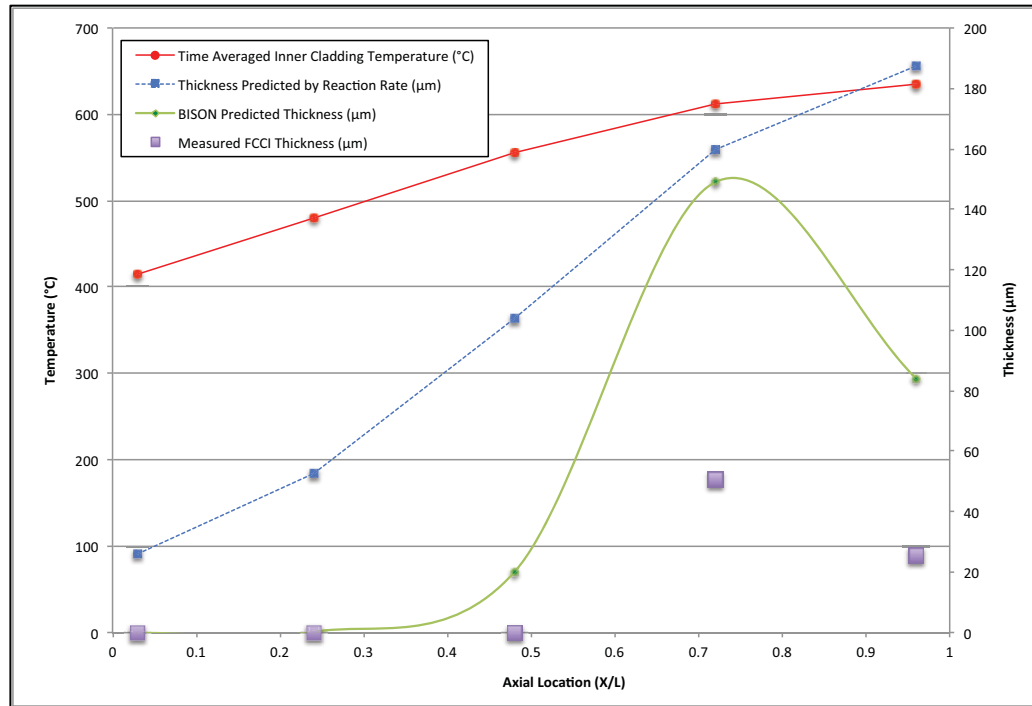


Figure 68. Time averaged inner cladding temperature, measured FCCI thickness, and predicted FCCI thickness for MFF-5 195011 fuel pin versus axial fuel column location.

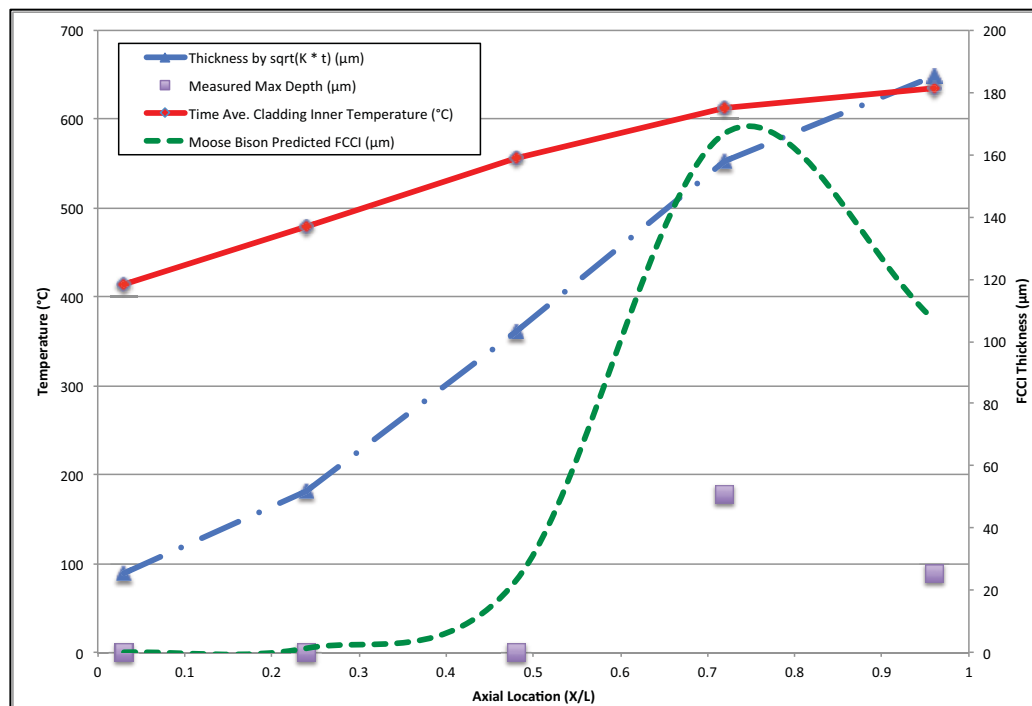


Figure 69. Graph depicting BISON simulation exceeding reaction rate correlation prediction indicating possibility of surface reaction controlled FCCI formation.

Figure 70 provides a comparative graph of the normalized (X/L) power profile typical of EBR-II Row 4 and that of Row 3 in the FFTF. Compared to peak power, the power at the top of the fuel column in FFTF is much lower than that experienced at the top of the fuel column in EBR-II experiments. This results in a lower generation of lanthanide fission product at the top of the fuel column relative to the mid-plane high power location as well as a distinct drop in the fuel centerline temperature that is not seen at in EBR-II experiments. These two operational conditions cause the FCCI layer formation to decrease at the top of the fuel column in FFTF fuels.

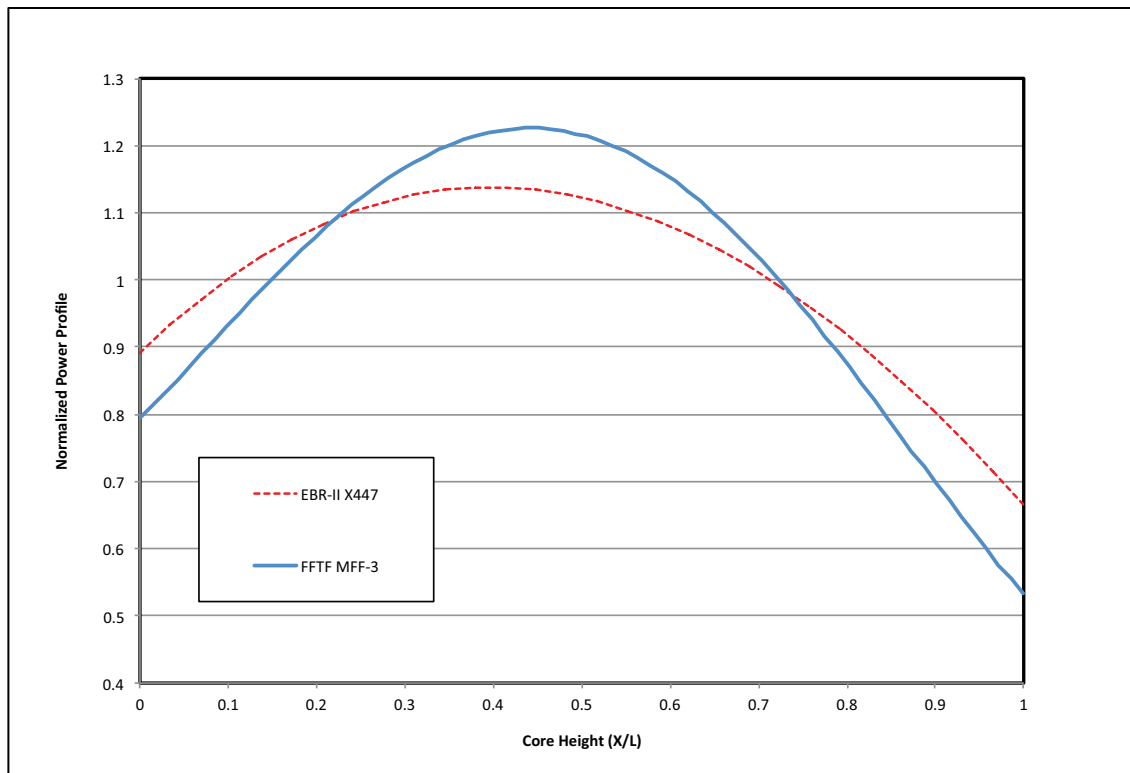


Figure 70. Comparative plot of normalized power profiles typical of EBR-II and FFTF.

A final consideration in the accurate modeling of the formation of FCCI is consideration of the cycle to cycle power and temperature. Figure 6, Figure 7, Figure 37, and Figure 39 present the cycle to cycle power and peak inner cladding temperature

histories for the X447, MFF-3, and MFF-5 fuel pins. Early in life, pin powers and temperatures tend to be high due to the low amount of neutron absorbing fission products and high fissile quantities at beginning-of-life. With increasing burnup, fissile quantities progressively decrease, and absorbing fission products increase resulting in a decrease in fuel pin powers and temperatures. The BISON model predicts that much of the formation of FCCI occurs during these early high power – high temperature cycles. An example is provided in the X447 DP-69 pin which operated for 5 cycles compared to 20 cycles for DP-04, DP-70, and DP-75, yet still developed over 100 μm of FCCI in the top of the fuel column compared with 140 μm developed by the DP-04, DP-70, and DP-75 pins. Figure 71 shows the model predicted FCCI formation on a cycle to cycle basis for the DP-75 fuel pin.

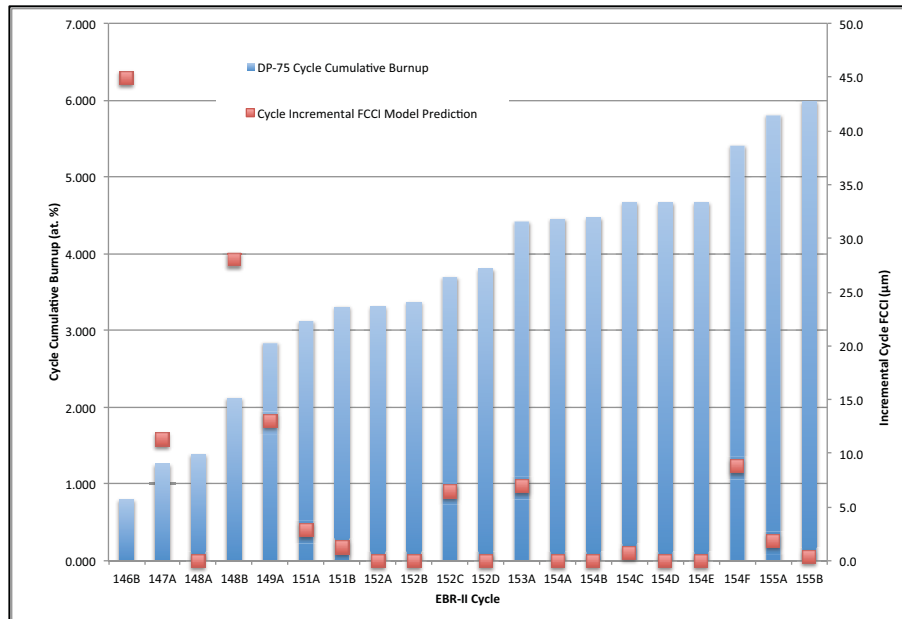


Figure 71. X447 DP-75 Cycle-by-cycle Cumulative Burnup and BISON model incremental FCCI formation.

Differences between experimental data and model prediction may be due to a number of factors that will require further study as the understanding of FCCI formation and behavior progresses. Temperatures used in the analysis are calculated from bulk outlet

coolant temperature measurements of the EBR-II and FFTF. These bulk coolant temperatures are used along with the estimated pin powers for each reactor cycle to calculate the radial temperature distributions of the fuel pins of interest. In many cases bulk temperature measurements may be the closest temperature measurements available during the experiments and may introduce significant error in the calculated fuel pin temperatures and distributions.

Microstructural analysis indicates that FCCI formation is not radially uniform in a fuel pin. This behavior may be explained by radial temperature gradients or by offset contact between fuel and cladding. Both may contribute and will need to be understood for a full mechanistic model to be fully effective.

The early life behavior of metallic fuel is not completely understood. The early life behavior of metallic fuel needs further study to determine the influence of non-contact between fuel and cladding, including the existence of a zirconium rind, on the formation of FCCI.

Lastly, the migration mechanisms and kinetics for each individual lanthanide fission product of interest needs additional study to determine diffusion coefficients and kinetic rate constants.

6 Conclusion

This dissertation has focused on studying the differences between relatively short experimental length sodium cooled fast reactor metallic fuel pins and longer prototypic length metallic fuel to determine the impact length may have on the formation of FCCI. Significant differences were found in the formation of FCCI between the EBR-II X447 metallic fuel experiment and the FFTF MFF experiments. FCCI formation tends to peak near the top of the fuel column in experimental length fuel pins while the FCCI formation peaks between 0.5 and 0.75 X/L height in the fuel columns of prototypic length fuel from the FFTF MFF series. Because FCCI accelerates cladding creep rupture, the life limiting condition in metallic fuel performance, fully understanding the mechanisms behind lanthanide fission product migration and interaction layer formation is critical to advanced sodium cooled fast reactor designs. Many sodium cooled fast reactor designs utilize extended length fuel columns to maximize performance [44, 45, 46]. The FCCI model and predictive capability developed during the course of this doctoral research should be of great value in predicting the behavior and performance of extended core length reactor fuel pins.

The MFF series of fuel experiments conducted in the FFTF are considered critical to proving that data obtained from experimental length fuel experiments in EBR-II, JOYO, and Phenix are representative of prototypic sized fuel. The work conducted under this doctoral research provides the data and FCCI predictive modeling capability necessary to answer scalability questions raised during design and licensing of future extended fuel length metallic fueled sodium cooled fast reactors with respect to predicting fuel pin failure accelerated FCCI.

Critical areas of research need have been identified during the conduct of this work. Future research efforts into the material properties, migration mechanisms, and interactive behavior of fuel, cladding, and fission product constituents are needed. Specifically diffusion and reaction kinetics coefficients are needed to understand and model the behavior of the complex mixture of species found in irradiated metallic fuels.

7 References

1. Porter, D. L. and Hilton, C. "Extending Sodium Fast Reactor Driver Fuel Use to Higher Temperatures," *Nuclear Technology*, v. 173, (2011) p. 222.
2. Crawford, D. C., D. L. Porter and S. L. Hayes, "Fuels for Sodium-Cooled Fast Reactors: US Perspective," *Journal of Nuclear Materials*, v.371, (2007) pp. 202-231.
3. Carmack, W. J., Porter, D. L., Chang, Y. I., Hayes, S. L., Meyer, M. K., Burkes, D. E., Lee, C. B., Mizuno, T., Delage, F., Somers, J. "Metallic Fuels for Advanced Reactors" *Journal of Nuclear Materials*, v.392, Issue 2, (2009), pp. 139-150.
4. Walters, L. C., Seidel, B.R., and Kittel, J. H., "Performance of Metallic Fuels and Blankets in Liquid-Metal Fast Breeder-Reactors" *Nuclear Technology*, v. 65 (1984) pp. 179-231.
5. Kittel, J. H., Frost, B. R. T., Mustellier, J. P., Bagley, K. Q., Crittenden, G. C., and Van Dievoet, J., "History of Fast Reactor Fuel Development." *Journal of Nuclear Materials*, v. 204 (1993) pp. 1-13.
6. Till, C. H. and Chang, Y. I. "The Integral Fast Reactor - An Overview." *Progress In Nuclear Energy*. v. **31**(1/2), pp. 3-11.
7. Lahm, C. E., Koenig, J. F., Pahl, R. G., Porter, D. L., and Crawford, D. C., "Experience with Advanced Driver Fuels in EBR-II." *Journal of Nuclear Materials*, v. 204 (1993), pp. 119-123.
8. Hofman, G. L. and Walters, L. C., "Metallic Fast Reactor Fuels," *Nuclear Materials, Part I Volume 10 A*, edited by B. R. T. Frost, appearing in *Materials Science and Technology, A Comprehensive Treatment*, R. W. Cahn, P. Haasen, and E. J. Kramer (eds.), VCH Verlagsgesellschaft mbH, (1994) pp. 1-43.
9. Pahl, R. G., Porter, D. L., Crawford, D. C., and Walters, L. C., "Irradiation Behavior of Metallic Fast Reactor Fuels" *Journal of Nuclear Materials*, v. 188 (1992) pp. 3-9.
10. Pahl, R. G., Wisner, R. S., Billone, M. C., Hofman, G. L., "Steady State Irradiation Testing of U-Pu-Zr Fuel to >18% Burnup," *Proc. Int. Conf. on Fast Reactor Safety IV*, vol. 129, Snowbird, UT, 12-16 August (1990), American Nuclear Society, La Grange Park, IL.
11. Walters, L. C., "Thirty Years of Fuels and Materials Information from EBR-II." *Journal of Nuclear Materials*, v. 270 (1999) pp. 39-48.

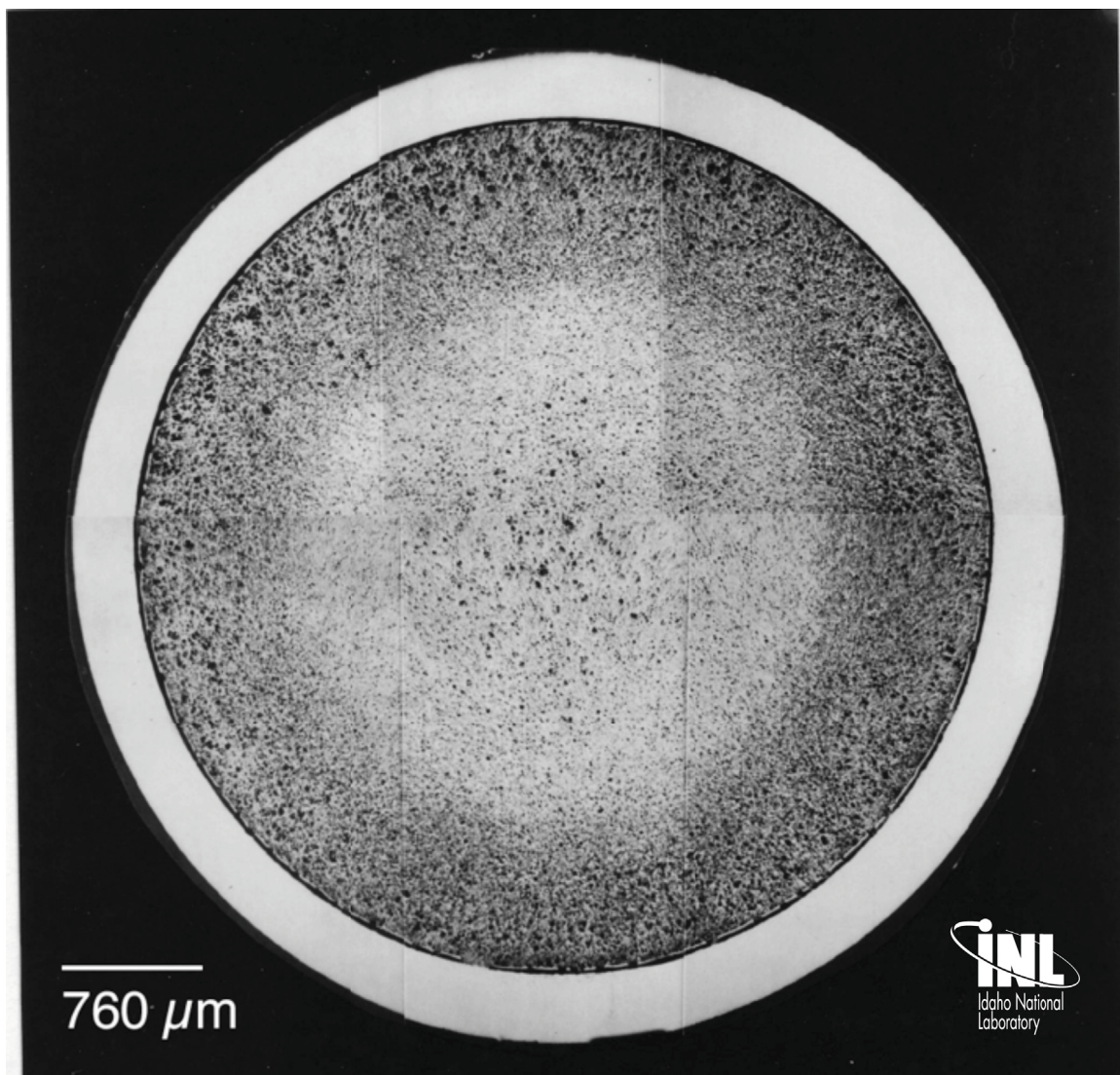
12. Porter, D. L., "Fuel Test Plan," Argonne National Laboratory, General Electric, and Westinghouse-Hanford Co., June 1994.
13. Pitner, A. L. and Baker, R. B., "Metal Fuel Test Program in the FFTF." *Journal of Nuclear Materials*, v. 204 (1993) pp.124-130.
14. Walter, C.M. and J.A. Lahti, "Compatibility of U-Pu-Fz Fuel Alloys with Potential Cladding Materials." *Nuclear Applications*, v. 2 (1966) pp. 308-319.
15. Zegler, S.T. and C.M. Walter, "Compatibility between Metallic U-Pu-base Fuels and Potential Cladding Materials." *AIME Nuclear Metallurgy Symposium on Plutonium Fuels Technology*. American Institute of Mechanical Engineering. (1967).
16. Inagaki, K. and Ogata, T. "Reaction of Rare Earth Elements with Iron Base Alloy" *Proceedings of GLOBAL-2011*, Makuhari Messe, Japan, Dec.11-16, 2011.
17. Pahl, R.G., et al., "Experimental studies of U-Pu-Zr fast reactor fuel pins in the Experimental Breeder Reactor-II." *Metallurgical Transactions A (Physical Metallurgy and Materials Science)*. 21A (7) (1990) pp. 1863-1870.
18. Keiser, D.D., "The Development of FCCI Zones in Irradiated U-Zr and U-Pu-Zr Fuel Elements with Stainless Steel Cladding." *Nuclear Reactors, Nuclear Fusion and Fusion Engineering*, A. Aasen and P.Olsson eds. ISBN: 978-1-60692-508-9, 2009.
19. Keiser, D. D. "Fuel-cladding Interaction Layers in Irradiated U-Zr and U-Pu-Zr Fuel Elements." Argonne National Laboratory Report # ANL-NT-240. Jan. 2006.
20. Leibowitz, L and Blomquist, R. A. "Thermal Conductivity and Thermal Expansion of Stainless Steels D9 and HT9," *International Journal of Thermophysics*, v. 9, No. 5 (1988) pp. 873 – 883.
21. Cohen, A. B., Tsai, H., and Neimark, L. A. "Fuel-cladding Compatibility in U-19Pu-10Zr/HT9-Clad Fuel at Elevated Temperatures." *Journal of Nuclear Materials*, v. 204 (1993) pp. 244-251.
22. Pahl, R.G., C.E. Lahm, and S.L. Hayes, "Performance of HT9 Clad Metallic Fuel at High Temperature." *Journal of Nuclear Materials*, v. 204 (1993) pp. 141-147.
23. Hayes, S. L. "SAFE: A Computer Code for the Steady State and Transient Thermal Analysis of LMR Fuel Elements." Argonne National Laboratory Report # ANL-IFR-221. Dec. 1993.

24. Carlson, B.G., ANL Memo to M. Vaughn, July 1989, Argonne National Laboratory Intralab Memo. Unpublished work.
25. Hofman, G. L., Hayes, S. L., and Petri, M. C., “ Temperature Gradient Driven Constituent Redistribution in U-Zr Alloys.” *Journal of Nuclear Materials*, v. 227, (1996) pp. 277-286.
26. Sanecki, J.E., ANL Memo to Hofman and Tsai, Jan 1991, Argonne National Laboratory Intralab Memo. Unpublished work.
27. Sanecki, J.E., ANL Memo to Strain and Petri, Jan 1993, Argonne National Laboratory Intralab Memo. Unpublished work.
28. Yeon, S.K, Hofman, G.L., and Yacout, A.M., “Migration of Minor Actinides and Lanthanides in Fast Reactor Metallic Fuel,” *Journal of Nuclear Materials*, v. 392 (2009) pp. 164-170.
29. Henslee, S. P. “Advanced LMFBR Fuel-cladding Susceptability to Stress Corrosion Due to Reprocessing Impurities.” Argonne National Laboratory Report, ANL/PPRNT—89-154, March 1987, p. 9.
30. Pitner, A.L. and Baker, R.B. “Metallic Fuel Test Program in the FFTF.” *Journal of Nuclear Materials*, v. 204 (1993) pp. 124-130.
31. Porter, D.L. and Tsai, H. “Full-length Metallic Fast Reactor Fuel Pin Test in FFTF (IFR-1),” Idaho National Laboratory Report, INL/LTD-11-21062, March 2011.
32. Tortorici, P. C. and Dayananda, M. A., "Interdiffusion of Cerium in Fe-base Alloys with Ni or Cr." *Journal of Nuclear Materials*, 204(0) (1993) pp. 165-172.
33. Weast, R. C. ed. CRC Handbook of Chemistry and Physics, 92nd Edition, Internet Version 2012. CRC Press Online, Taylor and Francis Group. 2012. p. 4-127.
34. Mariani, R.D., Porter, D.L., O’Holleran, T.P., Hayes, S.L, and Kennedy, J.R., “Lanthanides in Metallic Nuclear Fuels: Their Behaviour and Methods for Their Control.” *Journal of Nuclear Materials*, v. 419, (2011) pp. 263-271.
35. Kim, Y. S., Hayes, S. L., Hofman, G. L. and Yacout, A. M., “Modeling of Constituent Redistribution in U-Pu-Zr Metallic Fuel.” *Journal of Nuclear Materials*, v. 359 (2006) p. 17.

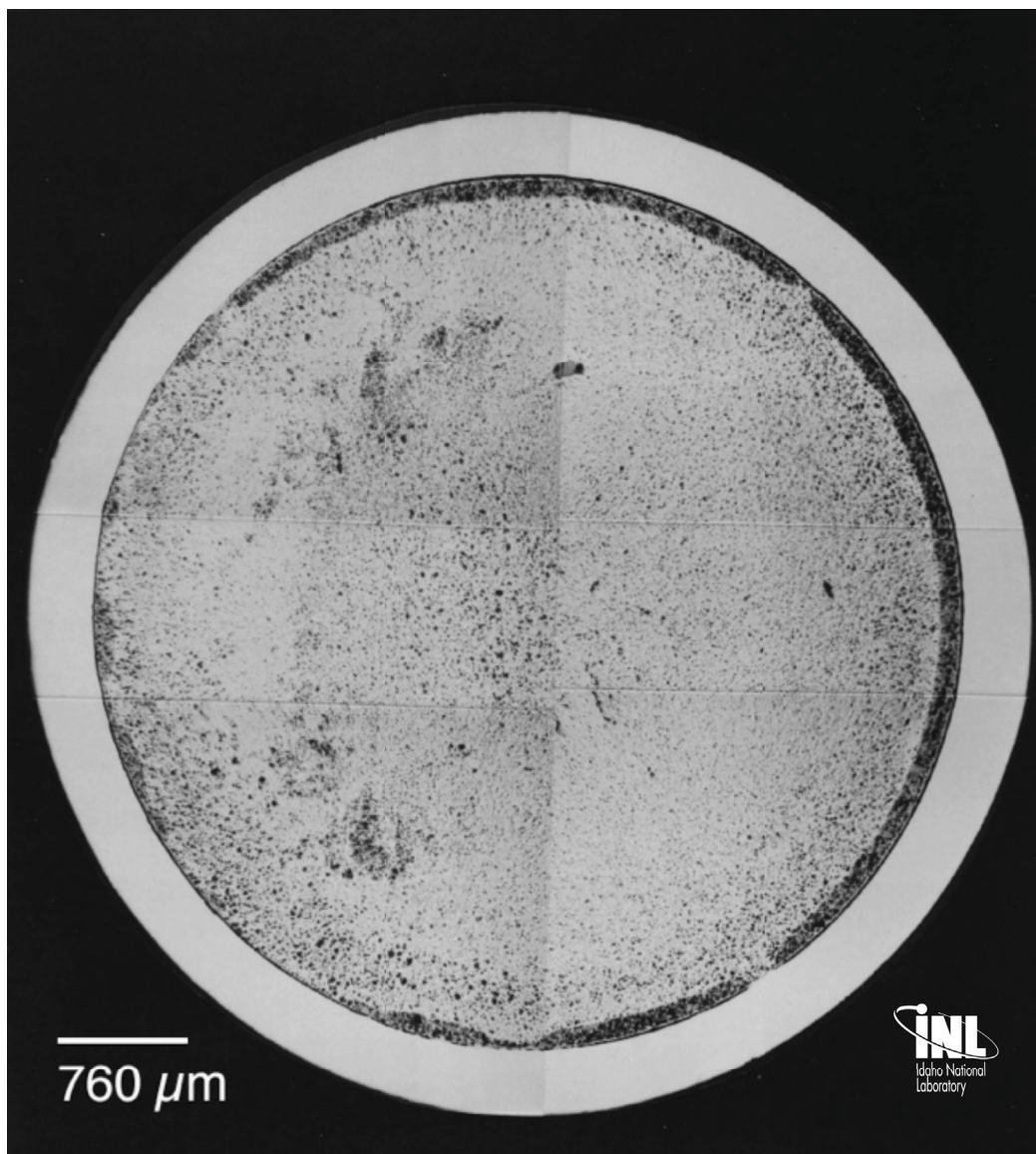
36. Karahan, A., Buongiorno, J., Kazimi, M. S. “Modeling the Steady-state Behavior of Metallic Fuels in Liquid-Metallic Fast Reactors.” MIT Center for Advanced Energy Studies Report # MIT-NFC-TR-107, April 2009.
37. Ogata, T., Akabori, M, and Itoh, A. “Diffusion of Cerium in Uranium-Zirconium Solid Solutions.” *Japan Institute of Metals, Materials Transactions*, v. 44 (2003) pp. 47 – 52.
38. Tournier, J. Commissariat a L’Energie Atomique Report # CEA-R2446, 1964.
39. Gaston, D., Newman, C., Hansen, G., and Lebrun-Grandie, D., “MOOSE: A Parallel Computational Framework for Coupled Systems of Nonlinear Equations,” *Nuclear Engineering and Design*, v. 239 (2009) p. 1768.
40. Newman, C., Hansen, G., and Gaston, D., “Three-dimensional Coupled Simulation of Thermomechanics, Heat, and Oxygen Diffusion in UO₂ Nuclear Fuel Pins,” *Journal of Nuclear Materials*, v. 392 (2009) p. 6.
41. Isnard O., Miraglia S., Soubeyroux J.L., Fruchart D., and Stergiou A.C., “Neutron Diffraction Study of the Structural and Magnetic Properties of the R₂Fe₁₇H_x(D_x) Ternary Compounds (R= Ce, Nd and Ho).” *Journal of Less-Common Metals*, v. 162 (1990) pp. 273-284.
42. Wolfram Research, Inc., Mathematica, Version 8.0, Champaign, IL (2010).
43. Sandia National Laboratory, CUBIT Mesh Generation Environment, Version 13.1, Albuquerque, NM (2011).
44. Kim, T. K. and Taiwo, T. A., “Feasibility Study of Ultra-Long Life Fast Reactor Core Concept”, *Proceedings of PHYSOR 2010*, Pittsburgh, PA, May 2010.
45. Minato, A., Ueda, N., Wade, D., Greenspan, E., and Brown, N. “Small Liquid Metal Cooled Reactor Safety Study.” Lawrence Livermore National Laboratory Report # UCRL-TR-217093, Nov. 2005.
46. Ellis, T., Petroski, R., Hejzlar, P., Zimmerman, G., McAlees, D., Whitmer, C., Touran, N., Hejzlar, J., Weaver, K., Walter, J. C., McWhirter, J., Ahlfeld, C., Burke, T., Odedra, A., Hyde, R., Gilleland, J., Ishikawa, Y., Wood, L., Myhrvold, N., and Gates, W.H. “Traveling-Wave Reactors: A Truly Sustainable and Full-Scale Resource for Global Energy Needs.” *Proceedings of ICAPP 2010*, San Diego, CA, June 2010.

Appendix A - Metallographic Montages of X447 DP-69 Fuel Pin

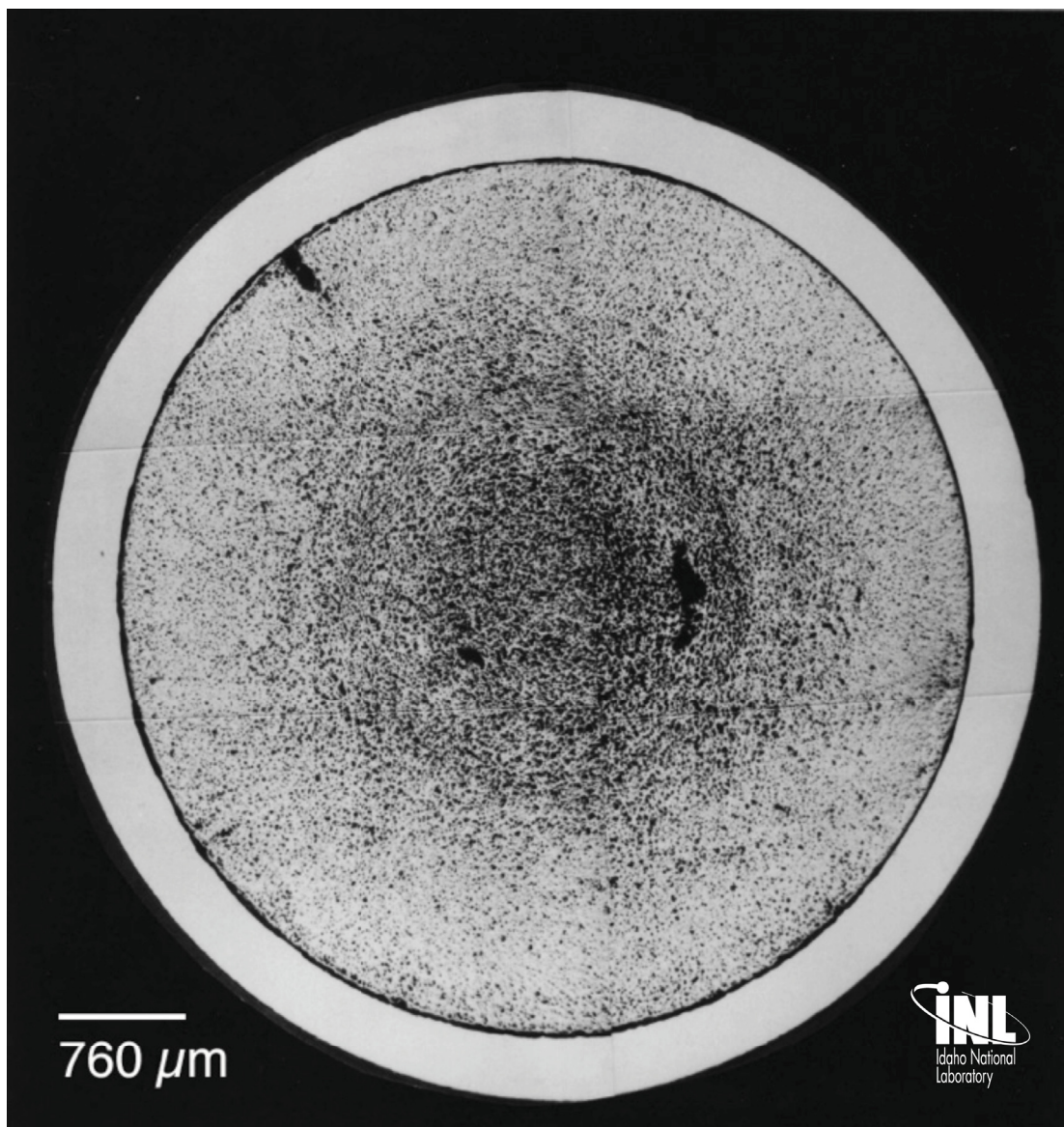
X447 Pin S/N	DP-69	MET Mount Number	
X/L	0.19	Analysis Date	
Distance from BOFP (inch) (cm)	3.5 8.9	Ave. PICT (°C)	463
Distance from BOFC (inch) (cm)	2.75 7.0	Ave. FCLT (°C)	574
Linear Power (W/cm)	335	Fission Density (fission/cm³)	1.68e21
FCCI (μm)	0	Burnup (at%)	4.7



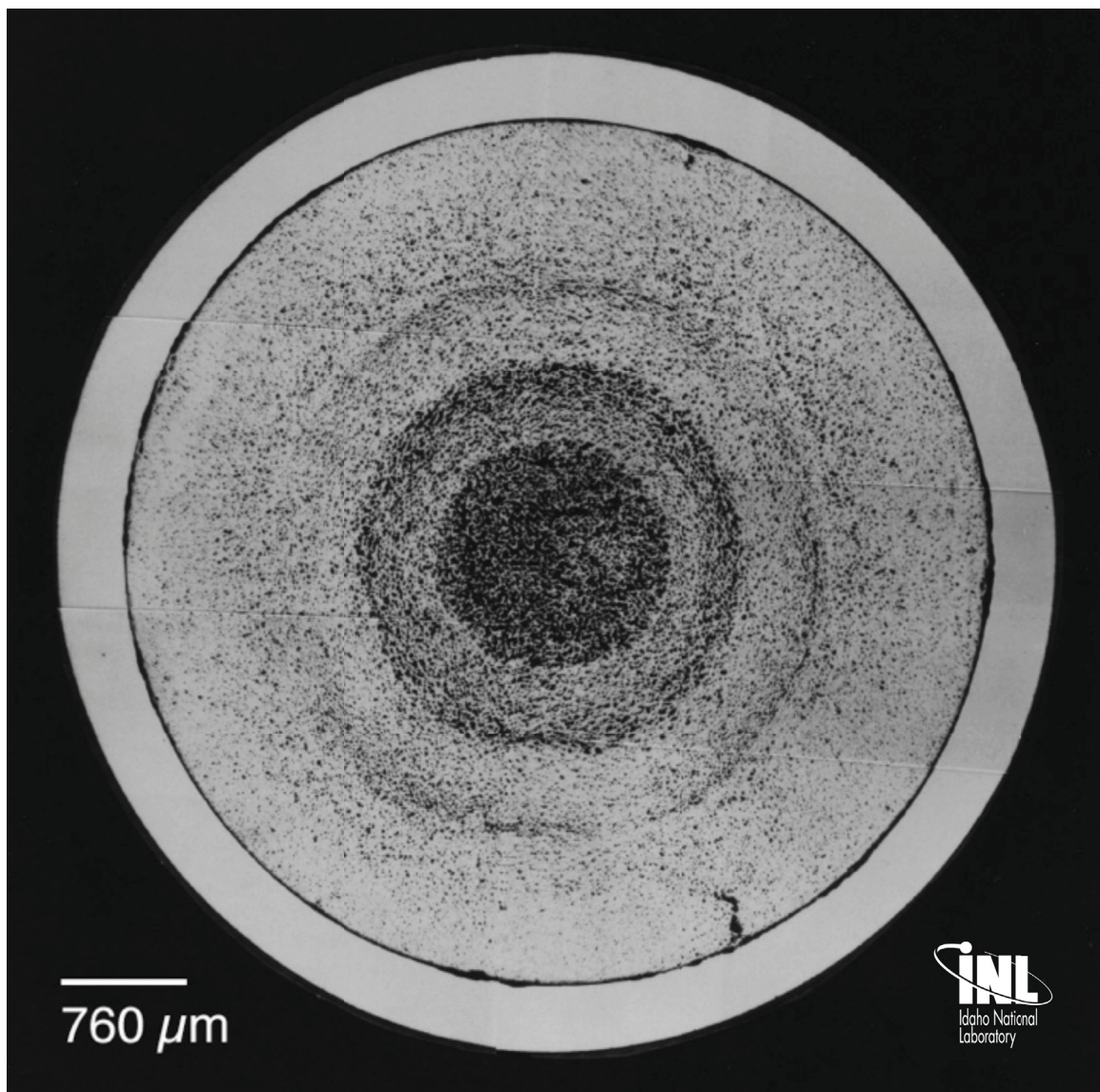
X447 Pin S/N	DP-69	MET Mount Number	
X/L	0.46	Analysis Date	
Distance from BOFP (inch) (cm)	7.5 19.1	Ave. PICT (°C)	552
Distance from BOFC (inch) (cm)	6.75 17.1	Ave. FCLT (°C)	661
Linear Power (W/cm)	350	Fission Density (fission/cm³)	1.74e21
FCCI (μm)	0	Burnup (at%)	4.9



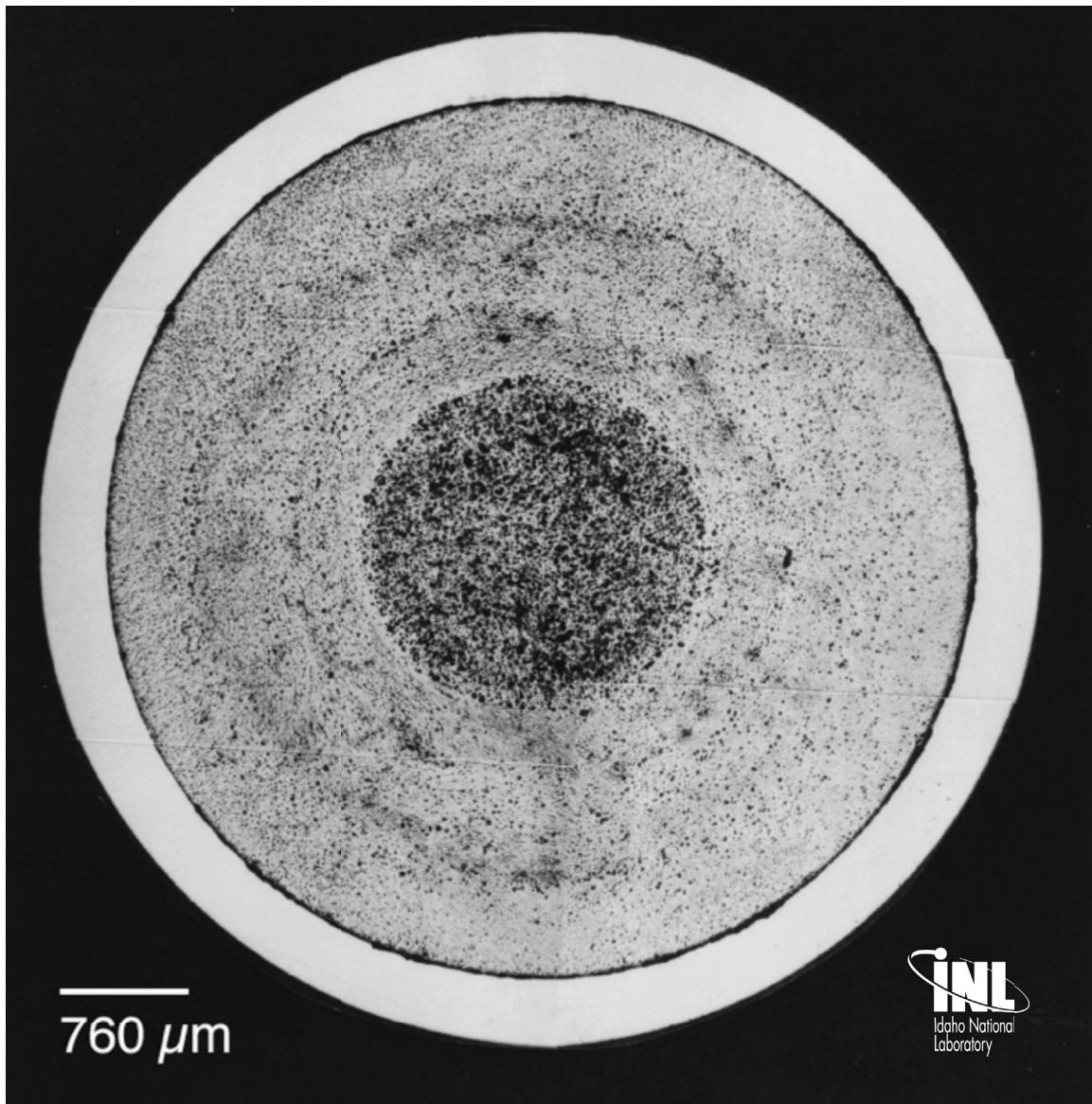
X447 Pin S/N	DP-69	MET Mount Number	
X/L	0.74	Analysis Date	
Distance from BOFP (inch) (cm)	10.75 27.3	Ave. PICT (°C)	626
Distance from BOFC (inch) (cm)	10.0 25.4	Ave. FCLT (°C)	713
Linear Power (W/cm)	287	Fission Density (fission/cm³)	1.44e21
FCCI (μm)	50.8	Burnup (at%)	4.1



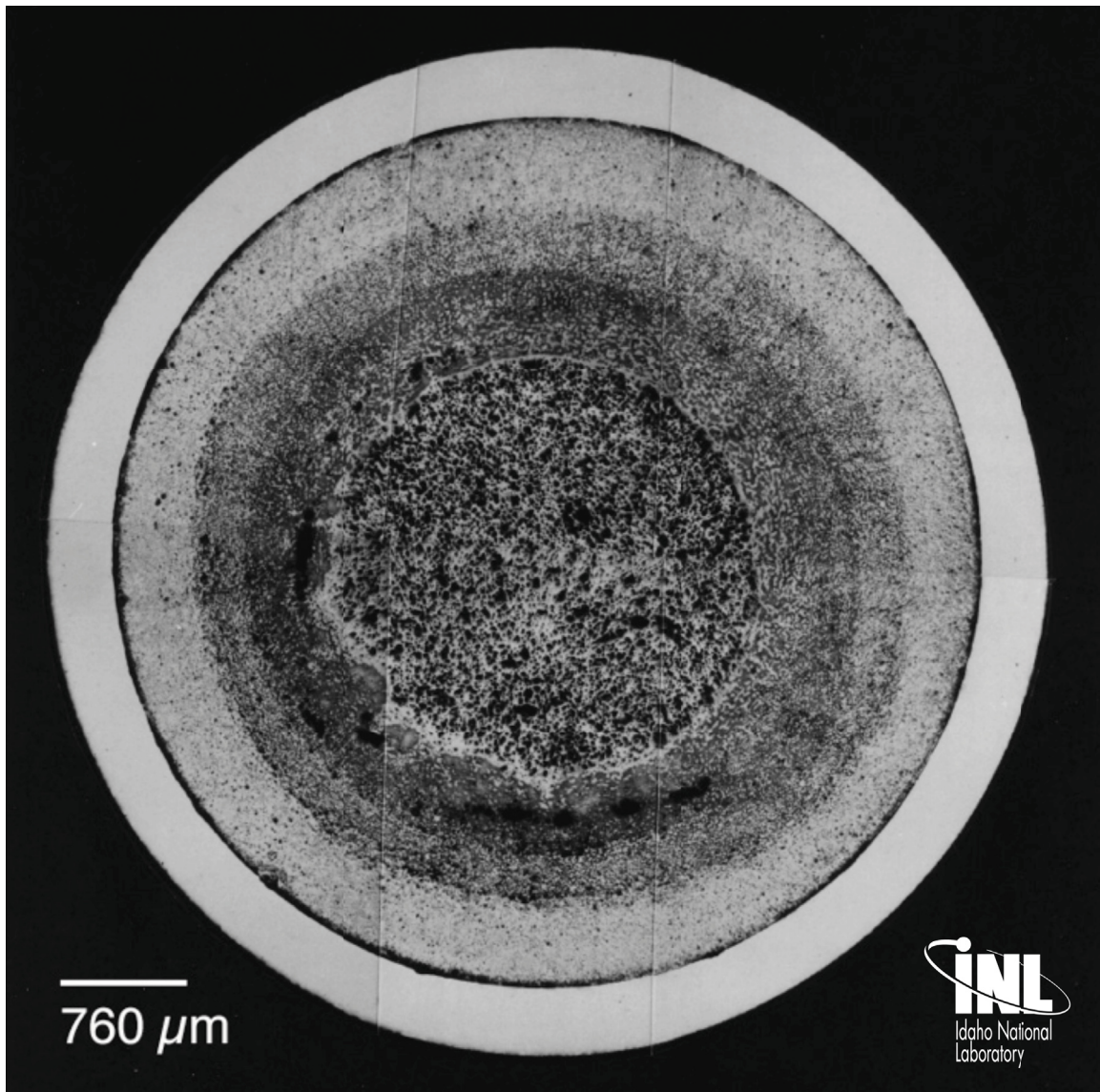
X447 Pin S/N	DP-69	MET Mount Number	
X/L	0.85	Analysis Date	
Distance from BOFP (inch) (cm)	12.25 31.1	Ave. PICT (°C)	648
Distance from BOFC (inch) (cm)	11.5 29.2	Ave. FCLT (°C)	720
Linear Power (W/cm)	243	Fission Density (fission/cm³)	1.22e21
FCCI (μm)	50.8	Burnup (at %)	3.5



X447 Pin S/N	DP-69	MET Mount Number	
X/L	0.95	Analysis Date	
Distance from BOFP (inch) (cm)	13.5 34.3	Ave. PICT (°C)	663
Distance from BOFC (inch) (cm)	12.75 32.4	Ave. FCLT (°C)	720
Linear Power (W/cm)	191	Fission Density (fission/cm³)	0.96e21
FCCI (μm)	101.6	Burnup (at%)	2.7

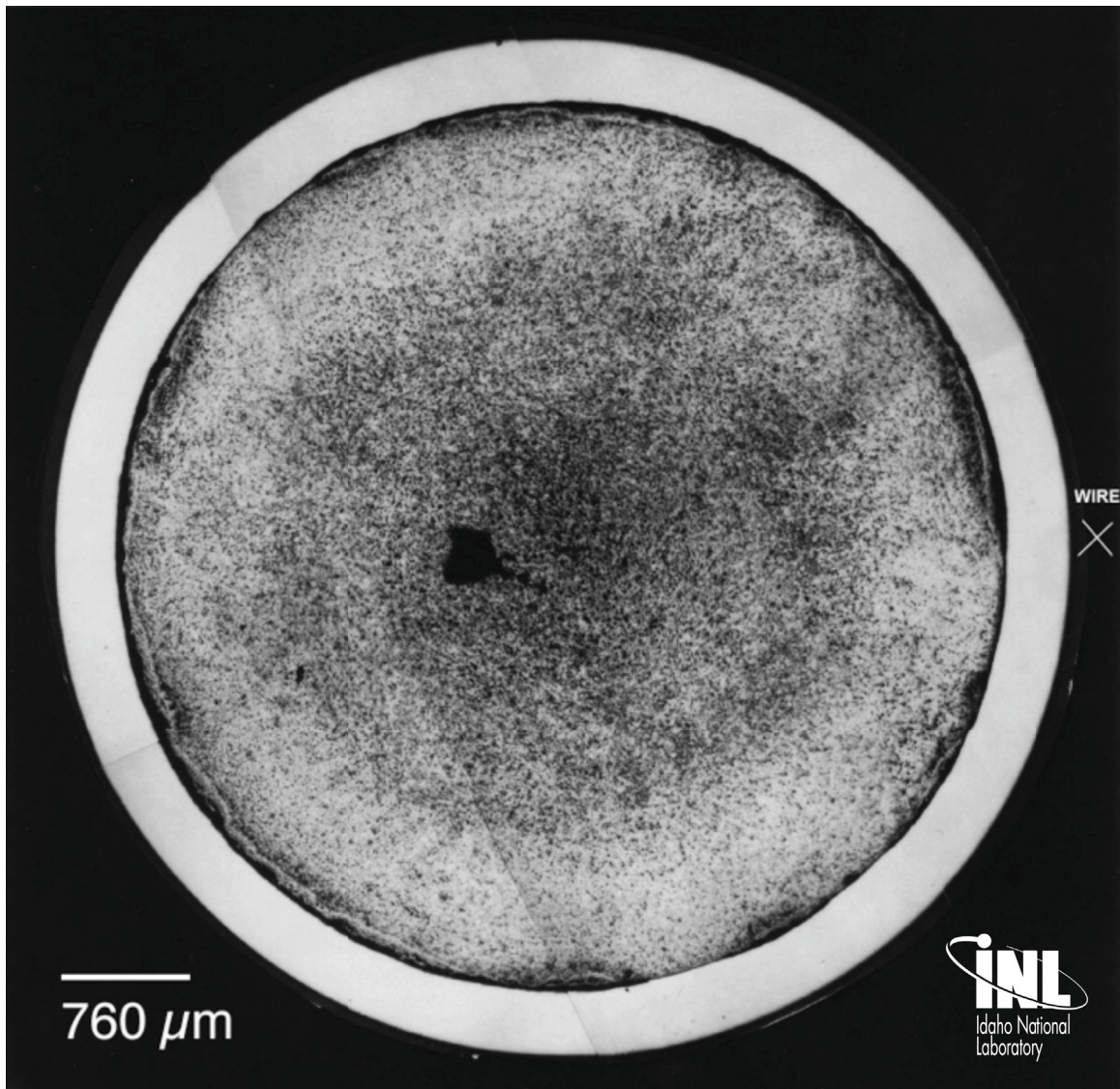


X447 Pin S/N	DP-69	MET Mount Number	
X/L	1.0	Analysis Date	
Distance from BOFP (inch) (cm)	14.25 36.2	Ave. PICT (°C)	664
Distance from BOFC (inch) (cm)	13.5 34.3	Ave. FCLT (°C)	720
Linear Power (W/cm)	171	Fission Density (fission/cm³)	0.86e21
FCCI (μm)	101.6	Burnup (at%)	2.4

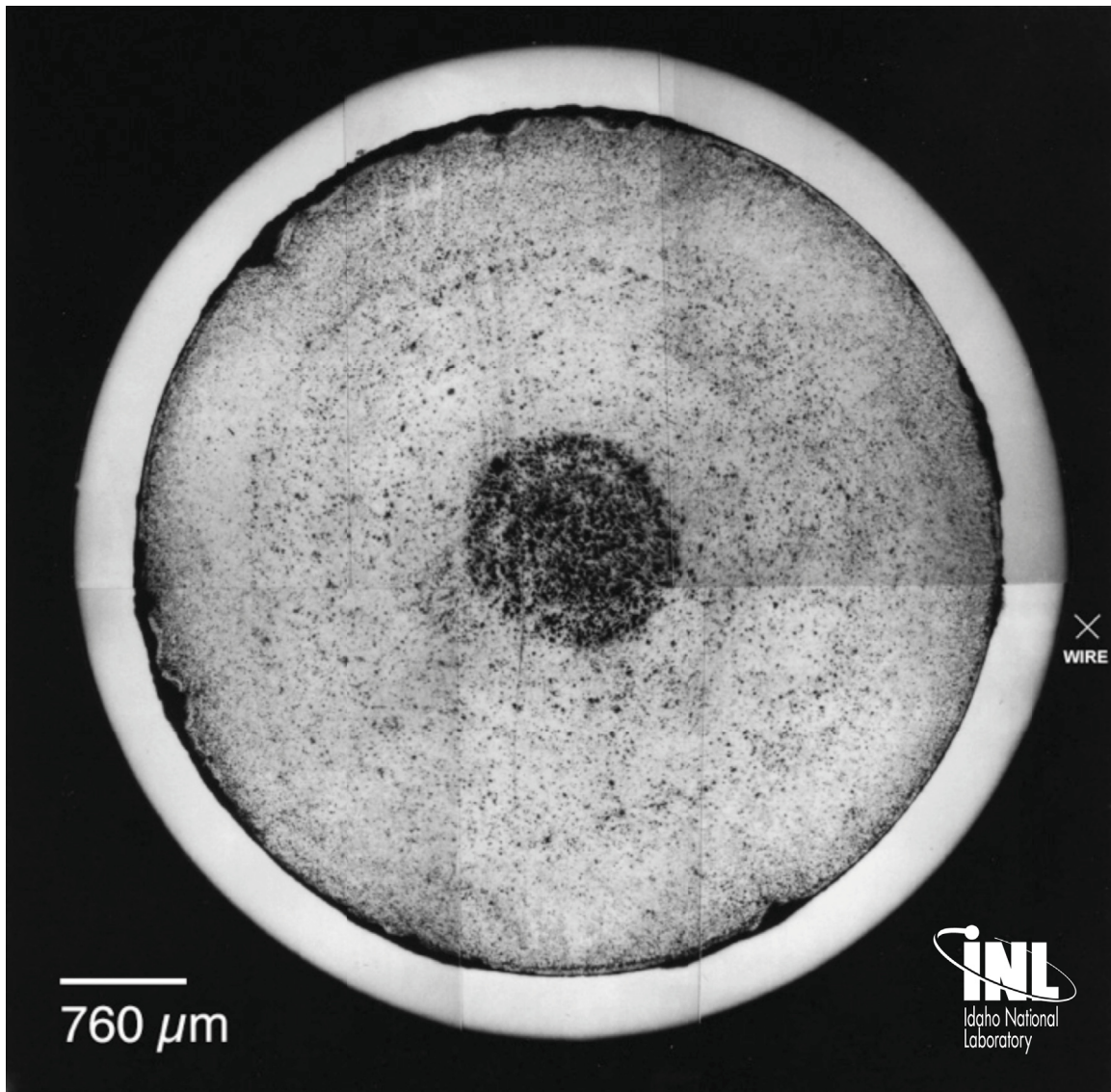


Appendix B - Metallographic Montages of X447 DP-04 Fuel Pin

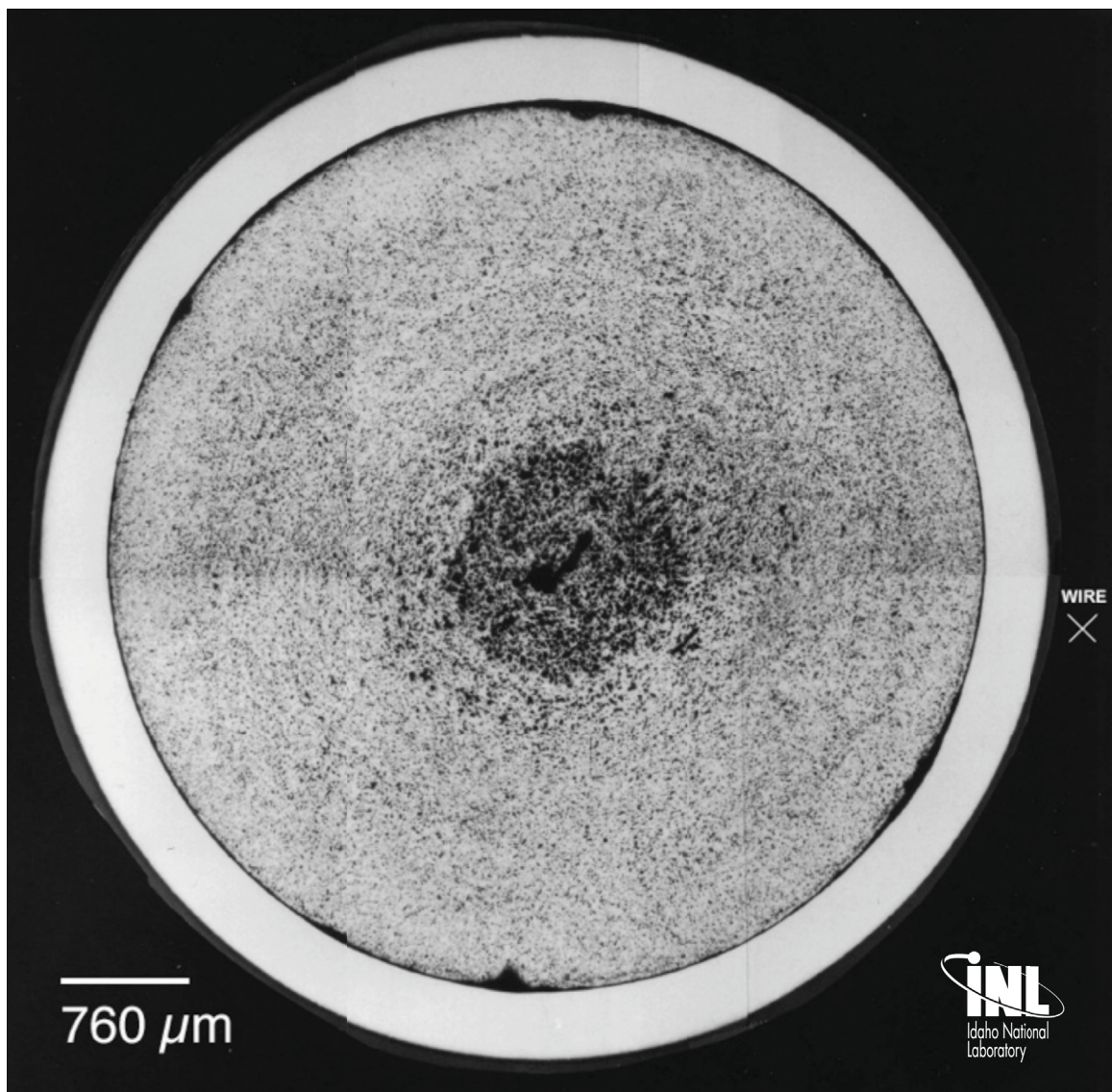
X447 Pin S/N	DP-04	MET Mount Number	
X/L	0.69	Analysis Date	
Distance from BOFP (inch) (cm)	10.5 26.7	Ave. PICT (°C)	605
Distance from BOFC (inch) (cm)	9.75 24.8	Ave. FCLT (°C)	693
Linear Power (W/cm)	126	Fission Density (fission/cm³)	3.27e21
FCCI (μm)	63.5	Burnup (at%)	9.24



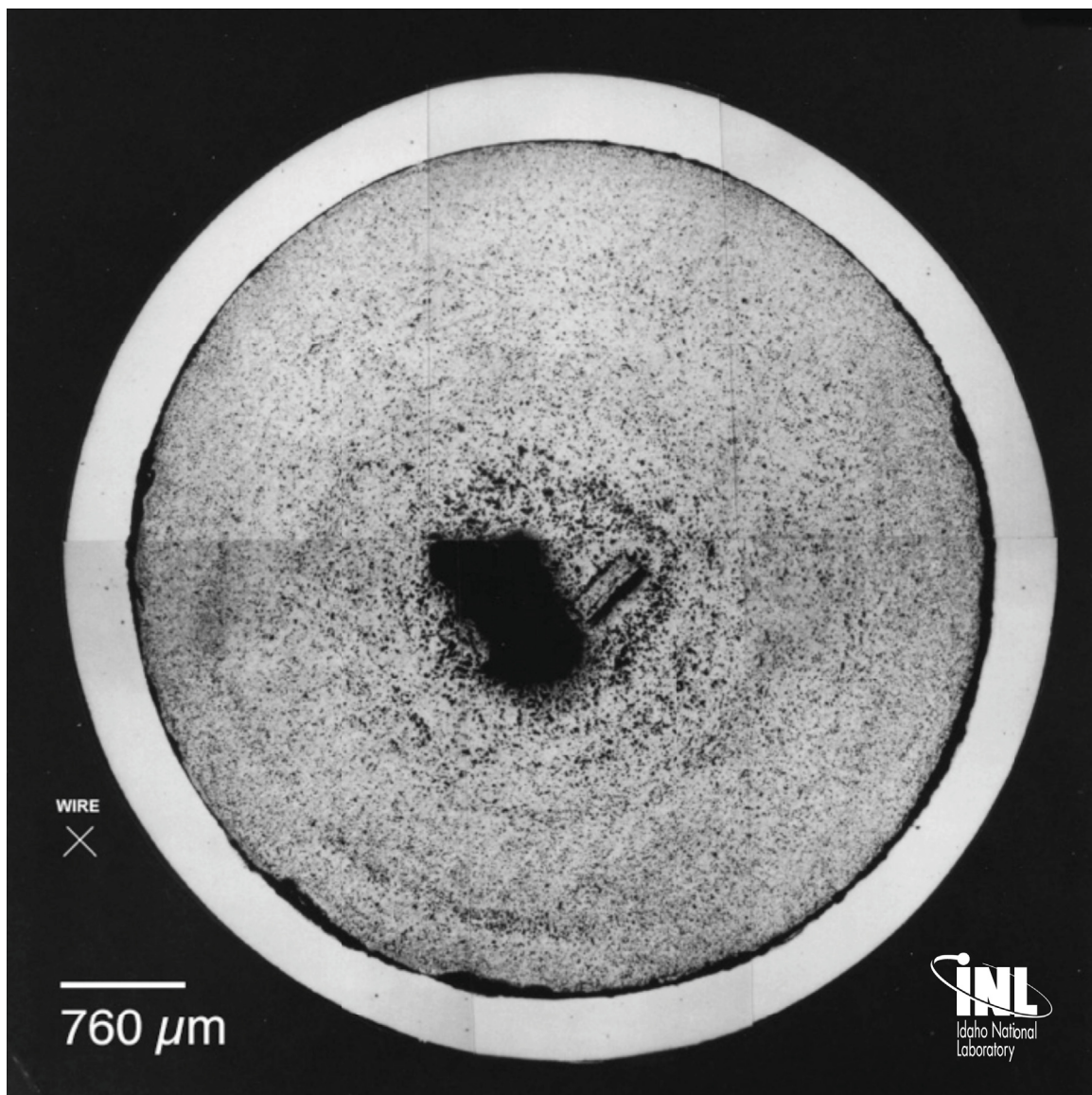
X447 Pin S/N	DP-04	MET Mount Number	
X/L	0.86	Analysis Date	
Distance from BOFP (inch) (cm)	12.85 32.6	Ave. PICT (°C)	634
Distance from BOFC (inch) (cm)	12.1 30.7	Ave. FCLT (°C)	704
Linear Power (W/cm)	234	Fission Density (fission/cm³)	2.66e21
FCCI (μm)	114.3	Burnup (at%)	7.5



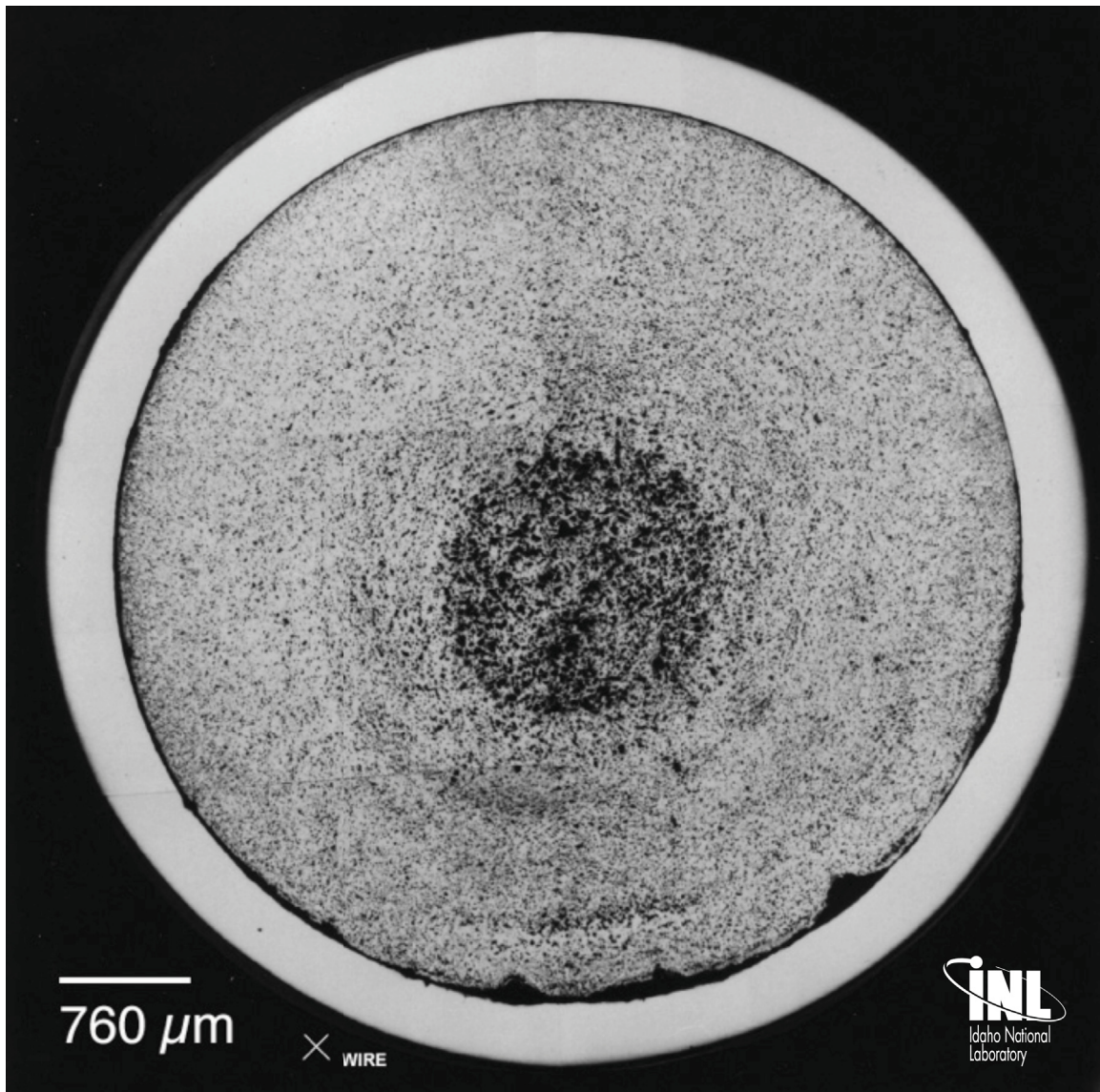
X447 Pin S/N	DP-04	MET Mount Number	
X/L	0.94	Analysis Date	
Distance from BOFP (inch) (cm)	14.0 35.6	Ave. PICT (°C)	644
Distance from BOFC (inch) (cm)	13.6 34.5	Ave. FCLT (°C)	705
Linear Power (W/cm)	202	Fission Density (fission/cm³)	2.29e21
FCCI (μm)	127	Burnup (at %)	6.5



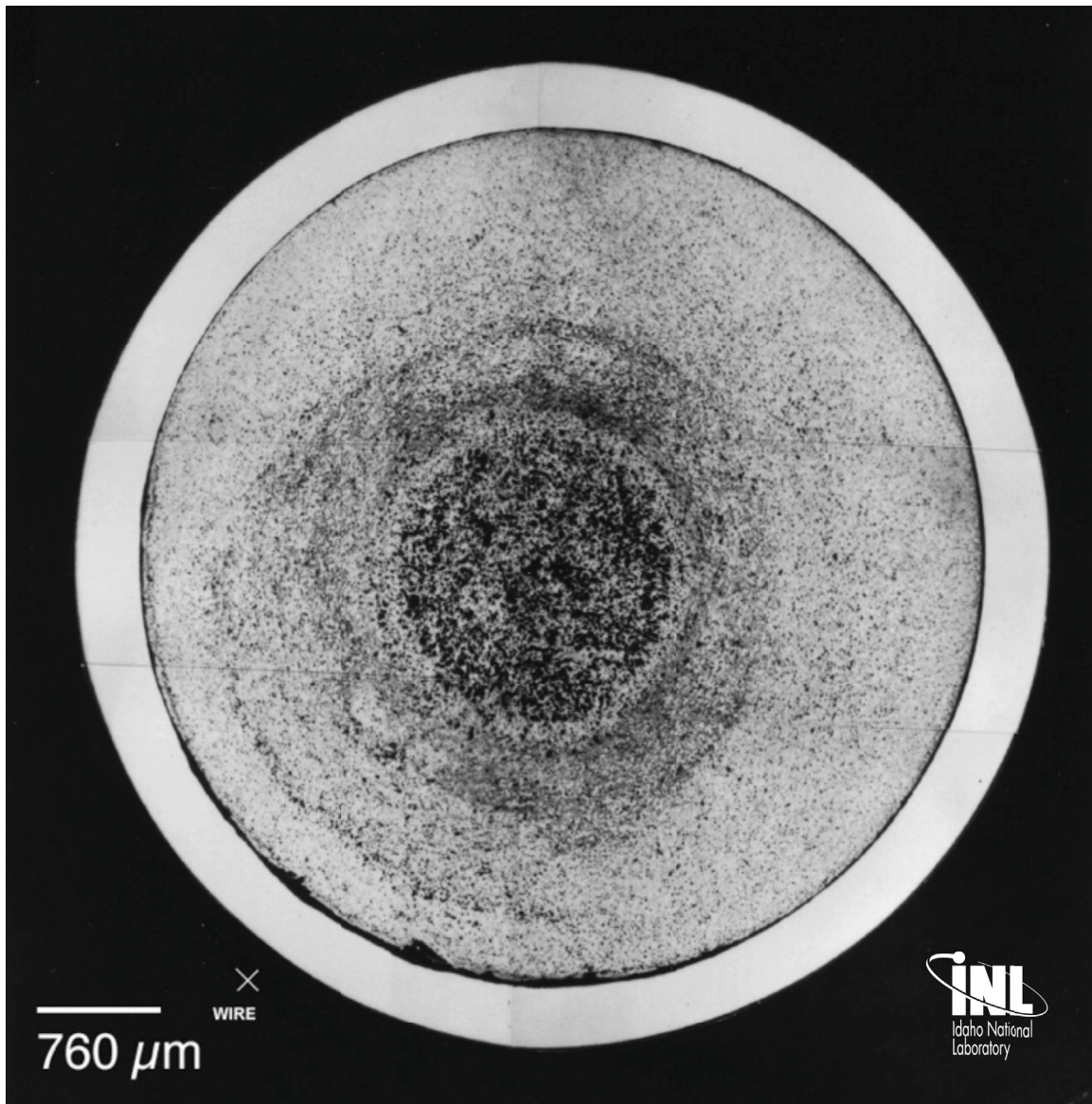
X447 Pin S/N	DP-04	MET Mount Number	
X/L	0.95	Analysis Date	
Distance from BOFP (inch) (cm)	14.25 36.2	Ave. PICT (°C)	649
Distance from BOFC (inch) (cm)	13.5 34.3	Ave. FCLT (°C)	704
Linear Power (W/cm)	184	Fission Density (fission/cm³)	2.09e21
FCCI (μm)	152.4	Burnup (at %)	5.9



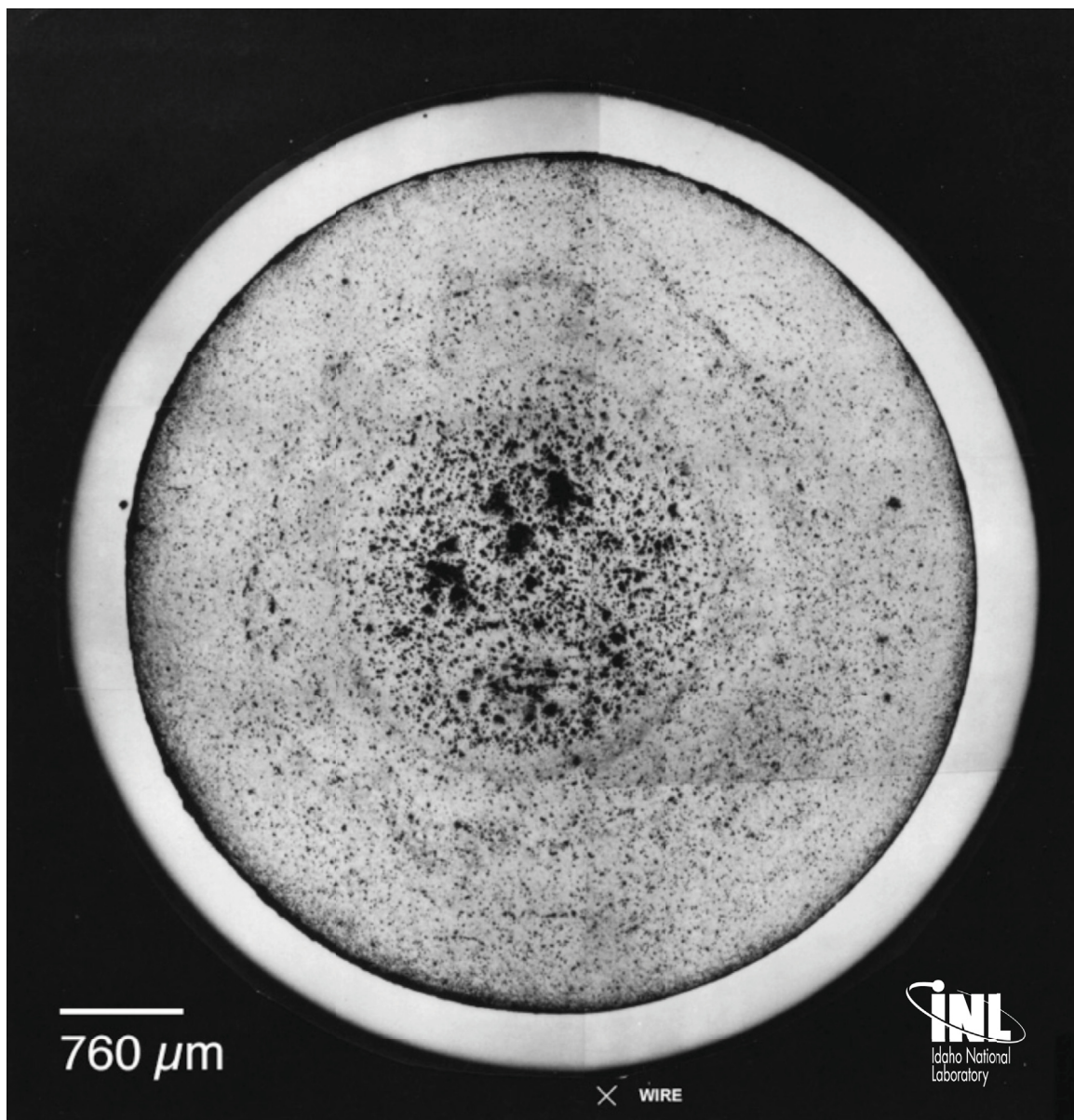
X447 Pin S/N	DP-04	MET Mount Number	
X/L	0.97	Analysis Date	
Distance from BOFP (inch) (cm)	14.5 36.8	Ave. PICT (°C)	649
Distance from BOFC (inch) (cm)	13.75 34.9	Ave. FCLT (°C)	704
Linear Power (W/cm)	179	Fission Density (fission/cm³)	2.86e21
FCCI (μm)	152.4	Burnup (at%)	5.75



X447 Pin S/N	DP-04	MET Mount Number	
X/L	0.98	Analysis Date	
Distance from BOFP (inch) (cm)	14.75 37.5	Ave. PICT (°C)	650
Distance from BOFC (inch) (cm)	14 35.6	Ave. FCLT (°C)	703
Linear Power (W/cm)	175	Fission Density (fission/cm³)	1.98e21
FCCI (mils)	139.7	Burnup (at%)	5.6

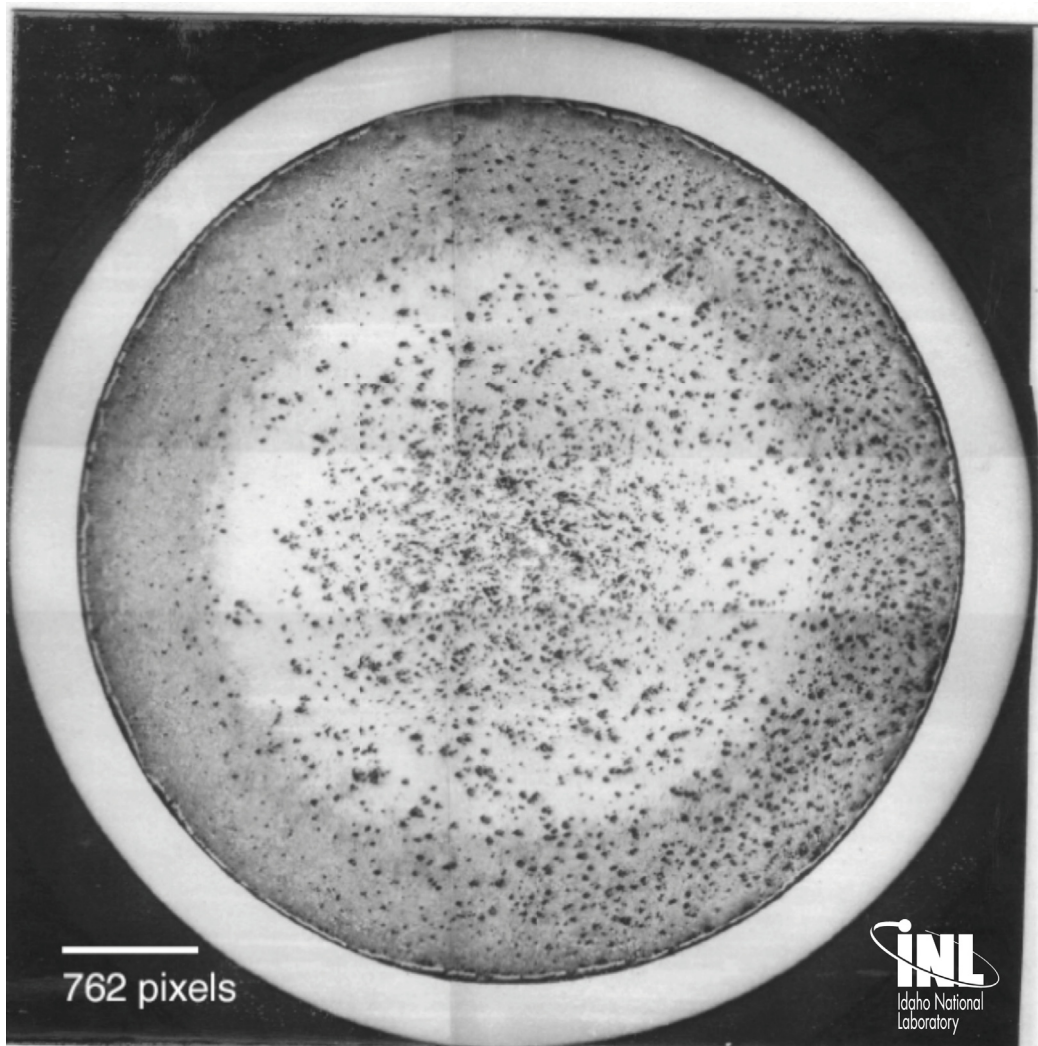


X447 Pin S/N	DP-04	MET Mount Number	
X/L	1.0	Analysis Date	
Distance from BOFP (inch) (cm)	15.0 38.1	Ave. PICT (°C)	652
Distance from BOFC (inch) (cm)	14.25 36.2	Ave. FCLT (°C)	703
Linear Power (W/cm)	165	Fission Density (fission/cm³)	1.87e21
FCCI (μm)	152.4	Burnup (at%)	5.3

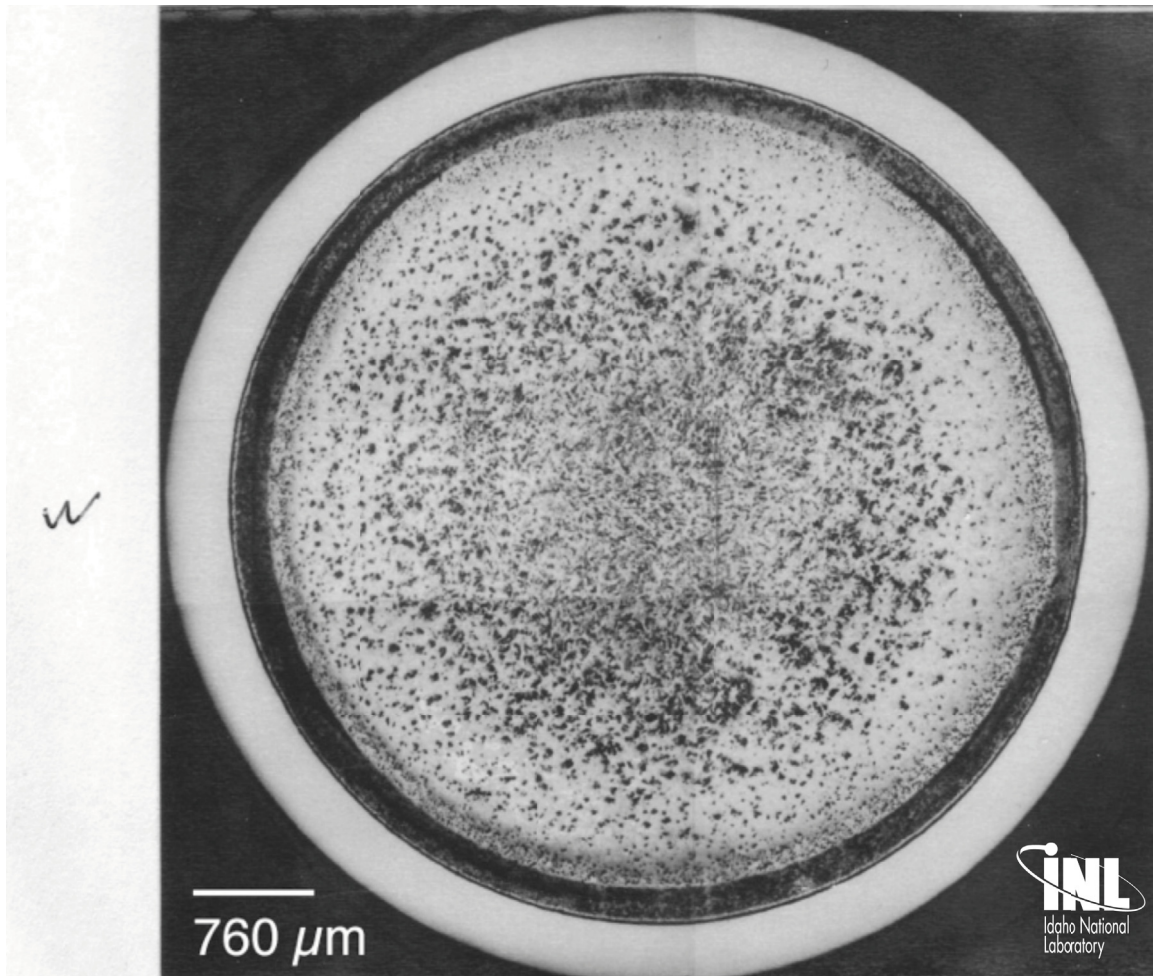


Appendix C - Metallographic Montages of X447 DP-70 Fuel Pin

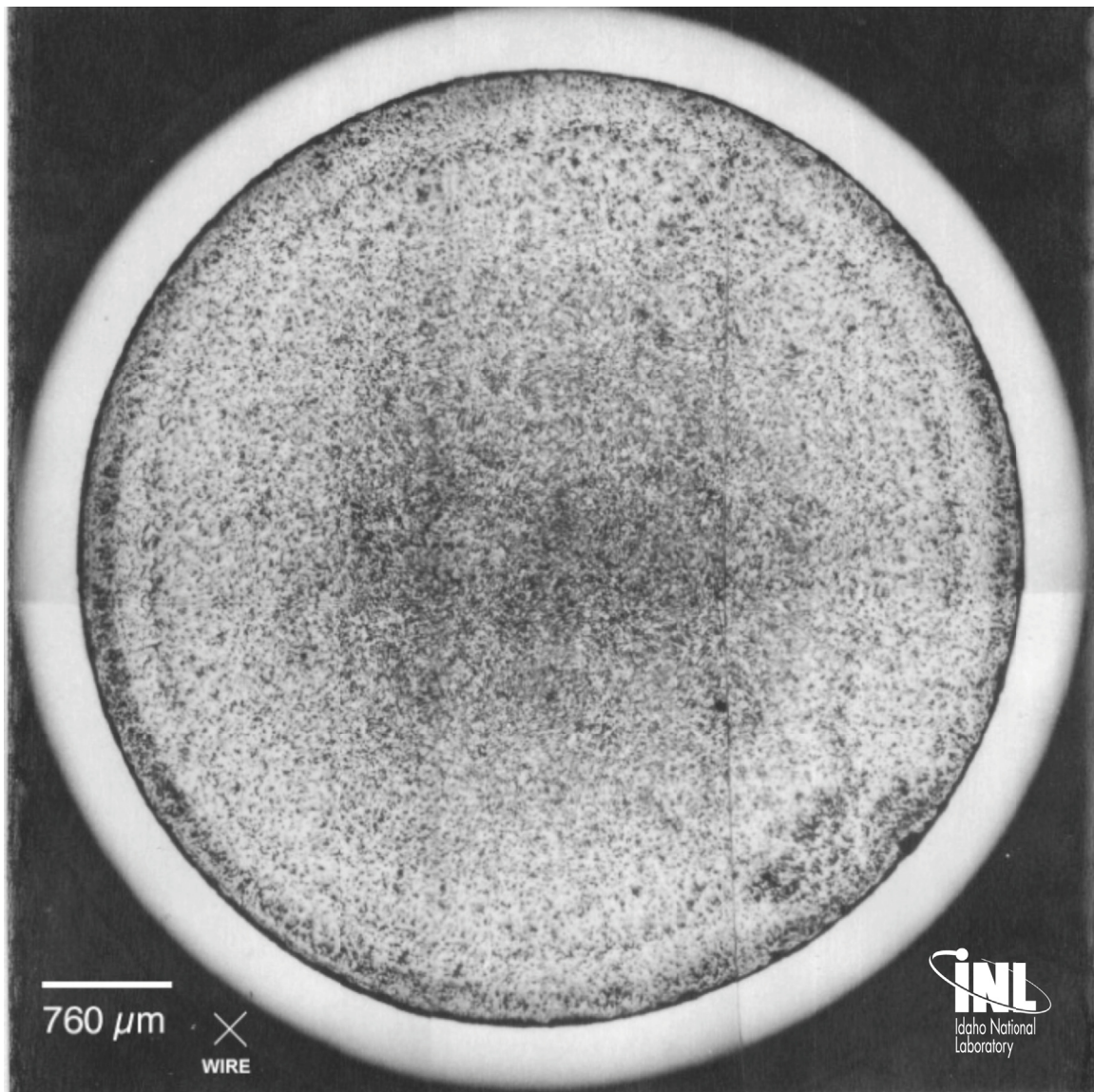
X447 Pin S/N	DP-70	MET Mount Number	
X/L	0.18	Analysis Date	
Distance from BOFP (inch) (cm)	3.5 8.9	Ave. PICT (°C)	457
Distance from BOFC (inch) (cm)	2.75 7.0	Ave. FCLT (°C)	563
Linear Power (W/cm)	319	Fission Density (fission/cm³)	3.62e21
FCCI (μm)	0	Burnup (at%)	10.2



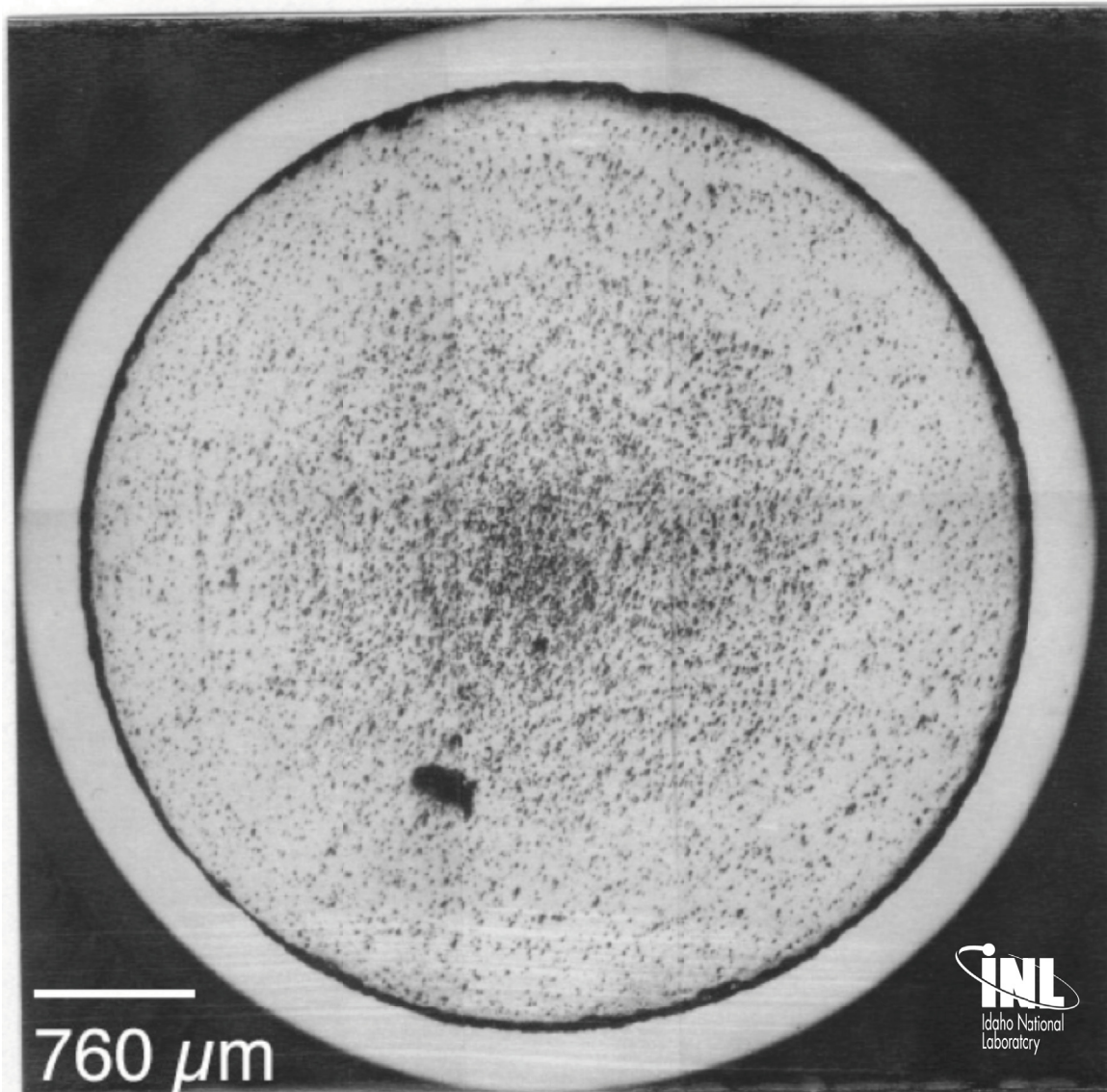
X447 Pin S/N	DP-70	MET Mount Number	
X/L	0.49	Analysis Date	
Distance from BOFP (inch) (cm)	7.5 19.1	Ave. PICT (°C)	543
Distance from BOFC (inch) (cm)	6.75 17.1	Ave. FCLT (°C)	648
Linear Power (W/cm)	333	Fission Density (fission/cm³)	3.78e21
FCCI (μm)	0	Burnup (at%)	10.7



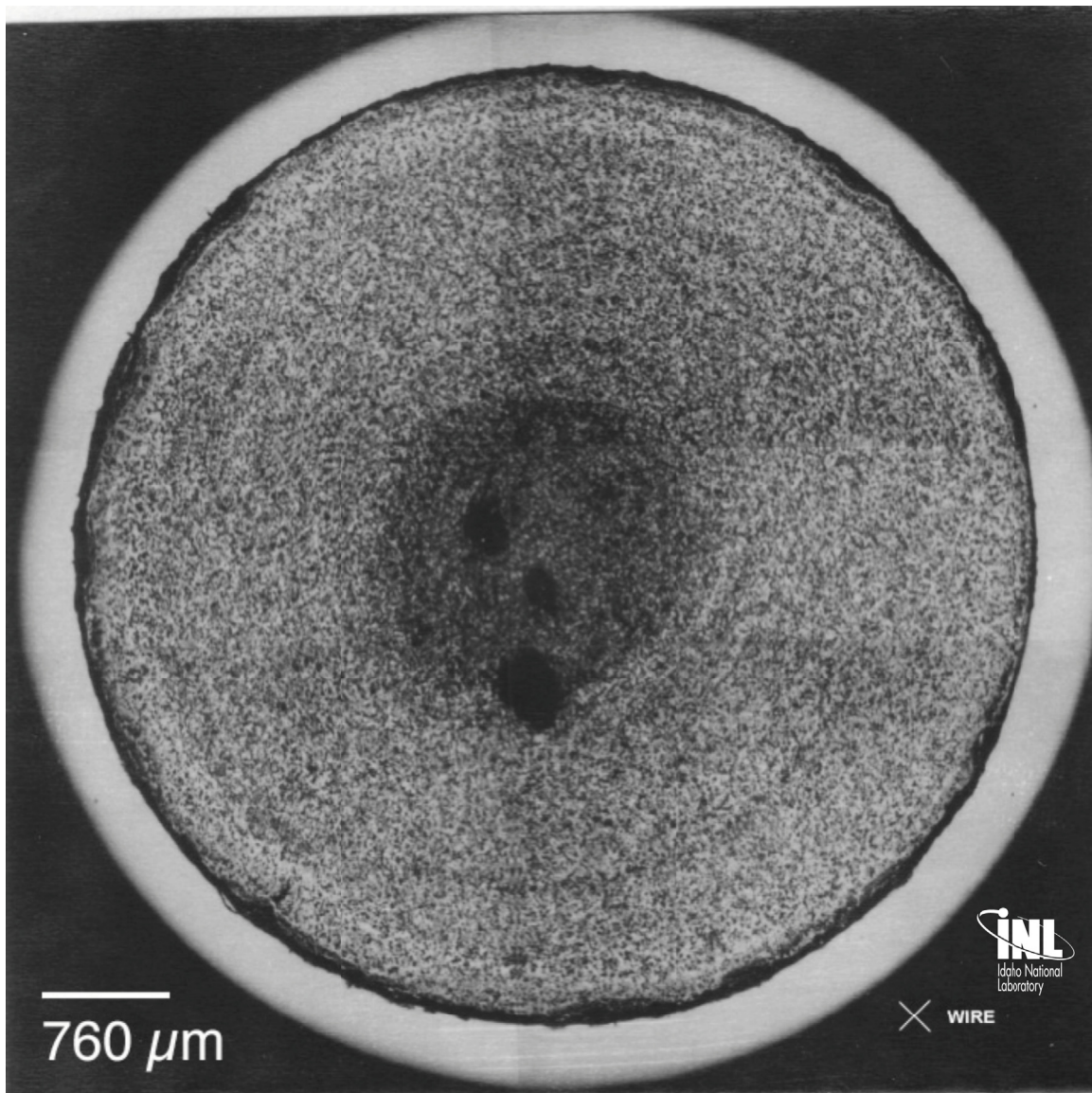
X447 Pin S/N	DP-70	MET Mount Number	
X/L	0.62	Analysis Date	
Distance from BOFP (inch) (cm)	9.75 24.8	Ave. PICT (°C)	582
Distance from BOFC (inch) (cm)	9.0 22.9	Ave. FCLT (°C)	677
Linear Power (W/cm)	309	Fission Density (fission/cm³)	3.51e21
FCCI (μm)	28	Burnup (at%)	9.9



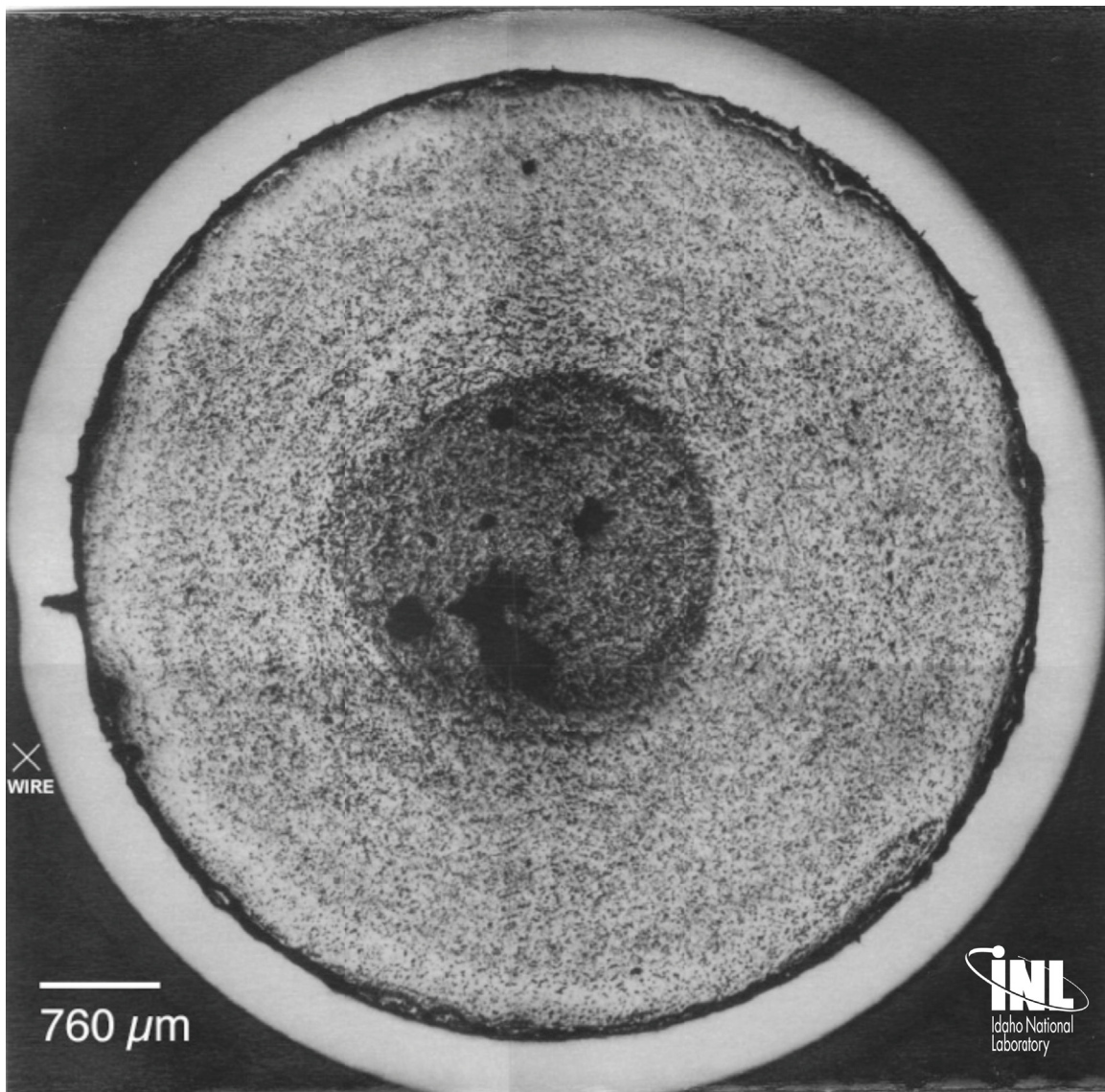
X447 Pin S/N	DP-70	MET Mount Number	
X/L	0.71	Analysis Date	
Distance from BOFP (inch) (cm)	10.75 27.3	Ave. PICT (°C)	599
Distance from BOFC (inch) (cm)	10.0 25.4	Ave. FCLT (°C)	688
Linear Power (W/cm)	291	Fission Density (fission/cm³)	3.31e21
FCCI (μm)	25.4	Burnup (at %)	9.4



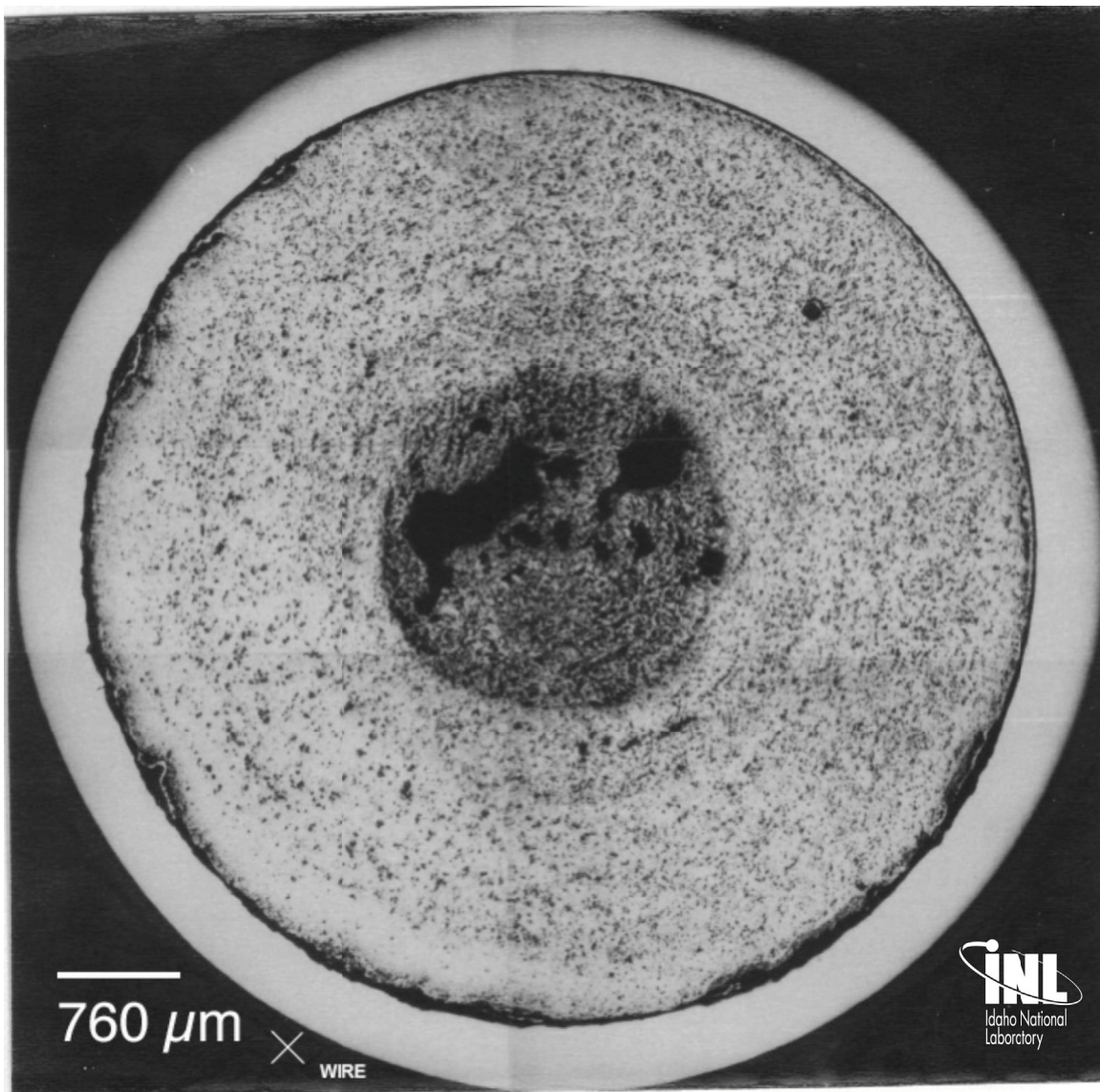
X447 Pin S/N	DP-70	MET Mount Number	
X/L	0.84	Analysis Date	
Distance from BOFP (inch) (cm)	12.85 32.6	Ave. PICT (°C)	628
Distance from BOFC (inch) (cm)	12.1 30.7	Ave. FCLT (°C)	700
Linear Power (W/cm)	242	Fission Density (fission/cm³)	2.75e21
FCCI (μm)	86.4	Burnup (at%)	7.7



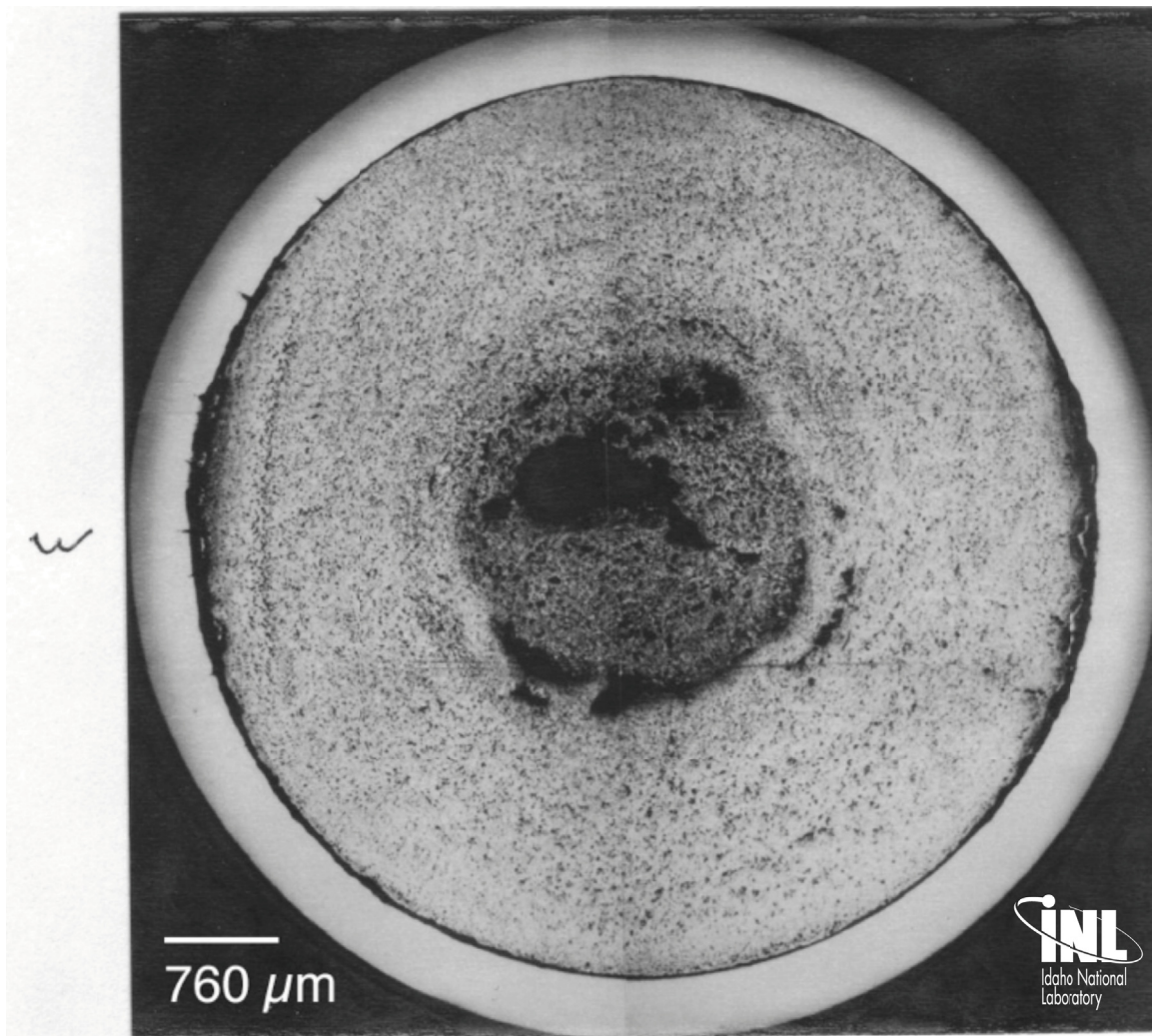
X447 Pin S/N	DP-70	MET Mount Number	
X/L	0.92	Analysis Date	
Distance from BOFP (inch) (cm)	14.0 35.6	Ave. PICT (°C)	639
Distance from BOFC (inch) (cm)	13.25 33.7	Ave. FCLT (°C)	702
Linear Power (W/cm)	211	Fission Density (fission/cm³)	2.40e21
FCCI (μm)	116.8	Burnup (at%)	6.8



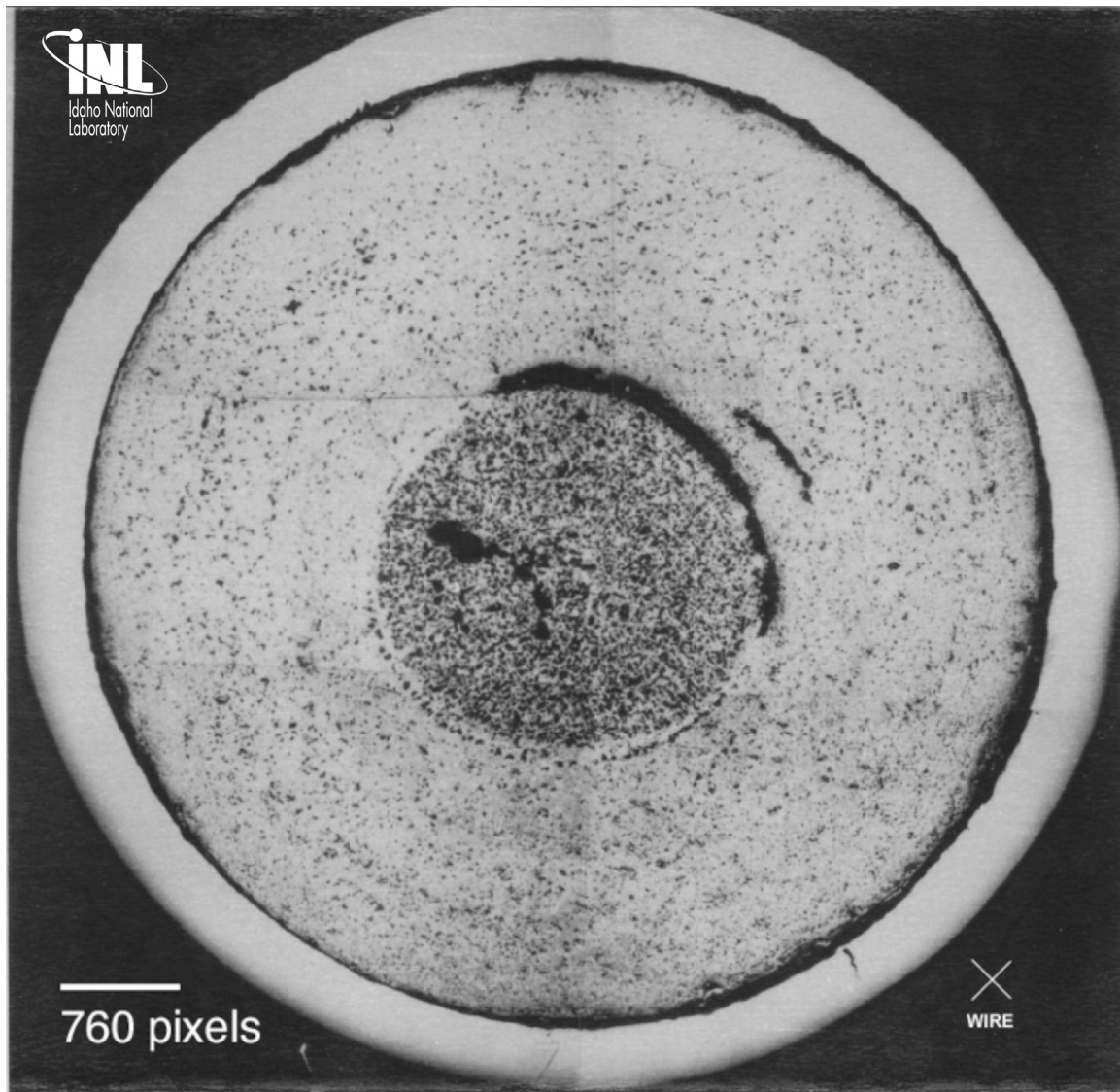
X447 Pin S/N	DP-70	MET Mount Number	
X/L	0.94	Analysis Date	
Distance from BOFP (inch) (cm)	14.25 36.2	Ave. PICT (°C)	641
Distance from BOFC (inch) (cm)	13.5 34.3	Ave. FCLT (°C)	702
Linear Power (W/cm)	203	Fission Density (fission/cm³)	2.31e21
FCCI (μm)	96.5	Burnup (at%)	6.5



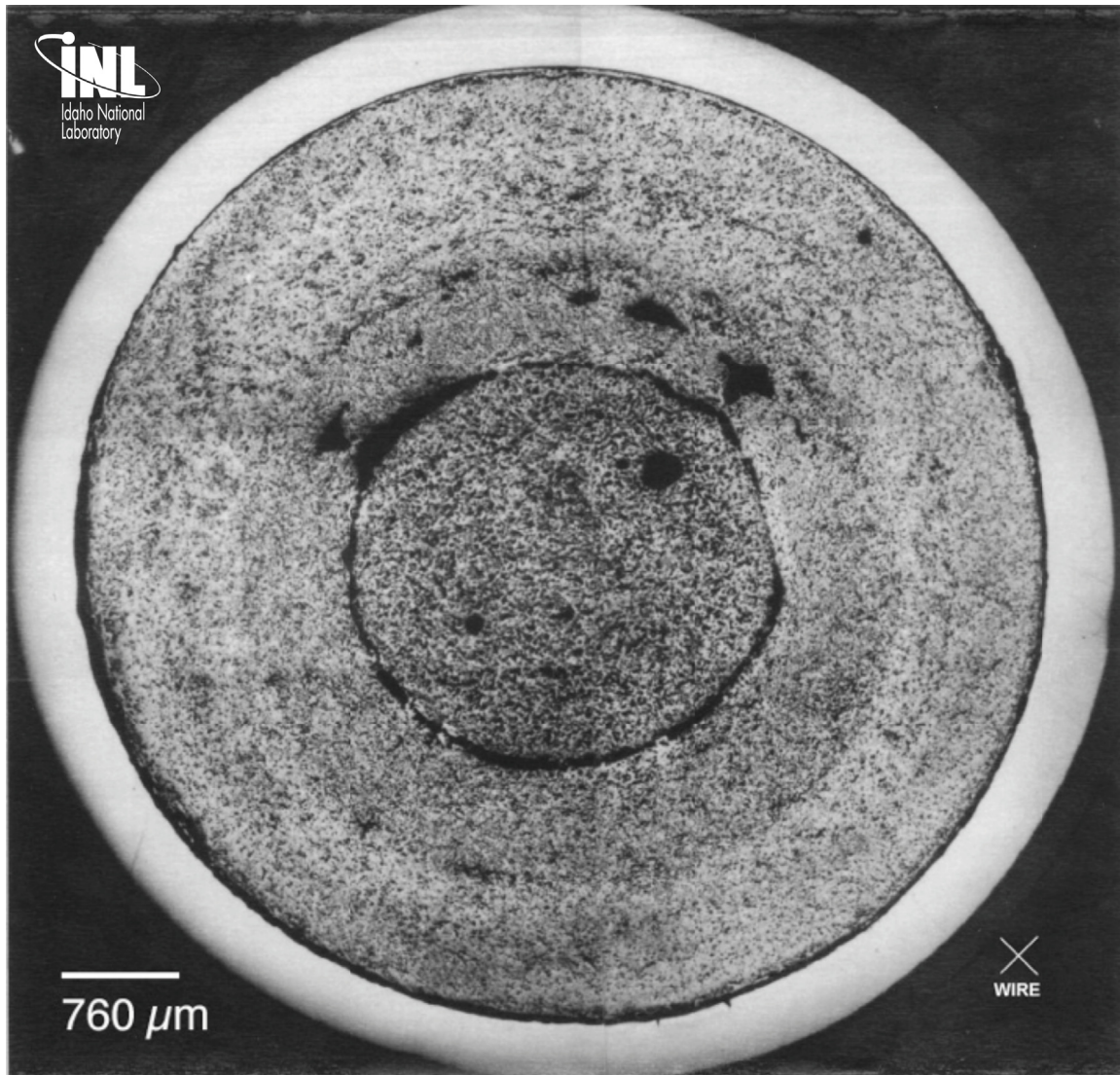
X447 Pin S/N	DP-70	MET Mount Number	
X/L	0.95	Analysis Date	
Distance from BOFP (inch) (cm)	14.5 36.8	Ave. PICT (°C)	643
Distance from BOFC (inch) (cm)	13.75 34.9	Ave. FCLT (°C)	702
Linear Power (W/cm)	195	Fission Density (fission/cm³)	2.21e21
FCCI (μm)	91.4	Burnup (at%)	6.3



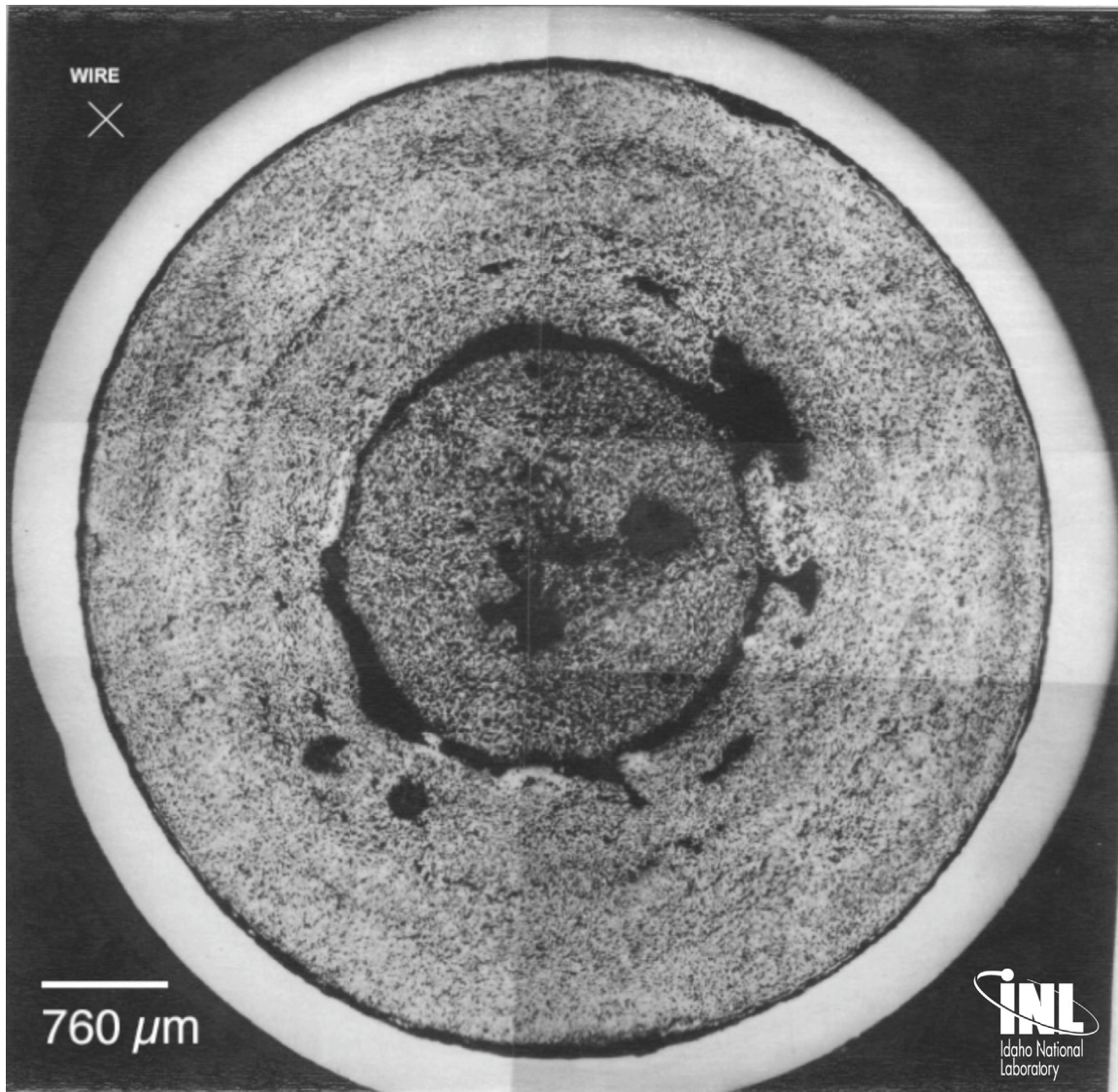
X447 Pin S/N	DP-70	MET Mount Number	
X/L	0.97	Analysis Date	
Distance from BOFP (inch) (cm)	14.75 37.5	Ave. PICT (°C)	644
Distance from BOFC (inch) (cm)	14.0 35.6	Ave. FCLT (°C)	701
Linear Power (W/cm)	191	Fission Density (fission/cm³)	2.69e21
FCCI (μm)	127	Burnup (at%)	6.1



X447 Pin S/N	DP-70	MET Mount Number	
X/L	0.98	Analysis Date	
Distance from BOFP (inch) (cm)	15.0 38.1	Ave. PICT (°C)	645
Distance from BOFC (inch) (cm)	14.25 36.2	Ave. FCLT (°C)	701
Linear Power (W/cm)	186	Fission Density (fission/cm³)	2.12e21
FCCI (μm)	140	Burnup (at%)	6.0

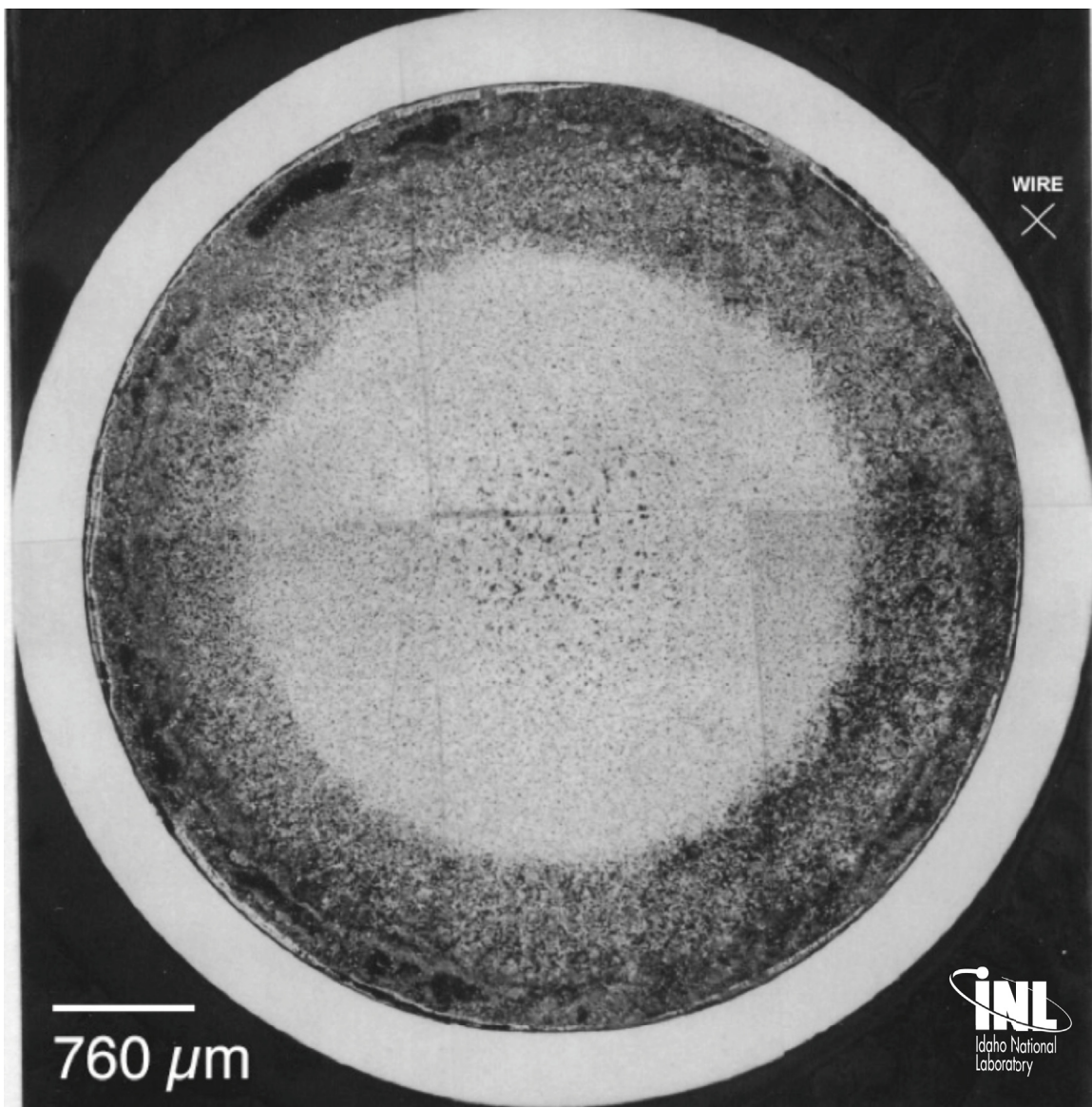


X447 Pin S/N	DP-70	MET Mount Number	
X/L	1.0	Analysis Date	
Distance from BOFP (inch) (cm)	15.25 38.7	Ave. PICT (°C)	647
Distance from BOFC (inch) (cm)	14.5 36.8	Ave. FCLT (°C)	700
Linear Power (W/cm)	186	Fission Density (fission/cm³)	2.02e21
FCCI (μm)	89	Burnup (at%)	5.7

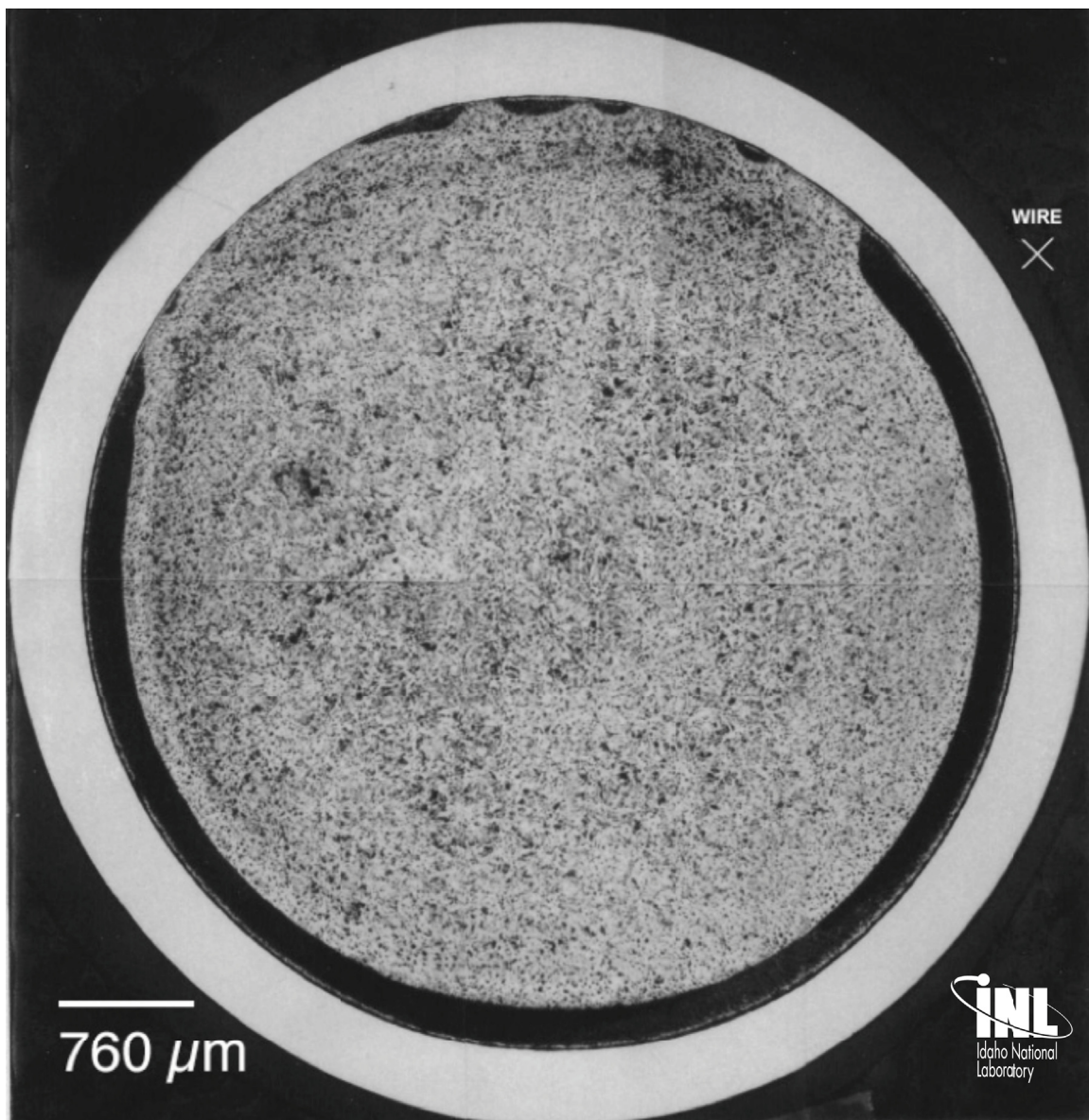


Appendix D - Metallographic Montages of X447 DP-75 Fuel Pin

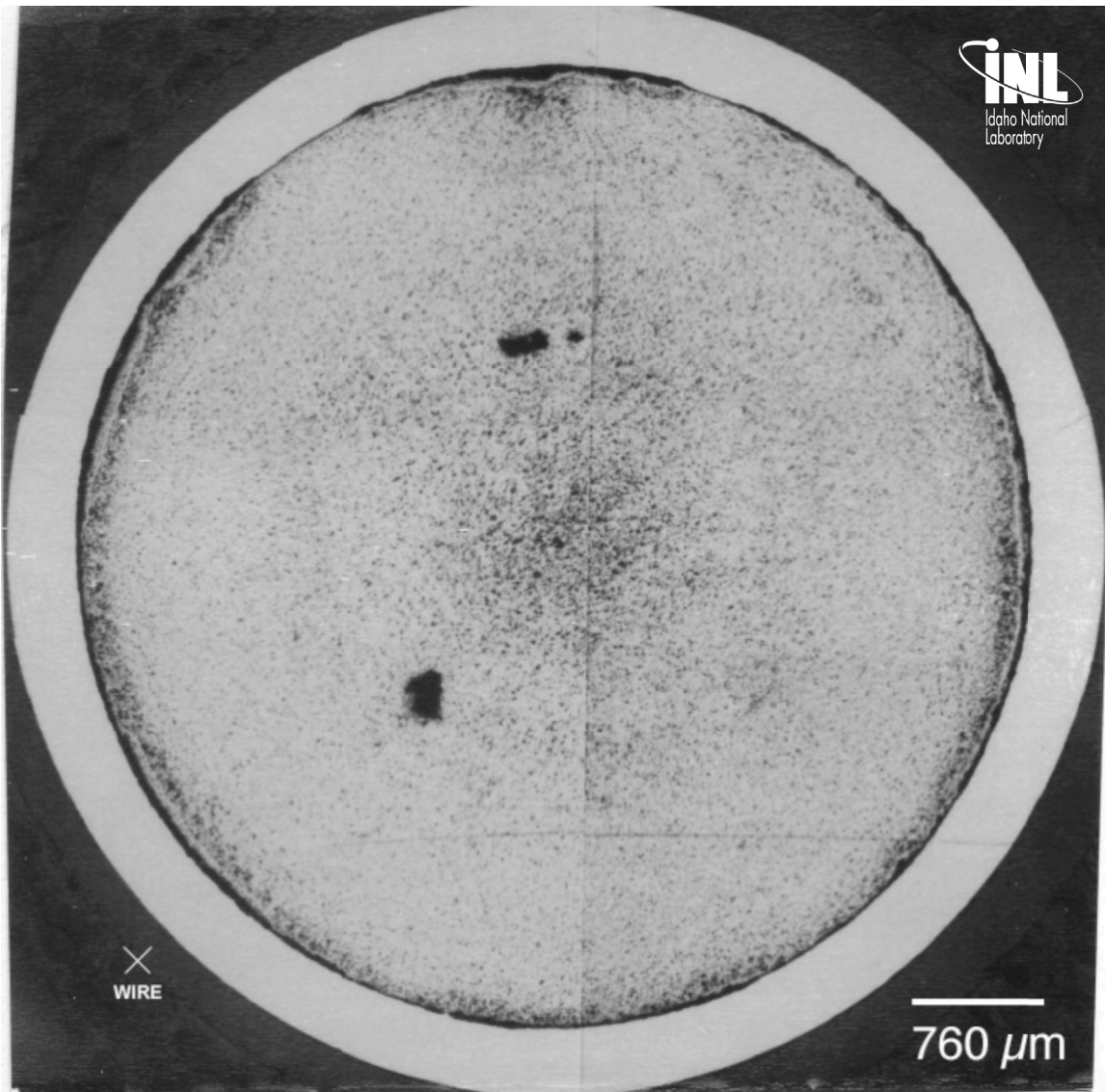
X447 Pin S/N	DP-75	MET Mount Number	
X/L	0.19	Analysis Date	
Distance from BOFP (inch) (cm)	3.5 8.89	Ave. PICT (°C)	457
Distance from BOFC (inch) (cm)	2.75 7.0	Ave. FCLT (°C)	581
Linear Power (W/cm)	329	Fission Density (fission/cm³)	3.62e21
FCCI (μm)	0	Burnup (at %)	10.2



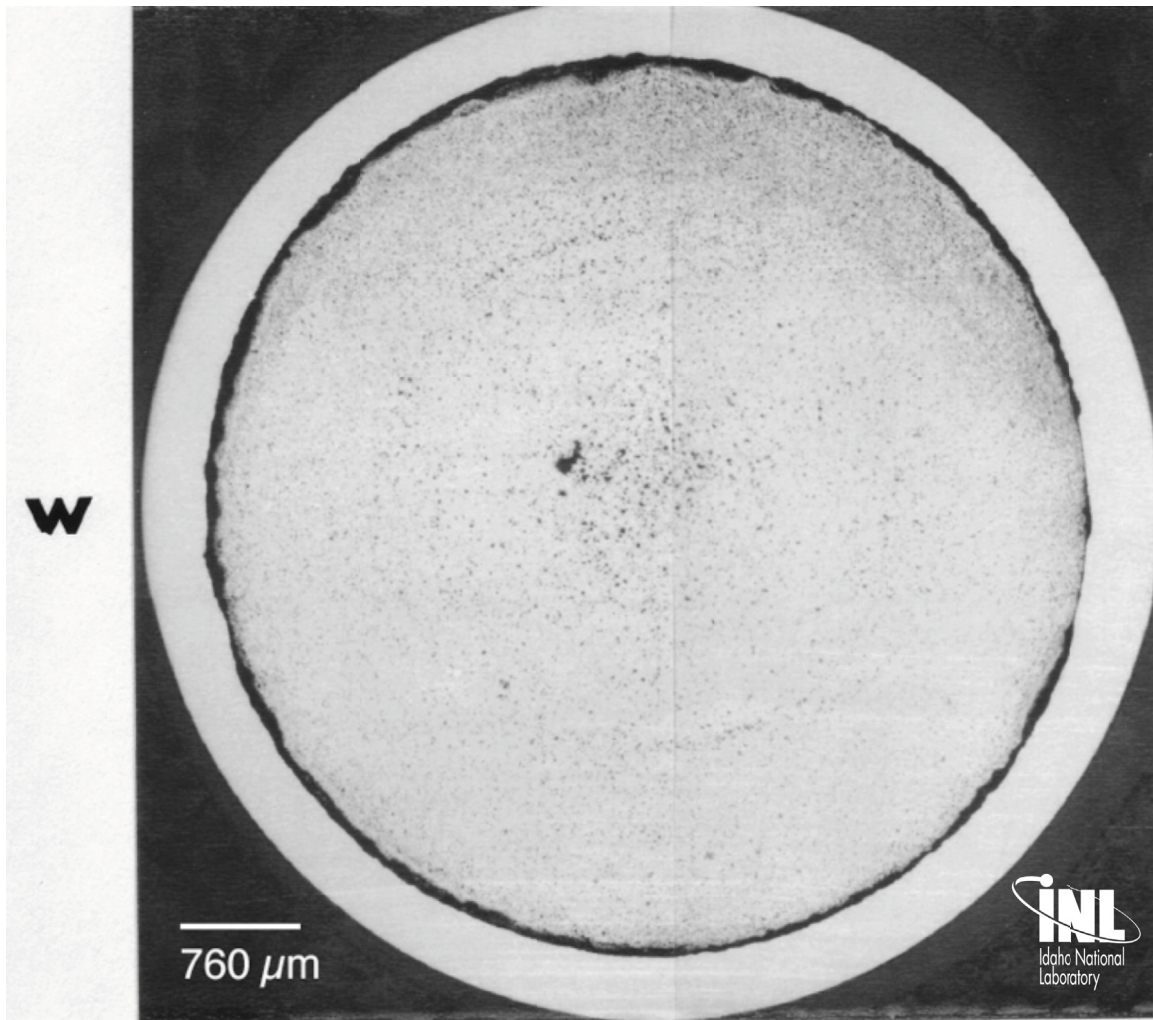
X447 Pin S/N	DP-75	MET Mount Number	
X/L	0.44	Analysis Date	
Distance from BOFP (inch) (cm)	7.5 19.1	Ave. PICT (°C)	533
Distance from BOFC (inch) (cm)	6.75 17.1	Ave. FCLT (°C)	659
Linear Power (W/cm)	346	Fission Density (fission/cm³)	3.81e21
FCCI (μm)	12.7	Burnup (at%)	10.8



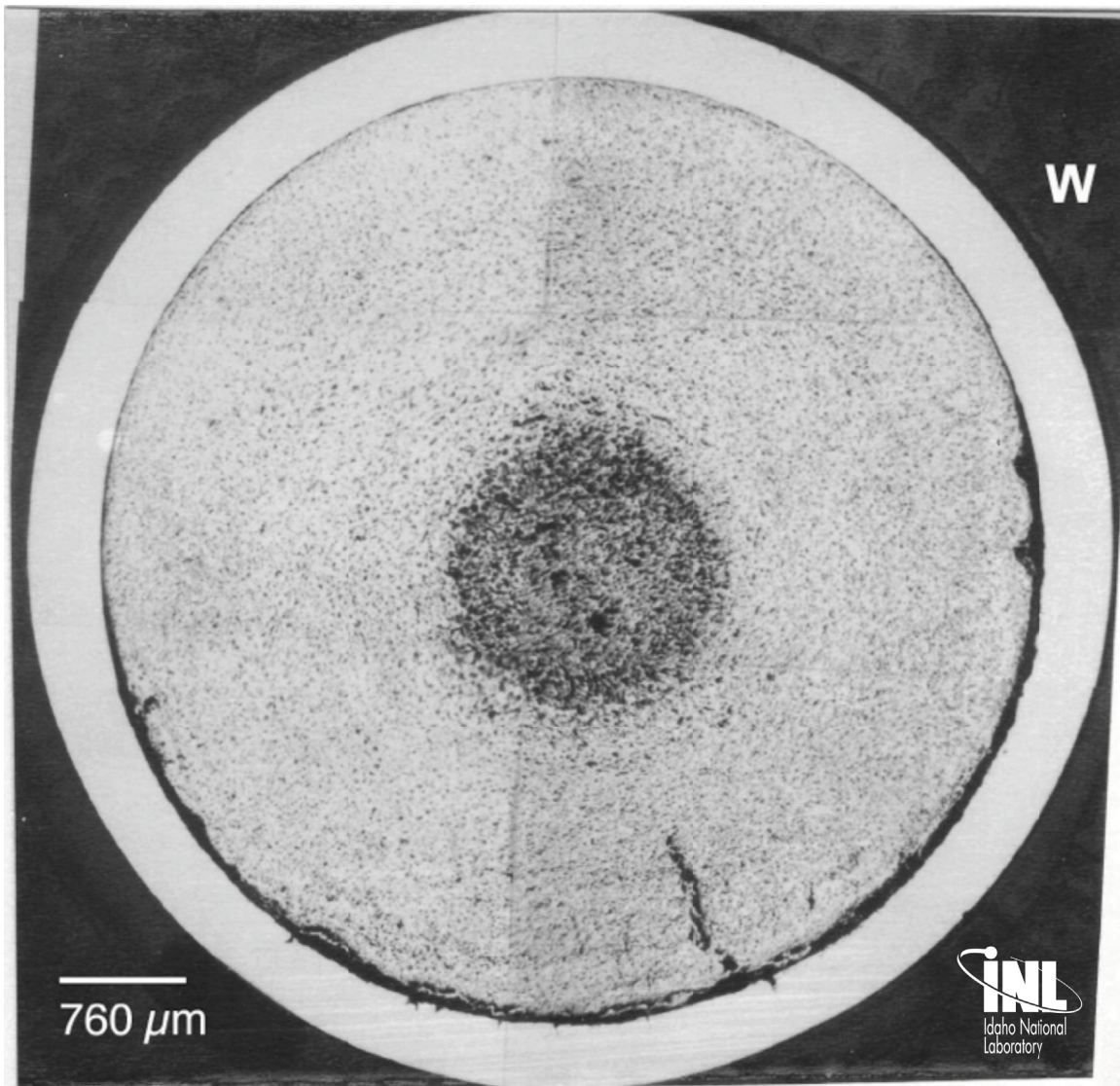
X447 Pin S/N	DP-75	MET Mount Number	
X/L	0.68	Analysis Date	
Distance from BOFP (inch) (cm)	10.75 27.3	Ave. PICT (°C)	596
Distance from BOFC (inch) (cm)	10.0 25.4	Ave. FCLT (°C)	707
Linear Power (W/cm)	305	Fission Density (fission/cm³)	3.36e21
FCCI (μm)	12.7	Burnup (at%)	9.5



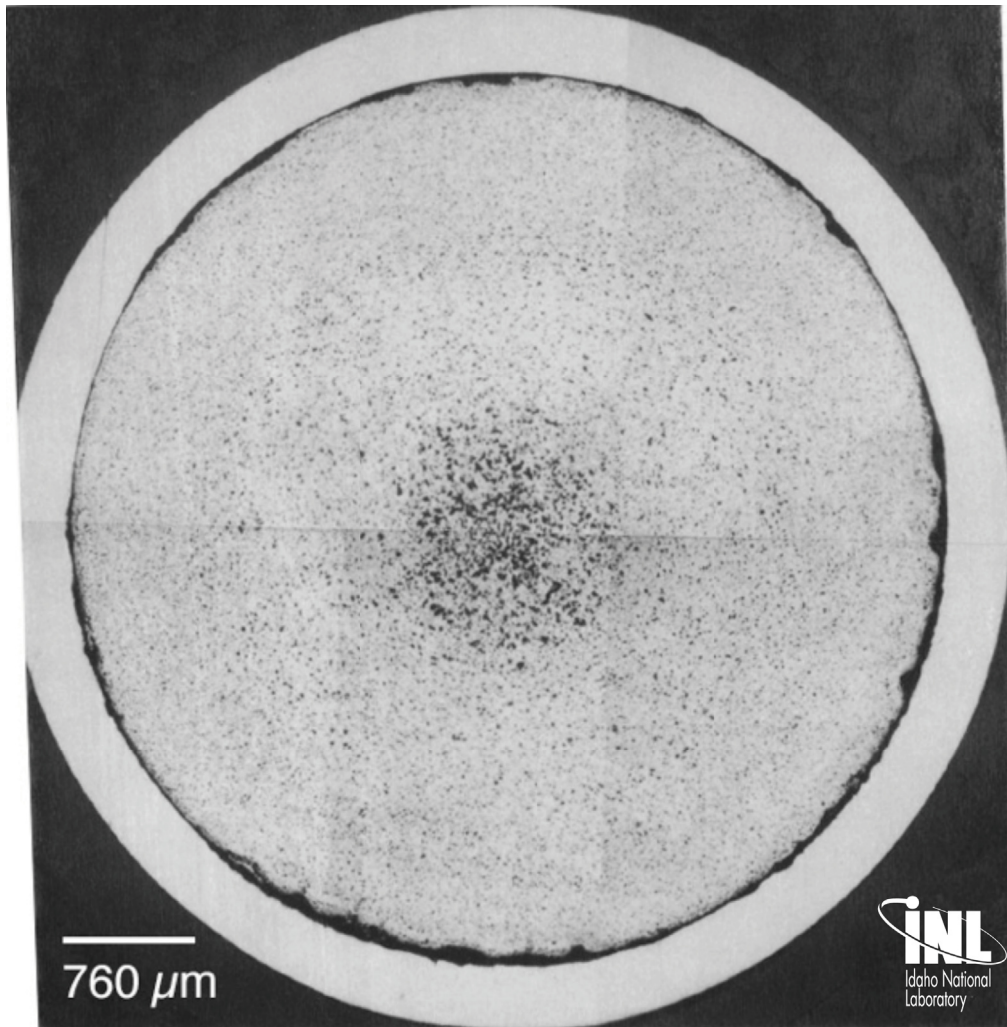
X447 Pin S/N	DP-75	MET Mount Number	
X/L	0.81	Analysis Date	
Distance from BOFP (inch) (cm)	12.75 32.4	Ave. PICT (°C)	622
Distance from BOFC (inch) (cm)	12.0 30.5	Ave. FCLT (°C)	721
Linear Power (W/cm)	264	Fission Density (fission/cm³)	2.90e21
FCCI (μm)	63.5	Burnup (at %)	8.2



X447 Pin S/N	DP-75	MET Mount Number	
X/L	0.90	Analysis Date	
Distance from BOFP (inch) (cm)	14.0 35.6	Ave. PICT (°C)	635
Distance from BOFC (inch) (cm)	13.25 33.7	Ave. FCLT (°C)	724
Linear Power (W/cm)	234	Fission Density (fission/cm³)	2.58e21
FCCI (μm)	127	Burnup (at%)	7.3

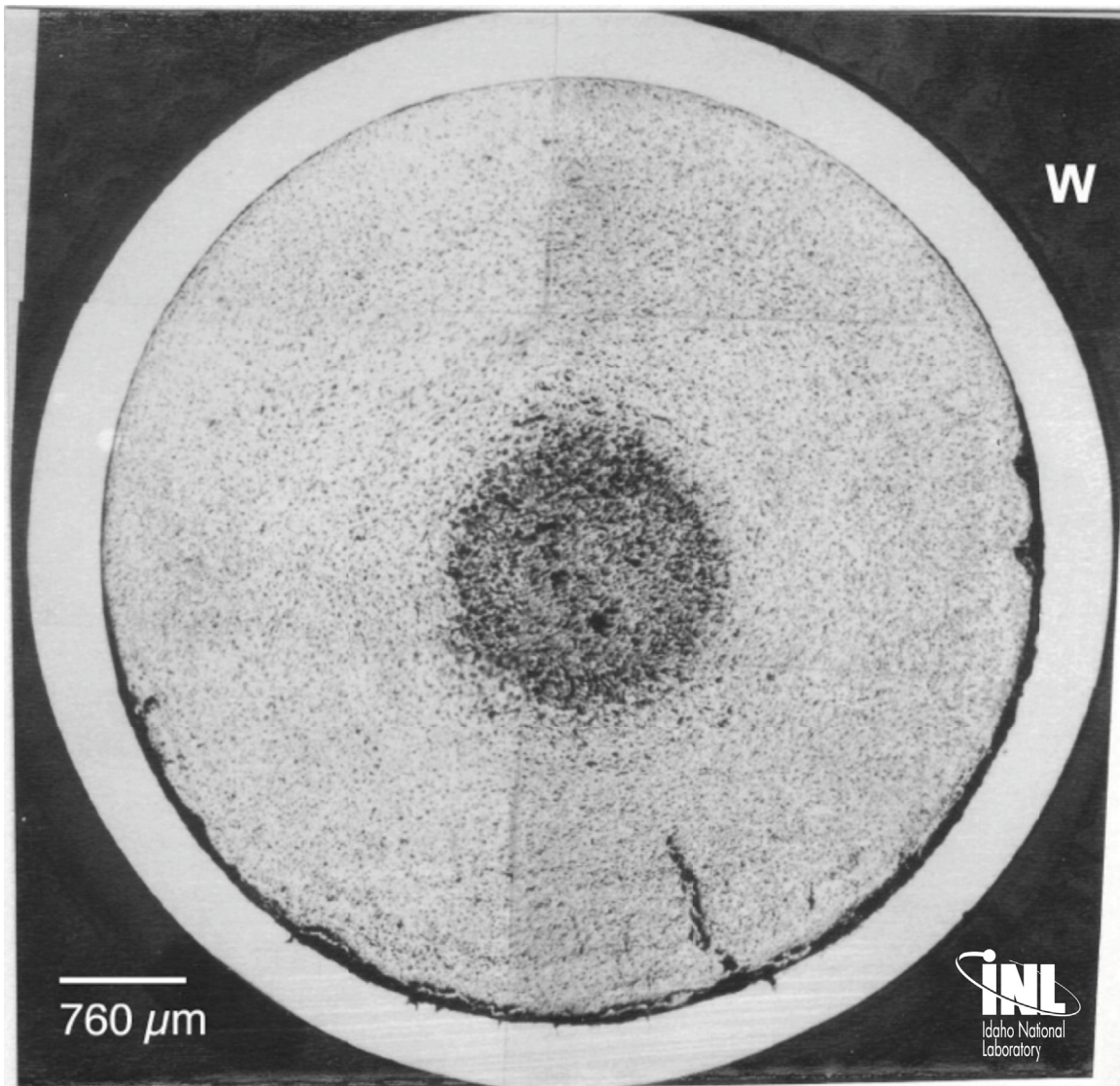


X447 Pin S/N	DP-75	MET Mount Number	
X/L	0.91	Analysis Date	
Distance from BOFP (inch) (cm)	14.25 36.2	Ave. PICT (°C)	637
Distance from BOFC (inch) (cm)	13.5 34.3	Ave. FCLT (°C)	724
Linear Power (W/cm)	226	Fission Density (fission/cm³)	2.49e21
FCCI (μm)	127	Burnup (at %)	7.0

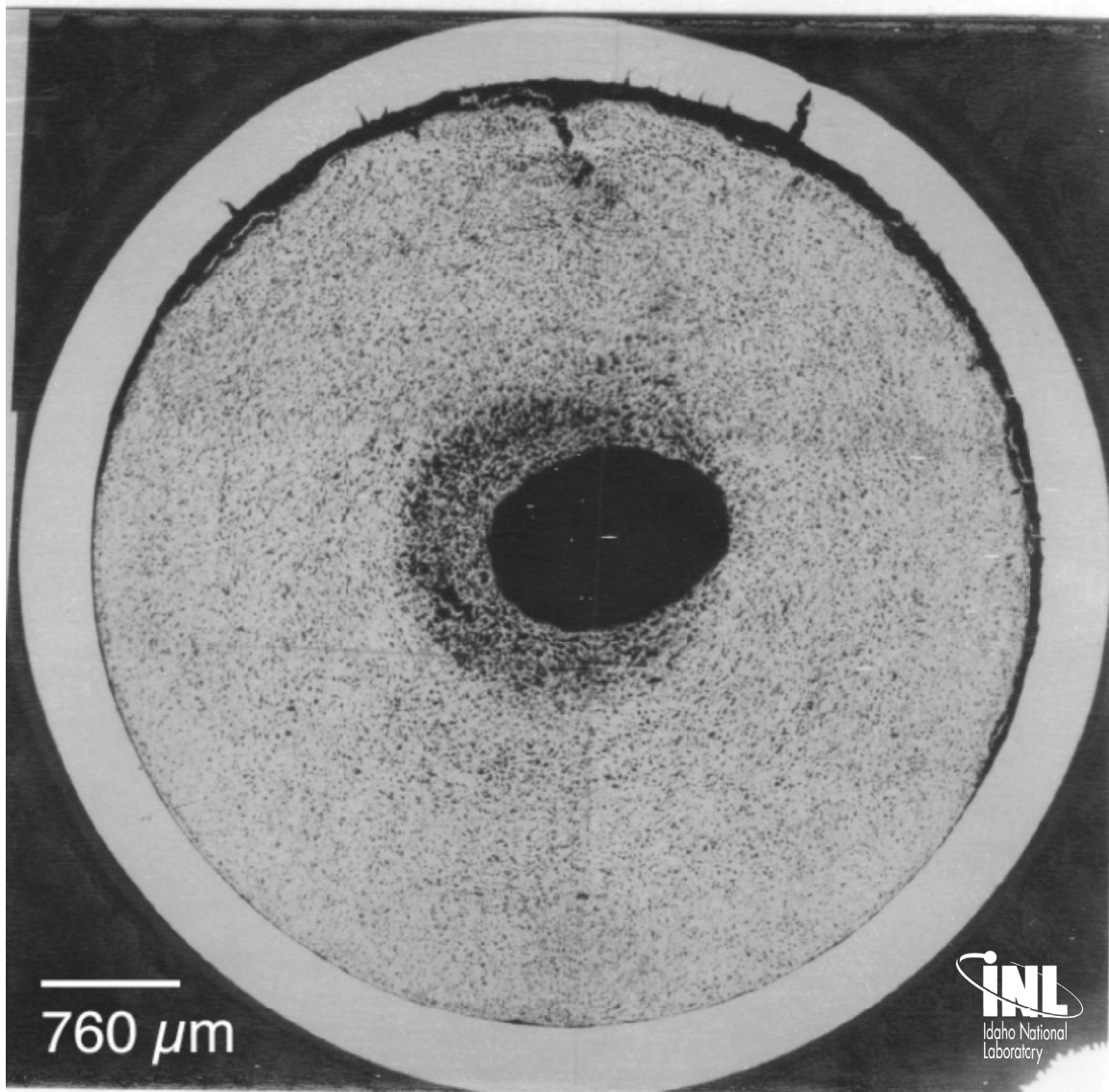


W

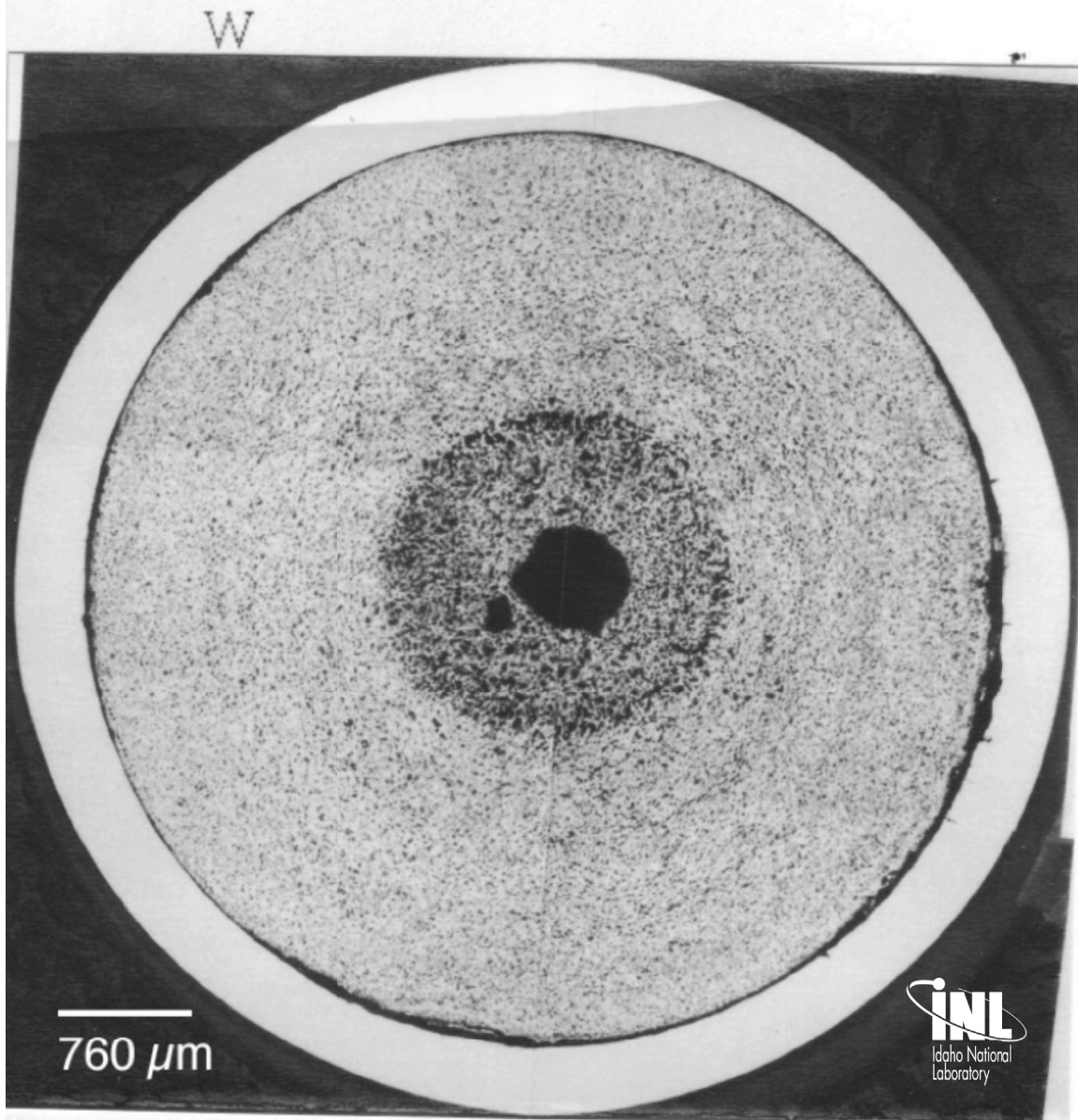
X447 Pin S/N	DP-75	MET Mount Number	
X/L	0.93	Analysis Date	
Distance from BOFP (inch) (cm)	14.5 36.8	Ave. PICT (°C)	640
Distance from BOFC (inch) (cm)	13.75 34.9	Ave. FCLT (°C)	725
Linear Power (W/cm)	218	Fission Density (fission/cm³)	2.40e21
FCCI (μm)	133	Burnup (at%)	6.8



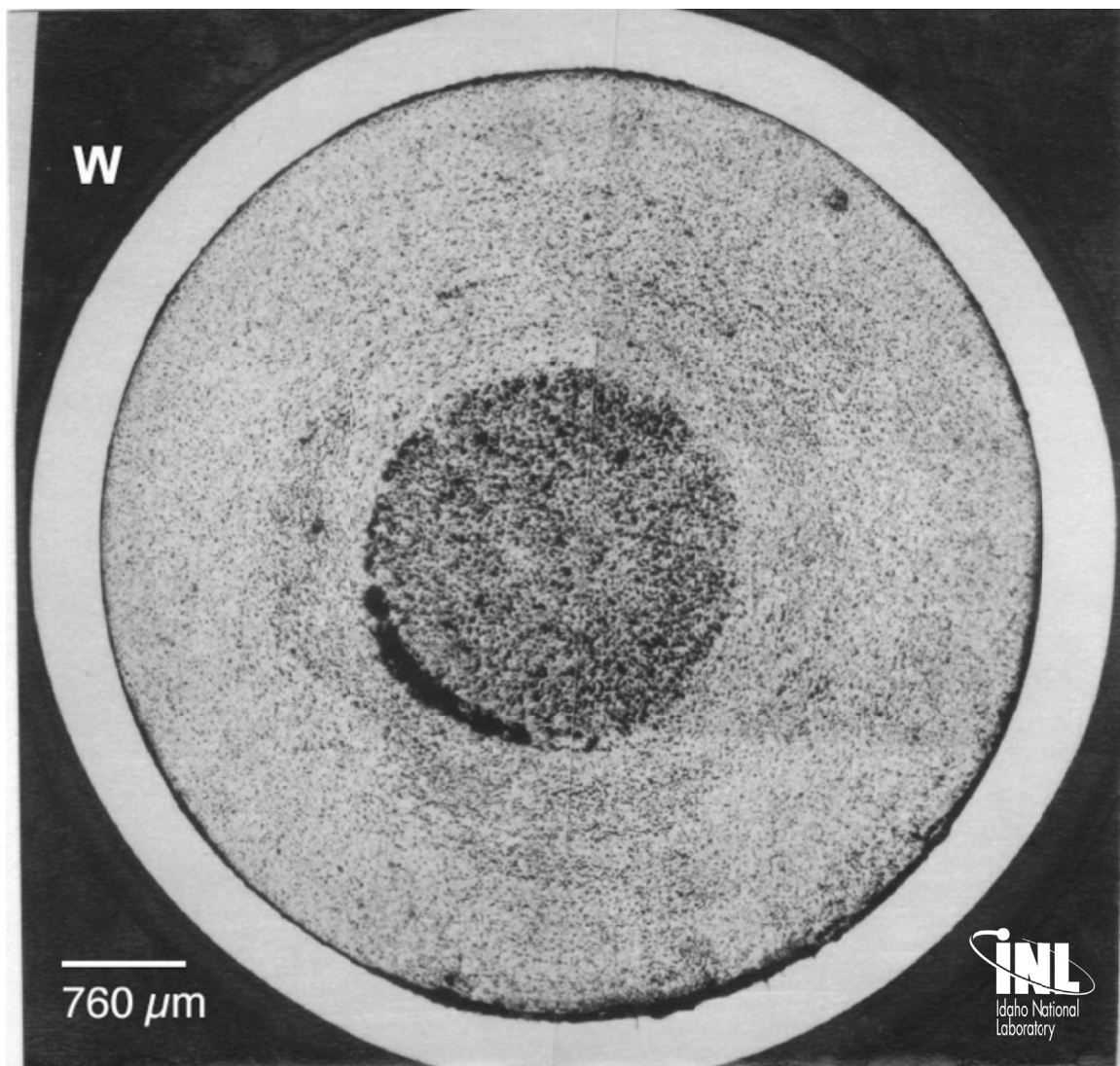
X447 Pin S/N	DP-75	MET Mount Number	
X/L	0.94	Analysis Date	
Distance from BOFP (inch) (cm)	14.75 37.5	Ave. PICT (°C)	648
Distance from BOFC (inch) (cm)	14.0 35.6	Ave. FCLT (°C)	699
Linear Power (W/cm)	210	Fission Density (fission/cm³)	2.31e21
FCCI (μm)	139	Burnup (at %)	6.8



X447 Pin S/N	DP-75	MET Mount Number	
X/L	0.96	Analysis Date	
Distance from BOFP (inch) (cm)	15.0 38.1	Ave. PICT (°C)	644
Distance from BOFC (inch) (cm)	14.25 36.1	Ave. FCLT (°C)	724
Linear Power (W/cm)	201	Fission Density (fission/cm³)	2.21e21
FCCI (μm)	146	Burnup (at %)	6.3

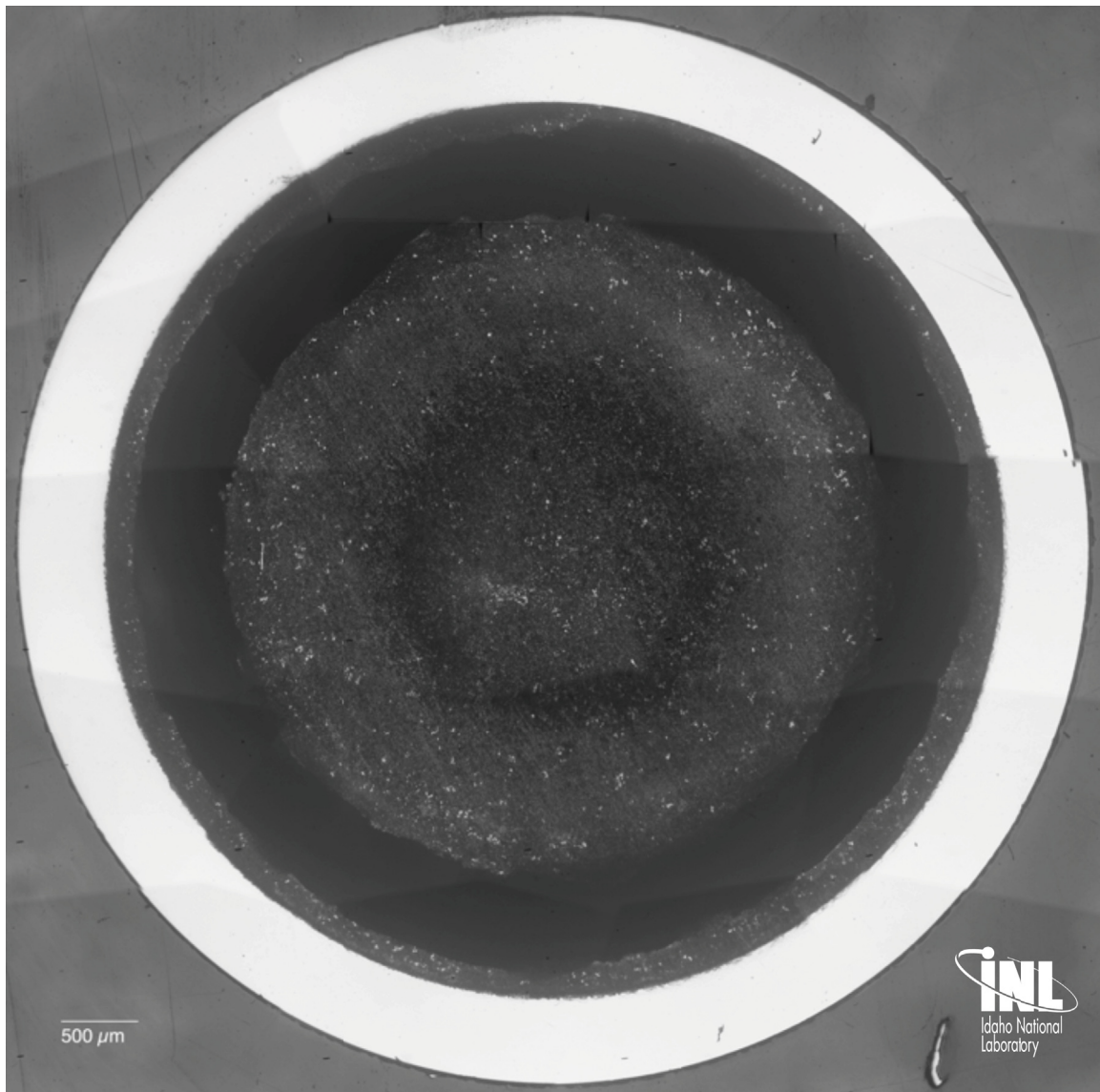


X447 Pin S/N	DP-75	MET Mount Number	
X/L	0.98	Analysis Date	
Distance from BOFP (inch) (cm)	15.25 38.7	Ave. PICT (°C)	640
Distance from BOFC (inch) (cm)	14.5 36.8	Ave. FCLT (°C)	724
Linear Power (W/cm)	192	Fission Density (fission/cm³)	2.12e21
FCCI (μm)	152	Burnup (at%)	7.4



Appendix E - Metallographic Montages of MFF-3 and MFF5 Fuel Pins

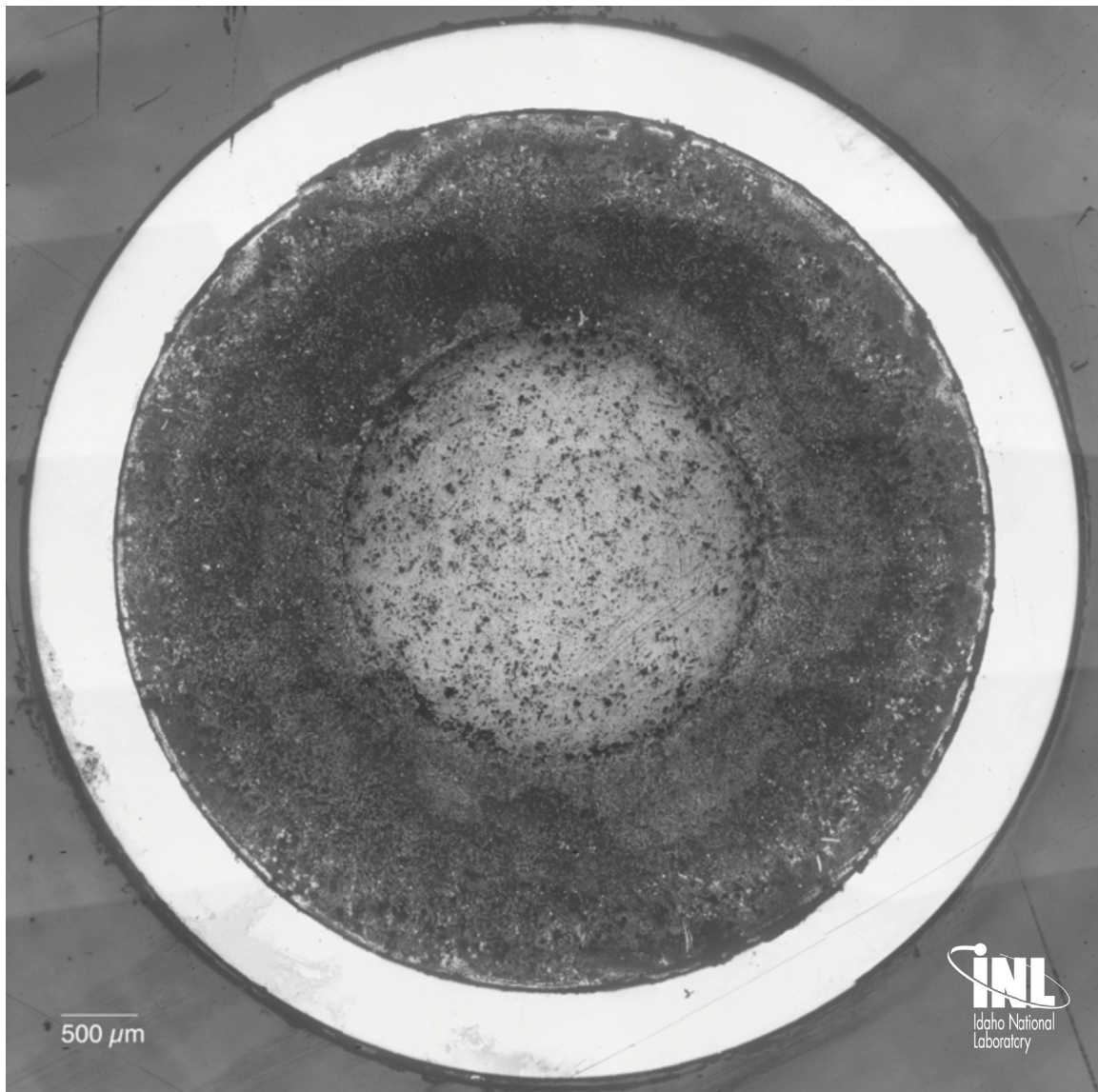
MFF 5 Pin S/N	195011	MET Mount Number	84T
X/L	0.03	Analysis Date	20110728
Distance from BOFP (inch) (cm)	4.75 12.1	Ave. PICT (°C)	414
Distance from BOFC (inch) (cm)	1 2.54	Ave. FCLT (°C)	532
Linear Power (W/cm)	345	Fission Density (fission/cm³)	2.37e21
FCCI (μm)	0	Burnup (at%)	6.7



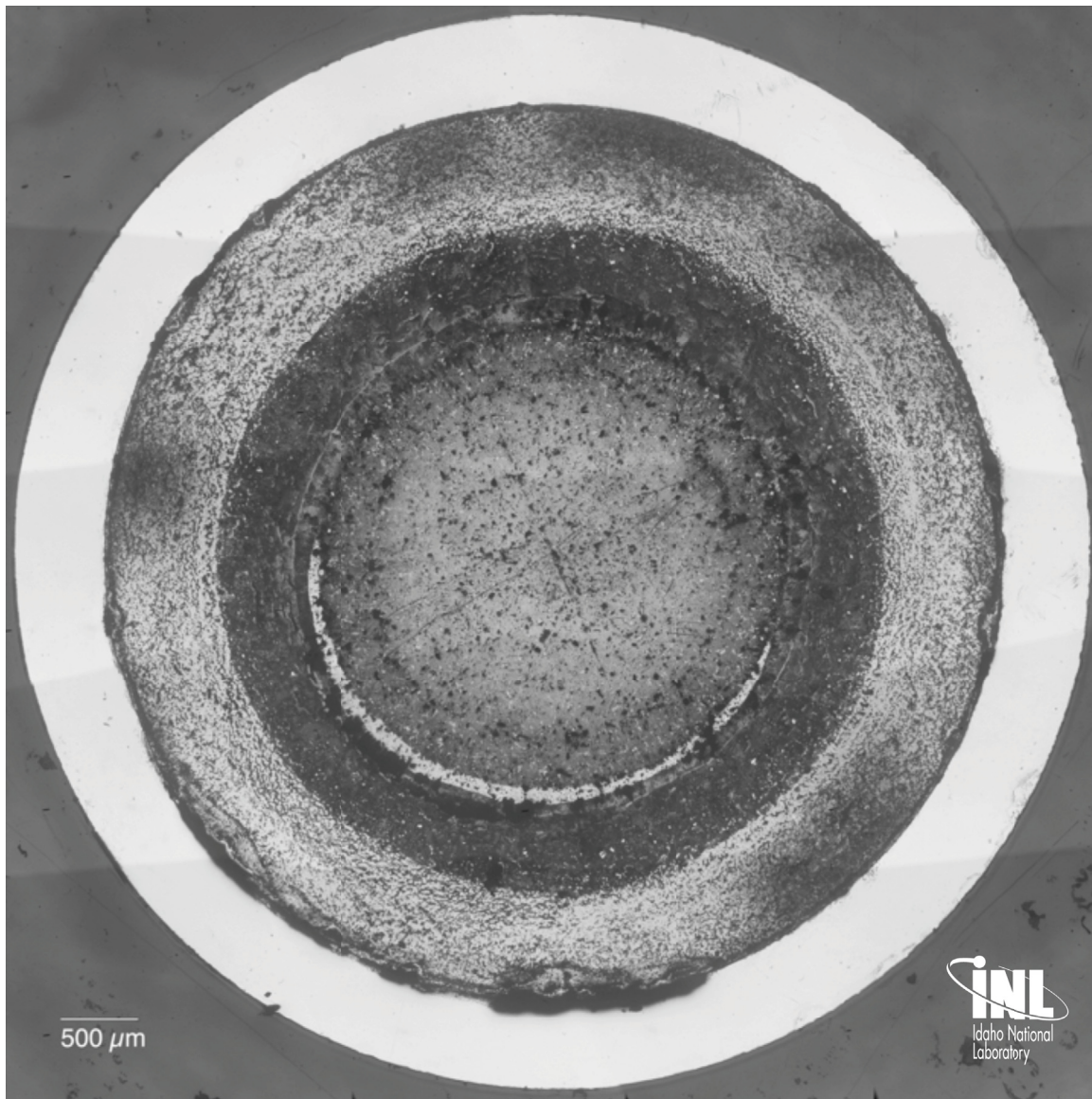
MFF 5 Pin S/N	195011	MET Mount Number	85T
X/L	0.24	Analysis Date	20110802
Distance from BOFP (inch) (cm)	12.75 32.4	Ave. ICT (°C)	480
Distance from BOFC (inch) (cm)	9.0 22.9	Ave. FCLT (°C)	628
Linear Power (W/cm)	461	Fission Density (fission/cm³)	3.17e21
FCCI (μm)	0	Burnup (at%)	8.9



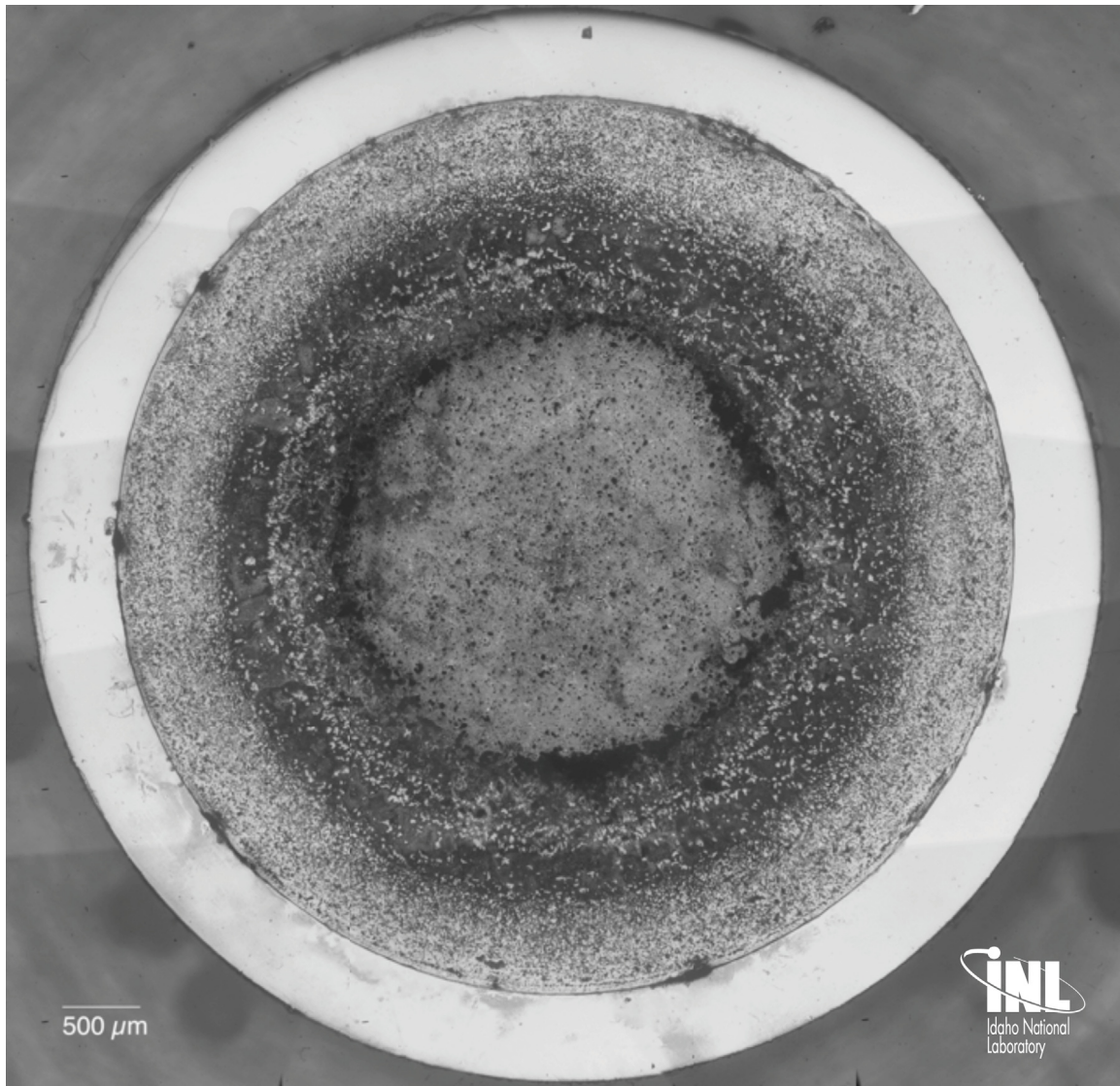
MFF 5 Pin S/N	195011	MET Mount Number	86T
X/L	0.48	Analysis Date	20110803
Distance from BOFP (inch) (cm)	21.75 55.24	Ave. PICT (°C)	556
Distance from BOFC (inch) (cm)	18.0 45.72	Ave. FCLT (°C)	712
Linear Power (W/cm)	507	Fission Density (fission/cm³)	3.49e21
FCCI (μm)	0	Burnup (at%)	9.8



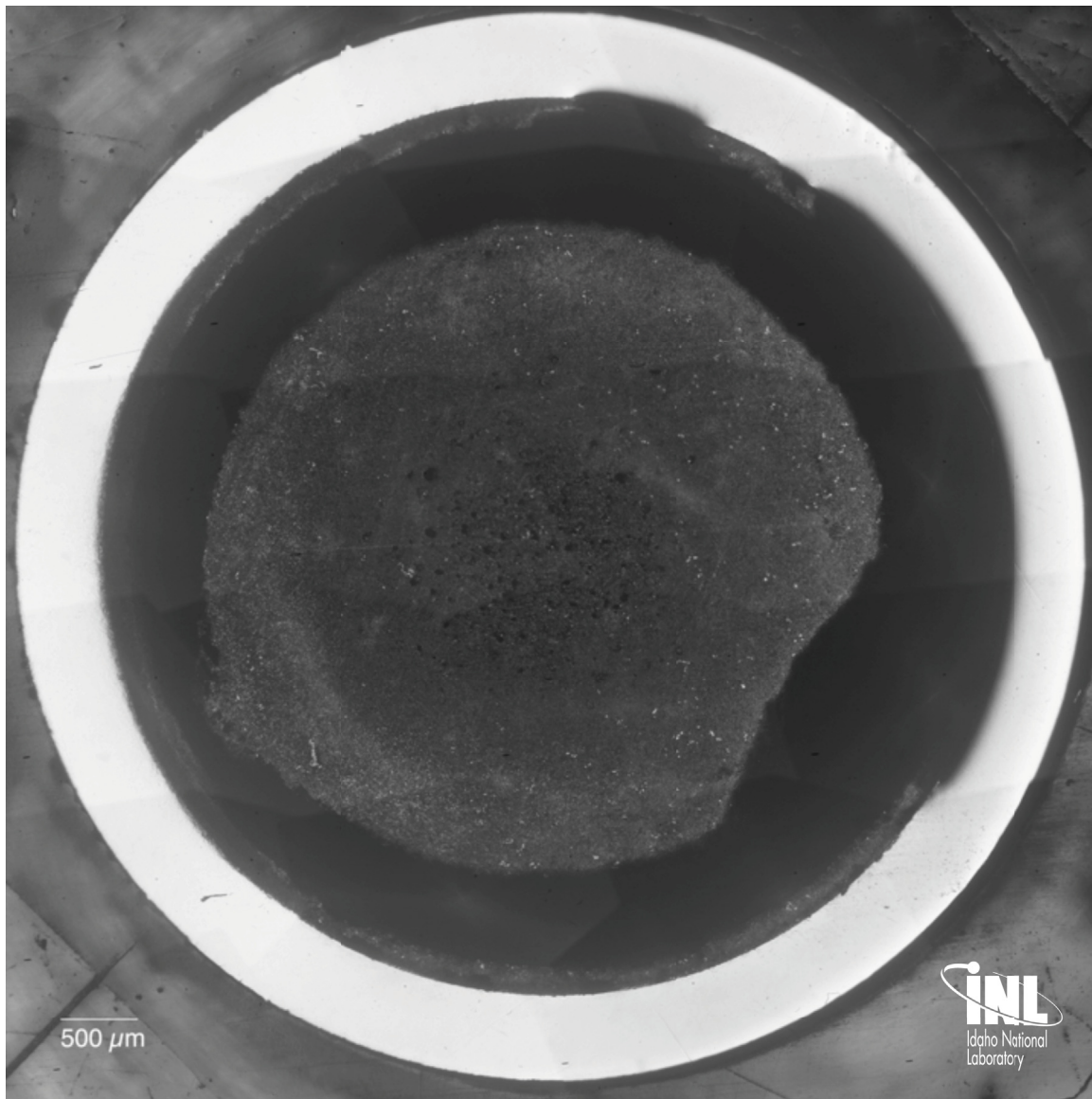
MFF 5 Pin S/N	195011	MET Mount Number	87T
X/L	0.72	Analysis Date	20110803
Distance from BOFP (inch) (cm)	30.75 78.1	Ave. PICT (°C)	612
Distance from BOFC (inch) (cm)	27.0 68.6	Ave. FCLT (°C)	736
Linear Power (W/cm)	417	Fission Density (fission/cm³)	2.87e21
FCCI (μm)	51	Burnup (at%)	8.1



MFF 5 Pin S/N	195011	MET Mount Number	88T
X/L	0.96	Analysis Date	2011
Distance from BOFP (inch) (cm)	39.75 100.9	Ave. PICT (°C)	635
Distance from BOFC (inch) (cm)	36.0 91.4	Ave. FCLT (°C)	709
Linear Power (W/cm)	249	Fission Density (fission/cm³)	1.71e21
FCCI (μm)	25.4	Burnup (at%)	4.8



MFF 3 Pin S/N	193045	MET Mount Number	79T
X/L	0.03	Analysis Date	20110801
Distance from BOFP (inch) (cm)	9.0 22.9	Ave. PICT (°C)	413
Distance from BOFC (inch) (cm)	1.0 2.54	Ave. FCLT (°C)	527
Linear Power (W/cm)	334	Fission Density (fission/cm³)	3.00e21
FCCI (μm)	0	Burnup (at %)	8.5



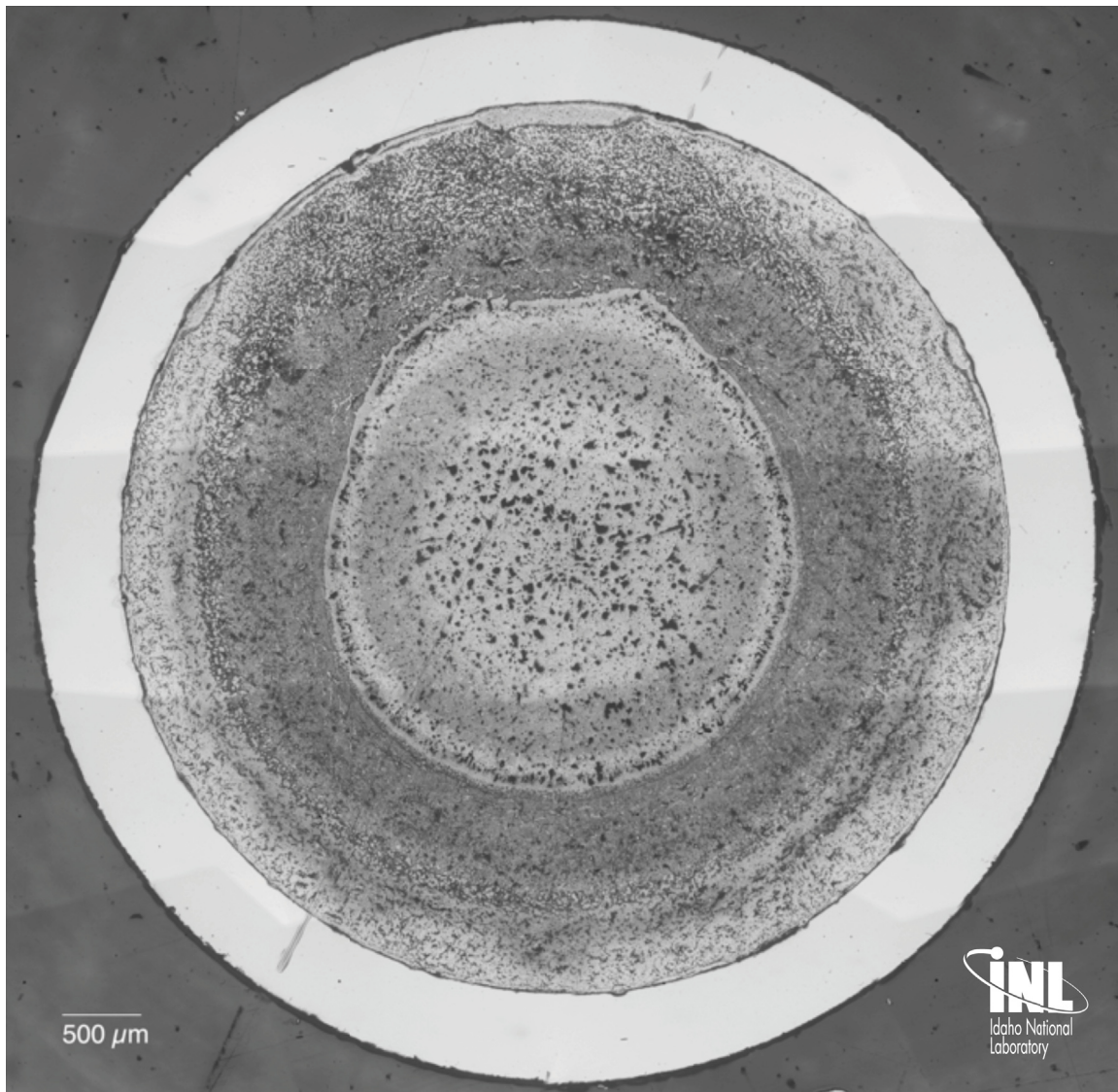
MFF 3 Pin S/N	193045	MET Mount Number	80T
X/L	0.25	Analysis Date	20110802
Distance from BOFP (inch) (cm)	17.0 43.2	Ave. PICT (°C)	475
Distance from BOFC (inch) (cm)	9.0 22.9	Ave. FCLT (°C)	619
Linear Power (W/cm)	446	Fission Density (fission/cm³)	4.02e21
FCCI (μm)	0	Burnup (at%)	11.3



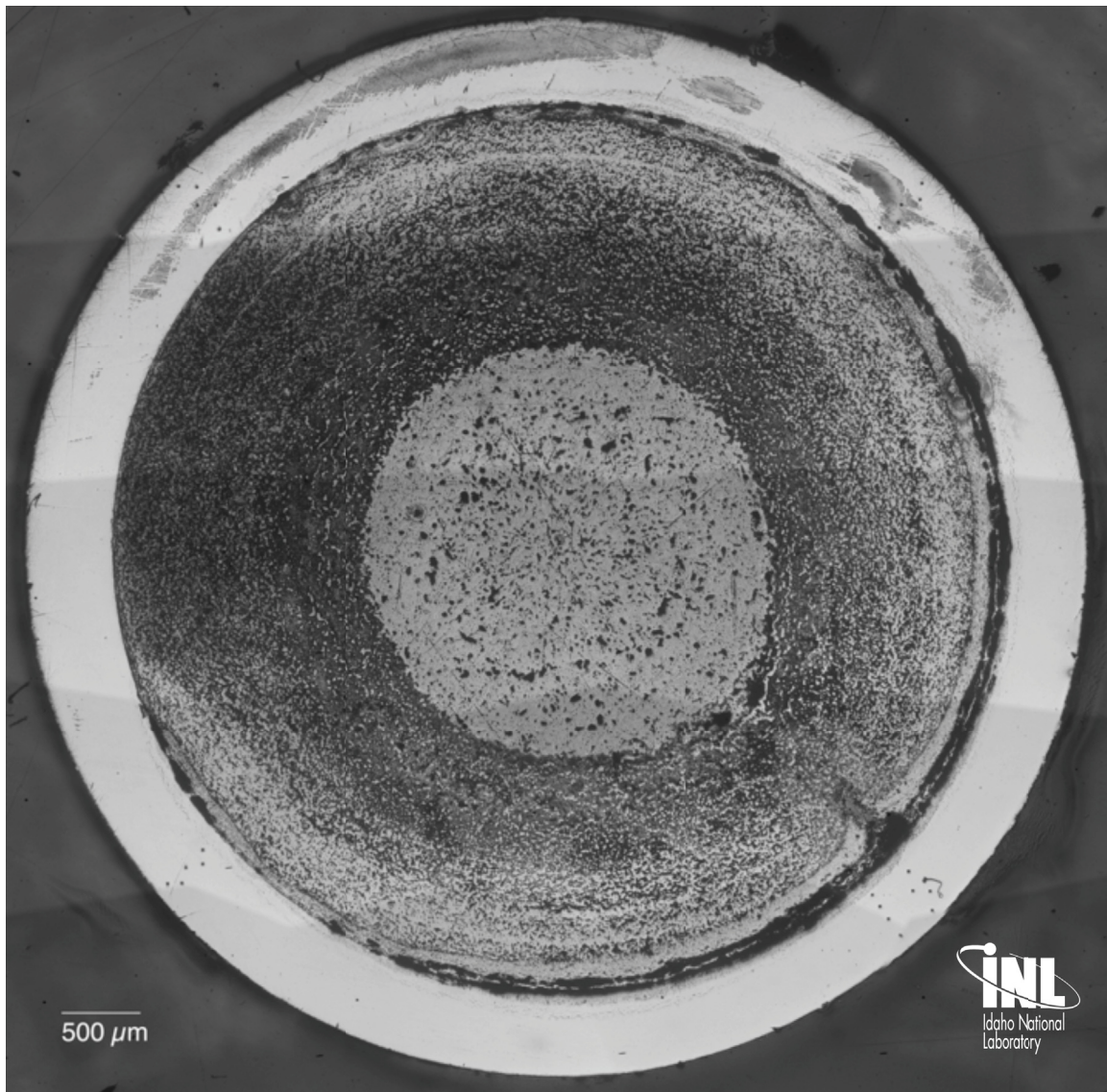
MFF 3 Pin S/N	193045	MET Mount Number	81T
X/L	0.49	Analysis Date	20110731
Distance from BOFP (inch) (cm)	26.0 66.0	Ave. PICT (°C)	550
Distance from BOFC (inch) (cm)	18.0 45.7	Ave. FCLT (°C)	700
Linear Power (W/cm)	489	Fission Density (fission/cm³)	4.39e21
FCCI (μm)	0	Burnup (at%)	12.4



MFF 3 Pin S/N	193045	MET Mount Number	82T
X/L	0.74	Analysis Date	20110801
Distance from BOFP (inch) (cm)	35.0 88.9	Ave. PICT (°C)	604
Distance from BOFC (inch) (cm)	27.0 68.5	Ave. FCLT (°C)	712
Linear Power (W/cm)	359	Fission Density (fission/cm³)	3.23e21
FCCI (μm)	76.2	Burnup (at%)	9.1



MFF 3 Pin S/N	193045	MET Mount Number	83T
X/L	0.98	Analysis Date	20110802
Distance from BOFP (inch) (cm)	44.0 111.8	Ave. PICT (°C)	615
Distance from BOFC (inch) (cm)	36.0 91.44	Ave. FCLT (°C)	682
Linear Power (W/cm)	223	Fission Density (fission/cm³)	2.0e21
FCCI (μm)	152.4	Burnup (at%)	5.7



Appendix F - Example BISON Model Input

```

[GlobalParams]
density = 13900. # [kg/m^3]
# uniform_refine = 1
[]

[Mesh]
file = X447_rz.e
[]

[ThermalContact]
[./thermal_contact]
type = GapHeatTransfer
variable = temp
master = 7
slave = 10
gap_conductivity = 1.4
min_gap = 1e-6
[../]

[]

[Variables]
active = 'temp C'

[./temp]
order = FIRST
family = LAGRANGE
initial_condition = 325 # initial temperature at ambient K
scaling = 1e-2
[../]

[./C]
order = FIRST
family = LAGRANGE
initial_condition = 0
scaling = 1e6
[../]

[]

[AuxVariables]
active = 'fission_rate burnup'

[./fission_rate]
order = FIRST
family = LAGRANGE
block = 2
[../]

[./burnup]
order = FIRST
family = LAGRANGE
block = 2
[../]

[]

[Functions]

```

```

active = 'initial_power_ramp '

[./initial_power_ramp]
  type = PiecewiseLinear
  x = '0 1e5' # secs to full power
  y = '0 1' # power is average normalized to peak of 1
[../]

[]

[Kernels]
  active = 'heat heat_ie heat_source ie_mass mass_fick mass_source mass_soret'

  [./heat]
    type = HeatConduction
    variable = temp
  [../]

  [./heat_ie]
    type = HeatConductionImplicitEuler
    variable = temp
  [../]

  [./heat_source]
    type = NeutronHeatSource
    variable = temp
    block = 2
    energy_per_fission = 3.57e-11 # [J/fission]
    fission_rate = fission_rate
  [../]

  [./ie_mass]
    type = ImplicitEuler
    variable = C
  [../]

  [./mass_fick]
    type = ArrheniusDiffusion
    variable = C
  [../]

  [./mass_soret]
    type = SoretDiffusion
    variable = C
    temp = temp
  [../]

  [./mass_source]
    type = BodyForce
    variable = C
    mass source in mol/m**3-s
    value = 6.95e-6
    block = 2
  [../]

[]

[AuxKernels]
  active = 'fissionrate burnup'

```



```

[./fissionrate]
    type = FissionRateAux
    variable= fission_rate
    block = 2
#    fission rate in fissions/m^3-s
    value = 1.96e19
    function = initial_power_ramp
[../]

[./burnup]
    type = BurnupAux
    variable = burnup
    block = 2
    fission_rate = fission_rate
    molecular_weight = 270.
[../]

[]

[BCs]
active = 'fixed_outer_temp fixed_clad_temp pellet_top fuel_surface'

[./fixed_outer_temp]
    type=DirichletBC
    boundary = '2'
    variable = temp
    value = 711
[../]

[./fixed_clad_temp]
    type=NeumannBC
    boundary = '1 3'
    variable=temp
    value=0
[../]

[./pellet_top]
    type = NeumannBC
    variable = C
    boundary = '4 11'
    value = 0.0
[../]

[./fuel_surface]
    type = ConvectiveMassFluxBC
    variable = C
    Boundary 10 is the fuel surface
    boundary = 10
    temp = temp
    dens = 7700 # [kg/m3]
    MW = 1.215 # [kg/mol]
    A1 = 1.8e-10
    Q = 11200
[../]

```

```
[]
```

```
[Materials]
```

```
active = 'fuel_thermal clad_thermal fuel_C fuel_soret clad_C clad_soret'
```

```
[/fuel_thermal]
```

```
type = HeatConductionMaterial
block = 2
thermal_conductivity = 33.
specific_heat = 330.
density = 13900
```

```
[../]
```

```
[/clad_thermal]
```

```
type = HeatConductionMaterial
block = 1
thermal_conductivity = 22
specific_heat = 330.
density = 6551.
```

```
[../]
```

```
# Diffusion coefficients in m2/sec
```

```
[/fuel_C]
```

```
type = ArrheniusDiffusionCoef
block = 2
d1 = 5e-3
q1 = 2.627e5
d2 = 0
q2 = 0
gas_constant = 8.3143
temp = temp
```

```
[../]
```

```
[/fuel_soret]
```

```
type = SoretDiffusionCoef
Ds = 0
```

```
# Heat of transport in J/mol
```

```
Qstar = 20000
d1 = 5e-3
q1 = 2.627e5
d2 = 0
q2 = 0
F = 1.0
gas_constant=8.3143
block=2
temp = temp
```

```
[../]
```

```
[/clad_C]
```

```
type = ArrheniusDiffusionCoef
block = 1
d1 = 5.
q1 = 150.
d2 = 0
q2 = 0
gas_constant = 8.3143
temp = temp
```

```

[../]

[./clad_soret]
type = SoretDiffusionCoef
Ds = 0
# Heat of transport in J/mol
Qstar = 20000
d1 = 5.
q1 = 150.
d2 = 0
q2 = 0
F = 1.0
gas_constant=8.3143
block=1
temp = temp
[../]

[]

[Executioner]
type = Transient

petsc_options = '-snes_mf_operator -ksp_monitor'
petsc_options_iname = '-snes_type -snes_ls -ksp_gmres_restart -pc_type -
pc_hypre_type -pc_hypre_boomeramg_max_iter'
petsc_options_value = 'ls          basic    101          hypre
boomeramg    4'

nl_rel_tol = 1e-4
nl_abs_tol = 1e-25
nl_abs_step_tol = 1e-25
nl_rel_step_tol = 1e-25

l_tol = 1e-4
l_max_its = 50

# time control
start_time = 0.0
dt = 10000
# end_time = 8.1562e6
end_time = 6.91e6 #X447 10% Burnup 641 EFPD
num_steps = 5000.

# direct control of time steps vs time (optional)
time_t = '0 1e5 1e6'
time_dt = '1e5 1e5 1e6'

[../]
[]

[Postprocessors]
# active = 'InnerTemp OuterTemp flux flux2 _dt E_Ce_Flux'
active = 'A_FCLTemp B_FuelSurfTemp C_InnerCladdingT D_OuterCladdingT _dt
E_Ce_Flux'

[./A_FCLTemp]

```

```

        type = SideAverageValue
        boundary = 12
        variable = temp
    [../]

[./B_FuelSurfTemp]
    type = SideAverageValue
    boundary = 10
    variable = temp
[../]

[./C_InnerCladdingT]
    type = SideAverageValue
    boundary = 5
    variable = temp
[../]

[./D_OuterCladdingT]
    type = SideAverageValue
    boundary = 2
    variable = temp
[../]

[./E_Ce_Flux]
    type = SideIntegralMassFlux_2
    variable = C
    boundary = 10
[../]

[./_dt]
    type = PrintDT
[../]
[]

[Output]
    file_base = met_diff_X447_2d_rz
    interval = 1
    output_initial = true
#   postprocessor_csv = true
    exodus = true
[]

```